



Departament d'Enginyeria Química
Escola Tècnica Superior d'Enginyeria Química
Universitat Rovira i Virgili

Catalysts for Steam Reforming of Ethanol in a Catalytic Wall Reactor

José Antonio Torres Rivero

Tarragona, December 2007

UNIVERSITAT ROVIRA I VIRGILI
CATALYSTS FOR STEAM REFORMING OF ETHANOL IN A CATALYTIC WALL REACTOR
José Antonio Torres Rivero
ISBN:978-84-691-3377-4/DL:T.710-2008

El Dr. DANIEL MONTANÉ CALAF, profesor titular del Departamento de Ingeniería Química de la Universidad Rovira i Virgili,

HACE CONSTAR

Que el presente trabajo titulado,

**CATALYSTS FOR STEAM REFORMING OF ETHANOL IN A CATALYTIC WALL
REACTOR**

Que presenta José Antonio Torres para optar al Grado de Doctor en Ingeniería Química y de Procesos, se ha realizado bajo mi supervisión en los laboratorios del Departamento de Ingeniería Química de la Universidad Rovira i Virgili, y que todos los resultados presentados y su análisis son fruto de la investigación realizada por el mencionado doctorando.

Y para vuestro conocimiento y los efectos que correspondan, firmo esta certificación.

Tarragona, 03 de Diciembre de 2007

Dr. Daniel Montané i Calaf
Profesor Titular de la Universidad Rovira I Virgili

UNIVERSITAT ROVIRA I VIRGILI
CATALYSTS FOR STEAM REFORMING OF ETHANOL IN A CATALYTIC WALL REACTOR
José Antonio Torres Rivero
ISBN:978-84-691-3377-4/DL:T.710-2008

Table of Contents

Table of Contents	v
List of Tables	viii
List of Figures	x
Acknowledgements	xvii
Summary	xix
Resumen	xxi
Nomenclature and Symbols	xxiii
1 Introduction	1
<hr/>	
1-1 Context	1
1-2 Objectives	2
1-3 Document overview	3
Chapter references	5
2 Fundamental Aspects and Background	7
<hr/>	
2-1 Basic Aspects on Fuel Cell Applications	7
2-1-1 Fuel Cell Features	7
2-1-2 Fuel Cells Feeding	8
2-1-3 Catalytic Reforming	9
2-1-4 Fuel Processors	10
2-2 Trends in reforming technologies	11
2-2-1 Multifunctional reactor concept	12
2-2-2 Structured reactor for heat reaction integration	16
2-2-3 Reforming Chemistry	20
2-3 Steam Reforming of Ethanol	29
2-3-1 SRE catalyst composition	29
2-3-2 SRE mechanism and kinetics	30
2-4 Structured catalyst preparation	36
Chapter references	43

3	Material and Methods	49
3-1	Materials	49
3-2	Catalyst preparation	51
3-2-1	Ni catalyst	53
3-2-2	Co catalyst	54
3-2-3	Catalytic plates by washcoating	54
3-2-4	Catalytic plates by precipitation	55
3-3	Experimental Equipment	57
3-3-1	Packed Bed Reactor Configuration	57
3-3-2	Catalytic Wall Reactor Configuration	60
3-4	Analytical techniques	64
3-4-1	Catalyst characterization techniques	64
3-4-2	Fluid analysis techniques	67
3-4-3	Calibration techniques	70
3-5	Results Management	72
3-6	Simulation techniques	73
3-4-1	Software Packages	73
3-4-2	Fluid analysis techniques	74
	Chapter references	76
4	Thermodynamic Simulation	79
4-1	Reaction equilibrium	80
4-2	Process thermodynamic	85
4-2-1	Black box	86
4-2-2	Fuel processor integrated with H ₂ separation	88
4-3	Catalytic Tests and Equilibrium Predictions	93
	Chapter references	96
5	Screening Catalyst Tests	97
5-1	Screen Catalyst Formulations	97
5-2	Characterize Ni and Co Powder Catalyst	100

5-3	Perform Multi-factorial Experiments	108
	Chapter references	117
6	Catalytic Plates Tests	119
6-1	Conceptual 2D model for designing the CWR	119
6-1-1	Mathematical Model	119
6-1-2	Gas phase results	123
6-1-3	Solid block results	130
6-2	Characterize catalyst plates	133
6-3	Test for catalytic plates	141
6-3-1	Steam Reforming of Ethanol	142
6-3-2	Steam Reforming of Methane and Water Gas Shift	146
6-4	Simulate catalytic wall reactor configuration with 1D model	148
	Chapter references	154
7	Conclusions and Future Work	155
7-1	Conclusions	155
7-1-1	Thermodynamic Analysis	155
7-1-2	Screening Catalysts Preparation and Evaluation	156
7-1-3	Catalytic Plates Preparation, Evaluation, and Catalytic Wall Reactor Simulation	156
7-2	Future Work	157
Appendix		
A-1	Internal Limitations by Mass and Heat Transport	159
A-2	Catalyst Preparation Procedures	171

List of Tables

Table		Page
2-1	Some characteristics for the different types of Fuel Cells	8
2-2	Basic reactions employed on reforming process. SR, POX, and ATR are used as chemical reactions to produce H ₂ ; while WGS and PROX are applied to remove undesired CO content	20
2-3	Chemical reactions of the six steps standard chemical process for SR of Hydrocarbons	24
2-4	Elementary steps according to a simplify model for SR of Ethane	26
2-5	Elementary steps according to a simplify model for SRM	27
2-6	Main possible reactions reported in literature for the SRE	33
2-7	Kinetic Parameters for SRE on previous studies	34
2-8	L-H mechanism for SRE on Co/Al ₂ O ₃ catalysts proposed by Sahoo (2006)	35
2-9	List of methods and materials employed in several structure catalyst preparation methods from Meille (2006)	42
3-1	Gases specifications	49
3-2	Chemicals specifications	50
3-3	Features and operation conditions for fluid analysis equipments Gas Chromatography, High Pressure Liquid Chromatography, and Mass Spectrometry	68
3-4	Sensitivity factors for Gas Chromatography and High Pressure Liquid Chromatography.	71
3-5	Complete lists of Mass Spectrometer sensitivity factors. Contributions of minority compounds which factors are in the order of 10 ⁶ can be assumed negligible.	71
3-6	Dimensional groups in transport process with chemical reaction	75
5-1	Composition of the catalysts and the operational conditions selected for the first series of PBR experiments.	98
5-2	Chemical composition of calcinated catalysts obtained from EDS and AAS techniques. Composition target was: 15% Ni and 8% La for Ni based catalyst; 10% Co for Co based catalyst; and 1% Fe or 1% Mn for promoter metals at Co-X/ZnO catalysts.	101
5-3	Crystallite Size for Ni particles using the Sherrer equation	102
5-4	Catalyst properties from N ₂ adsorption-desorption isotherms and H ₂ chemisorption	104

Table		Page
5-5	Operational factors selected for estimating significant influences on the experimental results according to the multifactorial experimental design.	108
5-6	Factor and interaction effects corresponding to Set I ($X_a < 50\%$) from the analysis of variance. Symbol x indicates a significant influence at 95% of probability.	109
5-7	Factor and interaction effects corresponding to Set II ($X_a > 50\%$) from the analysis of variance. Symbol x indicates a significant influence at 95% of probability.	109
6-1	Mathematical model applied to CWR shown on figure 6-1	121
6-2	Factors used for calculation: reactor geometry, inlet conditions and kinetic parameters	122
6-3	Thickness, Coating Parameters (from IFME) and EDS results	138
6-4	Operational conditions for evaluating Ni and Co catalytic plates for Steam Reforming of Ethanol, Steam Reforming of Methane, and Water Gas Shift	141
6-5	Kinetic and model parameters for cases I and II. C_{B0} to C_{A0} ratio was fixed at 0.773	150

List of Figures

Figure		Page
2-1	Standard fuel processor diagram which consists of: pre-heating step, reaction chamber, heat exchanger (which helps to maintaining an average reaction temperature), and combustion chamber.	11
2-2	Scheme of possible synergies due to a multidisciplinary approach among disciplines related with the catalysis (Centi and Perathoner 2003). More efficient process can be developed by taking advantage of: mature knowledge on basic sciences, better engineering products, and match information between experimental and theoretical methods.	13
2-3	Integration levels in reactor and catalytic processes (Schmidt 1998). Reactor designs focus on interaction with other process unit (such as separators and heat exchangers) and between different phases (fluid and solid); while catalyst involves mass/heat transport phenomena and surface reaction at pore level.	13
2-4	Fuel processor scheme, using multifunctional reactors to increment efficiency by enhancing thermal and mass transfer rates. A single device integrates multiple functions: reaction, heat exchange and separation.	14
2-5	Transport process (top scheme) are facilitated by arranging catalyst in structures as catalytic walls (at right-bottom) instead of using disordered configurations like packed bed reactors (at left-bottom).	15
2-6	Diagrams for Catalytic Wall Reactor and plate-type design which constitute examples of multifunctional reactor to integrated exothermic and endothermic reactions to intensify the heat transport (Ferreira-Aparicio, Benito et al. 2005).	16
2-7	Schemes of ceramic and metallic monoliths from (Tomasic and Jovic 2006). Monoliths are a structured support that receives catalyst as washcoat.	17
2-8	The integrated fuel processor is an example of multifunctional reactor with catalytic plates. It performs four functions: fuel evaporation, auto-thermal methanol reforming, preferential oxidation for CO removal and H ₂ burning	18
2-9	CWR scheme for coupling reforming and combustion reactions. Catalysts are deposited on both sides of the separating wall. As a result, major restrictions are caused by the mass transport between the bulk fluid and the catalyst active sites, at coat pores	18

Figure		Page
2-10	Classification of common fuels and catalyst employed in reforming process. Noble active metals are used in lower concentration than others because of economical reasons.	21
2-11	Process diagram for hydrogen production by SR of hydrocarbons (Bartolomew, 2006). Chemical reactions are showed on table 2-2. Reforming is carried out through two units -steps 2 and 3- to prevent undesired reactions like cracking at high temperatures.	25
2-12	Two important intermediates observed in several catalytic studies for SRE; as a result of two distinct reaction pathways: ethanol dehydration; and ethanol dehydrogenation (Benito et al., 2006; Haryanto et al., 2006).	31
2-13	Coating of γ -Al ₂ O ₃ on FeCrAl support; on top there is a layer of alumina adhered by washcoating; and whiskers product of thermal treatment are below it	39
2-14	Scheme representation of binder action during liquid evaporation, according to Nijhuis (2001) (a) wet slurry on surface (O large particles, black o binder); (b) first stage of drying; (c) large particles start to touch each other while binder is occupying interface places due to capilar forces; (d) binder deposited at the end of the dry process	40
3-1	Diagram with the procedure sequence followed to prepare powder catalysts. Catalysts can be classified on four groups as function of: active metal (nickel or cobalt) and structure (powder or coat deposited over a metallic plate)	51
3-2	Diagram with the sequential program followed to prepare catalytic coating over metal plates. The catalysts can be classified on four groups as function of: active metal (nickel or cobalt) and structure (powder or coat deposited over a metallic plate)	52
3-3	Paint applicator equipment (K-101P Coater Applicator; R.K. Print Coat Instruments) where plate was immersed under the slurry during 1 min and the storage container was removed using a constant velocity around 3cm min ⁻¹ : (a) Storage container and paint applicator images (Torras, 2005), (b) Lateral section of the wash-coating setup, (c) Lateral section during the immersion step, (d) Lateral section during the storage container withdraw.	56
3-4	Packed Bed Reactor equipment for screening catalyst experiments. Ethanol mixed with water and nitrogen is pump into the tubular reactor (15 mm inner diameter by 300 mm length, stainless steel 316L) which is filled with a powder mixture composed by catalyst and inert particles. (a) general scheme, (b) images for the most important equipments	58

Figure		Page
3-5	Diagram with details of the catalytic bed	59
3-6	Block designed for performing catalytic plate tests. Fluid enters at the pre-heating channel, until reach the catalytic plate. Two square electrical resistances heat the steel block at top and bottom block sides; while the laterals are isolated. A graphite sealing prevents gas losses before reaching the reactor output.	61
3-7	Catalytic Wall Reactor Unit designed and constructed for evaluating the reaction performance of catalytic plates. It is composed by five units: feeder, pre-heater, reactor, separator, and instruments for analyzing and measuring: (a) general scheme, (b) images from the most important components	62
3-8	Images for illustrating the five key steps for mounting catalytic plates in the Catalytic Wall Reactor Unit (a) put plate catalyst and graphite seal into the void spaces, (b) close steel block, (c) fit the block into the aluminum box, (d) close the aluminum box, and (e) introduce it into the drying oven and connect electrical and fluid connections	63
3-9	Images for some characterization equipments: (a) Scanning Electron Microscope (Torné, 2006), (b) BET instrument (Torné, 2006) (c) Shaker for vibrational tests	66
3-10	Mass spectrum for some components measured using the MS from reference (NIST, 2007)	69
4-1	Results for reactor equilibrium composition for final products and yield of hydrogen for SRE at 1, 5, and 10 atm; and SC ratios of 2, 3, and 4 mol/mol; in the temperature interval from 300 to 900°C.	81
4-2	Results for reactor equilibrium composition for final products and yield of hydrogen for SRM at 1, 5, and 10 atm; and SC ratios of 2, 3, and 4 mol/mol; in the temperature interval from 300 to 900°C.	83
4-3	Results for reactor equilibrium composition for final products and yield of hydrogen for WGS at 1, 5, and 10 atm; and SC ratios of 2, 3, and 4 mol/mol; in the temperature interval from 300 to 900°C.	84
4-4	Black box diagram considering Steam Reforming of Ethanol reaction stoichiometry to evaluate the final product composition at the fuel processor.	85
4-5	Stoichiometric analysis for the SRE: thermal efficiency, η_{LHV} , and hydrogen yield as a function of the SC ratio for the adiabatic system depicted on figure 3-4	87

Figure		Page
4-6	Diagram for the fuel processor integrated with a membrane separation unit for H ₂ purification. Convenience for including WGS unit is analyzed by process modeling	89
4-7	Reformer temperature required to achieve auto-thermal operation for three process configurations: (i) reformer without WGS and with condensed excess water -top-, (ii) reformer with WGS and with condensed excess water -middle-, and (iii) reformer with WGS and without condensing excess water -bottom-	90
4-8	Result for a fuel processor with condensed excess water and WGS: reformer temperature required to achieve auto-thermal operation of the fuel processor, thermal efficiency of the system (η_{LHV}), air consumption at 10% air excess	91
4-9	Experimental composition vs. thermodynamic equilibrium composition for three kind of catalyst reported in the literature.	94
5-1	First series of Packed Bed Reactor experiments results using three catalyst formulations with Ni as an active phase, fixing temperature at 500°C, liquid flow rate 4 g min ⁻¹ and SC at 3.	99
5-2	Schematic representation for powder catalysts used in this work.	100
5-3	Environmental Scanning Electron Microscopy (ESEM) images and EDS spectra for Co-Fe/ZnO and Ni/La ₂ O ₃ - γ Al ₂ O ₃ catalysts.	101
5-4	X Ray Diffraction (XRD) profiles of several calcined samples of: (a) Ni/La ₂ O ₃ -Al ₂ O ₃ catalysts before reduction (i, iii, v) and after reduction at 823K (ii, iv).	103
5-5	Transmission Electron Microscopy (TEM) images for fresh Ni/La ₂ O ₃ - γ Al ₂ O ₃ catalyst (Ni15La08)	104
5-6	Quantity adsorbed as function of the relative pressure, and pore volume distribution from N ₂ adsorption-desorption isotherms for the Ni/La ₂ O ₃ - γ Al ₂ O ₃	105
5-7	Quantity adsorbed as function of the relative pressure, and pore volume distribution from N ₂ adsorption-desorption isotherms for Co based catalysts	106
5-8	Scanning Electron Microscopy images of Ni/La ₂ O ₃ - γ Al ₂ O ₃ catalyst sample illustrating presence of carbon deposited after reaction	107
5-9	Effect of SC on H ₂ flow and X _a ; Temperature 500°C; W/Fao of 10 g min mol ⁻¹ ; catalyst formulation Ni15La08	110

Figure		Page
5-10	Intermediate and final products yield for three kind of Ni based catalysts. Experiments performed under similar operational conditions	111
5-11	Intermediate and final products yield for three kind of Ni based catalysts. Experiments performed under similar operational conditions	111
5-12	Ethanol conversion and H ₂ yield as a function of the contact time for Ni and Co based catalysts under similar operational conditions (SC=4, T=500°C)	112
5-13	Ni catalyst selectivity to final (H ₂ , CO, CO ₂ , CH ₄) and intermediate products (C ₂ H ₄ , C ₂ H ₆ , C ₂ H ₄ O, C ₂ H ₄ O ₂) as a function of the contact time (W/Fa_0)	114
5-14	Co catalyst selectivity to final (H ₂ , CO, CO ₂ , CH ₄) and intermediate products (C ₂ H ₄ , C ₂ H ₆ , C ₂ H ₄ O, C ₂ H ₄ O ₂) as a function of the contact time (W/Fa_0).	115
5-15	H ₂ to CH ₄ selectivity ratio for Ni and Co based catalysts as a function of the contact time (W/Fa_0). Operational conditions were: Temperature at 500°C and SC at 4. Dot line represents equilibrium	116
6-1	Diagram of studied catalytic plate, an adiabatic reactor with symmetry at the centerline of the channel. Main assumptions are: steady state, ideal gas behavior, chemical reaction only at the catalyst layers	120
6-2	Contour plot for gas velocity at mass flow rate $m=0.1 \text{ g min}^{-1}$. Other models parameters are: $Ea=97 \text{ kJ mol}^{-1}$ and $ko=1.3 \cdot 10^4 \text{ s}^{-1}$.	123
6-3	Contour plot for gas phase temperature and concentration under three different levels of reaction rate constant. Other models parameters are: $Ea=97 \text{ kJ mol}^{-1}$ and $m=0.1 \text{ g min}^{-1}$.	125
6-4	Temperature and concentration profiles for base case $-Ea=97 \text{ kJ mol}^{-1}$ and $m=0.1 \text{ g min}^{-1}$; with several reaction rate constants $-ko$ from $1.3 \cdot 10$ to $1.3 \cdot 10^4$; (a) Wall Temperature; (b) Wall concentration (c) Bulk temperature at the outlet (d) Bulk concentration at the outlet	126
6-5	Contour plot for the gas phase temperature and concentration under three different levels of activation energy. Other models parameters are: $ko=1.3 \cdot 10^4$ and $m=0.01 \text{ g/min}$.	128
6-6	Dimensionless groups Nu , Sh , and Da as function of axial length for three levels of the mass flow rate, from 0.01 to 1.00 g min^{-1} .	129

Figure		Page
6-7	Contour plot for block temperature under three different levels of reaction rate constant. Other models parameters are: $E_a=97 \text{ kJ mol}^{-1}$ and $m=0.1 \text{ g min}^{-1}$. Temperature range covers from 743 to 794 K.	131
6-8	Temperature profile at $z=L$ inside the steel block, considering three levels of the reaction rate constant from $1.3 \cdot 10^2$ to $1.3 \cdot 10^4 \text{ s}^{-1}$, mass flow rate at 0.10 g min^{-1} while the activation energy is 97 kJ mol^{-1} .	132
6-9	Screening different recipes for preparing the impregnation of catalyst over FeCr plates.	133
6-10	Environmental Scanning Electron Microscopy images from lateral perspective of catalytic plates prepared with variations in the slurry compound: acid from 2.38 to 4.05 $\text{mol mol}_{\text{Al}_2\text{O}_3}^{-1}$; bohemite from 0.03 to 0.13 $\text{g g}_{\text{Al}_2\text{O}_3}^{-1}$; and PVA from 0.6 to 2.0 $\text{g g}_{\text{Al}_2\text{O}_3}^{-1}$	135
6-11	Environmental Scanning Electron Microscopy images from lateral perspective of Ni/La ₂ O ₃ - γ Al ₂ O ₃ catalytic plates prepared with slurries with composition: acid 2.38 $\text{mol mol}_{\text{Al}_2\text{O}_3}^{-1}$; bohemite from 0.1 to 6.0 $\text{g g}_{\text{Al}_2\text{O}_3}^{-1}$; and PVA from 0.05 to 0.20 $\text{g g}_{\text{Al}_2\text{O}_3}^{-1}$	136
6-12	Environmental Scanning Electron Microscopy images from Ni/La ₂ O ₃ - γ Al ₂ O ₃ catalytic coating on metallic plates. It is employed a horizontal perspective at different magnification factors and using two kinds of electron detectors.	137
6-13	EDS and X-ray diffraction spectra for Ni/La ₂ O ₃ - γ Al ₂ O ₃ catalyst coating before reduction: (■) Nickel Oxide, NiO; (☆) aluminum oxide γ Al ₂ O ₃ ; (X) Lanthanum Aluminum Oxide, LaAlO ₃ ; (○) bohemite, and (△) Iron chromium Fe-Cr	139
6-14	Vibration test using 30 min steps, frequency from 20 to 50 Hz; acceleration from 2G to 10 G and velocity from 67 to 350 mms^{-1} .	140
6-15	Steam Reforming of Ethanol through Ni catalyst supported on metallic plates, using operational conditions 100 mg catalyst, $SC=4$, $m=1 \text{ ml h}^{-1}$. (a) average conversion 0.99, temperature 480°C; (b) average conversion 0.50, temperature 450°C.	143
6-16	Steam Reforming of Ethanol through Co catalyst supported on metallic plates, using operational conditions temperature 480°C, $SC=4$, $m=1 \text{ ml h}^{-1}$. (a) 80 mg catalyst, average conversion 0.32; (b) 110 mg catalyst, average conversion 0.38.	144
6-17	Temperature at different axial positions for the Steam Reforming of Ethanol Ni at ethanol conversion $x_a=0.99$, using operational conditions: temperature 480°C, SC from 4, and 100 mg catalyst	145

Figure		Page
6-18	Steam Reforming of Methane and Water Gas Shift with Ni and Co catalyst supported on metallic plates, using se operational conditions: temperature 480°C, SC at 10, and catalyst weight from 100 mg (Ni) to 110 mg (Co)	147
6-19	CWR conceptual model for coupling exothermic and endothermic reactions, such as SR (channel A) with combustion (channel B). Co-current flow is considered to simplify as much as possible the sensitivity analysis.	148
6-20	Results expressed in terms of dimensionless independent variables –conversion of the endothermic reaction (x_a) and temperature (θ)- as function of the dependent variable - conversion of the exothermic reaction (x_b)-; considering a CWR with complete combustion conversion (x_b from 0 to 1).	152
6-21	Normalized sensitivity for case I using conversion of endothermic reaction (x_a) and dimensionless temperature, θ as variables under study; varying velocities ratio V from 5/3.5 to 10/3.5 (black triangle), T_0 from 773 to 723 K (gray circle), and C_{A0} to C_{B0} ratio from 1.75/1.35 to 1.75/0.94 (white circle)	153

Acknowledgements

The author would like to communicate his genuine gratitude to:

- The tribunal members by their effort for attending this time consuming task.
- Prof. Daniel Montané for his supervision, support, and patience throughout the time required to complete this work.
- Members of the research group “Institut de Tècniques Energètiques”, from Universitat Politècnica de Catalunya; which collaborate on the preparation and characterization of Co based catalysts: Dr. Jordi Llorca and Albert Casanovas.
- Professors and technicians from the research group “Biopolimeros Vegetales”; who offer me facilities and valuable assistance: Dr. Joan Salvadó, Dr. Xavier Farriol, Dr. Ricard Garcia Valls, Dr. Francesc Ferrando, Dr. Marta Giamberini, and Dr. Vanessa Fierro, Sr. Josefa Lazaro, and Sr. Modest Ruana. Specially, thanks to Dr. Radka Nedialkova, Sr. Josefa Lazaro, and Sr. Modest Ruana because all of them gave me a lot of support at the beginning or at the end of this work.
- Universitat Rovira i Virgili for his PhD scholarship.
- Colleagues from Tarragona for giving support, and for offering their company and comprehension: Carles, Vanessa, Luizildo, Debora, Jorgelina, Henry, Camilo, Nour-eddine, Freddy, Daiyong and Guillermo. Also thanks to the Venezuelan community: Marlene, Aurelio, Alfredo, Izakar, Irama, and Carmelo.
- Friends for providing help in the appropriate moments: Marelys, Diego, Miguel, Norian, Alex, Maria Eugenia, Pedro, David, Silvia, Cinta, and Robert.
- To every person who helps me in the long way that lead to this point. I am in debt with them, although major part of them probably is not conscientious of their valuable contribution.
- To my beloved family; in particular to my grandparents, parents, brother, and of course thanks to my beloved wife and son.

Summary

Energy has become a fundamental necessity to guarantee modern society development. Among different alternatives possible to produce energy, hydrogen presents several characteristics which make it an attractive energy vector: first, more efficient processes to transform chemical energy into electricity –such as Fuel Cells that, in addition, will help to reduce significantly CO₂ emission levels-; and second, hydrogen can be produced from a large variety of feed stocks, including fossil and renewable resources. However, as hydrogen production technologies for Fuel Cell applications are not available commercially yet, it still requires additional R&D efforts.

The principal objective of this thesis was to evaluate technical feasibility for preparing and using catalytic plates in a Catalytic Wall Reactor configuration to produce hydrogen by Steam Reforming of Ethanol under conditions of high thermal efficiency. To fulfill the overall and specific objectives, a systematic experimental plan was designed and executed. It was composed of three main parts: documentation, experimentation and numerical simulation. Background information is divided into three branches, first a detailed overview of technical features for reforming technology, followed by a descriptive review of Steam Reforming of Ethanol key aspects for catalysts preparation and reaction performance. Third is presented a comprehensive examination on structured reactor and catalyst preparation methods. In this part is exposed a detailed explanation of materials, equipments, and methods employed for screening catalyst and evaluating catalytic reactor performance. Also, is presented employed techniques for catalyst characterization and fluid analysis. Finally are described tools for numerical simulation.

First component of numerical simulations evaluates possible thermodynamic constrains through specific analyses based on thermodynamic equilibrium of reactor and integrated fuel processor. Then, is performed a mapping for the set of four operational variables (temperature, steam to carbon ratio, pressure, and hydrogen recovery in the membrane separator), that allow an auto-thermal operation of the fuel processor. The suitability and advantages of the different catalysts preparations that are known from recent publications are discussed on the basis of the operation conditions determined on the thermodynamic analysis.

Experimental work is performed for powder catalyst characterization and catalytic experimentation using a Packed Bed Reactor (PBR). It has conducted a systematic study to compare the activity and selectivity of two types of catalyst at moderate temperature and steam to carbon (SC) ratios. Nickel-based catalysts (Ni/La₂O₃-Al₂O₃) and novel Co-based catalysts (Co-Fe/ZnO and Co-Mn/ZnO) have been prepared and tested at temperatures of 400 and 500 °C, Steam to Carbon (SC) molar ratios of 2 and 4, and contact times from 4.3 to 1100 min·g_{cat} mol_{EIOH}⁻¹, covering a range of ethanol conversion from 20 to 100%. A multifactorial design analysis has been conducted to establish the significance of temperature, SC ratio, contact time and catalyst formulation on ethanol conversion and selectivity towards the different reaction products.

At last, it is carried out the catalytic plate characterization, simulation and experimentation using a Catalytic Wall Reactor configuration. First, is used a 2D modeling to analyze main characteristics of the Catalytic Wall Reactor designed and constructed to perform reactions on the prepared catalytic plates. Prepared catalytic plates are characterize in a similar way to that employed for the powder catalysts. After that, it was conducted a systematic study to compare the activity and selectivity of two types of catalytic plates. 1D model reveals main aspects on thermal performance for a theoretical Catalytic Wall Reactor using two co-current channels with endothermic and exothermic reactions respectively.

Main conclusion from this work is that Steam Reforming of Ethanol can be performed at high thermal efficiency if the design of the fuel processor is based on structured catalytic wall reactors with integrated heat recovery coupled to a separation unit for hydrogen purification. Catalytic plates have proven to be a key component on CWR because improves significantly the heat transfer which is required to sustain endothermic reactions.

Resumen

La energía se ha convertido en una necesidad vital para garantizar el desarrollo de las sociedades modernas. Entre las diferentes posibles alternativas para producir energía, el hidrogeno presenta varias características que lo convierten en un atractivo vector energético: primero, se trata de una tecnología más eficiente para transformar la energía química en electricidad –por ejemplo, utilizando pilas de-combustible, las cuales también reducen de manera significativa los niveles de emisión de CO_2 -; en segundo lugar, el hidrogeno puede ser producido a partir de una amplia variedad de materias primas, incluyendo recursos renovables y no renovables. Sin embargo, las tecnologías para producir hidrogeno para aplicaciones con pilas de combustible aun requieren de un esfuerzo en investigación y desarrollo.

El objetivo principal de esta tesis fue de evaluar técnicamente las opciones para preparar y utilizar catalizadores en placas insertados en un reactor de pared catalítica para producir hidrogeno mediante el reformado por vapor de etanol bajo condiciones de alta eficiencia térmica. Para completar el objetivo general y los objetivos específicos, se diseñó un plan experimental sistemático, compuesto de tres partes: documentación, experimentación y simulación numérica. La información utilizada se puede clasificar en tres ramas: primero, una revisión detallada de las características generales que presentan las técnicas de reformado, seguido por una revisión descriptiva del reformado por vapor de etanol, enfocado en los principales aspectos de la preparación de catalizadores y la realización de la reacción química. A continuación en segundo lugar, se presenta una descripción acerca de reactores estructurados y los métodos para preparar catalizadores. Por último, en tercer lugar, se expone una explicación centrada en los materiales, equipos y métodos empleados para explorar el rendimiento de los catalizadores. Esta parte incluye la descripción de: algunas de las técnicas analíticas más comunes para caracterizar y evaluar tanto catalizadores como compuestos químicos y la descripción de las herramientas utilizadas en la simulación numérica.

El primer bloque de simulación numérica tiene como fin evaluar las posibles restricciones termodinámicas por medio de análisis específicos basados en el equilibrio termodinámico, tanto del reactor como del proceso integrado. Luego, se ejecuta un mapeo del conjunto de condiciones operacionales, compuesto por cuatro variables principales: (temperatura, relación vapor carbón, presión y factor de recobro de hidrogeno en el separador

de membrana). Ello con el fin de garantizar una operación auto-térmica del procesador de combustible. Se compara la habilidad y la ventaja entre los diferentes tipos de catalizadores publicados en trabajos previos en base a las condiciones termodinámicas ideales determinadas en el análisis termodinámico.

Para los catalizadores en polvo, se realizó experimentos de caracterización y reacción mediante el empleo de un reactor de lecho fijo. Se ha efectuado un estudio sistemático para comparar la actividad y la selectividad de dos tipos de catalizadores, bajo condiciones moderadas de temperatura y relación vapor carbón. Los catalizadores basados en níquel ($\text{Ni/La}_2\text{O}_3\text{-Al}_2\text{O}_3$) y cobalto (Co-Fe/ZnO y Co-Mn/ZnO) han sido preparados y probados a las siguientes condiciones: temperatura en el rango de $400\text{-}500^\circ\text{C}$, relación vapor carbono entre 2 y 4, tiempo de contacto desde 4.3 hasta 1100 $\text{min}\cdot\text{gcat mol}_{\text{EtOH}}^{-1}$, cubriendo un rango de conversión de etanol desde 20 hasta 100%. Se ha efectuado un diseño de análisis multifactorial para establecer la influencia de las variables (temperatura, relación vapor carbón, tiempo de contacto y formulación del catalizador) en términos de la conversión de etanol y la selectividad hacia los diferentes productos.

Por último, se ha efectuado la caracterización, simulación y experimentación utilizando una configuración de reactor de pared catalítica. Primero, se emplea un modelo en 2D para analizar las características principales del reactor de pared catalítica diseñado y construido para realizar la reacción sobre las placas con catalizador previamente preparadas. En segundo lugar, se expone de manera detallada el método seguido para preparar dos tipos diferentes de placas catalíticas. Estas placas con catalizador son caracterizadas de manera similar al método empleado con los catalizadores en polvo. Luego, se ha realizado un estudio sistemático para comparar la actividad y la selectividad de los dos tipos de placas catalíticas. Por último, mediante un modelo 1D se revelan aspectos fundamentales de la configuración del reactor de pared catalítica utilizando una configuración con dos canales paralelos, en los cuales se ejecutan una reacción endotérmica y otra exotérmica respectivamente.

La principal conclusión de este trabajo es que el reformado por vapor de etanol puede ser realizado bajo condiciones de alta eficiencia térmica si se emplea un diseño basado en un reactor de pared catalítica con recobro de calor integrado a una unidad de separación para la purificación del hidrogeno. Las placas catalíticas han demostrado ser un elemento fundamental en este tipo de reactor porque incrementan de manera significativa el transporte de calor que se requiere para sostener las reacciones endotérmicas.

Nomenclature and Symbols

FC	Fuel Cells
R&D	Research and Development
PEMFC	Proton-Exchange Membrane Fuel Cell
SOFC	Solid Oxide Fuel Cell
SRM	Steam Reforming of Methane
SRE	Steam Reforming of Ethanol
SR	Steam Reforming
ATR	Auto-Thermal Reforming
POX	Partial Oxidation
PI	Process Intensification
CWR	Catalytic Wall Reactor
URV	Universitat Rovira i Virgili
WGS	Water Gas Shift
XDR	X-ray Diffraction
HRTEM	High Resolution Transmission Microscopy
L-H	Langmuir-Hinshelwodd
ESEM	Environmental Scanning Electron Microscopy
EDS	Energy-Dispersive Spectroscopy
AAS	Atomic Absorption Spectroscopy
TEM	Transmission Electron Microscopy
SEM	Scanning Electron Microscopy
PBR	Packed Bed Reactor

P_j	Partial pressure of component j
r_{ni}	net reaction reforming rate
r_{fi}	forward turnover frequency
K_{eq}	Equilibrium constant
K_p	is the equilibrium constant
c_j	constant parameters
d_v	crystallite size weighted by volume

K_s	Scherrer constant (somewhat arbitrary)
B	integral breadth of peak (in radians 2θ)
x_b	conversion of the exothermic reaction
x_a	conversion of the endothermic reaction
E	activation energy
K	pre-exponential factor of linear kinetic
ΔH	heat of reaction
R	gas constant
c_p	specific heat
C_0	initial concentration
T	absolute temperature
h	channel height
u_z	axial velocity
T_0	initial temperature
D_0	diffusion coefficient
$S(y, \phi)$	Normalized sensibility
Y	Independent variable for sensitivity analysis
V	Endothermic to exothermic velocity ratio
K	Endothermic to exothermic specific reaction rate ratio
C_{j0}	Initial concentration for element j
Nu	Nusselt number
Sh	Sherwood number
Da	Damkohler number
T_{ave}	average temperature for the gas phase
C_{ave}	average concentration for the gas phase
β	approach to equilibrium parameter
η	efficiency
θ	dimensionless temperature
ϕ_j	input parameter for sensitivity analysis
λ	wavelength of radiation

Chapter 1

Introduction

1-1 Context

Energy has become a fundamental necessity to guarantee modern society development. In fact, there is an intensive discussion, on a global scale, about diverse features of the coming energy processes. Two recurrent questions related with energy production are: how long will be the lifespan of present energy resources (fossil fuels) and what will be the economic and environmental impact of present and future energy production technologies (Birol, 2004). Agreement on the first query appears to be more difficult because it involves a great amount of uncertain data, such as how much it will cost to extract hydrocarbons and deliver them to consumers (Birol, 2004). On the other hand, the second issue – potential economical and environmental risks- is getting increasing attention because climate change constitutes a key challenge for sustainable development. In particular, CO₂ emission levels from fossil combustion could lead to unacceptable economical costs (Stern, 2006). In consequence, a sustainable energy system requires for technological improvements in the way in which energy is produced and used (Birol, 2004).

Among different possible alternatives to produce energy, the system based on Fuel Cell (FC) presents two characteristics that make it an attractive option (Turner, 2004): (i) augment the overall process efficiency by transforming chemical energy into electricity, through a reduction in the number of low efficient process based on mechanical and thermal energy exchange; and (ii) expand present energy sources because FC work with hydrogen; which can be produced from a large variety of feed stocks, including fossil and renewable resources (Song 2002).

Usually an efficient FC system requires highly pure hydrogen. As hydrogen is not available in large amounts in nature, has to be produced through chemical processes. Hydrogen is called an energy vector since once it is produced from renewable sources it may be transformed into electricity releasing water, a by-product that also contains hydrogen. Although it is produced at large scale in refineries, chemical companies, and steel industries,

hydrogen production technology for FC applications still requires additional R&D efforts (Trygve, Hagen et al 2006).

European countries constitute an example of those societies who could obtain profit from development of hydrogen as an energy vector. With a high level of energy dependence on foreign resources, close to 80% in some countries (PERE, 2005), and a potential availability of biomass resources, they have a golden opportunity to impulse their own sustainable development by implementing R&D in the field of energy production with FC applications.

Depending on the FC type, power systems may include additional advantages, such as fuel flexibility, co-generation, modular design, and rapid response (Song, 2002). It is expected that FC applications emerge as a promissory technology for three kinds of powder plants: stationary (for industry, commerce, and residence purposes), mobile (for transport by car, bus, train, ship, etc.) and portable micro-generator (Song, 2002).

Hydrogen for feeding FC applications could be produced by reforming reactions, on devices called fuel processors. Obtaining a high efficiency fuel processor represents a key step on the FC system development. Higher efficiencies must be obtained using a scale unit according to the application characteristics that obliges searching for the optimal process integration among chemical reaction, heat exchange, and mass transport.

1-2 Objectives

The long term framework of the study would be to develop an integrated fuel processor for feeding small scale and stationary FC application, working with a Proton-Exchange Membrane Fuel Cell (PEMFC). Main hypothesis is based on the statement that the overall process efficiency would be optimized by coupling mass and heat transfer rates with chemical reaction dynamics. It was decided to design a fuel processor based on a structured Catalytic Wall Reactor (CWR) with integrated heat recovery coupled to a separation unit for hydrogen purification.

The overall objective of the present work was to focus on evaluation of technical feasibility of preparing and using catalytic plates in a Catalytic Wall Reactor to perform Steam Reforming of Ethanol (SRE) under conditions of high thermal efficiency. It was decided to work at an intermediate temperature range (from 400 to 500°C) to moderate thermal stress and make use of economical materials. Specific objectives to be covered were:

- Evaluate possible thermodynamic constrains on the performance of: (i) reactor under thermodynamic equilibrium and (ii) integrated fuel processor. Perform a mapping for the principal operational variables to guarantee an auto-thermal operation of the fuel processor.
- Assess suitability and usefulness among several catalyst options known from previous works. Screen catalysts for Steam Reforming of Ethanol at intermediate temperature range, as well as evaluate its performance in terms of activity, selectivity, and yield. Select appropriate catalyst to be implemented on structured catalytic plates.
- Apply adequate preparation methods to deposit catalytic coating on metallic plates which later will be integrated into a structured Catalytic Wall Reactor. Design and construct a reactor to perform tests on catalytic plates. Analyze the catalytic plate reaction performance at intermediate temperature range, using theoretical and experimental method.

1-3 Document Outline

A systematic experimental plan was executed to fulfill the overall and specific objectives, composed of three modules: documentation, experimentation and numerical simulation. The first module, documentation, included revision of bibliography and previous studies. Next, to execute the experimentation module, we employed existing equipments at the Universitat Rovira i Virgili, adapted standard laboratory reactors (such as Packed Bed Reactor) and constructed new equipments for specific purposes (such as the Catalytic Wall Reactor). Part of the catalyst preparation and characterization was developed with help from “Institut de Tècniques Energètiques” group, from Universitat Politècnica de Catalunya. Finally, numerical simulation was performed using specialized software from different areas, such as: process thermodynamic (Aspen PlusTM), multiphysic modeling (FEMLAB), and applied mathematics (MATLAB^(R)).

This document is structured as follows:

- Chapter 2 presents pertinent background information divided into four parts: first, a brief description of basic concepts; then, a detailed overview of technical features for reforming technology; third, a descriptive review of key aspects on SRE, catalysts preparation, and reaction performance. Finally, a comprehensive examination is present of structured reactors and catalyst preparation methods.

- Chapter 3 lists materials, equipments, and methods employed for screening catalyst and evaluating catalytic reactor performance. It also, presents techniques for catalyst characterization and fluid analysis. Finally, it describes tools for numerical simulation.
- Chapter 4 analyses thermodynamic equilibrium of the reactor and the integrated fuel processor to evaluate possible thermodynamic constrains. Then, it performs a mapping for the set of four operational variables -temperature, Steam to Carbon (SC) ratio, pressure, and hydrogen recovery in the membrane separator- that allow an auto-thermal operation of the fuel processor. Suitableness and usefulness of the different catalysts preparations that are known from recent publications are discussed on the basis of the operation conditions determined from thermodynamic analysis.
- Chapter 5 presents powder catalyst characterization and catalytic experimentation using a Packed Bed Reactor (PBR). A systematic study has been conducted to compare the activity and selectivity of two types of catalyst at moderate temperature and SC ratios. Nickel-based catalysts (Ni/La₂O₃-Al₂O₃) and novel Co-based catalysts (Co-Fe/ZnO and Co-Mn/ZnO) have been prepared and tested at temperatures of 400 and 500 °C, Steam to Carbon (SC) molar ratios of 2 and 4, and contact times from 4.3 to 1100 min·g_{cat}⁻¹·mol_{EtOH}⁻¹, covering a range of ethanol conversion from 20 to 100%. A multifactorial design analysis has been conducted to establish the significance of temperature, SC ratio, contact time and catalyst formulation on ethanol conversion and selectivity towards the different reaction products.
- Chapter 6 shows catalytic plates characterization, simulation and experimentation using a Catalytic Wall Reactor (CWR) configuration. First, 2D modeling is used to analyze main characteristics of a CWR designed and constructed to perform reactions on the prepared catalytic plates. Prepared catalytic plates are characterized in a similar way to those employed for powder catalysts. After that, a systematic study has been conducted to compare the activity and selectivity of two types of catalytic plates. Finally, a 1D model is used to expose main aspects on thermal performance for a theoretical CWR using two co-current channels with endothermic and exothermic reactions respectively.
- Chapter 7 lists main conclusions and future work recommendations.

References

1. Birol, F., Ed. (2004). World Energy Outlook 2004. Paris, International Energy Agency.
2. PERE, 2005: Plan de Energías Renovables en España 2005-2010. Madrid, Ministerio de Industria, Turismo y Comercio: 80.
3. Song, C. (2002). "Fuel processing for low-temperature and high-temperature fuel cells: Challenges, and opportunities for sustainable development in the 21st century." *Catalysis Today* 77(1-2): 17-49.
4. Stern, N., Ed. (2006). The Economics of Climate Change. Cambridge, Cambridge University Press.
5. Trygve, R., E. F. Hagen, et al (2006). Hydrogen Production R&D: Priorities and Gaps. Paris, International Energy Agency: 33.
6. Turner, J. A. (2004). "Sustainable Hydrogen Production." *Science* 305: 972-977.

Chapter 2

Fundamental Aspects and Background

This chapter presents a review of pertinent background information. Four main subjects are described: concepts and new trends in reforming technologies, literature background in the catalytic steam reforming field, key features on reaction and mechanism for the Steam Reforming of Ethanol, and an overview of structured catalyst preparation.

2-1 Basic Aspects of Fuel Cell Applications

2-1-1 Fuel Cells Features

A Fuel Cell (FC) is an electrochemical device that transforms chemical energy of a fuel and an oxidant into electricity. FC are considered direct energy converters because they transform the fuel's chemical energy into electricity without additional thermal and mechanical process, such as those occurring in thermo-electrical plants. In consequence, a FC presents two main advantages compared with internal combustion engines: (i) it works at higher efficiencies because it is not limited by the Carnot cycle, and (ii) it produces lower net greenhouse emissions when fuels are obtained from renewable sources (Kordesch, 1995).

Usually, FC systems are designed as modular process and there is a wide range of power requirements from a few hundred Watts to Megawatt sizes. FC offers more flexibility than other power plants technologies because it can be built in proportion to the local energy consumption. An important disadvantage is that a FC requires hydrogen as fuel to work efficiently. This hydrogen has to be produced from other fuels. In nature hydrogen is found combined with other elements, such as oxygen (in water) or carbon (in organic compounds). As hydrogen makes energy transmission possible, it is called an energy vector. Commonly, an additional unit has to be added to transform available fuels (renewable or fossil fuels) into highly pure hydrogen stream (Kordesch, 1995).

Table 2-1 shows some FC types and their characteristics. Among the different options, FC can be operated from the low temperature range -70°C to 90°C - such as the Proton-Exchange Membrane Fuel Cell (PEMFC) to high temperature -800°C to 1000°C - as in the

Solid Oxide Fuel Cell (SOFC). This diversity offers several design strategies, whilst on one hand PEMFC is appropriate for stationary small scale and portable power sources using an additional unit for fuel processing, on the other side SOFC have been proposed as electrical power plants (Ferreira-Aparicio et al 2006, Benito et al 2005; Song 2002).

Table 2-1 Some characteristics for the different types of Fuel Cells (Song 2002)

FC type	Temperature Range (°C)	Fuel Source
Polymer Electrolyte	70-90	<ul style="list-style-type: none"> • External Reforming • Direct MeOH
Phosphoric Acid	180-220	<ul style="list-style-type: none"> • External Reforming
Molten Carbonate	650-700	<ul style="list-style-type: none"> • External or Internal • Reforming
Solid Oxide	800-1000	<ul style="list-style-type: none"> • External or Internal Reforming • Direct CH₄, gasoline, diesel, etc

FC characteristics determine in great extent the kind of feed to implement, and again there are numerous options such as fuelling the cell directly with hydrocarbons or providing a high purity hydrogen stream. For instance, PEMFC contains platinum as an electro-catalyst which is poisoned by carbon monoxide and sulfur (Ahmed and Krumpelt 2001). Then, it requires additional separation steps to remove impurities produced by reforming and to deliver a high purity hydrogen stream. On the other hand, SOFC could perform internal reforming since it operates in the high temperature regime (Song 2002).

2-1-2 Fuel Cells Feeding

The main feed-stocks for hydrogen production are water, coal, natural gas and biomass. Coal gasification and Steam Reforming of Methane (SRM) are the most important commercial technologies for large scale production and both produce CO₂ emissions (Turner 2004). In contrast, using biomass instead of fossil hydrocarbons provides the additional advantage that it can reduce the net generation of CO₂ (Marquevich 2001). Among the multiple candidates, bio-ethanol recently has gained attention because it is a non toxic fuel which is already produced economically at large scale. In concrete, Steam Reforming of Ethanol (SRE) is an attractive candidate because of economical reasons -it offers the

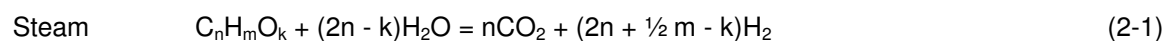
possibility to employ water mixtures in fuel processors, avoiding the cost of high purity alcohol distillation (Ferreira-Aparicio et al 2006, Benito et al 2005)-. Also, there are some developments on technical processes of hydrogen production using similar organic compounds (Deluga, Salge et al 2004; Garcia, French et al 2000).

Concerning fuel processing, hydrocarbon reforming processes are fully developed at industrial scale, in particular the steam reforming, which contributes around 48% to the world's hydrogen production. These chemical processes are endothermic reactions that require an external heat supply. Furthermore usually they are carried out under high temperature and pressure conditions to overcome thermodynamic limitations. As a result, to guarantee an economic production at industrial process scales, it is common practice to employ a large-scale and centralized distribution scheme. However, to become visible benefits from recent advances in FC in areas like small-scale and decentralized power generation units, it is necessary to develop a new kind of fuel processor (Ferreira-Aparicio, Benito et al 2005).

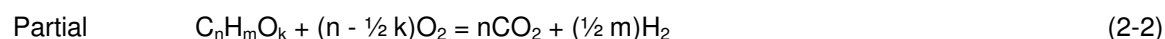
In summary, each application determines major economical and technical requirements and is important to match compatible a FC, fuel, and a reforming process. For large scale power supply, SOFC and hydrocarbon feed are compatible, while PEMFC and hydrogen production by fuel reforming are suitable for small scale applications. The major difficult is that the small scale process has specific characteristics different from well established technology (basically, at large scale) and requires development of new reformers.

2-1-3 Catalytic Reforming

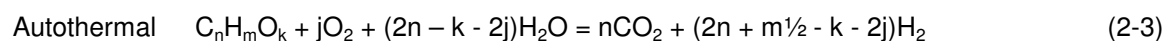
Catalytic reaction probably represents the heart of the fuel reforming process. There are three basic catalytic reactions for hydrocarbon production: Steam Reforming (SR), Auto-Thermal Reforming, (ATR), and Partial Oxidation (POX). Equations (2-1), (2-2) and (2-3) normally consist on multiple reactions dynamic.



Reforming



Oxidation



Reforming

SR is more efficient for H₂ production, but as it is an endothermic reaction it requires an external heat source. For that reason is difficult to control the temperature profile along the reactor. On the other hand, POX is an exothermic reaction attractive when the feed is composed of heavy hydrocarbons, but has a lower hydrogen yield of H₂ compared to SR. Finally, ATR combines both reactions trying to balance the energy consumption required by SR with the energy produced by POX (Ferreira-Aparicio, Benito et al 2005).

Concerning catalyst, researchers have made numerous efforts looking for improve activity, selectivity and stability. Catalytic studies commonly involve tests on preparation method and catalyst formulation; especial attention has been paid to interactions between support type, active metal, and promoters added (Cheekatamarla and Finnerty 2006). There are two major drawbacks that reduce the reforming catalyst performance: the existence of undesired pathways (like coke formation) and catalyst deactivation. Carbon deposition can be avoided to some extent operating under conditions where the thermodynamic equilibrium favors the H₂ production, commonly at high temperature and SC ratio. However, catalyst enhancement stills constitutes a relevant issue to be addressed.

2-1-4 Fuel Processors

A standard diagram for an industrial reforming process is presented in figure 2-1. It consists of a pre-heating unit placed before the reaction chamber where the reforming takes place; while a heat exchange helps maintaining an average temperature in the desired range. After that, optionally another reaction steps could be placed for guaranteed elimination of some by-products like CO, which are difficult to remove in a single step because of the thermodynamic equilibrium. Finally a combustion chamber is required to satisfy heat requirements (Ahmed and Krumpelt 2001).

Due to the nature of the heterogeneous catalyst, it is expected that inside a reforming unit different phenomena will take place: a complex chemical reaction mechanism, heat and mass transport, and thermodynamic equilibrium. In the past, the better technological approach to overcome this complexity was employing large scale equipments, and having separate units with specific functions as figure 2-1 shows. For instance, inside the reactor the chemical reaction takes place while the heat exchanger provides energy transaction between low and high temperature streams, and the combustion chamber produces the heat required by the system. This approach demonstrated to work adequately for large scale and centralized distribution systems, but is not satisfactory for small scale and decentralized units which have

to comply with strict limits on volume, weight, and costs; maintaining a high performance at the same time.

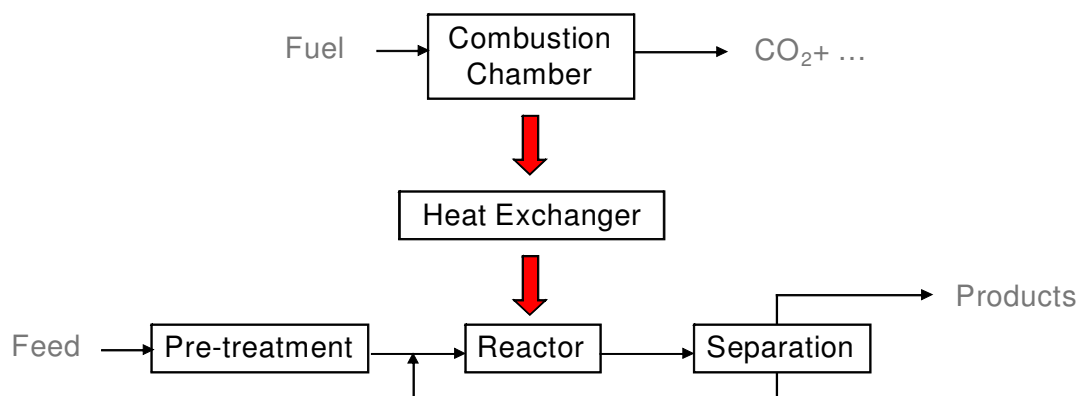


Figure 2-1 Standard fuel processor diagram which consists of: pre-heating step, reaction chamber, heat exchanger (which helps maintaining an average reaction temperature), and combustion chamber. Also additional reaction steps could be placed for guaranteed elimination of by-products like CO

A recent trend in process engineering called Process Intensification (PI) take advantage of the possibility to design integrated devices with multiple functions, increase efficiency of the overall process, and allow a significant scale reduction (Stankiewicz and Moulijn 2004). PI objectives are to develop cheaper processes, to diminish investment costs, to extract as much profit as possible from raw materials, and to optimize waste processing. At the end of the day, PI reflexes a paradigm change in which it is necessary to find new technologies for reducing the environmental impact and for ensuring sustainable development (Stankiewicz and Moulijn 2004).

2-2 Trends in Reforming Technologies

In recent years, companies and researchers have been studying several commercial and technical strategies to supply hydrogen for different kind of FC applications. In general, they remark the necessity to design and develop new reforming technologies at small scale, which must be compact and efficient (Qi, Peppley et al 2007; Yang and Ogden 2007; Ogden 2002; Giroux, Hwang et al 2005). Interesting options can be obtained from PI methods, especially in the form of multifunctional and structured catalysts and reactors.

Monoliths constitute a successful example of a structured reactor. They consist in a catalyst supported by a ceramic or metallic structure which facilitates handling, heat supply and hydrodynamics, and at the same time diminishes pressure drop and transport resistance

(Stankiewicz and Moulijn 2004). The next section will be devoted to highlight principal aspects on actual trends in reforming technologies.

2-2-1 Multifunctional Reactor Concept

At the heart of the reforming technology is heterogeneous catalysis; which according to Fogler (Fogler 2001) is composed by seven steps: external/internal diffusion, adsorption onto or desorption of molecules from a surface, and finally the surface chemical reaction. These phenomena are affected by transport, kinetic, and thermodynamic parameters; as a result the entire cycle is a complex event. An adequate coupling of processes -such as reaction and separation- can be used to minimize or partially overcome thermodynamic and kinetic constrains (Alpay, Chadwick et al 1999). As a consequence, reactor and catalysis design constitutes an excellent opportunity to increase dramatically efficiency by PI.

In that sense, figure 2-2 represents a scheme of the synergy possibilities due to interaction between multiple disciplines related to catalyst development. It is important to remark the fact that those disciplines have experienced an extraordinary development during last decades. In fact, today there is a favorable confluence of factors: mature knowledge acquired from basic sciences (like chemistry and physics), better engineering products (such as new kinds of materials, surface treatments, analytical instruments, etc.), and design procedures based on matching information between experimental and theoretical methods. This confluence of factors augments the options for obtaining a closer integration among mass, energy, and reaction events. As a final result, more efficient processes is achievable obtaining.

Reactors commonly manage the presence of two or more phases and allow the heat transport to sustain chemical reaction. Therefore, conventional catalytic reactors constitute an example of integration features, as is illustrated by figure 2-3. In this case, reactor design is engaged with process integration through different devices (inter-reactor) and inside the same unit (intra-reactor). On the other hand, usual catalytic function focuses on phenomena at pore and particle scales. At the end of the day, the overall process deals with interactions at different orders of magnitude. Although this approach has been successful for other process, the requirement to obtain efficient and compact process for FC applications cannot be only reached through process integration. It is necessary to get the most efficiency with the minimum size possible, which is a PI task.

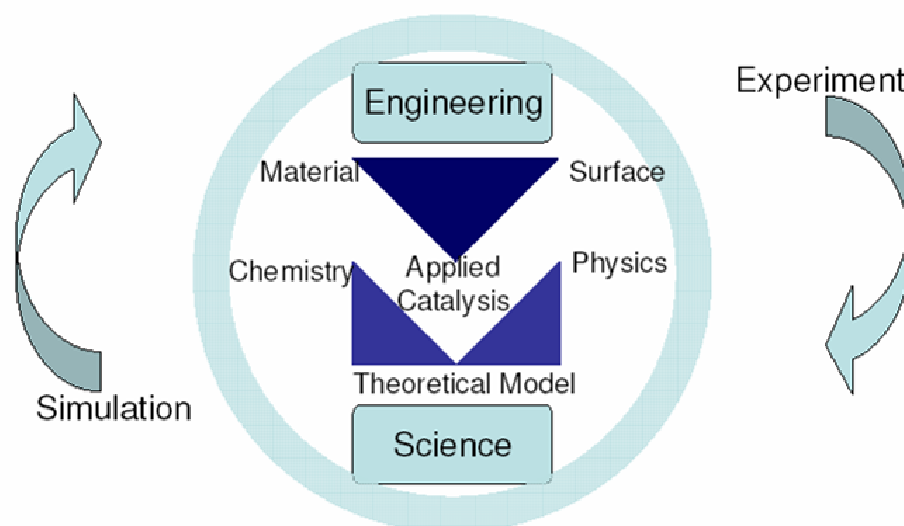


Figure 2-2 Scheme of possible synergies due to a multidisciplinary approach among disciplines related with the catalysis (Centi and Perathoner 2003). A more efficient process can be developed by taking advantage of: mature knowledge of basic sciences (like chemistry and physics), better engineering products (such as new kinds of materials, surface treatments, analytical instruments, etc.), and information match between experimental and theoretical methods.

Recently, the expectative for present and future catalyst improvements were reviewed by several authors (Centi and Perathoner 2003; Dautzenberg 2004; Cybulski and Moulijn 2006). Centi et al (2003) remarked that catalysts design has the possibility to be improved at three different scales: (i) nano, by controlling active sites at nanopores, (ii) micro, through the possibility of constructing micro-devices, and (iii) macro, pointing the opportunity offered by structures like monoliths and membranes. Each single item by itself can improve the process performance, but the progress level can be higher if the different components are synchronized into a single process unit.

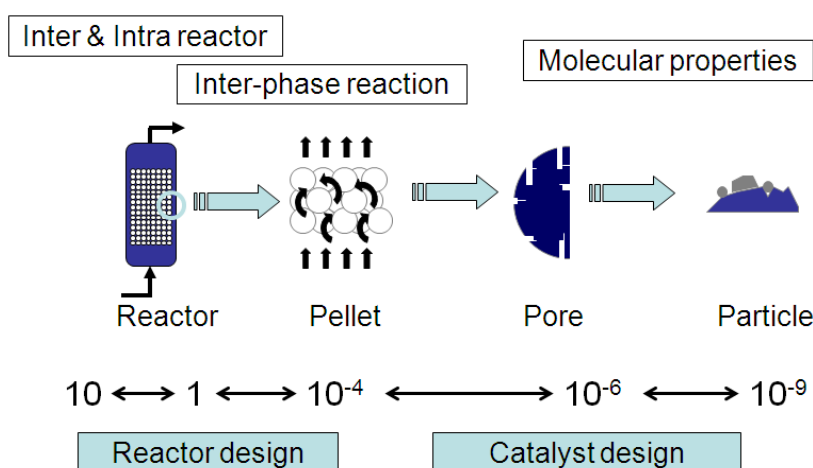


Figure 2-3 Integration levels in reactor and catalytic processes (Schmidt 1998). Reactor designs focus on interaction with other process unit (such as separators and heat exchangers) and between different phases (fluid and solid); while catalyst involves mass/heat transport phenomena and surface reaction at pore level.

In addition, Dautzenberg (2004) remarked that both catalyst and reactor share considerable progress opportunities by using two different approaches:

- First, the synthesis can be used to adjust the catalyst properties to accelerate diffusion in mass transfer limited reactions, since synthesis plays an important role in the optimization of catalyst structural parameters (such as particle size, pore structure, crystal size, active site distribution, etc.).
- The second approach concerns multifunctional reactors, based on combining reactor configurations to increase intra-reactor transport, as occurs with heat transfer in highly endothermic and/or exothermic reactions. The goal of a multifunctional reactor is to maintain both concentration and temperature profiles to ensure maximum conversion rate and minimum production of undesired by-products. For instance, heat transfer limitations could be reduced by minimization of heat resistance using the catalytic wall concept; which consists in depositing the catalyst directly at the reactor wall surface (Kolios, Glockler et al 2005).

The multifunctional concept refers to a device which integrates reaction with heat and separation dynamics. As an example, figure 2-4 represents a fuel processor diagram that could increment efficiency by enhancing thermal and mass transfer rates. A direct consequence of multifunctional conception is the application of especial structures for augmenting efficiency of complex reactions. For instance, in the case of highly exothermic or endothermic reactions, and mass limited reactions the transport process are significantly improved by ordering the catalyst particles; shown by the diagram on figure 2-5.

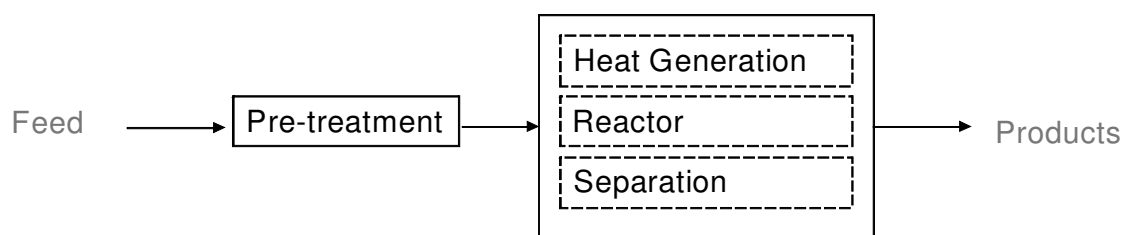


Figure 2-4 Scheme of a fuel processor using multifunctional reactors to increment efficiency by enhancing thermal and mass transfer rates. A single device integrates multiple functions: reaction, heat exchange and separation. It is then possible to avoid some mass/heat transport resistances and obtain higher efficiencies

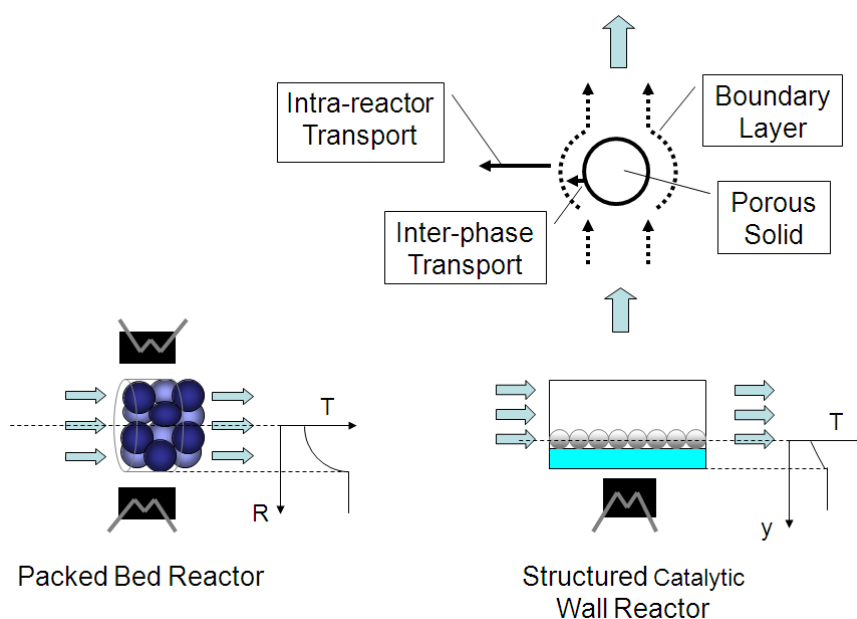


Figure 2-5 Transport processes (top scheme) are facilitated by arranging catalyst in structures as catalytic walls (at right-bottom) instead of using disordered configurations like packed bed reactors (at left-bottom).

In the case of fuel reforming technologies, the multifunctional reactor concept emerges as an adequate method for intensifying heat, and reaction process. Device configurations composed by structured catalysts and reactors have gained especial interest, and are the subject of novel applications. The advantage of structures is that they allow a better control of the chemical process compared to a random configuration; especially in the case of possible presence of non-uniform flow, concentration and temperature profiles.

Ferreira-Aparicio et.al. (2005) and more recently, Qi et.al. (2007) have reviewed key technological progress in the development of fuel reforming for FC applications. Among different attempts, there are several outstanding examples of multifunctional and structure reactors: the plate assembly steam reformer (International Fuel Cells), the serpentine ATR reformer (General Motors and Toyota) and the ATR annular reformer (Argonne National Laboratory). Especially, both the Catalytic Wall Reactor (CWR) and the plate-type reformer illustrate how exothermic and endothermic reactions could be integrated to intensify the heat transport, as shows figure 2-6. Another important topic for the hydrogen production process is the development of membranes for obtaining high purity hydrogen streams in a single step; avoiding additional reactor units.

In next years, it is expected that the micro-scale technology will lead PI efforts for increasing efficiency and compactness, bringing up new options in the field of small scale fuel processors for FC applications.

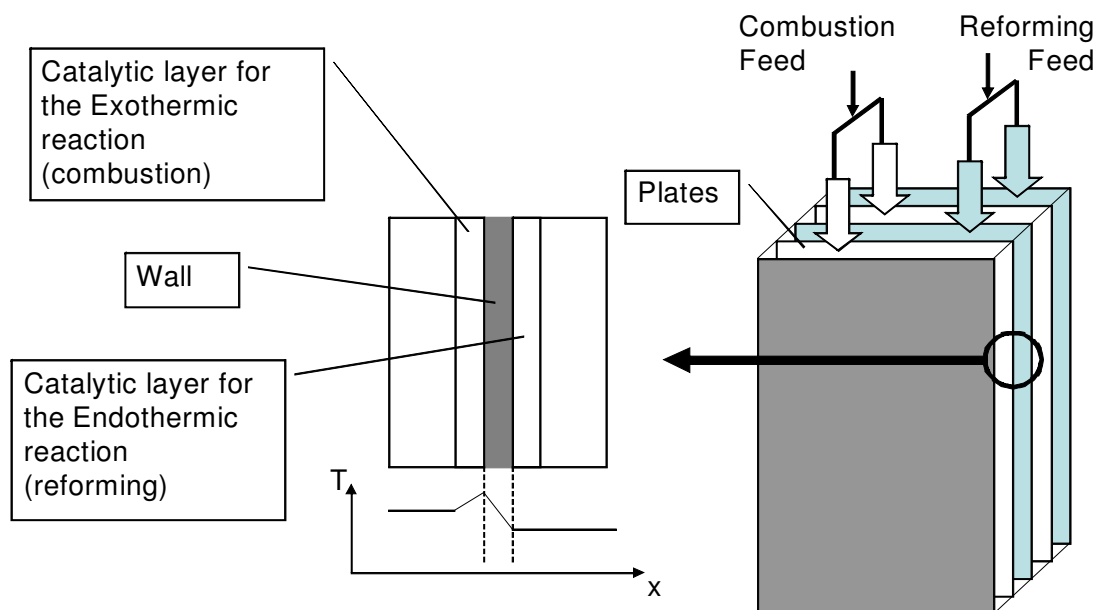


Figure 2-6 Diagrams for Catalytic Wall Reactor and plate-type design which constitute examples of multifunctional reactors that integrate exothermic and endothermic reactions to intensify the heat transport (Ferreira-Aparicio, Benito et al 2005).

2-2-2 Structured Reactor for Heat-Reaction Integration

Three key features to obtain major benefits from structured reactors in terms of thermal efficiency are: (i) the process must be thermally self-sufficient with a minimum temperature gradient between feed and exit streams, (ii) the maximum temperature should be maintained as low as possible to reduce material exposition from thermal stresses, and (iii) the reaction kinetic and transfer phenomena should be combined to reduce equipment size (Kolios, Glockler et al 2005).

There is a large variety of structured reactors as monolith, gauze, structured packing, foam, and arranged catalyst (Stankiewicz and Moulijn 2004). Figure 2-7 shows a scheme of ceramic and metallic monoliths, which probably are the structured reactor most extended in chemical engineering applications. In general, a monolith consists on structured support that receives a washcoat which contains the catalyst; so the structure function is to promote mass/heat transport with adequate surface area to volume ratio. Tomasic (2006) listed some advantages for this kind of structure, such as: high specific surface, small pressure drop, favor inter-phase mass transfer, reduce resistance to mass transfer by intra-phase diffusion through a catalytic layer, good thermal and mechanical properties, and simple scale up. Depending on the application, a monolith can be made of ceramic or metal; metallic monoliths being more appropriate to a process that requires heat transfer between adjacent channels because of its

high thermal conductivity. On the other hand, ceramic monoliths are suitable for chemical controlled reactions since they allow a larger amount of catalyst deposited on the walls (Tomasic and Jovic 2006). At present, monolith application to fast reactions at high temperature, as SR and POX, is a subject of study (Stankiewicz and Moulijn 2004).

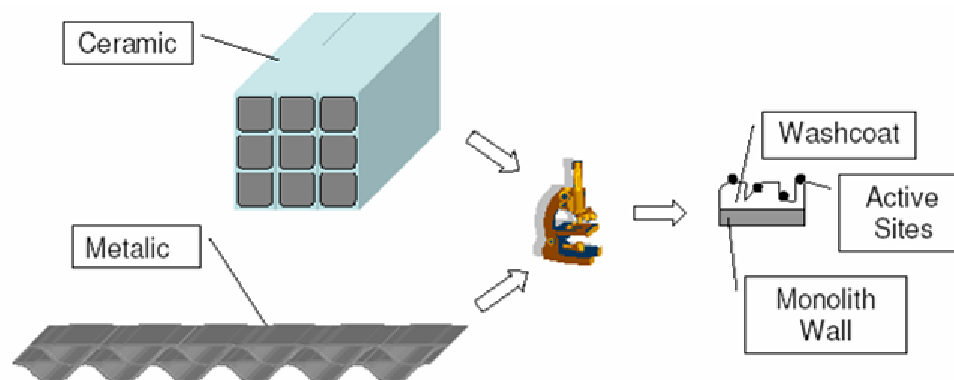


Figure 2-7 Schemes of ceramic and metallic monoliths from Tomasic and Jovic (2006). Monoliths are a structured support that receives catalyst as washcoat. Structures are designed to favor mass/heat transport by increasing the reaction surface area to reactor volume ratio

Kolios et al (2005) presented several examples of multifunctional structured reactors applied to the fuel reforming process. An outstanding case was the CWR, which is used to construct adiabatic devices that integrate exothermic and endothermic reactions. As an example, the integrated fuel processor was a device that performs four functions: fuel evaporation, auto-thermal methanol reforming, preferential oxidation for CO removal, and H₂ burning (Schuessler and Portscher 2003). This device was described by Kolios et al (2005) as: "...a stack of identical, structured plates which divide its volume in two compartments with micro-structured rectangular channels. These plates were made from alumina and copper, thus ensuring high thermal conductivity for a uniform temperature over the entire reactor volume...". The catalysts were supported by the plates, only at their respective reaction zones. Figure 2-8 shows a picture to illustrate the function of this CWR: a liquid fuel/water mixture enters into the first compartment, which evaporated the fluid because an exothermic reaction releases heat on the other side. Then, the reactants mix with air and enter into porous plates, where the reforming reaction takes place. Finally, the reaction products pass to the second chamber where occurs an exothermic reaction (CO oxidation), both incrementing the stream's H₂ content and producing heat.

CWR concept can also be employed with steam reforming reactions. In this case, the most common configuration consists of two parallel channels, performing the endothermic

reaction (reforming) and the exothermic reaction (combustion) respectively, as shown in figure 2-9. The catalysts are deposited on both sides of the separating wall; in this way the unique resistance to heat transfer is due to the wall. Then, transport restrictions are caused mainly by the mass transport between the bulk fluid and the catalyst pores (Sundmacher, Kienle et al 2005).

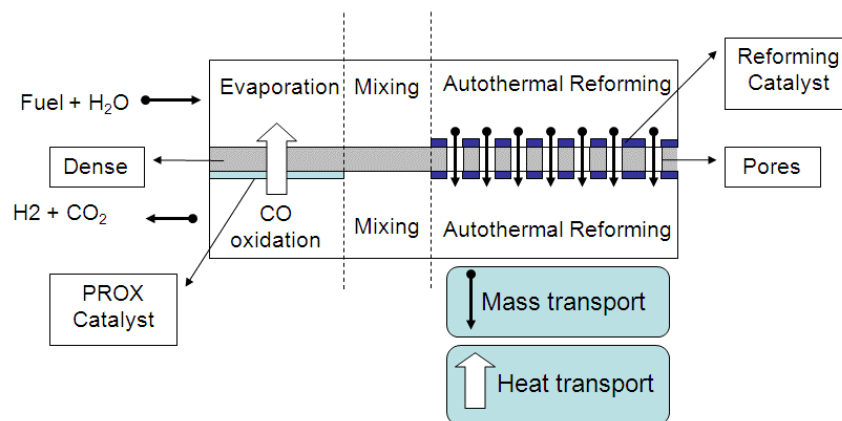


Figure 2-8 The integrated fuel processor is an example of a multifunctional reactor with catalytic plates. It performs four functions: fuel evaporation, auto-thermal methanol reforming, preferential oxidation for CO removal and H₂ burning (Schuessler and Portscher 2003).

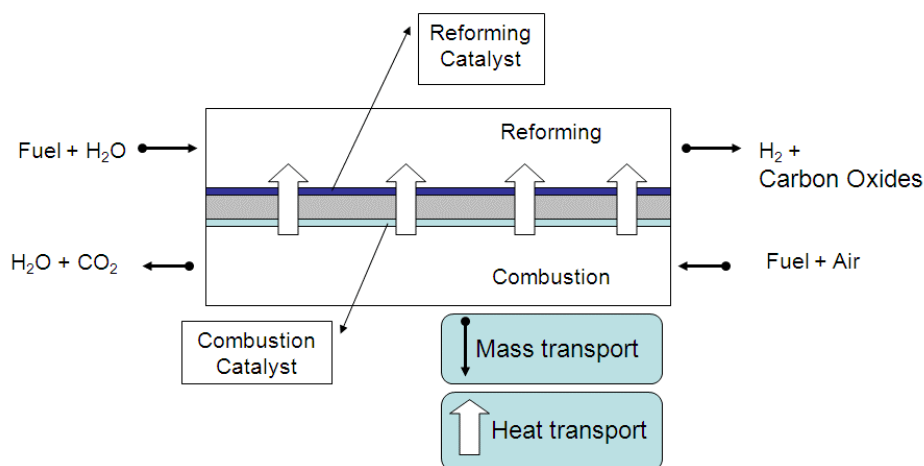


Figure 2-9 CWR scheme for coupling reforming and combustion reactions. Catalysts are deposited on both sides of the separating wall. As a result, major restrictions are caused by the mass transport between the bulk fluid and the catalyst active sites, at coat pores

Recently, Kolb et al (2007) reviewed the role of micro-structures with gas phase reactions for FC applications. The heat exchange was intensified at CWR by micro-reactor devices with channel dimension in the range of 50-1000 μm and length between 20 and 100

mm (Kiwi-Minsker and Renken 2005; Qi, Peppley et al 2007). CWR were constructed using different configurations, such as flat plate or cylindrical geometry, and helped to increase heat transfer coefficient by a factor of around 200 when compared with conventional steam reforming (Wanat, Venkataraman et al 2004). CWR were applied to different kind of reactions, such as SR of several fuels (methane, methanol, and ethanol), Water Gas Shift (WGS), and combustion (Wanat, Venkataraman et al 2004; Karim, Bravo et al 2005).

First attempts tried to explore thermal and/or kinetic performance for a single reaction, especially high endothermic/exothermic reactions difficult to perform under isothermal conditions in packed bed reactors. For instance, Amon (1999) used a tubular CWR for kinetic measurements of coke formation. Also with a cylindrical geometry, Venkataraman (2002) investigated heat exchange at 1000°C between catalytic combustion of methane and homogeneous dehydrogenation of ethane. The existence of previous industrial knowledge related with plate heat exchanger, had suggested to researchers the utility for extending CWR to this kind of arrangement as an alternative to multi-tubular and micro-reactor strategies (Cybulsky and Moulijn, 2006). Tronconi et al (2000) verified theoretical predictions about thermal behavior of a structured seven plate-type reactor using an exothermic reaction (CO oxidation) with slabs of 46 mm wide and 200 mm length. Then, using the same structure Groppi et al (2001) deposited PdO/ γ -Al₂O₃ over both metallic plates and annular reactor to compare kinetic measurements of methane catalytic combustion. Besides, Holgado et al (2001) deposited by electrophoresis a Cu/ZrO₂ catalyst over stainless steel to evaluate the plate reactor performance.

CWR flexibility facilitates the coupling of endothermic and exothermic reactions. For example, Zalc (2002) reported a coated-catalyst plate reformer using methane reforming and combustion to feed a 50 kW FC system. Also, Venkataraman et al (2003) examined the coupling between SRM and combustion, using corrugated plates of dimensions 8 cm by 5 cm by 0.1 cm with several co-current configurations. Wanat et al (2004) extended the previous work for SRE, using as catalysts Rh-Ce for reforming, and Pt-Ce for combustion. Morillo et al (2004) designed an auto-thermal folder sheet reactor, based on the plate heat exchanger concept, by SR of methanol and catalytic combustion of hydrogen.

2-2-3 Reforming Chemistry

Traditionally, fuel reforming is made through SR, POX and ATR. Table 2-2 presents important reforming reactions and figure 2-10 introduces possible options for fuels and catalysts. SR is an endothermic reaction which has shown to be efficient for hydrogen production at high temperatures (700-900°C). POX is an exothermic reaction that consists in limiting the oxygen feed to produce a H₂ rich stream, and can be conducted with or without catalyst (Krumpelt, 2002). Additionally, ATR -a combination between POX and SR- is employed for assuring heat requirements and maintaining an adiabatic operation. Both WGS and SRM are important reactions that commonly participate in hydrocarbon reforming chemistry. Finally, Preferential Oxidation (PROX) is used to catalyze the oxidation of CO, and is supposed to guarantee a high selectivity to CO₂, minimizing the H₂ oxidation. In this case, the major difficulty is caused by large differences in composition -H₂ is a bulk component while the CO proportion could be as low as two or three orders of magnitude less- (Cheekatamarla, 2006; Ghencui, 2002).

Table 2-2. Basic reactions employed on reforming process. SR, POX, and ATR are used as chemical reactions to produce H₂; while WGS and PROX are applied to remove undesired CO content. WGS and SRM are present in reforming reactions of hydrocarbons (Ghencui, 2002)

Name	Reaction	ΔH_{298} [kJ/mol]	#
SR	$C_nH_mO_k + (2n-k)H_2O = nCO_2 + (2n+m/2-k)H_2$	$\Delta H > 0$	(2-4)
POX	$C_nH_mO_k + (n-k/2)O_2 = nCO_2 + m/2H_2$	$\Delta H < 0$	(2-5)
ATR	$C_nH_mO_k + jO_2 + (2n-k-2j)H_2O = nCO_2 + (2n+m/2-k-2j)H_2$	$\Delta H \approx 0$	(2-6)
WGS	$CO + H_2O = CO_2 + H_2$	41.2	(2-7)
SRM	$CH_4 + H_2O = CO + 3H_2$	-206.2	(2-8)
PROX	$CO + \frac{1}{2} O_2 = CO_2$	-283.6	(2-9)
	$H_2 + \frac{1}{2} O_2 = H_2O$	-243.5	(2-10)

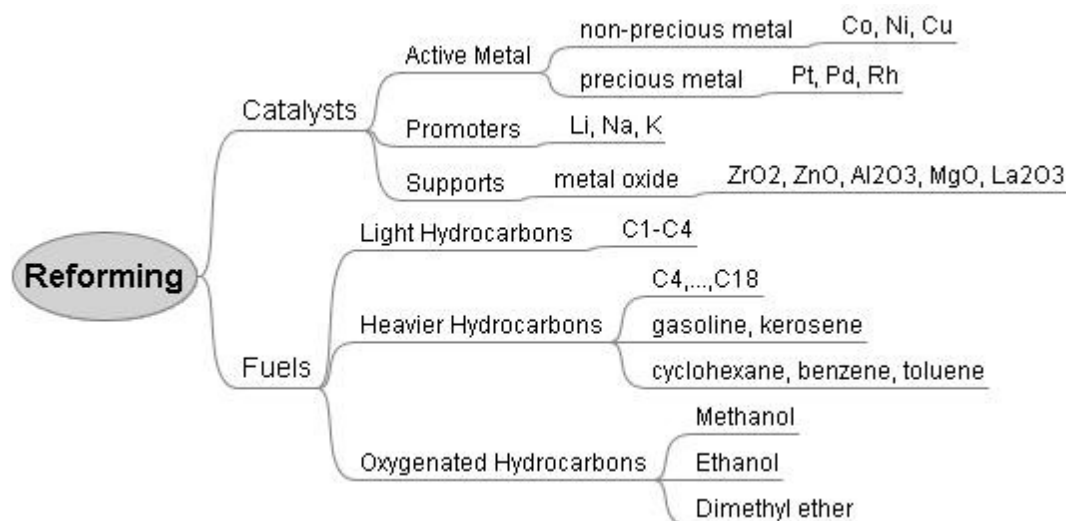


Figure 2-10 Classification of common fuels and catalyst employed in reforming process. Noble active metals are used in lower concentration than others because of economical reasons. Most common fuel is natural gas, but oxygenated hydrocarbons are gaining more attention (Cheekatamarla, 2006)

The choice of the chemical reaction depends on several factors: characteristics of the application (power demand, start-up, shutdowns), type of FC and fuel, equipment size restrictions, even heat and mass transport strategies (Krumpelt, 2002). ATR process is supposed to be practical for small or medium scale fuel processors because it favors heat transfer and allows a faster start-up compared to SR; however, design of ATR catalysts has to cope with the complexity of managing both SR and POX at the same time. Besides, POX is faster than SR but it has a lower H₂ yield (Ghencui, 2002). In addition, SR is a flexible and widespread technique used for more than 40 years in a large scale H₂ production (Bartholomew, 2006).

In the case of high temperature FC, such as SOFC, hydrogen production is carried out through internal reforming because materials and temperature employed allow it. On the other hand, for the low temperature range it is better to employ PEMFC with an external unit for the fuel reforming reaction. In this case, it is important to protect PEMFC from poisons, such as CO. Frequently, an additional step of CO oxidation is included in the fuel processors, such as WGS, to guarantee feed stream with CO concentrations lower than 50 ppm (Ghencui, 2002).

As catalysts are the principal component in fuel processors, the next section will summarize principal features related with catalysis for hydrocarbon reforming, with focus on SR reactions.

Preparation

Impregnation is one of the most common techniques to prepare catalysts, which consists in depositing metal particles onto pores of a high surface area support (normally in the 100-400 m² s⁻¹ range). Another preparation method is co-precipitation, based on preparing a solution of metal salts, maintaining pH constant, and adding a precipitation agent to obtain the desired solid. Then here after, the catalyst synthesis follows two additional heating steps, first in air (calcination) and second under a hydrogen rich atmosphere (reduction). Once metal atoms are fixed onto the support pores, they behave as active elements for chemical reactions. Parameters related with the preparation method (chemical proportions, contact time, temperature, pH, etc.) have shown to influence significantly in catalytic behavior and, as a result, constitute a subject of interest for researchers (van Beurden, 2004).

Active metal and surface effects

There is an extensive list of materials for preparing SR catalysts; among it are: γ -Al₂O₃ as support, and Ni, Ru, Rh, Pd, or Pt as active metals. However, composition is not the only parameter that affects catalytic activity because the interactions at catalyst surface have a strong influence on the reaction steps.

Some important factors related with surface effects are: support structure, active metal distribution, and support-metal interaction. In general, these factors have to be adjusted to achieve specific functions. For instance, the metal dispersion tends to favor activity; however, in some cases, once a critical value has been reached, an additional increment in the metal dispersion does not augment activity.

Another example is the common practice of employing small quantities of promoters to modify some catalytic features of the support-metal couple, such as: to increase the surface area available for adsorption and reaction, to slow down the rate of unwanted side reactions, or to augment the catalyst activity per unit surface area (van Beurden, 2004). Although it is useful to add such promoter, there is a critical value after which it will negatively affect the desired reaction performance. At the end of the day, a careful study of the metals surface properties by characterization techniques is necessary to balance properly the catalyst function.

Support effects

Support effects have been defined by Barholomew (2006) as “an interaction of the support or carrier with the active catalytic phase, which causes a measurable change in Turnover Frequency”. Also Barholomew (2006) classify support effects as:

1. Strong interaction of unreduced metal oxide with an oxide support (leads to an incomplete reduction of the metal)
2. Support-induced size and morphology
3. Contamination of the metal by support material
4. Reactions on both metal and support (bifunctional catalysis)
5. Spillover of species from the metal to the support
6. Change in the electronic properties of small crystallites

For example it was observed in reforming that acid supports like $\gamma\text{-Al}_2\text{O}_3$ facilitate the hydrocarbon decomposition, but also promote undesired reaction, like polymerization, which leads to carbon deposition.

Classical catalyst for SRM

During last four decades, nickel catalyst has been used for hydrogen production by SRM, in particular Ni/ $\gamma\text{-Al}_2\text{O}_3$ is widespread used with optimal composition in the order of 2-5% dispersion and 15% Ni content. Nickel based catalysts have the advantage of being a tolerable active catalyst, available at lower cost than other materials, like noble metals.

On the other hand, main disadvantages are sulfur poisoning, sintering (which refers to Ni particles grow due to migration or transport phenomena) and carbon formation. For the last case, there are three principal deposition mechanisms: (i) pyrolytic coke, caused by hydrocarbon exposition to high temperatures, (ii) encapsulating carbon (gum), which consists on a thin film composed by CH_x , and (iii) whisker carbon, produced by nucleation of graphitic carbon on nickel particles and is the most destructive form of carbon formation. (Sehested, 2006). Briefly, although nickel catalyst is an interesting option for reforming, some features like deactivation and carbon deposition still require improvement.

New trends for reforming catalyst

Recent advances in different field make available new analytical and spectroscopic tools that impulse catalytic study. Especially, new characterization techniques -such as *in situ* XDR and *in situ* HRTEM- are continuously providing hints about new possible ways for catalyst improvement (Bartholomew, 2006). In particular, there are some important trends as new catalyst preparation routes using precursors like hydrotalcites, or alternative supports like Zeolites.

Another outstanding example is the development of bimetallic catalysts, which are synergic systems composed of two active metals joined that increase activity and selectivity in a proportion that is not possible for a single metal. In summary, although reforming catalysis has reached a sophistication level after many years, it still is possible to gain significant advances in catalytic performance.

Hydrogen Production Process by SRM

Natural gas is the main feedstock to produce hydrogen and syngas at large scale, and SRM probably is the principal reaction (Bartholomew, 2006). Hydrogen production by SRM consists of six steps, shown in Table 2-3 and figure 2-11. The first step consists in protecting catalysts from sulfur poisoning through step 1. Then, reforming is carried out through two units -steps 2 and 3- to prevent undesired reactions like cracking at high temperatures, allowing the possibility of handling multiple feeds. Also, WGS is executed in steps 4 and 5 to favor H₂ production, which is limited by thermodynamic equilibrium. At last, six step permits to recover remaining chemical energy in form of CH₄.

Table 2-3. Chemical reactions of the six steps standard chemical process for SR of Hydrocarbons (Bartholomew, 2006)

Step #	Name	Reaction	Catalyst
1	Desulfurization	$R-S + H_2 \rightleftharpoons H_2S + R-H$	CoMo/Al ₂ O ₃
2	Primary SR	$HC + H_2O \rightleftharpoons H_2 + CO + CO_2 + CH_4$	Ni/Mg/Al ₂ O ₄
3	Secondary SR	$2CH_4 + 3H_2O \rightleftharpoons 7H_2 + CO + CO_2$	Ni/Al ₂ O ₃
4	WGS, Low Temperature	$CO + H_2O \rightleftharpoons H_2 + CO_2$	Fe ₃ O ₄ /Cr ₂ O ₃
5	WGS, High Temperature	$CO + H_2O \rightleftharpoons H_2 + CO_2$	Cu/Zn/Al ₂ O ₃
6	Methanation	$CO + 3H_2 \rightleftharpoons CH_4 + H_2O$	Ni/Al ₂ O ₃

Due to the commercial relevance of SR process, there is an extensive literature on SR mechanism and kinetics. The next section will summarize some relevant features, recently described in detail by Bartholomew (2006). Although this information is focused on the SRM, it is relevant for understanding reforming of oxygenated hydrocarbons, such as ethanol (Bartholomew, 2006).

Mechanism and kinetics for SR and WGS

A SR mechanism is composed of elementary reactions that cover three kind of paths: hydrocarbon adsorption, reaction of intermediate components adsorbed on active sites, and desorption of final products. Table 2-4 presents a simplified mechanism model for reforming ethane into four final products H_2 , CH_4 , CO , and CO_2 . According to this mechanism, first ethane is absorb on active sites by eq (I) and intermediate compounds are stabilized; after that decomposition reactions take place, such as C-C rupture through eq (II), dehydrogenation of CH_x compounds –eqs (III) and (IV)–, and water dissociation by eq (V). At the same time, other surface reaction occur, such as eq (VI). At last, desorption of final products H_2 , CH_4 , CO , and CO_2 takes place, from eq (VII) to eq (X).

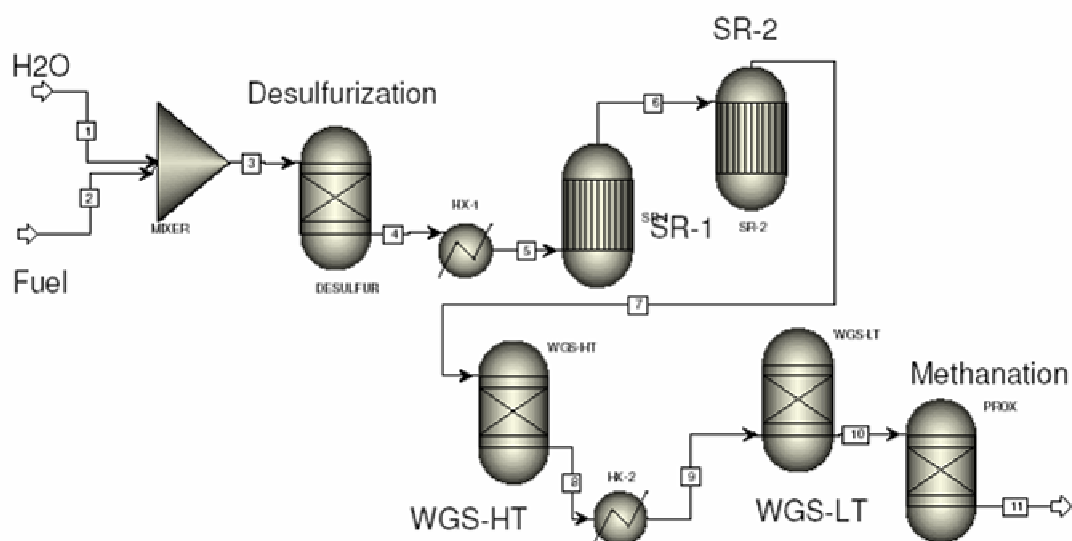


Figure 2-11 Process diagram for hydrogen production by SR of hydrocarbons (Bartolomew, 2006). Chemical reactions are shown in table 2-2. Reforming is carried out through two units -steps 2 and 3- to prevent undesired reactions like cracking at high temperatures. WGS is executed in steps 4 and 5 to favor H_2 production, which is limited by thermodynamic equilibrium. The last step allows recovering the chemical energy in form of CH_4 .

Table 2-4. Elementary steps according to a simplify model for SR of Ethane (Bartholomew, 2006)

eq #	Elementary Step	Reaction
I	Ethane adsorption	$\text{CH}_3\text{CH}_3 + 2\text{S} \rightleftharpoons \text{CH}_3\text{CH}_2\text{S} + \text{HS}$
II	C-C rupture	$\text{CH}_3\text{CH}_2\text{S} + 2\text{S} \rightarrow \text{CH}_2\text{S}_2 + \text{CH}_3\text{S}$
III	Methyl dehydrogenation	$\text{CH}_3\text{S} + 4\text{S} \rightleftharpoons \text{CS}_3 + 3\text{HS}$
IV	Methyl dehydrogenation	$\text{CH}_2\text{S}_2 + 2\text{S} \rightleftharpoons \text{CS}_3 + 2\text{HS}$
V	Water dissociation	$\text{H}_2\text{O} + 2\text{S} \rightleftharpoons \text{OHS} + \text{HS}$
VI	CO adsorbed	$\text{CS}_3 + \text{OS} \rightarrow \text{COS}_2 + \text{S}_2$
VII	Methyl hydrogenation	$\text{CH}_3\text{S} + \text{HS} \rightleftharpoons \text{CH}_4 + 2\text{S}$
VIII	H ₂ desorption	$2\text{HS} \rightleftharpoons \text{H}_2 + 2\text{S}$
IX	CO desorption	$\text{COS}_2 \rightleftharpoons \text{CO} + \text{S}_2$
X	CO ₂ desorption	$\text{COS}_2 + \text{OS} \rightleftharpoons \text{CO}_2 + \text{S}_3$

An extensive scientific production exists on mechanism and kinetic studies for SR; however. However, it is unusual to find a unified model able to explain features observed by different authors under varied operational conditions. Two key factors responsible of that disagreement are: (i) the presence of heat and mass transport disguises, and (ii) the difficulty to operate under kinetic regime because of the thermodynamic chemical equilibrium.

A recent study by Wei and Iglesia (2004) has reported a simple, unified mechanistic picture for CH₄-CO₂ and CH₄-H₂O reforming, CH₄ decomposition, and WGS reactions for Ni catalysts. The relevance of this model is that it allows comparing turnover rates between Ni and noble metal catalysts. They estimated the activation energy for SRM around 102 kJ mol⁻¹ and the pre-exponential factor as 2.5 10⁵ s⁻¹ kPa⁻¹.

Wei and Iglesia (2004) employed isotopic measurement for rigorous exclusion of transport and thermodynamic disguises. They found for SRM that the reaction rate is proportional to CH₄ partial pressure, but independent of H₂O concentration. As both rate constants and activation energy were found to be similar to methane decomposition, they concluded that the C-H bond activation step was the rate determining step. At the same time, other steps like carbon chemisorption are fast, and are equilibrated by the water gas-shift reaction. Table 2-5 shows a summary of possible mechanism for CH₄ activation and WGS; where the rate determining step is methane dissociation, eq. (i). Some elementary steps, such as methyl dehydrogenation, – eqs (ii) to (iii) - are common to the mechanism for SR of Ethane, already presented in Table 2-3.

Table 2-5. Elementary steps according to a simplify model for SRM (van Beurden, 2004, Wei, and Iglesia 2003)

	Elementary Step	Reaction
(i) *	Methane adsorption	$\text{CH}_4 + 2\text{S} \rightarrow \text{CH}_3\text{S} + \text{HS}$
(ii)	Methyl dehydrogenation	$\text{CH}_3\text{S} \rightarrow \text{CH}_2\text{S} + \text{HS}$
(iii)	Methyl dehydrogenation	$\text{CH}_2\text{S} \rightarrow \text{CHS} + \text{HS}$
(iv)	Methyl dehydrogenation	$\text{CHS} \rightarrow \text{CS} + \text{HS}$
(v)	CO ₂ dissociation	$\text{CO}_2 + 2\text{S} \rightleftharpoons \text{COS} + \text{OS}$
(vi)	CO adsorbed	$\text{CS} + \text{OS} \rightleftharpoons \text{COS} + \text{S}$
(vii)	CO desorption	$\text{COS} \rightleftharpoons \text{CO} + \text{S}$
(viii)	H ₂ adsorbed	$\text{HS} + \text{HS} \rightleftharpoons \text{H}_2\text{S} + \text{S}$
(ix)	OH adsorbed	$\text{HS} + \text{OS} \rightleftharpoons \text{OHS} + \text{S}$
(x)	Water dissociation	$\text{OHS} + \text{HS} \rightleftharpoons \text{H}_2\text{OS} + \text{S}$
(xi)	Water desorption	$\text{H}_2\text{OS} \rightleftharpoons \text{H}_2\text{O} + \text{S}$

* Rate determining step

Related with reaction kinetic, Wei and Iglesia employed an approach to determine the equilibrium parameter, η , measuring forward reforming rates,

$$\eta_1 = \frac{(P_{CO})^2 (P_{H_2})^2}{P_{CO_2} P_{CH_4}} \frac{1}{Keq_1} \quad (2-11)$$

$$\eta_2 = \frac{(P_{CO})^2 (P_{H_2})^3}{P_{CH_4} P_{H_2O}} \frac{1}{Keq_2} \quad (2-12)$$

where 1 refers to dry reforming and 2 refer to steam reforming reaction, and P_j refers to partial pressure of component j . The net reaction reforming rate, r_{ni} , is expressed in terms of the forward turnover frequency, r_{fi} , and the approach to equilibrium parameter, η_i , as,

$$r_{fi} = \frac{r_{ni}}{1 - \eta_i} \quad (2-13)$$

Also the WGS reaction has been the subject of several kinetic studies, but there are still disagreements in literature (Choi, 2003). There are two distinct mechanisms that may explain experimental observations, called adsorptive and regenerative. In the adsorptive mechanism, H₂O and CO adsorb on the active sites and form an intermediate compound

which finally desorbs in H₂ and CO₂. On the other hand, the regenerative or redox mechanism is a two step cycle, with H₂O adsorption and dissociation on reduced sites of catalyst, eq (ix) and (x) in table 2-4, and then follows CO oxidation.

Both mechanisms can produce a variety of kinetic models, but even an empirical rate expression was found to fit experimental data with a high degree of accuracy (Choi, 2003),

$$r_{CO} = kP_{CO}P_{H_2O}(1 - \beta) \quad (2-14)$$

where β is the factor of reversible reaction or approach to equilibrium, given by

$$\beta = \frac{P_{H_2}P_{CO_2}}{P_{CO}P_{H_2O}K_p} \quad (2-15)$$

and K_p is the equilibrium constant of WGS. Besides, Phatak (2007) determine WGS rate, reaction orders, and activation energies on Pt catalysts supported over alumina and ceria using operational conditions close to those required by fuel reformers for FC applications. The overall reaction rate proposed by Pathak is based on the redox mechanism, as follows,

$$r_{WGS} = k \frac{[CO]^{0.1}[H_2O]^{1.0}}{[CO_2]^{0.1}[H_2]^{0.5}}(1 - \beta) \quad (2-16)$$

Finally, for compute the equilibrium constant for the WGS, the following equation can be employed,

$$\ln(K_{eq}) = \frac{c_1}{T} + c_2 \ln T + c_3 T + c_4 T^2 + \frac{c_5}{T^2} + c_6 \quad (2-17)$$

where $K_{eq} \approx K_p$ and c_j are constant parameters.

2-3 Steam Reforming of Ethanol

SRE has gained a lot of attention for its potential utility in FC applications. On the next section a brief summary will be presented of the state of the art of relevant aspects, such as catalyst preparation, reaction mechanism and kinetic.

2-3-1 SRE Catalyst Composition

In recent years, catalytic investigations on SRE have been attempted by different researchers (Haryanto et al, 2005; Vaidya and Rodrigues, 2006). In order to obtain an optimal catalyst (it must be active, selective to hydrogen and stable) they had attempt different strategies like starting from classical catalyst formulations which had proved successfully for other reforming reactions (metal catalysts on oxide supports) (Cheekatamarla and Finnerty, 2006) or performing combinatorial chemistry (Duan and Senkan, 2005). According to literature available up to date (Haryanto et al, 2005; Duan and Senkan, 2005) it is possible to classify SRE catalyst according to the material used as active phase. There are two groups: noble metal such as Rh, Pd, and, Pt; and non-noble metal, mainly Ni, Co, and Cu. Noble metal catalysts has the inconvenient of high cost, for that reason are used in low concentrations and at high dispersions.

Supported Ni-based catalysts have high SRE activity and acceptable cost. Several metal oxides have been tested as supports, including Al_2O_3 , MgO , La_2O_3 , and Y_2O_3 . In general, Ni favors dehydrogenation, adsorption of the dehydrogenated species and C-C bond breaking, thus promoting reforming reactions, although the nature of the support plays a determinant role on the characteristics of the catalyst. Addition of K or Na was needed to reduce the acidity of the surface and reduce ethylene formation. Better results were obtained when basic oxides were used as supports; for instance, Ni/MgO doped with alkali metals had high hydrogen selectivity with reduced catalyst coking, improving stability by preventing Ni sintering (Frusteri et al, 2004).

Detailed studies have been reported for Co catalysts. ZnO was identified as the best support among several metal oxides (Llorca et al, 2002). The influence of the metallic precursor on the structure of the Co/ZnO catalysts and its activity and selectivity (Llorca et al, 2003), and the effect of sodium addition to prevent catalyst coking and deactivation (Llorca et al, 2004) were investigated. Complete conversion of ethanol and high selectivity towards hydrogen and carbon dioxide at temperatures from 350 to 450°C and a Steam to Carbon

molar ratio (SC) of 6.5 were observed (Llorca et al, 2003, 2004). A Co/ZrO₂ catalyst was also more active and selective towards hydrogen and carbon dioxide than Ni/ZrO₂ and Cu/ZrO₂ (Benito et al, 2005), having good stability through prolonged tests at 700°C and a SC ratio of 4.84.

Catalysts synthesized from Rh supported on metal oxides are also promising materials. Rh supported on Al₂O₃ had larger activity when compared to other supports like MgO and CeO₂, but Rh/CeO₂ had better selectivity towards H₂ and CO₂ than Rh/Al₂O₃ (Aupetre et al, 2002). The formation of coke on the Rh/Al₂O₃ catalyst surface at high temperature (700°C) required a sufficient excess of water and a Rh load of 5% (Cavallaro et al, 2000). Coke prevention was also improved by addition of 0.4 vol% of O₂ to the reactor feed, but it promoted metal sintering by the apparition of hot-spots due to the combustion of the carbon deposits (Cavallaro et al, 2003). Even if the Rh/Al₂O₃ catalyst is reported to be superior to the Ni-based catalysts in terms of activity, its main drawback is probably the cost of the metal (Klouz et al, 2002, Fierro et al, 2005). Unless the load of metal in the catalyst is small enough to make it cost effective, cost may limit its use in ethanol fuel processors for hydrogen production.

2-3-2 SRE mechanism and kinetic

Several authors have agreed about the complexity of the reaction mechanism for the SRE (Benito et al, 2005; Fatsikostas and Verykios, 2002; Cavallaro et al, 2003). Actually, depending on both catalyst composition and operational condition several pathways can occur. Figure 2-12 shows two of the main paths reported in literature. The most important reactions that may explain the results in different works (Benito et al, 2005, Haryanto et al, 2005, Vaidya and Rodrigues, 2006) are summarized in Table 2-6. In general, the overall stoichiometry could be represented as follows,



Though an illustrative study using DRIFT experiments, Llorca (2004) has found that the ethanol dehydrogenation eq (2-19) is favored at low temperatures (from 573 to 673 K) over ZnO supports, and acetaldehyde is an intermediate product in the SRE over Co/ZnO catalysts. In a second step, the presence of Co may favor the C-C rupture by acetaldehyde decomposition eq (2-24) or reforming eq (2-32) to produce carbon oxides, methane and

hydrogen in the presence of water. Carbon deposition indicates that some CH_x species might not progress to CH_4 or CO_2 , but place on the surface generating carbonaceous residues. On another study using SC of 4.84 and 700°C , Benito (2005) verify that Co/ZrO_2 could reform methane in a subsequent step to produce H_2 by eq (2-36). Also, under same conditions WGS eq (2-37) takes place. Benito observed that changing Co by Cu on ZrO_2 catalyzes the ethanol dehydration for producing ethylene by eq (2-20), which finally leads to carbon deposition by decomposition reaction eq (2-26).

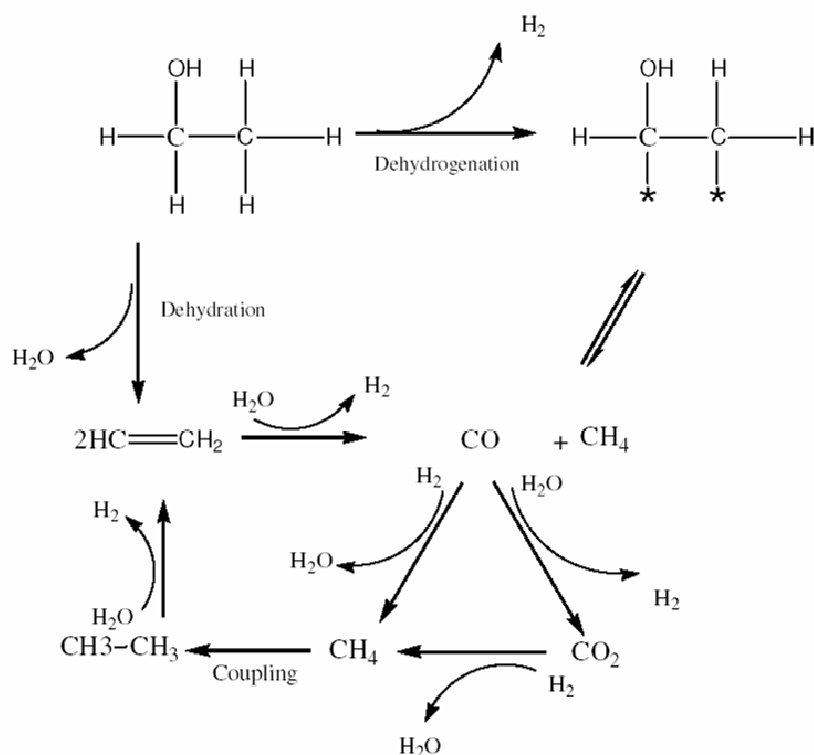


Figure 2-12 Two important intermediates observed in several catalytic studies for SRE; as a result of two distinct reaction pathways: ethanol dehydration that leads to ethylene formation; while ethanol dehydrogenation tends to produce acetaldehyde (Benito et al, 2006; Haryanto et al, 2006).

Fatsikostas (2004) investigated the interaction of ethanol with Ni and the surface of several catalyst supports: $\gamma\text{-Al}_2\text{O}_3$, La_2O_3 , and $\text{La}_2\text{O}_3/\gamma\text{-Al}_2\text{O}_3$. Again, ethanol dehydration eq (2-20) on Al_2O_3 was observed, which leads to ethylene production and coke formation by eq (2-26). On the other hand, La_2O_3 as support tends to favor acetaldehyde production by eq (2-19) and also promotes in small extent ethanol dehydration eq (2-20). When a combination of $\text{La}_2\text{O}_3/\gamma\text{-Al}_2\text{O}_3$ is used as support, a competition between dehydration and dehydrogenation reactions may be detected. Ni as active metal seems to catalyze several reactions, such as: the

WGS eq (2-37) -even at low temperatures, above 250°C-, the reforming of ethanol eqs (2-29) and (2-30), the reforming of acetaldehyde eqs (2-31) and (2-32), and the methane reactions eq (2-35).

Noble metals catalysts follow different paths depending on support interactions. Cavallaro et al (2000) studied the reaction pathway on Rh/Al₂O₃ which appears to proceed through ethanol dehydrogenation to acetaldehyde eq (2-19) and the decomposition of acetaldehyde into CO and CH₄ eq (2-24). After that, the reaction evolves towards both H₂ and CO₂ by the SRM eq (2-36) and WGS reactions eq (2-37). Recently, Roh et al (2006) found that using Rh, ethanol dehydration is favorable over either acidic or basic supports such as γ -Al₂O₃ and MgAl₂O₄, while ethanol dehydrogenation is more favorable over neutral supports like CeO₂.

CH₄ is an important by-product that can be obtained as a consequence of side reactions that consume H₂. This is the case of the methanation reactions –inverse of SRM eq (2-36)- which are catalyzed by active metals such as Ni, Rh and Pt (Haryanto et al, 2006). It is important to point out that once formed CH₄, by thermodynamic restrictions high temperatures are required to reform CH₄ and recover H₂ by eq (2-35). Then, to obtain a high selectivity to H₂ a catalyst which not favor CH₄ production is desirable.

Another undesired side reaction is the ethanol dehydration eq (2-20) because it produces C₂H₄, which later tends to generate carbon deposits in subsequent steps. Thermodynamic calculations show that carbon deposition through the Boudouard reaction is not favored even when the stoichiometric SC ratio of 1.5 is used, provided that the temperature is above 270°C (Mas et al, 2006). Catalyst coking by ethylene polymerization is a well known problem in steam reforming catalysts. Therefore suitable catalysts require combinations of active components and supports that do not promote ethanol dehydration and ethylene formation (Haryanto et al, 2006), being capable to reform ethylene. Finally, ethanol decomposes through homogeneous thermal cracking into ethylene and water, at a temperature above 600°C (Li et al, 2001, Fatsikostas and Verykios, 2004), which is in the middle of the range of typical SR temperatures.

In general, SRE experiments under packed bed reactors suffer from transport disguises as occurs with the SRM, as were discussed in section 2-2. Table 2-7 presents a summary of available kinetic studies that show important discrepancies in kinetic models, which may be caused by the difficult to obtain experimental data under true kinetic regime. As consequence, it is important to handle carefully these model under an operational condition different from the original one.

Table 2-6 Main possible reactions reported in literature for the SRE

Decomposition reactions			
Ethanol	$\text{CH}_3\text{CH}_2\text{OH} \rightleftharpoons \text{CH}_3\text{CHO} + \text{H}_2$	(2-19)	Dehydrogenation
	$\text{CH}_3\text{CH}_2\text{OH} \rightarrow \text{CH}_2=\text{CH}_2 + \text{H}_2\text{O}$	(2-20)	Dehydration
	$\text{CH}_3\text{CH}_2\text{OH} \rightarrow \text{CO} + \text{CH}_4 + \text{H}_2$	(2-21)	Cracking
	$\text{CH}_3\text{CH}_2\text{OH} + \text{H}_2\text{O} \rightarrow \text{CH}_3\text{COOH} + 2 \text{H}_2$	(2-22)	Oxidation
Acetaldehyde	$2 \text{CH}_3\text{CHO} \rightarrow \text{CH}_3\text{COCH}_3 + \text{CO} + \text{H}_2$	(2-23)	Acetone formation
	$\text{CH}_3\text{CHO} \rightarrow \text{CO} + \text{CH}_4$	(2-24)	Decarbonilation
Acetic	$\text{CH}_3\text{COOH} \rightarrow \text{CO}_2 + \text{CH}_4$	(2-25)	Decarboxilation
Ethylene	$\text{CH}_2=\text{CH}_2 \rightarrow 2 \text{C} + 2 \text{H}_2$	(2-26)	Carbon deposition
Methane	$\text{CH}_4 \rightarrow \text{C} + 2 \text{H}_2$	(2-27)	Carbon deposition
Carbon monoxide	$2 \text{CO} \rightleftharpoons \text{C} + \text{CO}_2$	(2-28)	Carbon deposition
Steam reforming reactions			
Ethanol	$\text{CH}_3\text{CH}_2\text{OH} + \text{H}_2\text{O} \rightarrow 2 \text{CO} + 4 \text{H}_2$	(2-29)	
	$\text{CH}_3\text{CH}_2\text{OH} + \text{H}_2\text{O} \rightarrow \text{CO}_2 + \text{CH}_4 + 2\text{H}_2$	(2-30)	
Acetaldehyde	$\text{CH}_3\text{CHO} + \text{H}_2\text{O} \rightarrow 2 \text{CO} + 3 \text{H}_2$	(2-31)	
	$\text{CH}_3\text{CHO} + \text{H}_2\text{O} \rightarrow \text{CH}_4 + \text{CO}_2 + \text{H}_2$	(2-32)	
Acetic	$\text{CH}_3\text{COOH} + 2 \text{H}_2\text{O} \rightarrow 2 \text{CO}_2 + 4 \text{H}_2$	(2-33)	
Acetone	$\text{CH}_3\text{COCH}_3 + 2 \text{H}_2\text{O} \rightarrow 3 \text{CO} + 5 \text{H}_2$	(2-34)	
Ethylene	$\text{CH}_2=\text{CH}_2 + 2 \text{H}_2\text{O} \rightarrow 2 \text{CO} + 4 \text{H}_2$	(2-35)	
Methane	$\text{CH}_4 + \text{H}_2\text{O} \rightleftharpoons \text{CO} + 3 \text{H}_2$	(2-36)	
	$\text{CH}_4 + 2\text{H}_2\text{O} \rightleftharpoons \text{CO}_2 + 4 \text{H}_2$	(2-37)	MSR
Carbon monoxide	$\text{CO} + \text{H}_2\text{O} \rightleftharpoons \text{CO}_2 + \text{H}_2$	(2-38)	WGS
Carbon	$\text{C} + \text{H}_2\text{O} \rightleftharpoons \text{CO} + \text{H}_2$	(2-39)	Carbon gasification

Table 2.7 Kinetic parameters for SRE reported in previous studies (Vaidya and Rodrigues, 2006a, 2006b, and Sahoo et al, 2006)

Catalyst	Temp, [K]	Rate Constant [mol kg ⁻¹ s ⁻¹]	Reaction order *	Activation Energy [kJ*mol ⁻¹]	Remarks
Ni/Al ₂ O ₃	403	5.20 x 10 ⁻⁵	n1=1	16.88	Sun et al i.d. = 6 mm
Ni/La ₂ O ₃	403	4.28x10 ⁻⁴	n1=1	1.87	Sun et al i.d. = 6 mm
Ni/Y ₂ O ₃	403	6.61x10 ⁻⁵	n1=1	7.04	Sun et al i.d. = 6 mm
Cu-plated Radney Ni	523-573		n1=1	149	Morgenstern et al i.d. = 12.7 mm L = 400 mm
Ni/Al ₂ O ₃	673	77.8 [kmol kg ⁻¹ s ⁻¹ atm ^{-9.52}]	n1= 2.52; n2=7		Therdthiangwong et al i.d. = 12.7 mm; L = 400 mm Bed not diluted
Ni/Al ₂ O ₃	593-673	3.03x10 ⁻³	n1=0.43	4.41	Akande et al i.d. = 8.0 mm Eley-Rideal and power law
Co/Al ₂ O ₃	773	2.97 x10 ⁻⁵		82.7	Sahoo et al i.d. = 19 mm; Langmuir-Hinshelwodd
Rh/Al ₂ O ₃	873 973	4.17 x10 ⁻² - 1.64 x10 ⁻¹	n1=1	96.0	Vaidya et al i.d. = 4.75 mm L= 45 mm

n₁...EtOH; n₂...H₂O

There is a variety of kinetic models for SRE, commonly using power law, Langmuir-Hinshelwodd, and Eley Rideal expresions. Akande et al (2006) propose two models for Ni/Al₂O₃ catalyst in the temperature range 573-793 K; first of those is a power law model with a value for the activation energy – 4.41 kJ mol⁻¹ – that seems to be far from the expected one – around 90 kJ mol⁻¹ –, and the second is a Eley-Rideal model. Vaidya and Rodrigues (2006) obtain a more realistic activation energy –96 kJ mol⁻¹ – using a linear rate law for a

Ru/ γ -Al₂O₃ catalyst, operating at 873-973 K. Sahoo et al (2007) fit experimental data at 773 K with a Langmuir-Hinshelwood kinetic model, including SRE, WGS and ethanol decomposition reactions. The elementary steps for this L-H model are present in Table 2-8.

Table 2-8 L-H mechanism for SRE on Co/Al₂O₃ catalysts proposed by Sahoo et al, 2006

Steam Reforming of Ethanol	#
$2\mathbf{S} + \text{CH}_3\text{CH}_2\text{OH} \rightleftharpoons \text{CH}_3\text{CH}_2\text{OS} + \mathbf{HS}$	(2-40)
$\mathbf{S} + \text{CH}_3\text{CH}_2\text{OS} \rightleftharpoons \text{CH}_3\text{CHOS} + \mathbf{HS}$	(2-41)
$2\mathbf{S} + \text{H}_2\text{O} \rightleftharpoons \text{OHS} + \mathbf{HS}$	(2-42)
$\mathbf{HS} + \text{CH}_3\text{CHOS} \rightleftharpoons \text{CH}_3\mathbf{S} + \text{HCHOS}$	(2-43)
$\text{CH}_3\mathbf{S} + \text{OHS} \rightleftharpoons \text{CH}_3\text{OHS} + \mathbf{S}$	(2-44)
$\mathbf{S} + \text{CH}_3\text{OHS} \rightleftharpoons \text{CH}_3\text{OS} + \text{OHS}$	(2-45)
$\text{CH}_3\text{OS} + \mathbf{S} \rightleftharpoons \text{HCHOS} + \mathbf{HS}$	(2-46)
$\text{HCHOS} + \text{OHS} \rightleftharpoons \text{HCOOHS} + \mathbf{HS}$	(2-47)
$\mathbf{S} + \text{HCOOHS} \rightleftharpoons \text{CO}_2\mathbf{S} + \mathbf{HS}$	(2-48)
$\text{CO}_2\mathbf{S} \rightleftharpoons \text{CO}_2 + \mathbf{S}$	(2-49)
$2\mathbf{HS} \rightleftharpoons \text{H}_2 + 2\mathbf{S}$	(2-50)
Water Gas Shift	
$\mathbf{S} + \text{HCOOHS} \rightleftharpoons \text{HCOOS} + \mathbf{HS}$	(2-51)
$\mathbf{S} + \text{HCOOS} \rightleftharpoons \text{COS} + \text{OHS}$	(2-52)
$\text{COS} \rightleftharpoons \text{CO} + \mathbf{S}$	(2-53)
$\text{HCOOS} \rightleftharpoons \text{CO}_2\mathbf{S} + \mathbf{HS}$	(2-54)
Ethanol Decomposition	
$\mathbf{S} + \text{CH}_3\text{CH}_2\text{OS} \rightleftharpoons \text{CH}_4\mathbf{S} + \text{COS}$	(2-55)
$\text{CH}_4\mathbf{S} \rightleftharpoons \text{CH}_4 + \mathbf{S}$	(2-56)

The rate determining step for SRE, WGS and ethanol decomposition are taken as dehydrogenation of adsorbed etoxy (2-41), decomposition of an intermediate species (2-52), and decomposition of ethanol (2-55), respectively.

2-4 Structured Catalyst Preparation

Structured catalysts have been employed extensively in environmental applications using the monolith configuration (Avila, 2005). Due to the success of this emerging application, preparation of structured catalyst has attracted significant attention. This section reviews principal features reported in recent literature, mainly focusing on ceramic and metallic monoliths.

Preparation of the monolithic structure

Monoliths can be prepared by extrusion and corrugation methods. Extrusion is the common technique employed in preparing ceramic monoliths. It consists in making a mixture with proper material (talc, clay, alumina, etc.), mold, dry, and heat at high temperature (1473-1773 K). Metallic monoliths are prepared by corrugation, that consist in combining corrugated and flat laminated layers, winding the laminates, pressing the coiled stacks from periphery and heating at 873-1173 K to form oxide on the plate's surface, and finally heating at 1273 K to join the plates (Cybulsky and Moulijn, 2006).

Once the monolith structure is available, the next step is adding the catalyst coat. In general, a monolith has a low surface area that frequently is coated first with a high surface area layer that serves as catalyst support. Ceramic monoliths have macro-pores which serve as reservoirs that facilitate to some extent this coating step, whereas metal surfaces usually do not have significant void spaces and require an additional pre-treatment step. Once the monolith is pre-treated, the catalyst is deposited on the monolith surface through a second coating step (Cybulsky and Moulijn, 2006). Next sections will be dedicated to a description of each step of the catalyst deposition process: pre-treatment, coating and deposition methods.

Pre-treatment

This step is gaining considerable attention because previous works have shown that optimizing the surface pre-treatment it is possible to increase the coat adherence. Depending on the monolith material, simple thermal oxidation or more complex chemical methods may be employed. Three popular methods are summarized as follows, according to information presented in a recent critical review (Meille, 2006):

- Anodic oxidation is a widespread method to obtain a porous alumina layer on aluminum structure. It consists of applying a direct current to an electrolyte in contact with an aluminum surface. This produces a competition between formation of an oxide layer and dissolution of the substrate, generating a porous layer. The temperature is an important factor to be controlled since the process is exothermic and temperature carries the dissolution process. Researches employ anodic oxidation either as a pre-treatment before another coating step, or as a method to obtain a porous layer.
- Thermal oxidation is basically a surface modification method, although it can be used either as a pretreatment step to enhance layer adhesion, or as a catalyst supporter. It is commonly employed with an important kind of metallic support: the FeCrAl substrate. When this material is heated in air at 840°C, an oxide layer forms on the surface with a thickness in the order of 1µm. In literature, the term “whiskers” is accepted to describe the morphology resulting of FeCrAl thermal pre-treatment. Alumina whiskers present an adequate roughness for a posterior washcoating (Avila, 2005). For instance, figure 2-13 shows a coating of $\gamma\text{-Al}_2\text{O}_3$ on top and whiskers below it.
- Chemical treatment consists of employing chemicals to induce changes in the surface of the support. For example, metallic surfaces are cleaned by immersion in acids such as HCl. Also, some acids like HNO_3 help to form a pseudo-layer that favors to some extent chemisorption of small charged particles on aluminum supports. Finally, alkali treatment can be used to perform etching and/or oxidation of silicon and titanium substrates.

Coating Methods

After pretreatment, the major part of coating methods require some kind of solvent to prepare dispersions with the catalytic components. The interaction between liquid and solids can present different degrees of complexity, from simple water-powder dispersion to customized sol-gel method. According to Meille (2006), liquid phase solutions can be classified into three main groups:

- Suspensions contain catalyst support or catalyst active phase in powder form, binder, acid, and solvent. Water is the standard solvent and the concentration of components varies over a large range depending on the application restrictions, such as layer thickness. The size of suspended particles has a great influence on final coat adherence. Nijhuis (2001) explained that the binder particles favor the attachment of

the coat layer by occupying places where larger particles touch each other once liquid is evaporated, as figure 2-14 shows. On the other hand, the acidity of suspension affects the viscosity and stability of particle dispersion (Avila, 2005). Other important factors are: particle geometry that can influence the homogeneity of final coat layer, and solid concentration which affects the viscosity solution.

- Sol-gels consist in a solution with a colloidal dispersion is acting as the chemical precursor of the material to be deposited. The sol can be prepared using a hydrolytic route, or a non-hydrolytic route, by forming a polymer-like compound with an appropriate alkoxide (Nijhuis, 2001). The hydrolysis is usually accelerated by the presence of an acid or a base; for this reason concentration of water, acid or base, and alkoxide, as well as temperature, are important parameters for sol formation. Another important parameter is ageing time which is the period were gelation (peptisation) of sol occurs, leading to cross-linking.
- Hybrid method between suspension and gel: in this case a sol acts as a binder, but also participates in the chemical and textural properties of the final layer. It is difficult to anticipate success possibilities due to the complex interaction of multiple parameters. In some cases, the use of binders composed by nano-particles is not recommended because it covers active sites (Meille, 2006).

Deposition Methods

After obtaining the suspension, it is a general practice to apply the washcoating by dip-coating. It consists in immersing the monolith in the slurry, waiting during a period of time, and withdrawing it at constant velocity. However, there are other alternatives:

- Spray-coating consists in applying a spray of the suspension over the support. Advanced related techniques exists that can offer significant benefits: electrostatic-spray deposition employs smaller drops and gives higher dispersion of catalysts (Benitez, 2005), or plasma-spray that also allows a more uniform distribution and enhances catalyst activation (Liu, 2002).

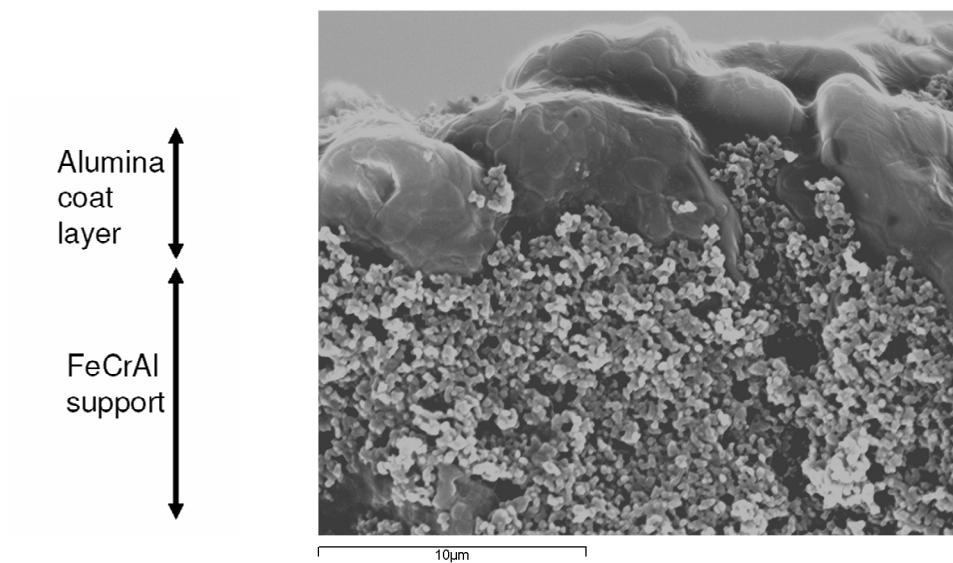


Figure 2-13 Coating of $\gamma\text{-Al}_2\text{O}_3$ on FeCrAl support; on top there is a layer of alumina adhered by washcoating;. Whiskers product of the thermal treatment are below it

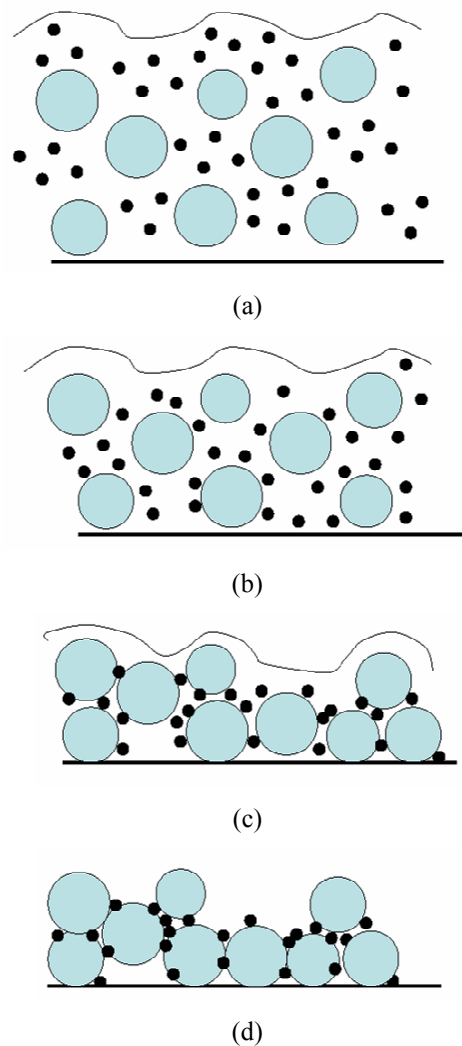


Figure 2-14 Schematic representation of binder action during liquid evaporation, according to Nijhuis (2001)
(a) wet slurry on surface (O large particles, black o binder); (b) first stage of drying; (c) large particles start to touch each other while binder is occupying interface places due to capillary forces; (d) binder deposited at the end of the drying process

- Spin-coating offers an easy control of film thickness by changing spin speed and solution viscosity. However, its application is limited because of geometry constraints.
- Electrophoresis deposition is a colloidal process where a direct-current electric field is applied across a stable suspension of charged particles attracting them to an oppositely charged electrode. The cathode is made of the kind of substrate to be coated, while the anode may be of aluminum or stainless steel. The thickness of the layer coated is a function of the distance between the two electrodes, DC current applied, the properties of the suspension and the time extent. This technique is used to deposit a previous coat of aluminum oxide to augment the adhesion of a catalyst, deposited in a second step (Meille, 2006).
- Electrochemical deposition and electroless plating employ ionic solutions to produce a metallic coating on a surface by the action of electric current. The metal is deposited on the cathode, which has the surface to be covered, by immersing it into a solution containing the salt to be deposited (Meille, 2006).
- Impregnation: another possible but less predictable method is direct impregnation of suspension using a brush. It is more common to employ an immersion method using a salt solution instead of sol suspension. However, this case is useful when dealing with structures possessing some macro-porosity, such as ceramics or previous oxide layer (Meille, 2006).
- Precipitation: is similar to the method employed in catalysis synthesis. It consists in submerging the support in a solution containing the active metals and adding a precipitation agent. Difficulties related with stirring might cause concentration gradients in the precipitation phase. Also, the pore volume of the substrate may constrain the amount of catalyst deposited (Nijhuis, 2001).

In summary, an extended list of possible methods to deposit catalyst on structures exist. The choice of an adequate method depends on the characteristics of materials to be employed. Table 2-9 shows a brief list of preparation method reported in open literature recently (Nijhuis, 2001; Meille, 2006; Avila, 2005). Nowadays, apart from available options, as interest on structured catalyst and reactor applications grows, the appearance of new developments concerning preparation methods is probable.

Table 2-9 List of methods and materials employed in several structure catalyst preparation methods from reference Meille, 2006

Method			Materials		Observations
Pretreatment	Coating	Deposition	Catalyst	Support	
T	S		Pt/Al ₂ O ₃	FeCrAl foam	Loading: 1.5 g/in ³
T	S		Pd/Al ₂ O ₃	FeCrAl foam	5.5 mg/cm ²
AO	S		Vanadium oxides	Al plates	Thickness: 10 – 40 μm
	H	I	CeO ₂ -Al ₂ O ₃	Ceramic monoliths	Thickness: 10 μm
T	SG		Al ₂ O ₃	FeCrAl fibres	Thickness: 1 μm
	SG	I	Ni/La ₂ O ₃ Rh/Al ₂ O ₃	Ceramic monoliths, foams and tubes	13% Ni 100-300 nm Rh 2 μm/layer
	S	EPD	Al ₂ O ₃	Stainless steel	Thickness: 2 – 4 μm
	S	EPD	ZrO ₂ , La ₂ O ₃ /ZrO ₂	Stainless steel	Thickness: 0.5 – 2 μm
T	S	I	Rh	Al ₂ O ₃ foams, FeCrAl monoliths	
	S	I	Ni/La ₂ O ₃	Cordierite monoliths	9 wt %
	S	P	Al ₂ O ₃	Glass fibres	6 wt %
	S	SpD (plasma)	Al ₂ O ₃	FeCrAl mesh	Thickness: 50 μm
T & C	S	I	Al ₂ O ₃	FeCrAl plates	

AO=Anodic oxidation

T=Thermal

C=Chemical

S=Suspension

SG=Sol-Gel

H=Hybrid

SpD=Spray-coating

SpC=Spin-coating

EPD=Electrophoresis

I=Impregnation

P=Precipitation

References

1. Akande (2006). "Kinetic modeling of hydrogen production by the catalytic reforming of crude ethanol over a co-precipitated Ni-Al₂O₃ catalyst in a packed bed tubular reactor." *International Journal of Hydrogen Energy* 31: 1707-1715.
2. Alpay, E., D. Chadwick, et al (1999). *Strategies for Enhanced Conversions and Yields in Catalysed Reversible Reactions*. 16th Colloquium on Chemical Reaction Engineering: Novel Chemical Reaction Engineering for Cleaner Technologies, Veszprém, Hungary, European Federation of Chemical Engineering.
3. Amon, B., H. Redlingshöfer, et al (1999). "Kinetic investigations of the deactivation by coking of a noble metal catalyst in the catalytic hydrogenation of nitrobenzene using a catalytic wall reactor." *Chemical Engineering and Processing* 38: 395-404.
4. Aupretre, F., C. Descorme, et al (2002). "Bio-ethanol catalytic steam reforming over supported metal catalysts." *Catalysis Communications* 3(6): 263-267.
5. Avila, P., M. Montes, et al (2005). "Monolithic reactors for environmental applications: A review on preparation technologies." *Chemical Engineering Journal* 109: 11-36.
6. Bartholomew, C. H. and R. J. Farrauto (2006). *Fundamentals of industrial catalytic processes*. Hoboken, N.J, Wiley.
7. Benitez (2005). "Novel method for preparation of PEMFC electrodes by the electrospray technique." *Journal of Power Sources* 151: 108-113.
8. Benito, M., J. L. Sanz, et al (2005). "Bio-ethanol steam reforming: Insights on the mechanism for hydrogen production." *Journal of Power Sources* 151: 11-17.
9. Cavallaro, S. (2000). "Ethanol steam reforming on Rh/Al₂O₃ catalysts." *Energy & Fuels* 14(6): 1195-1199.
10. Cavallaro, S., V. Chiodo, et al (2003). "Performance of Rh/Al₂O₃ catalyst in the steam reforming of ethanol: H₂ production for MCFC." *Applied Catalysis A: General* 249(1): 119-128.

11. Centi, G. and S. Perathoner (2003). "Integrated design for solid catalysts in multiphase reactions." *cattech* 7(3): 78-88.
12. Cheekatamarla, P. K. and C. M. Finnerty (2006). "Reforming catalysts for hydrogen generation in fuel cell applications." *Journal of Power Sources* 160(1): 490-499.
13. Choi, Y. and H. G. Stenger (2003). "Water gas shift reaction kinetics and reactor modeling for fuel cell grade hydrogen." *Journal of Power Sources* 124(432-439).
14. Cybulski, A. and J. A. Moulijn, Eds. (2006). *Structured catalysts and reactors*. Boca Raton, Florida, Taylor & Francis.
15. Dautzenberg, F. M. (2004). "New Catalyst Synthesis and Multifunctional Reactor Concepts for Emerging Technologies in the Process Industry." *Catalysis Reviews* 46(3-4): 335-368.
16. Duan, S. and S. Senkan (2005). "Catalytic conversion of ethanol to hydrogen using combinatorial methods." *Industrial & Engineering Chemistry Research* 44(16): 6381-6386.
17. Fatsikostas, A. N., D. I. Kondarides, et al (2002). "Production of hydrogen for fuel cells by reformation of biomass-derived ethanol." *Catalysis Today* 75(1-4): 145-155.
18. Fatsikostas, A. N. and X. E. Verykios (2004). "Reaction network of steam reforming of ethanol over Ni-based catalysts." *Journal of Catalysis* 225(2): 439-452.
19. Fierro, V. (2005). "Ethanol oxidative steam reforming over Ni-based catalysts." *Journal of Power Sources* 145(2): 659-666.
20. Fogler, H. S. (2001). *Elements of chemical reaction engineering*. New Jersey, Prentice Hall.
21. Frusteri, F., S. Freni, et al (2004). "Steam reforming of bio-ethanol on alkali-doped Ni/MgO catalysts: hydrogen production for MC fuel cell." *Applied Catalysis A: General* 270(1-2): 1-7.
22. Ghenciu, A. F. (2002). "Review of fuel processing catalysts for hydrogen production in PEM fuel cell systems." *Current Opinion in Solid State and Materials Science* 6: 389-399.

23. Giroux, T., S. Hwang, et al (2005). "Monolithic structures as alternatives to particulate catalysts for the reforming of hydrocarbons for hydrogen generation." *Applied Catalysis B: Environmental* 56: 95-110.
24. Groppi, G., W. Ibashi, et al (2001). "Structured reactors for kinetic measurements in catalytic combustion." *Chemical Engineering Journal* 82: 57-71.
25. Haryanto, A., S. Fernando, et al (2005). "Current status of hydrogen production techniques by steam reforming of ethanol: A review." *Energy & Fuels* 19(5): 2098-2106.
26. Holgado, J. P., J. Morales, et al (2001). "Plate reactor for testing catalysts in the form of thin films." *Applied Catalysis B: Environmental* 31: L5-L10.
27. Karim, A., J. Bravo, et al (2005). "Comparison of wall-coated and packed-bed reactors for steam reforming of methanol." *Catalysis Today* 110: 86-91.
28. Kiwi-Minsker, L. and A. Renken (2005). "Microstructured reactors for catalytic reactions." *Catalysis Today* 110: 2-14.
29. Klouz, V., V. Fierro, et al (2002). "Ethanol reforming for hydrogen production in a hybrid electric vehicle: process optimisation." *Journal of Power Sources* 105(1): 26-34.
30. Kolb, G., V. Hessel, et al (2007). "Selective oxidations in micro-structured catalytic reactors—For gas-phase reactions and specifically for fuel processing for fuel cells." *Catalysis Today* 120: 2-20.
31. Kolios, G., B. Glockler, et al (2005). "Heat-Integrated Reactor Concepts for Hydrogen Production by Methane Steam Reforming." *Fuel Cells* 5(1): 52-65.
32. Kordesch, K., Simader, G. (1995) *Fuel Cells and their applications*. Weinheim. Germany. VCH.
33. Krumpelt, M., T. R. Krause, et al (2002). "Fuel processing for fuel cell systems in transportation and portable power applications." *Catalysis Today* 77: 3-16.
34. Li, J., A. Kazakov, et al (2001). "Ethanol pyrolysis experiments in a variable pressure flow reactor." *Int. J. Chem. Kinet* 33: 859-867.
35. Liu, C.-j., G. P. Vissokov, et al (2002). "Catalyst preparation using plasma technologies." *Catalysis Today* 72: 173-184.

36. Llorca, J., P. R. de la Piscina, et al (2003). "CO-free hydrogen from steam-reforming of bioethanol over ZnO-supported cobalt catalysts - Effect of the metallic precursor." *Applied Catalysis B-Environmental* 43(4): 355-369.
37. Llorca, J., N. Homs, et al (2004). "In situ DRIFT-mass spectrometry study of the ethanol steam-reforming reaction over carbonyl-derived Co/ZnO catalysts." *Journal of Catalysis* 227(2): 556-560.
38. Llorca, J., N. Homs, et al (2002). "Efficient production of hydrogen over supported cobalt catalysts from ethanol steam reforming." *Journal of Catalysis* 209(2): 306-317.
39. Mas, V., R. Kipreos, et al (2006). "Thermodynamic analysis of ethanol/water system with the stoichiometric method." *International Journal of Hydrogen Energy* 31: 21-28.
40. Meille, V. (2006). "Review on methods to deposit catalysts on structured surfaces." *Applied Catalysis A: General* 315: 1-17.
41. Morillo, A., A. Freund, et al (2004). "Concept and Design of a Novel Compact Reactor for Autothermal Steam Reforming with an Integrated Evaporation and CO Cleanup." *Industrial and Engineering Chemistry Research* 43: 4624-4634.
42. Nijhuis, T. A., A. E. W. Beers, et al (2001). "Preparation of Monolithic Catalysts." *Catalysis Reviews* 43(4): 345-380.
43. Ogden, J. (2002). *Review for Small Stationary Reformers for Hydrogen Production*, International Energy Agency: 49.
44. Phatak, A. A., N. Koryabkina, et al (2007). "Kinetics of the water-gas shift reaction on Pt catalysts supported on alumina and ceria." *Catalysis Today* 123: 224-234.
45. Qi, A., B. Peppley, et al (2007). "Integrated fuel processors for fuel cell application: A review." *Fuel Processing Technology* 88: 3-22.
46. Roh, H.-S., Y. Wang, et al (2006). "Low temperature and H₂ selective catalysts for ethanol steam reforming." *Catalysis Letters* 18(1-2): 15-19.
47. Schmidt, L. D. (1998). *The Engineering of Chemical Reactions*. New York, Oxford University Press.
48. Schuessler, M. and M. Portscher (2003). "Monolithic integrated fuel processor for the conversion of liquid methanol." *Catalysis Today* 79-80: 511-520.

49. Stankiewicz, A. and J. A. Moulijn, Eds. (2004). Re-engineering the chemical processing plant : process intensification. New York, Marcel Dekker.
50. Sundmacher, K., A. Kienle, et al, Eds. (2005). Integrated Chemical Processes: Synthesis, Operation, Analysis, and Control. Weinheim, Wiley-VCH.
51. Tomasic, V. and F. Jovic (2006). "State-of-the-art in the monolithic catalysts/reactors." *Applied Catalysis A: General* 311: 112-121.
52. Tronconi, E. and G. Groppi (2000). "A study on the thermal behavior of structured plate-type catalysts with metallic supports for gas/solid exothermic reactions." *Chemical Engineering Science* 55: 6021-6036.
53. Vaidya, P. D. and A. E. Rodrigues (2006). "Insight into steam reforming of ethanol to produce hydrogen for fuel cells." *Chemical Engineering Journal* 117(1): 39-49.
54. Vaidya, P. D. and A. E. Rodrigues (2006). "Kinetics of Steam Reforming of Ethanol over a Ru/Al₂O₃ Catalyst." *Industrial & Engineering Chemistry Research* 45: 6614-6618.
55. van Beurden, P. (2004). On the catalytic aspects of steam-methane reforming: a literature survey. Petten, Energy Research Center of the Neetherlands: 27.
56. Venkataraman, K., J. M. Redenius, et al (2002). "Millisecond catalytic wall reactors: dehydrogenation of ethane." *Chemical Engineering Science* 57: 2335 – 2343.
57. Venkataraman, K., E. C. Wanat, et al (2003). "Steam Reforming of Methane and Water-Gas Shift in Catalytic Wall Reactors." *AIChE Journal* 49(5): 1277-1284.
58. Wanat, E. C., K. Venkataraman, et al (2004). "Steam reforming and water–gas shift of ethanol on Rh and Rh–Ce catalysts in a catalytic wall reactor." *Applied Catalysis A: General* 276: 155-162.
59. Wei, J. and E. Iglesia (2004). "Isotopic and kinetic assessment of the mechanism of reactions of CH₄ with CO₂ or H₂O to form synthesis gas and carbon on nickel catalysts." *Journal of Catalysis* 224: 370-383.
60. Yang, C. and J. Ogden (2007). "Determining the lowest-cost hydrogen delivery mode." *International Journal of Hydrogen Energy* 32: 268-286.
61. Zalc, J. M. and D. G. Löffler (2002). "Fuel processing for PEM fuel cells: transport and kinetic issues of system design." *Journal of Power Sources* 111: 58-64.

Chapter 3

Materials and Methods

This chapter describes different materials, equipments, and methods employed to cover objectives in this work. Methods can be classified into four key topics: catalyst preparation, reaction configuration, characterization techniques, and simulation tools.

3-1 Materials

Table 3-1 presents a list with specifications about gases used in this work. Gases perform important roles: fluid motion, calibration, catalyst reduction, and reaction feed.

Table 3-1 Gases specifications

Gas	Features	Function	Supplier
Ar	Premium (99.999%)	Carrier gas on CWR	Air Liquide
He	High Purity (99.995%)	Carrier gas on GC*	Carbueros Metálicos S.A.
N ₂	High Purity (99.995%)	Carrier gas on PBR	Carbueros Metálicos S.A.
CO ₂	Premium (99.998%)	MS Calibration**	Air Liquide
CO	Premium (99.998%)	MS Calibration and WGS Reactant	Air Liquide
CH ₄	Premium (99.998%)	MS Calibration and SRM Reactant	Air Liquide
Mixture	H ₂ (52%), N ₂ (20%), CO (12%), CO ₂ (12%), CH ₄ (1%), C ₂ H ₂ (1%), C ₂ H ₄ (1%), and C ₂ H ₆ (1%)	GC Calibration	Carbueros Metálicos S.A.
H ₂	High Purity (99.99%)	Catalyst reduction	Carbueros Metálicos S.A.

*GC...Gas Chromatography

**MS...Mass Spectrometry

Table 3-2 shows the main features of all chemicals employed for catalyst preparation. Catalytic plates were prepared by deposition of catalysts over structured metallic plates (width 20 mm, length 50 mm, thick 1 mm) composed by Fe, Cr, and Al (FeCrAlloy^(R), Goodfellow).

Table 3-2 Chemicals specifications

Gas	Features	Function	Supplier
C ₂ H ₅ OH	99.5% purity	Reactant	Panreac
C ₂ H ₄ O	99.9% purity	Solvent	J.T. Baker
H ₂ O	Ultrapure (18.5 MΩ)	Solvent/Reactant	Millipore purification system
CH ₃ COCH ₃	99.5% purity	Solvent	Panreac
αAl ₂ O ₃	High purity	Bed inert	Alcoa
Cordierite	High purity	Bed inert	Gimex
γAl ₂ O ₃	99.9%	Catalyst support	Aldrich
Ni(NO ₃) ₂ ·6H ₂ O	99.999%	Metal catalyst	Aldrich
Cu(NO ₃) ₂ ·3H ₂ O	99.999%	Metal catalyst	Aldrich
La(NO ₃) ₂ ·6H ₂ O	99.999%	Basic promoter	Aldrich
Zn(NO ₃) ₂ ·6H ₂ O	99.999%	Catalyst support	Aldrich
Co(NO ₃) ₂ ·6H ₂ O	99.999%	Metal catalyst	Aldrich
Mn(NO ₃)·4H ₂ O	99.999%	Catalyst dopant	Aldrich
Fe(NO ₃) ₄ ·9H ₂ O	99.999%	Catalyst dopant	Aldrich
Urea	99.0%	Precipitation agent	Aldrich
Poly-Vinyl Alcohol	High purity	Binder	Celanese
Poly-Ethyene Imine	50%wt in water	Binder	Aldrich
Bohemite	High purity	Sol preparation	Disperal
Triton	High purity	Binder	Acros

3-2 Catalyst Preparation

Catalysts used in this work can be classified on four groups according to: active metal (nickel or cobalt) and structure (powder or coat deposited on a metallic plate). Figure 3-1 shows a diagram with the procedure followed to prepare powder catalysts; while Figure 3-2 describes two methods employed to deposit catalytic coating over metallic plates: impregnation by washcoat for Ni based catalysts, and precipitation for Co based.

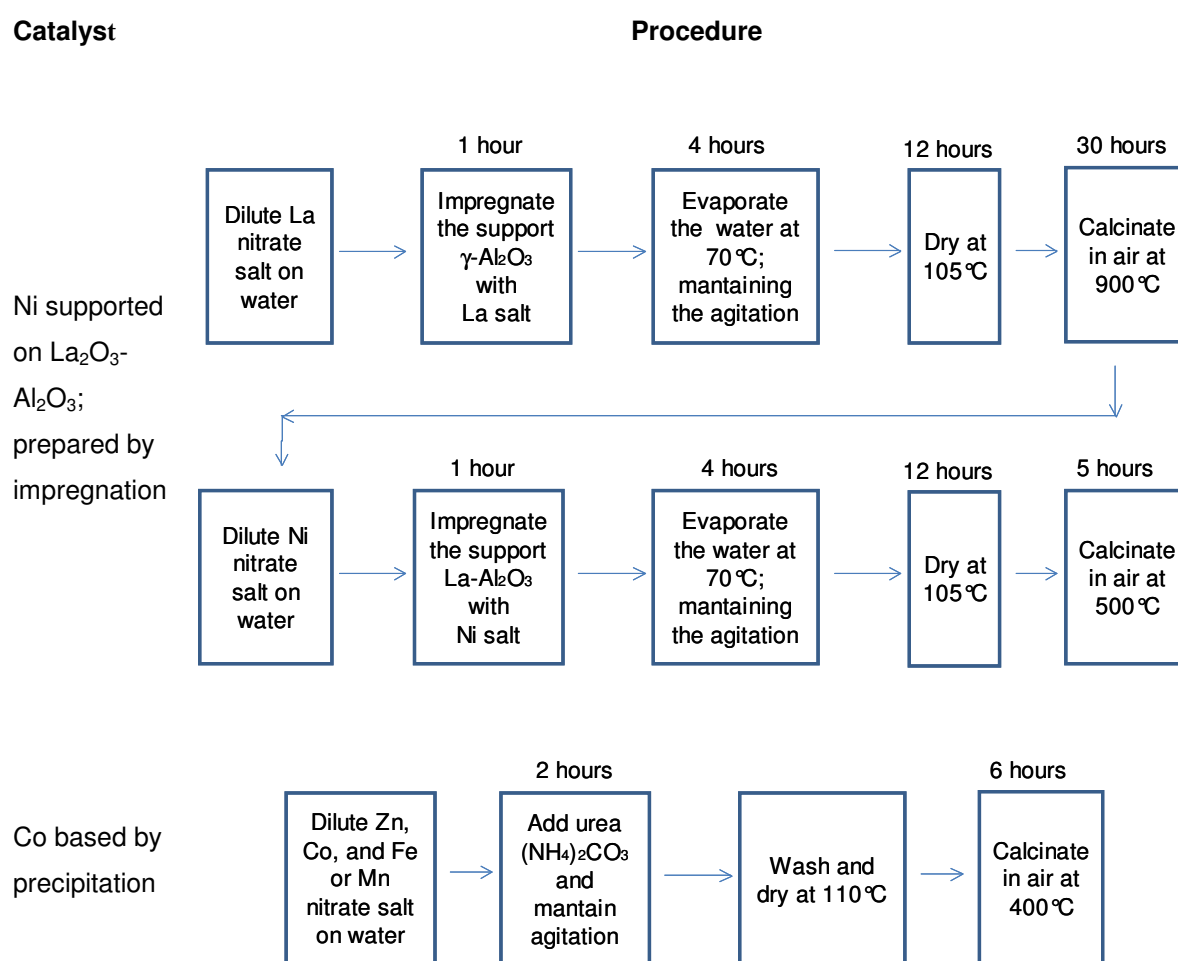


Figure 3-1 Diagram with the procedure sequence followed to prepare powder catalysts. Catalysts can be classified on four groups as function of: active metal (nickel or cobalt) and structure (powder or coat deposited over a metallic plate)

Coating

Procedure

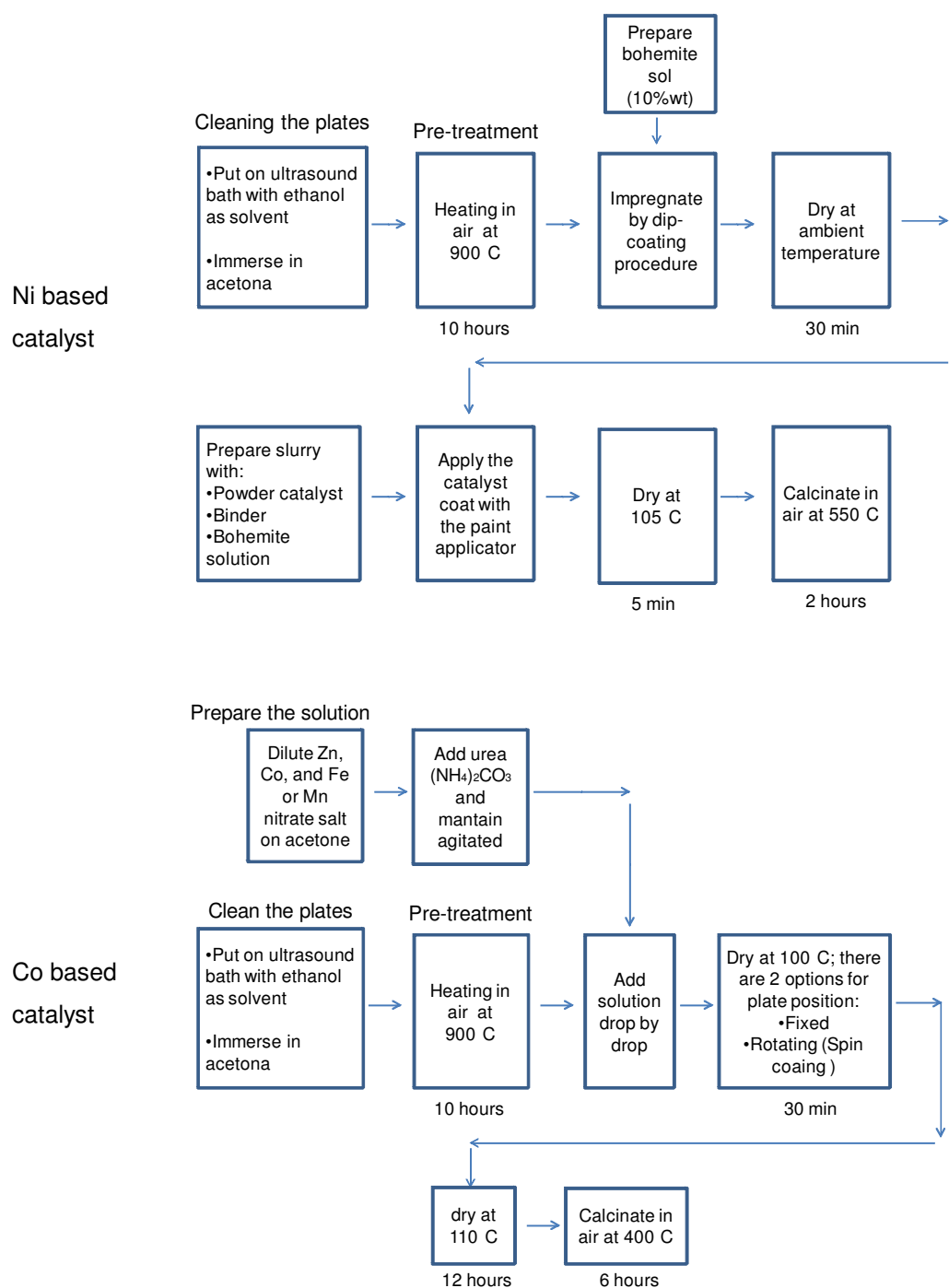


Figure 3-2 Diagram with the sequential program followed to prepare catalytic coating over metal plates. The catalysts can be classified on four groups as function of: active metal (nickel or cobalt) and structure (powder or coat deposited over a metallic plate)

3-2-1 Ni catalysts

Impregnated nickel catalyst supported on $\gamma\text{-Al}_2\text{O}_3$ (150 mesh) were obtained from nickel hydrated salt ($\text{Ni}(\text{NO}_3)_2 \cdot 6\text{H}_2\text{O}$). Other metals were added with the same kind of salt ($\text{Cu}(\text{NO}_3)_2 \cdot 3\text{H}_2\text{O}$ for the copper; and $\text{La}(\text{NO}_3)_3 \cdot 6\text{H}_2\text{O}$ for lanthanum). Commercial catalyst was ICI-46-1, provided by ICI-Katalco. Also, it was employed another catalyst obtained using hidrotalcite as precursor which originally was developed for oil steam reforming (Marquevich 2001), which is composed by Ni/Mg/Al in 1:1:1 proportion. Two different inert materials were used to dilute catalyst on PBR: powder cordierite (particle diameter in the range 0-0.5 mm) and tabular $\gamma\text{-Al}_2\text{O}_3$ (T-60).

Ni/La₂O₃/γ-Al₂O₃ catalyst preparation method was the same followed by Fatsikostas (Fatsikostas 2002). First was impregnated the lanthanum by dissolving the salt in ultra pure water and adding the aluminum oxide. This slurry was agitated at ambient temperature for 1 hour. Then, it was heated slowly until 70°C and temperature was maintained to allow water evaporation. At this point, solid residue was dried during 24 hours at 105 °C. Next, it was calcinated in air at 900 °C during 30 hours. After that, second impregnation was made using the nickel salt; and evaporation and dry steps were repeated. After that, calcinations in air were performed at 550 °C during 2 h.

Finally, catalyst reduction was executed under a gas stream composed by 50% H₂ and 50 % N₂. It was slowly heated following a 2°C min⁻¹ ramp until it achieved 550°C for 5 hours. Similar preparation method was followed for Ni-Cu/La₂O₃/γ-Al₂O₃ catalyst; except for the second impregnation that was made with a solution containing both nickel and copper nitrate salts. The resulting material was crushed and sieved into several diameter ranges (three ranges: 0-0.04, 0.04-0.2, and 0.2-0.5 mm). Different catalyst formulations (Ni/La₂O₃/γ-Al₂O₃) were obtained through variation on the metals content: nickel from 10% to 15% and lanthanum from 5-8%. Ni-Cu/La₂O₃/γ-Al₂O₃ catalyst maintained fix values for Ni and La composition (10% and 5% respectively); and Cu (at 2% weight).

3-2-2 Co catalysts

Catalysts based on Co (both powder and plate configurations) were prepared on the laboratories of the research group “Institut de Tècniques Energètiques”, from Universitat Politècnica de Catalunya. Co was supported on ZnO and contained 10% of cobalt metal by weight and a 1% of Fe or Mn. Nitrate salts and urea were main starting materials ($\text{Zn}(\text{NO}_3)_2 \cdot 6\text{H}_2\text{O}$, $\text{Co}(\text{NO}_3)_2 \cdot 6\text{H}_2\text{O}$, $\text{Mn}(\text{NO}_3)_2 \cdot 4\text{H}_2\text{O}$, and $\text{Fe}(\text{NO}_3)_3 \cdot 9\text{H}_2\text{O}$). It was prepared by co-precipitation at 30 °C by addition of a $(\text{NH}_4)_2\text{CO}_3$ solution (0.6 M) to a mixture of $\text{Zn}(\text{NO}_3)_2$, $\text{Co}(\text{NO}_3)_2$, and $\text{Fe}(\text{NO}_3)_3$ or $\text{Mn}(\text{NO}_3)_2$ aqueous solutions ($[\text{M}^{x+}] = 0.8 \text{ M}$). After aging for 2 h, resulting solids were washed with distilled water, dried at 110 °C overnight, and calcined in air at 400 °C for 6 h. These catalysts were labeled as Co-Fe/ZnO and Co-Mn/ZnO. For comparative purposes a monometallic cobalt catalyst, Co/ZnO, was prepared in a similar way. Prior to the catalytic tests, catalysts were reduced under hydrogen at 400 °C for 4 h.

3-2-3 Catalytic plates by washcoating

Figure 3-2 shows a procedure outline to prepare catalytic plates by washcoating deposition over metallic structure; following a similar method reported in literature (Meille et al., 2005). Metallic plates (width 20 mm, length 50 mm, thick 1 mm) were composed by Fe, Cr, and Al (FeCrAlloy^(R), Goodfellow).

Impregnation is based on applying aqueous slurry that contains catalytic material and other compounds which have two main functions: improving solid dispersion stability and to increase attachment between catalyst particles. Catalyst plate deposition by impregnation consists of four steps:

- Plate pretreatment to favor the segregation of an alumina layer on the metal surface. First, the plate was cleaned with acetone and introduced into an ultrasonic bath with ethanol as solvent. After that, plates were oxidized at 900 °C for 10 h, employing a ramp of 3 °C min⁻¹ from ambient temperature to 600 °C; and a second ramp of 0.5 °C min⁻¹ from 600 °C until 900 °C.
- Primer deposition with bohemite solution (10% aluminum hydroxide powder) to improve the washcoat adherence. This solution was prepared in a 0.4% HNO₃ aqueous solution, stirring for 10 min after that was obtained a stable dispersion with 20 mPa s viscosity. Calcinated plates were impregnated by a dip coating procedure submerging

for 15 s and retiring with a velocity around 3 cm min^{-1} . This bohemite coat was dry at ambient temperature during 30 min.

- Slurry preparation and impregnation. It was prepared an aqueous slurry composed by three key components: powder catalyst, binder, and bohemite dispersed in aqueous solution; stirring for 12 h in a close vessel at ambient temperature. Plate was immersed under the slurry during 1 min and with a paint applicator (K-101P Coater Applicator; R.K. Print Coat Instruments) was moved the slurry storage container using a constant velocity around 3 cm min^{-1} . Figure 3-3 shows a detailed image of this equipment, and a scheme that explain how it works.
- Plates were dried at $105\text{ }^{\circ}\text{C}$ during 5 min and calcinated in air at $550\text{ }^{\circ}\text{C}$ during 2 hours. Finally, plates were reduced under a gas stream composed by 50% H_2 and 50 % N_2 ; heating slowly by a $2^{\circ}\text{C min}^{-1}$ ramp until it achieved a temperature of 550°C for 5 hours, using a tubular oven with proper dimensions (Hobersal).

3-2-4 Catalytic plates by precipitation

Precipitation method consists on preparing a solution with nitrate salts (Zn, Co, and optionally Fe or Mn), urea, and acetone as solvent. This solution formed a reactive complex that was strongly adhered to the metallic surface after calcination. Solution was deposited drop by drop on the metallic plates and solvent was evaporated slowly by heating until 100°C . Catalytic plates with Co based catalyst were also coated by spin coating method. It consists in apply the same procedure described before (add the solution drop by drop and heat until 100°C), but rotating the plate at 300 rpm with a magnetic stirrer (Agimatic E) during the drying step. Precipitation method can be summarized into five steps:

- Prepare the starting solution by dissolving nitrate salts in acetone.
- Clean the metallic plates employing first an ultrasound bath and then by immersion in a solvent, as acetone, to remove impurities.
- Add salt solution drop by drop on the plate surface.
- Evaporate acetone by heating slowly until 100°C . At this point is possible to maintain plates on fixed position or rotating at 300 rpm (spin coating).
- Dried at $110\text{ }^{\circ}\text{C}$ during 12 h. Plates were reduced under a stream composed by H_2 and N_2 ; heating slowly ($2^{\circ}\text{C min}^{-1}$ ramp) until achieve 400°C for 4 h.

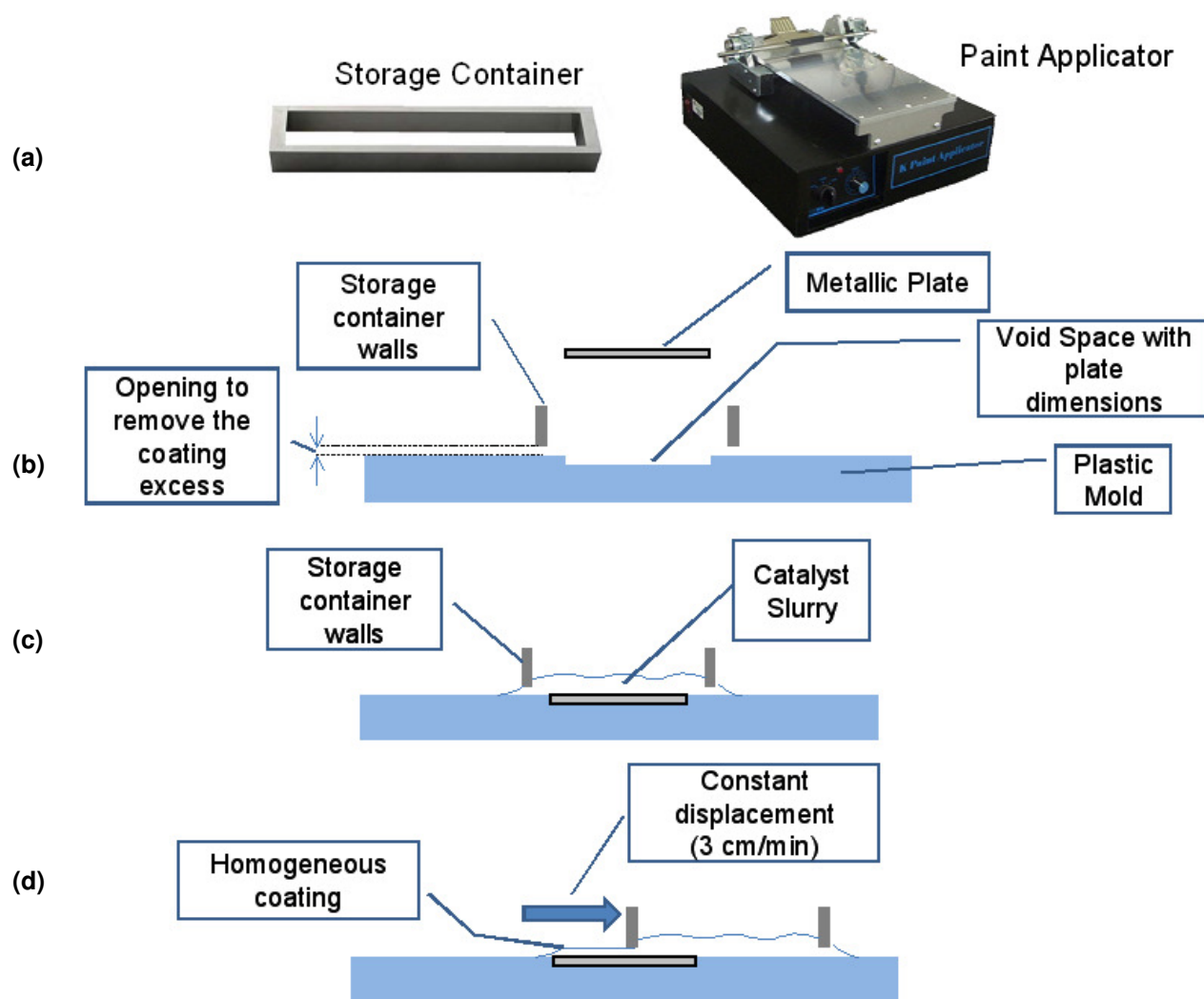


Figure 3-3 Paint applicator equipment (K-101P Coater Applicator; R.K. Print Coat Instruments) where plate was immersed under the slurry during 1 min and the storage container was removed using a constant velocity around 3 cm min^{-1} : (a) Storage container and paint applicator images (Torras, 2005), (b) Lateral section of the wash-coating setup, (c) Lateral section during the immersion step, (d) Lateral section during the storage container withdraw.

3-3 Experimental Equipments

Two reactor configurations are described: PBR for screening catalysts experiments and CWR configuration for analyzing the catalytic plate reaction performance.

3-3-1 Packed Bed Reactor Configuration

Catalysts were tested on tubular PBR; adapted from a unit previously used in the Biopolymers group (Marquevich, 2001). Major modifications were performed to the separation unit to improve recuperation and condensation of volatile products, such as acetaldehyde. In figure 3-4 is shown the PBR equipment; which is composed by five units: feeder, pre-heater, reaction, separation, and instruments for analysis and measurement. Measuring instruments are connected to a data acquisition software package (Genie PCLS-920).

Liquid phase is deposited on bottles over balances (Scaltec SBA 52) to measure the mass flow rate by registering changes on weight. A piston pump (Pulsatron Series E-plus) impulses liquid; which is mixed with N₂ and evaporated by an electrical resistance. This mixture enters into the tubular reactor (15 mm inner diameter by 300 mm length, stainless steel 316L) which is filled with a mixture composed by powder catalyst and inert solid. This tube is sustained inside a tubular oven (Hobersal) equipped with a digital control for adjusting temperature. At the reactor center is located a 1/8'' tube that contains three K-type thermocouples at different axial length. Reaction products are cooled and conducted to a separator unit where condensed liquid is extracted and analyzed, while gases are conducted to the gas chromatograph for being analyzed. Pressure and volumetric flow rates are measured at the reactor outlet. Gas analyses were hold by a Gas Chromatograph (HP 5890), using helium as carrier and a TCD detector. The separation column employed was Carboxen-1000 (Supelco, S.A., 1.5m; 1/8''OD; 60/80 mesh). Liquid analyses were performed by a HPLC Agilent 1100 Series, coupled with column Aminex HPX87H and the solvent phase was sulfuric acid solution 0.005 M.

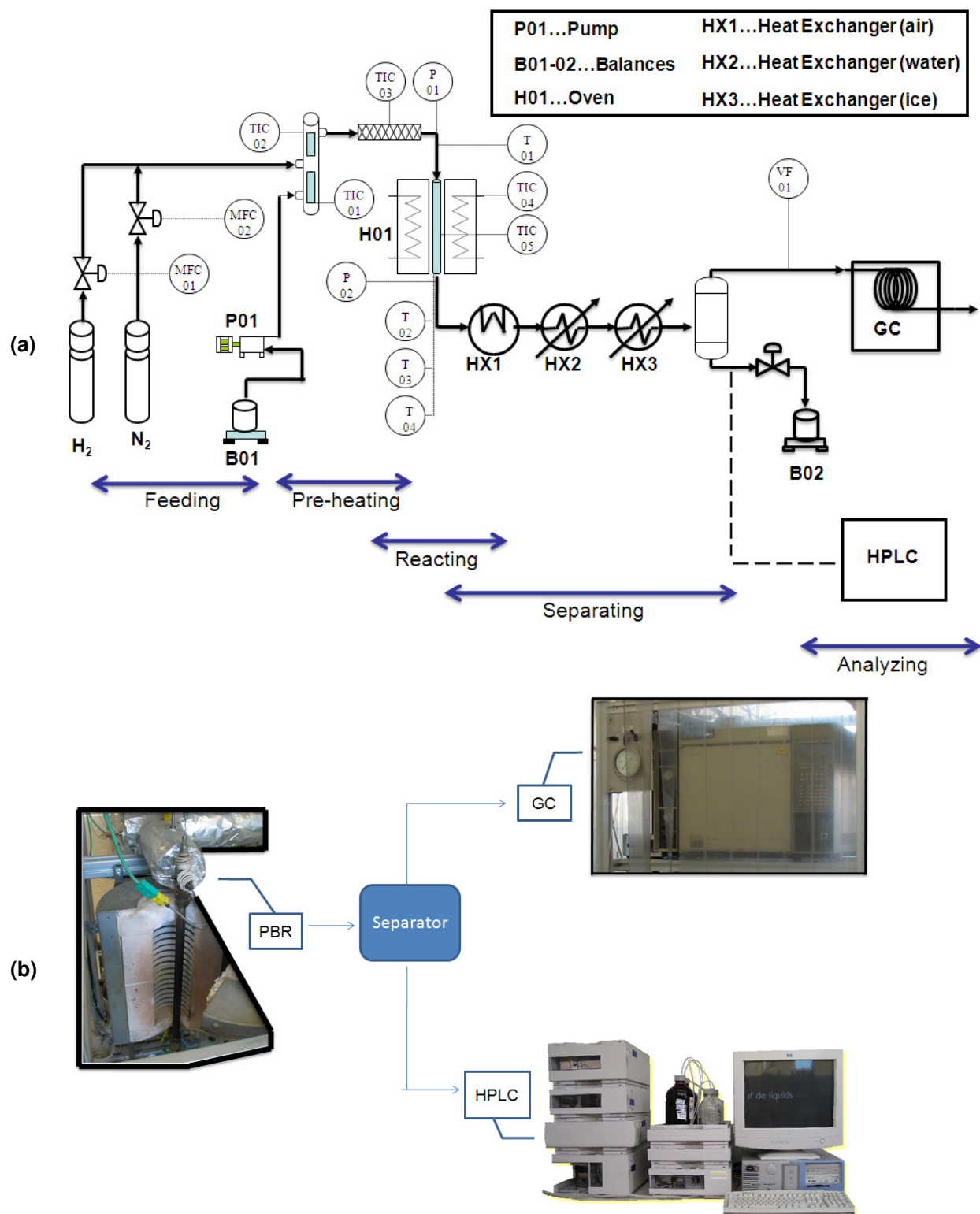


Figure 3-4 Packed Bed Reactor equipment for screening catalyst experiments. Ethanol mixed with water and nitrogen is pump into the tubular reactor (15 mm inner diameter by 300 mm length, stainless steel 316L) which is filled with a powder mixture composed by catalyst and inert particles. Catalyst dilution contributes to avoid thermal gradients caused by energy consumption of the endothermic Steam Reforming of Ethanol reaction: (a) general scheme, (b) images for the most important equipments

The general sequence was: (i) mount reactor, (ii) start equipment, (iii) reduce catalyst, (iv) prepare feeding and (v) set parameters -furnace temperature and pump mass flow rate-. It was required a stabilization period, in order to guarantee stationary conditions. Along the hole experiments, sampling analysis were performed for both gas and liquid streams. Liquid samples were freeze immediately. Once experiment was over, liquid samples were analyzed by HPLC and calculations were performed using a Microsoft Excel worksheet. Cautions were considered in order to minimize mass and thermal internal gradients as much as possible. The range of operational conditions is:

- Feed mass rate: $0.1-4.0 \text{ g min}^{-1}$
- Particle diameter: $0.2-0.5 \text{ mm}$
- Bed mass: inert material (30 g), and catalyst (from 0.1 to 2.0 g respectively).
- Bed temperature: $450-550^\circ\text{C}$
- Steam to Carbon ratio: from 2 to 4
- Inert gas flow rate (N_2): $0.20-0.40 \text{ ml min}^{-1}$
- Bed pressure gradient: from 0.5 to 1.0 bar

From 0.1 to 2.0 g of catalysts were sieve to $0.1-0.2 \text{ mm}$ before testing; and diluted with 30 g of cordierite powder sieved to less than 0.5 mm to improve mass and heat transfer in the catalytic bed. Figure 3-5 presents some bed details in a typical catalytic test.

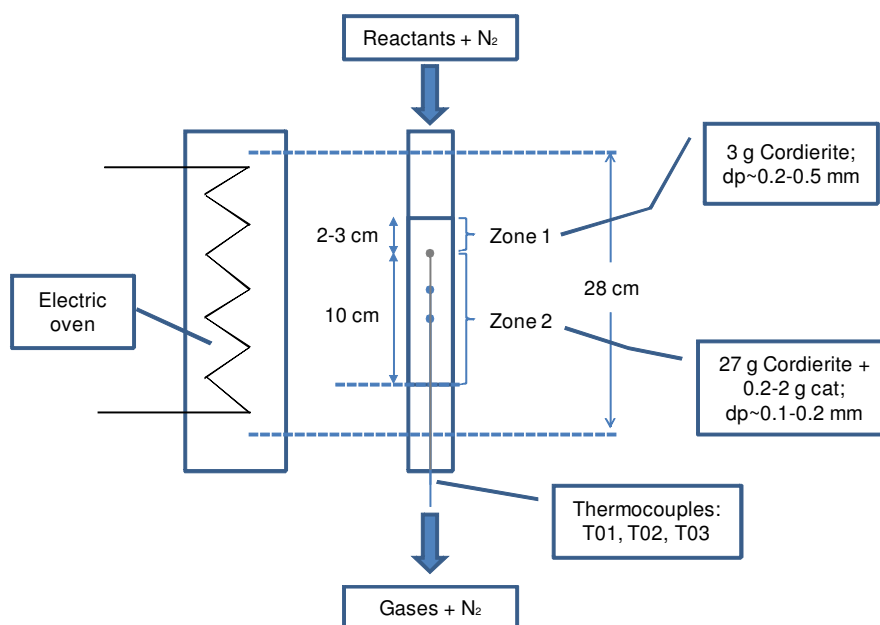


Figure 3-5 Diagram with details of the catalytic bed

3-3-2 Catalytic Wall Reactor Configuration

A CWR was designed and constructed for evaluating the reaction performance of catalytic plates. It is composed by five units: feeder, pre-heater, reactor, separator, and instruments for analyzing and measuring. Reactor consists in a stainless steel block, divided into two symmetric parts, which contain a pre-heating channel and a rectangular void space where attach two plates horizontally, as shown figure 3-6. Reactants enter at the pre-heating channel; at the same time, fluid is heated until reach the catalytic plate where the chemical reaction takes place. Two square electrical resistances (Watlow, Thickfilm Heater; width 101.6 mm, length 101.6 mm; 25W inch⁻²) heat the steel block at top and bottom block sides; while the laterals are isolated. A graphite seal prevents gas losses before reaching the reactor output. Temperature is measured in the steel block along pre-heating channel and catalytic plate region by six k-type thermocouples. The steel block is encapsulated into an aluminum box with the walls covered by an insulator material, to reduce as much as possible the heat losses.

Figure 3-7 shows a general scheme for CWR unit. Liquid is feed by a syringe pump (Kd Scientific, KDS100) and mixed with argon, which is used as inert gas and impulsed by a mass flow controller (Bronkhorst, EL-Flow). Reactor is placed inside a drying oven (Digitronic, 2000 series), maintained at constant temperature (175°C) to evaporate the liquid before the reactor input. Once products reach the reactor exit, stream composition is analyzed by a Mass Spectrometer (Pfeiffer, QMS 200) before condense vapors by a plate heat exchanger (Supercool, DA-075).

Finally, mass flow rate is measured with a gas flow meter (Bronkhorst, EL-Flow); and gas composition is analyzed by a gas chromatograph (HP 5890) using helium as carrier, TCD as detector, and the separation column Carboxen-1000 (Supelco, S.A., 1.5m; 1/8''OD; 60/80 mesh). Measuring instruments are connected to a data acquisition software package (LabView^(R)). Once experiment is finished, mass balance is performed using computational code developed under MATLAB^(R) environment.

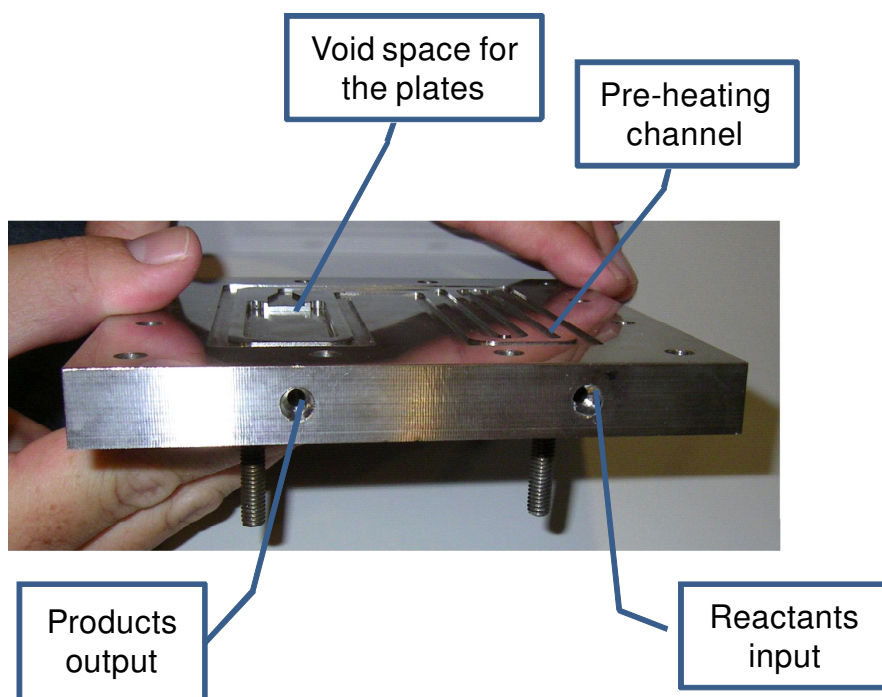
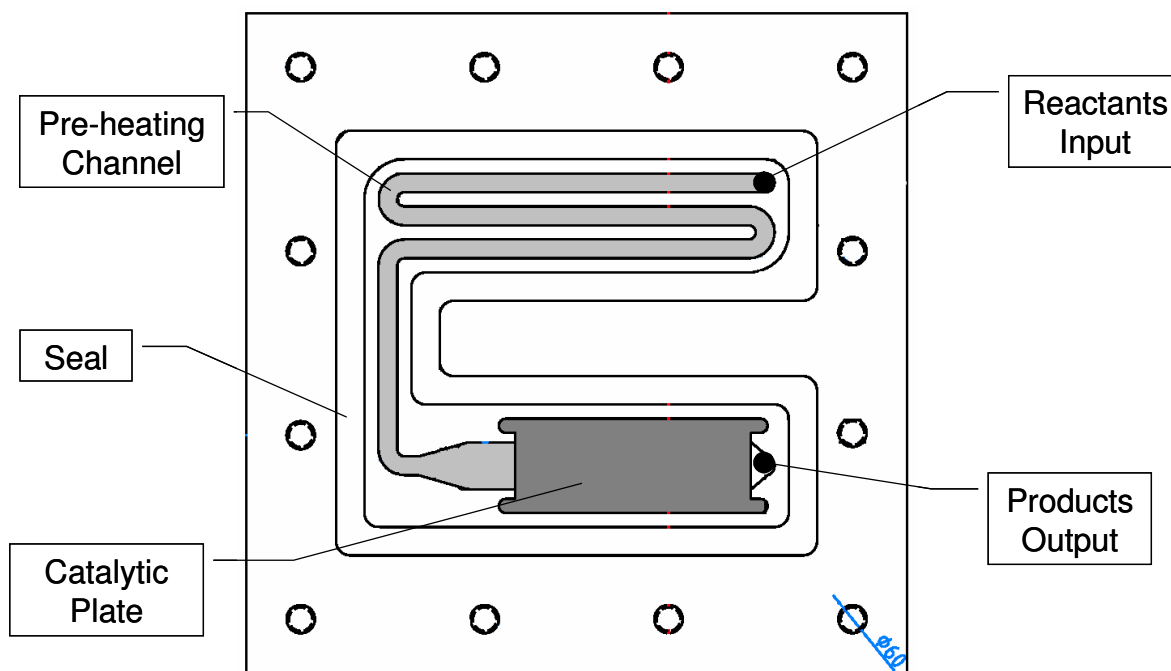


Figure 3-6 Block designed for performing catalytic plate tests. Fluid enters at the pre-heating channel, until reach the catalytic plate. Two square electrical resistances heat the steel block at top and bottom block sides; while the laterals are isolated. A graphite sealing prevents gas losses before reaching the reactor output.

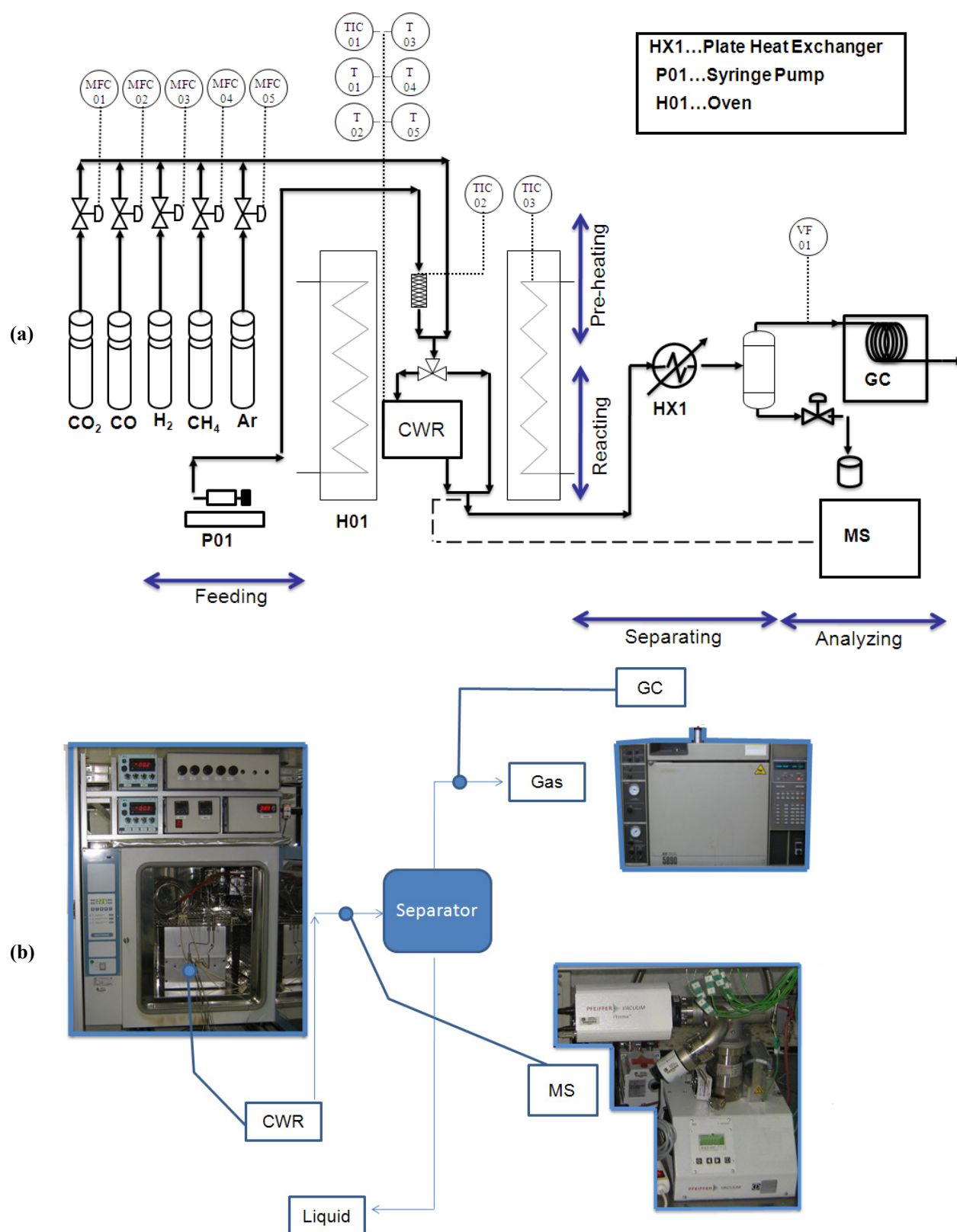


Figure 3-7 Catalytic Wall Reactor Unit designed and constructed for evaluating the reaction performance of catalytic plates. It is composed by five units: feeder, pre-heater, reactor, separator, and instruments for analyzing and measuring: (a) general scheme, (b) images from the most important components

Figure 3-8 shows images for the five key steps on the CWR mounting: (i) plate catalyst and graphite seal is placed into the void spaces on the open steel block, (ii) the steel block is closed by inserting each part in front of the other, (iii) the entire block is fitted into the aluminum box and additional insulator material is placed if necessary, (iv) the aluminum box is closed, and (v) introduced it into the drying oven; where electrical and fluid connections are joined.

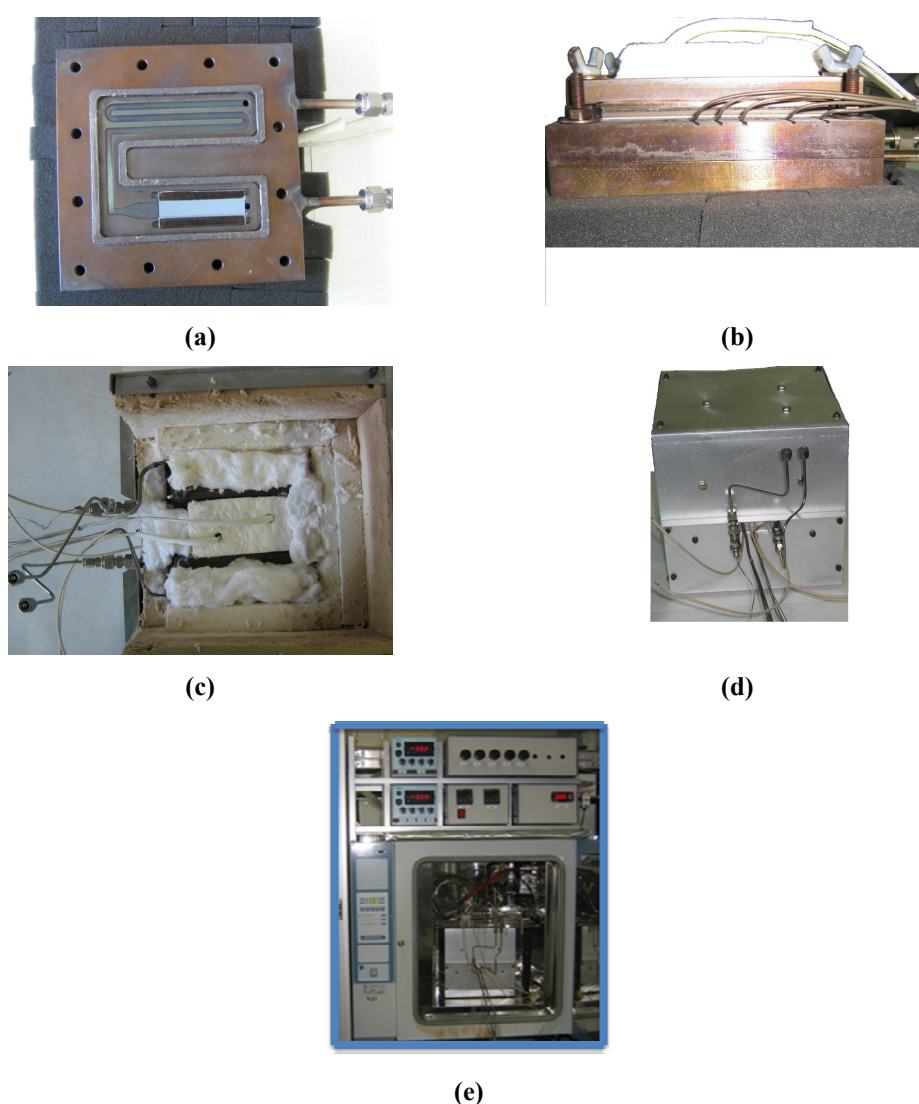


Figure 3-8 Images for illustrating the five key steps for mounting catalytic plates in the Catalytic Wall Reactor Unit (a) put plate catalyst and graphite seal into the void spaces, (b) close steel block, (c) fit the block into the aluminum box, (d) close the aluminum box, and (e) introduce it into the drying oven and connect electrical and fluid connections

3-4 Analytical Techniques

3-4-1 Catalysts Characterization

Catalyst characterization is the study of catalytic surfaces at microscopic and mesoscopic levels with the aim of gaining knowledge about the catalytic behavior. In particular, an exploration of surface composition and structure properties facilitates the task of discriminating efficient from less efficient catalysts. Next is presented principal characteristics and function of characterization techniques employed in this work:

1. *X-Ray Diffraction (XRD)*

X-rays have wavelengths sufficiently energetic to penetrate solids that allow exploring its internal structure; XRD is commonly used to identify bulk phases, to monitor the kinetics of the bulk transformations, and to estimate particle sizes (Niemantsverdriet, 1995). It was employed a diffractometer, Siemens, D5000, with $\text{CuK}\alpha$ radiation from a Cu X-ray tube at 40kV and 30mA. XRD spectra were performed from 5 to 70° 2θ with 3s steps of 0.05°. Crystalline phases were identified with the JCPDS database.

2. *Electron Microscopy*

It is a set of useful techniques for catalyst characterization tasks, such as: produce high resolution images of a sample surface, determine size and shape of supported particles, and reveal information on the composition and internal structure of the particles. It consists on putting in contact the sample surface with a primary electron beam (commonly in the order of 100 keV). This interaction leads to emission of electrons and electromagnetic radiation which produces a number of detectable signals revealing information about the sample nature. Images obtained with Scanning Electron Microscope (SEM), JEOL JSM-6400, were employed to observe possible carbon formation in catalytic surface. Also, Environmental Scanning Electron Microscope (ESEM), Quanta 600 FEI, was used for assessing catalyst surface composition by Energy-Dispersive Spectroscopy (EDS) and for obtaining images of catalytic plates. Transmission Electron Microscopy (TEM), JEM-1011 JEOL, was employed for determining size and shape of supported catalyst particles.

3. *Atomic Absorption Spectroscopy (AAS)*

It is a technique for determining the concentration of metals in a sample. This technique transforms a liquid sample into an atomic gas in form of flame; which passes through a

light beam. The energy emitted by this light depends on the particular metal atoms; so is possible to obtain a signal proportional to the metal concentration. In this work the AAS equipment, Perkin Elmer 3110, was employed specifically for evaluating Ni content on prepared catalysts.

4. *Adsorption isotherms*

BET analysis is a method to evaluate sample porosity and internal surface area. It was employed a BET equipment, Micromeritics ASAP 2020, using N₂ and temperature at 77 K. First, samples are subject to degasification at 523K to remove gas adsorbed under atmospheric conditions. Then, progressively is introduced a small amount of N₂ and the adsorbed gas volume is obtained as the difference between added volume and volume required to fill space under equilibrium pressure. The isotherm adsorption is obtained through variations on the pressure ratio (P/P_0) in the range from 10^{-5} to 0.99. With this experimental data is possible to compute the sample surface area. Metal surface was estimated by hydrogen chemisorption using a Micromeritics ASAP 2010 instrument.

5. *Characterization of porous morphology*

It was performed using IFME^(R), software developed at URV (Torras, 2005). IFME^(R) realizes a quantitative analysis through examination of porous symmetry and density starting from microscopy images. Systematic image analysis is based on difference in colors along the image caused by the porous distribution. Analysis is reported in terms of pore parameters (such as number, density, and distribution), and the degree of image symmetry along horizontal and vertical directions.

6. *Coating adherence*

Catalytic plate adherence was evaluated by a vibration test. It consist in attach the coated plates to a plane surface where are produced vibrations using a stationary and continuous shaker (TIRAvib). This system control produces controlled vibrations in a similar way than loudspeakers, by the interaction of electric current passing through the plunger coil and a magnetic field. The vibration level can be controlled by variations on electric current intensity (TIRA, 2007).

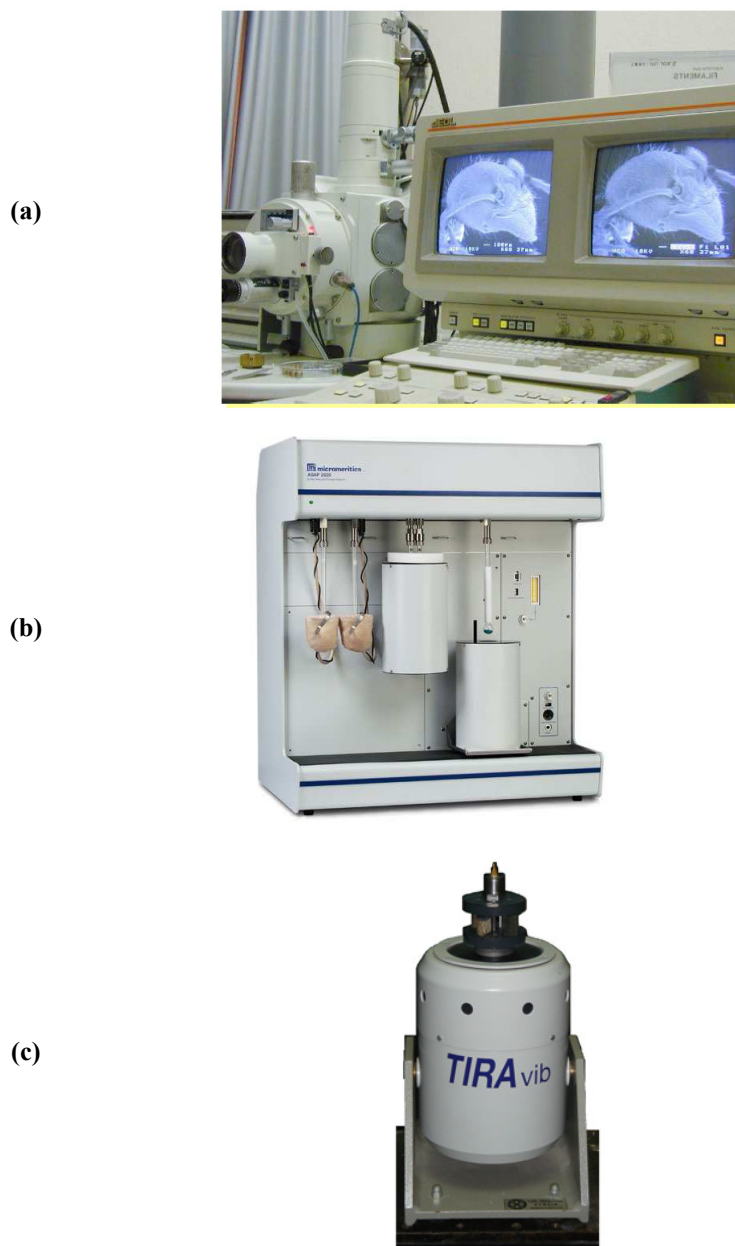


Figure 3-9 Images for some characterization equipments: (a) Scanning Electron Microscope (Torné, 2006), (b) BET instrument (Torné, 2006) (c) Shaker for vibrational tests

3-4-2 Fluids Analysis

Fluid composition at reactor inlet and outlet was analyzed for PBR and CWR configurations using standard analytical techniques, such as:

1 Chromatography:

It is a physical method for separating mixtures components between stationary and mobile phases (IUPAC, 2007). Mobile phase could be gas (GC) or liquid, which requires high pressures and is often described by the term High Performance (or Pressure) Liquid Chromatography (HPLC). The separation is commonly held in columns which contain the active solid phase called packing material.

- **GC instrument** (Hewlett-Packard 5890) was employed for PBR and CWR; using a pneumatic valve (Valco A-4C10UWT) for the injection system. The separation column was Carboxen-1000 (Supelco, S.A., 1.5m; 1/8" OD; 60/80 mesh); employed for separating gases (such as H₂, O₂, N₂, CO, and CO₂) and light hydrocarbons (like CH₄, C₂s). Time of analysis is a function of the mixture components; if the mixture contains two carbons molecules (C₂s) the analysis time reaches 20 min, but if are present CH₄, CO₂, and CO, it arrive at 10 min only. Data acquisition, chromatogram integration, and GC control was performed through specialized software (HP G2078AA). Working conditions are shown on Table 3-3.
- **HPLC instrument** (Agilent 1100 Series) was employed for the PBR, using a column Aminex HPX87H and the solvent phase was sulfuric acid solution 0.005 M. Principal components analyzed by HPLC were acetaldehyde, ethanol, acetic acid and acetone. Flow rate was 0.5 ml min⁻¹. Before measurements all the samples (2 ml) were filtered through a 0.22 μm filter. An ultraviolet diode-array detector and a Refractive Index (RI) detector were connected in series; but only the RI detector was used for detecting ethanol, acetic acid and acetone. Data acquisition, chromatogram integration, and HPLC control was performed through specialized software (ChemStation). Working conditions are shown on Table 3-3.

2 Mass Spectrometry:

It is an analytical technique that measures the ion mass to charge ratio (m/z), commonly used to identify unknown compounds, to reveal the structure of organic molecules, and to find the composition of a mixture. A Mass Spectrometer (MS) is composed by three parts: ion source for producing ions from sample, mass analyzer for separating the types of ions produced by the ionization process, and detector for recognizing the number of ions produced for each mass.

MS instrument (Peiffer, QMS200) with quadrupole as mass analyzer was connected to the CWR. The electron energy was fixed at 90eV. The equipment was calibrated before initiate each reaction test by measuring several fluid mixtures composed by standard gases CO, CH₄, CO₂ and Ar (Air Liquide); which were fixed at different mass flow levels with the help of their respective mass flow controller (Bronkhorst, E-Flow). Data acquisition, mass spectra evaluation, and MS control was performed through specialized software (Quadstar 32-bit). Working conditions are shown on Table 3-3.

Table 3-3 Features and operation conditions for fluid analysis equipments Gas Chromatography, High Pressure Liquid Chromatography, and Mass Spectrometry

Feature	GC	HPLC	MS
Carrier	He	Sulfuric acid solution (0.005 M)	Ar
Analysis time	10-20 min	35 min	μs
Components detected	H ₂ , N ₂ , CO, CH ₄ , CO ₂ , C ₂ H ₄ , C ₂ H ₆	C ₂ H ₅ OH, C ₂ H ₄ O, CH ₃ COCH ₃	H ₂ , Ar, CO, CH ₄ , CO ₂ , C ₂ H ₅ OH, C ₂ H ₄ O, CH ₃ COCH ₃
Detector	Thermal Conductive Detector (TCD)	Refractive Index (RI)	Secondary Electron Multiplier (SEM)
Working conditions	40 °C/min from 60 °C to 220 °C	Flow rate: 0.5 ml/min	Electron energy 90eV
Time required to stabilize the instrument from shut down	1 h	2 h	4 h
Reactor Configuration	PBR & CWR	PBR	CWR

Inside a MS instrument, Gas molecules are split into ions once electrons beam impacts on the sample. Each ion originates its own peak along the mass to charge ratio spectrum. Signal intensity is a function of the amount of fragments received at the detector as result of one compound or to the sum of multiple contributors (Pfeiffer, 2006). For instance, CO gives one peak at mass to charge ratio (m/z) value of 28; while CO_2 presents peaks at 28, 44, 16, and 12. Figure 3-10 presents mass spectrum in terms of the relative abundance for principal mixture components.

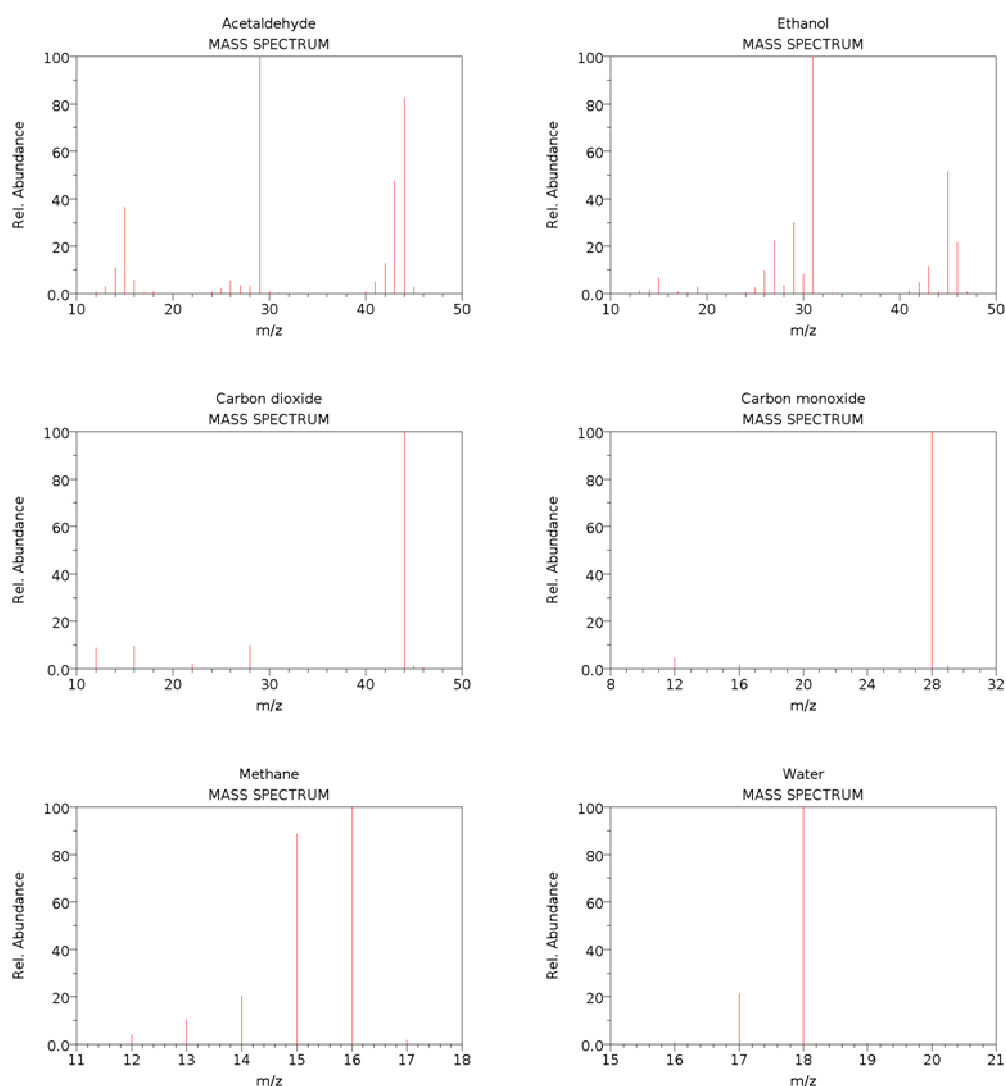


Figure 3-10 Mass spectrum for some components measured using the MS from reference (NIST, 2007)

Partial pressures can be obtained by solving first for compounds with main sensitivity to peaks at unique positions, and then for the rest of components. Ethanol, water, and argon

present main signal at mass to charge ratio (m/z) of 31, 18 and 40 respectively. In this case, the partial pressure could be obtained by equation (3-1):

$$p_j = \frac{I_n}{S_{j,n}} \quad (3-1)$$

where I_n [A] is the ion current measured at n peak; $S_{j,n}$ [A mbar⁻¹] is the corresponding sensitivity for the j component at the respective peak, and p_j is the partial pressure [mbar]. After obtain ethanol partial pressure, it is computed the C₂H₄O, CO₂, and CO fractions (from 28, 29, and 44 signals respectively) as a sum of contributions. Linear set of equations can be expressed as,

$$\left(\sum_k p_k * S_k \right)_n = I_n \quad (3-2)$$

in a similar way, H₂ and CH₄ can be obtained from peaks at 2 and 16. Results from MS could be compared with GC measurements for CO₂, which usually is present at higher proportion than other by-products.

3-4-3 Calibration Methods

GC equipment was calibrated periodically using a unique standard gas mixture. Calibration procedure is based on inject diverse quantities, in order to increase sequentially the sample pressure. An augment in pressure produces an increase on the number of gas molecules present in the GC column; which later is reflected on a proportional increment on the measured area. Gas mixture was composed by: H₂ (52%), N₂ (20%), CO (12%), CO₂ (12%), CH₄ (1%), C₂H₂ (1%), C₂H₄ (1%), and C₂H₆ (1%). A manometer with a 0.02 bar precision was used to measure variations on the pressure loop. GC calibration procedure consists in inject five different samples with relative pressures between 0.20 and 1.00 bar. Each measure was repeated three times to evaluate standard deviation on calibration factors. All gases, except hydrogen, showed a linear regression $y=mx$. Hydrogen usually requires a second order polynomial. Table 3-4 shows calibration factors for both GC and HPLC.

HPLC equipment was calibrated before measure each catalytic test, using liquid solutions containing known quantities of ethanol, water, and acetaldehyde. It was prepared five liquid mixtures covering a concentration range similar to those expected in the catalytic experiments. An augment in the sample concentration produces an increase on the number of each molecule in the system; proportional to the peak area registered in the chromatogram.

Table 3-4 Sensitivity factors for Gas Chromatography and High Pressure Liquid Chromatography.

Component	HPLC factor [mol L ⁻¹]	GC factor [bar _i bar ⁻¹]
C ₂ H ₅ OH	3.20 10 ⁻⁷	-
C ₂ H ₄ O	2.52 10 ⁻⁷	-
CH ₃ COOH	6.40 10 ⁻⁸	-
H ₂	-	7.12 10 ⁻⁶
N ₂	-	4.00 10 ⁻⁷
CO	-	3.77 10 ⁻⁷
CH ₄	-	4.29 10 ⁻⁷
CO ₂	-	3.37 10 ⁻⁷
C ₂ H ₄	-	2.96 10 ⁻⁷
C ₂ H ₆	-	2.73 10 ⁻⁷

Table 3-5 shows MS sensitivity factors, including cross contributions by multiple ion generation. Quantitative analysis with the MS was periodically checked with standard gases by a routine calibration procedure to take into account possible modifications in the sensitivity factors along operating time. MS instrument was calibrated by registering signals of the four key gases: H₂, CO, CO₂, and CH₄. Also, CWR unit allowed to calibrate carrier gas (Ar) and reactants (H₂O and C₂H₅OH) during each catalytic test.

Table 3-5 Complete lists of Mass Spectrometer sensitivity factors. Contributions of minority compounds which factors are in the order of 10⁶ can be assumed negligible.

m/z	Sensitivity Factor [A mbar ⁻¹]							
	2	15	18	28	29	31	40	44
H ₂	1.82 10 ⁴							
CH ₄	2.72 10 ⁶	8.79 10 ⁵		7.92 10 ⁶				
H ₂ O	1.60 10 ⁶		8.89 10 ⁵					
Ar							1.83 10 ⁴	
C ₂ H ₅ OH	4.47 10 ⁶	8.44 10 ⁶		6.96 10 ⁶	1.64 10 ⁵	6.23 10 ⁵		1.78 10 ⁶
C ₂ H ₄ O	3.06 10 ⁶	3.43 10 ⁵		5.31 10 ⁶	6.36 10 ⁵	2.27 10 ⁷		2.97 10 ⁵
CO ₂				1.43 10 ⁵				1.18 10 ⁴
CO				1.62 10 ⁴				

3-5 Results Management

Experimental results were expressed in terms of ethanol conversion, (X), selectivity towards the different products (S_j), and their yields (Y_{ij}). Results were calculated according to equations (3-3) to (3-5) where F_j (mol min^{-1}) is the flow of species j at the reactor exit and F_{EtOH0} the flow rate of ethanol feed to the reactor,

$$X = \frac{F_{EtOH0} - F_{EtOH}}{F_{EtOH0}} \quad (3-3)$$

$$S_j = \frac{F_j}{\sum_{\text{products}} F_j} \quad (3-4)$$

$$Y_{ij} = \frac{F_j}{F_{EtOH0} - F_{EtOH}} \quad (3-5)$$

Other two important quantities were Steam to Carbon ratio (SC) and contact time (W Fa_0^{-1}) expressed respectively by equations (3-6) and (3-7)

$$SC = \frac{F_{H2O}}{2 * F_{EtOH0}} \quad (3-6)$$

$$\frac{W}{Fa_0} = \frac{m_{cat}}{F_{EtOH0}} \quad (3-7)$$

Four mass balances were computed as function of each element: carbon (C), hydrogen (H), oxygen (O), and inert (N in PBR and Ar in CWR). Inert elements allowed detecting possible leaks in the system. On the other hand, in the case of the catalyst screening experiments was applied an analysis of variance to detect significant influence of variables on experimental results, in the studied range.

3-6 Simulation Techniques

3-6-1 Software Packages

Numerical simulations were performed to provide complementary information connected with experiments; in order to promote deeper analysis. Specialized software packages were used for realizing this task

- **Thermodynamic:** Aspen PlusTM is a modeling tool for simulating steady state chemical process. It contains extends database with physical properties and models, coupled with process flowsheet that facilitates the solution of resulting equations set obtained from chemical process modeling. Two distinct types of analysis were performed using Aspen PlusTM: final products composition under thermodynamic equilibrium conditions for SR reactions and process efficiency with different fuel processor configurations.
- **Reactor Modeling:** it is required to solve models governed by transport phenomena, which commonly lead to complex set of differential equations. Two examples are: initial value problems illustrated in equation (3-8); and space dimension problems with boundary conditions such as equation (3-9).

$$u \frac{dc}{dx} = -kc ; c(x=0) = c_o \quad (3-8)$$

$$k \frac{d^2T}{dx^2} = 0 ; \quad (3-9)$$

$$T(x=0) = T_o ; T(x=L) = T_L$$

MATLAB^(R) is a computing language and interactive environment for developing algorithms, numerical simulation, data visualization and data analysis; which was employed for solving 1D initial value problems for CWR modeling. FEMLAB^(R) is a modeling environment to simulate physical models described by partial differential equations using the finite element method. This software was employed for studying 2D models which represent the CWR configuration developed for the experimental catalytic plate tests.

3-6-2 Conservation Equations and Dimensionless Numbers

Conservation equations constitute a common approach in physics to account for a measurable property of an isolated system. In this case, fluid dynamics studies a fluid in motion that borders a stationary wall; where the fluid velocity generates gradients that exert viscous stresses over the surface. The velocity is one of the most important variables in fluid dynamics, evaluated through the equation of motion; which can be simplified by neglecting pressure and gravitational forces and expressed as the continuity equation (3-10a). In addition, when chemical reactions take place, it is necessary to perform the mass transfer equation for each component j , as follows on equation (3-10b); or in dimensionless form eq (3-10c). Finally, heat transfer is evaluated through equation (3-10d) or in dimensionless form equation (3-10e).

$$\frac{\partial \rho}{\partial t} + \nabla \cdot \rho u = 0 \quad \text{Continuity} \quad (3-10a)$$

$$C_0 \left(\frac{\partial y_j}{\partial t} + u \cdot \nabla y_j \right) = C_0 (D_j \nabla^2 y_j) + \sum_i v_{ij} r_j \quad \text{Mass transfer} \quad (3-10b)$$

$$\text{Re} \cdot \text{Sc} \left(\frac{\partial y_j}{\partial t^*} + u^* \cdot \nabla^* y_j \right) = \nabla^{*2} y_j + \sum_i v_{ij} Da_{ij} r_j^* \quad \text{Dimensionless Mass} \quad (3-10c)$$

transfer

$$\rho c_p \left(\frac{\partial T}{\partial t} + u \cdot \nabla T \right) = k_j \nabla^2 T + \sum_i v_{ij} r_j \Delta H_i \quad \text{Energy transfer} \quad (3-10d)$$

$$\left(\frac{\partial T^*}{\partial t^*} + u^* \cdot \nabla^* T^* \right) = \frac{1}{Pe} \nabla^{*2} T^* + \sum_i v_{ij} r_j^* \left(\frac{\Delta H_i}{\rho c_p u_0} \right) \quad \text{Dimensionless Heat} \quad (3-10e)$$

transfer

The principal variables on the set of equations (3-10) are velocity (u), temperature (T), and mass fraction (y_j). Also, there are presents parameters related with the phenomena, like the mass and thermal diffusion coefficients (D_j and k_j), and the reaction rate (r_j); as well as diverse physical parameters, such as density (ρ), heat capacity (c_p), reaction enthalphy (ΔH). Finally, there are parameters describing the operational conditions or system configuration, like initial concentration (C_0) and initial velocity (u_0). The analysis of set of eq (3-10) it is

simplified by grouping several parameters into dimensionless factors, such as Re, Sc, and Pr; these numbers are helpful as an order of magnitude estimate for comparing mechanisms. Table 3-6 presents a list of common dimensionless numbers in transport phenomena coupled with chemical reaction.

Table 3-6 Dimensional groups in transport process with chemical reaction

Expression	Group	Remarks	#
$Re = \frac{\rho \cdot u \cdot L}{\mu}$	Reynolds	Fluid dynamics: Inertial / Viscous Rate	(3-11a)
$Pr = \frac{\mu \cdot c_p}{k}$	Prandtl	Fluid dynamics: Viscous / Thermal Diffusion	(3-11b)
$Sc = \frac{\nu}{D}$	Schmidt	Fluid dynamics: Viscous / Mass Diffusion	(3-11c)
$Sh = \frac{k \cdot L}{D}$	Sherwood	Mass transfer: Convection / Mass Diffusion	(3-11d)
$Pe = \frac{\rho \cdot c_p \cdot u \cdot L}{k} = Re \cdot Pr$	Péclet	Heat transfer: Convection / Diffusion	(3-11e)
$Nu = \frac{h \cdot L}{k}$	Nusselt	Heat transfer: Convection / Conduction	(3-11f)
$Da_{ij} = \frac{k_i(T) \cdot C_{j0}^{n-1} \cdot L^2}{D_j}$	Damkholer	Chemical Reaction: Reaction rate / Mass Diffusion	(3-11g)

Finally, the set of equations (3-12) present equations employed for average profiles of the three main variables when dealing with 2D analysis,

$$u_{ave} = \left(\int_0^{\delta} u \cdot \rho \, dx \right)_{x=L} / \left(\int_0^{\delta} \rho \, dx \right)_{x=0} \quad \begin{array}{l} \text{Average} \\ \text{velocity} \end{array} \quad (3-12a)$$

$$C_{j,ave} = \left(\int_0^{\delta} u \cdot C_j \, dx \right)_{x=L} / \left(\int_0^{\delta} u \, dx \right)_{x=0} \quad \begin{array}{l} \text{Average} \\ \text{concentration} \end{array} \quad (3-12b)$$

$$T_{ave} = \left(\int_0^{\delta} \rho \cdot c_{p,j} \cdot u \cdot T \, dx \right)_{x=L} / \left(\int_0^{\delta} \rho \cdot c_{p,j} \cdot u \, dx \right)_{x=0} \quad \begin{array}{l} \text{"Cup of} \\ \text{coffee"} \\ \text{(average)} \\ \text{temperature} \end{array} \quad (3-12c)$$

References

1. Agilent HPLC 1100 Series, User Manual, USA, 1990.
2. Aspen Plus User Guide, vol. 1, Cambridge, USA: Aspen Technology, 2004.
3. Fatsikostas, A. N., D. I. Kondarides, et al. (2002). "Production of hydrogen for fuel cells by reformation of biomass-derived ethanol." *Catalysis Today* 75(1-4): 145-155
4. FEMLAB 3.0 User's Guide, Stockholm, Sweden: Comsol, 2004.
5. Hewlett Packard GC HP 5890 Series II, User Manual, USA, 1991.
6. IUPAC (2007). Compendium of Chemical Terminology of the International Union of Pure and Applied Chemistry. Found on the web, 28 September 2007 at: <http://goldbook.iupac.org/C01075.html>
7. Marquevich, M. (2001). "Producción de hidrógeno a partir de biomasa: steam reforming de aceites vegetales". Departament d'Enginyeria Química. Tarragona, Universitat Rovira i Virgili.
8. MATLAB 3.0 Notebook User's Guide, Massachusetts, USA: The Mathworks, Inc., 1998.

9. Mielle, V., S. Pallier, et al. (2005). "Deposition of $\gamma\text{Al}_2\text{O}_3$ layers on structured supports for the design of new catalytic reactors". Applied Catalysis A 286: 232-238
10. NIST (2007). Chemistry Web book of the National Institute of Standards and Technology. Found on the web, 22 October 2007 at: <http://www.nist.gov/>
11. Niemantsverdriet, J.W., (1995) Spectrometry in catalysis: an introduction. Chichester, Wiley.
12. Pfeiffer Vacuum "Mass Spectrometer Catalog", Germany, 2006.
13. Pfeiffer Vacuum "Partial Pressure Measurement in Vacuum Technology", Germany, 2005.
14. TIRA, Vibration Test Systems (2007). Found on the web, 18 October 2007 at: <http://www.tira-gmbh.de/>
15. Torne, V. (2006) "Preparacion, caracterizacion y aplicaciones de carbones activados preparados a partir de lignina Kraft". Departament d'Enginyeria Química. Tarragona, Universitat Rovira i Virgili.
16. Torras, C. (2005) "Obtenció de membranes poliméricas selectives". Departament d'Enginyeria Química. Tarragona, Universitat Rovira i Virgili.

Chapter 4

Thermodynamic Analysis

In a complex system, such as fuel processors, thermodynamic analysis gives valuable information that, combined with experimental results, make possible a greater control on the process operation. This chapter presents main results related to numerical simulation using two types of thermodynamic modeling: composition limitations by equilibrium and process efficiency related with heat requirements for sustaining the chemical reactions.

Engineering analysis on fuel processors has shown that multifunctional reactor concepts based on structured Catalytic Wall Reactors (CWR) with integrated heat recovery, provide optimal designs and high thermal efficiencies (Morillo et al., 2004; Kolios et al., 2005). Thermodynamic helps to predict process efficiency for different configurations by performing mass and energy balances, coupled with thermodynamic models. Once is evaluated the maximum theoretical efficiency; the information obtained could be used as a reference framework to evaluate progress from experimental and design strategies in next development stages.

The next sections will describe three possible steps for the process analysis; each of them provides specific information useful for optimizing the process design:

- (i) Prediction of the product composition at the reformer by thermodynamic equilibrium
- (ii) Estimation of the process thermal efficiency based on: products composition by reaction stoichiometry (without other process constrains) and products composition by chemical equilibrium (considering process limitations, such as chemical reaction equilibrium, and mass/heat transport resistances)
- (iii) Evaluation of differences between experimental and theoretical results.

4-1 Reaction Equilibrium Analysis

It is convenient to analyze the thermodynamic limitations in the reformer before consider the complexity caused by interactions with others components at the fuel processor. Thermodynamic equilibrium at the reformer reactor has been studied by several authors (Ioannides 2001; Vasudeva et al. 1996); commonly the employed approach is based on the minimization of the system free Gibbs energy; which is already available in commercial simulators packages as Aspen PlusTM (Aspen Plus User Guide, 2004). Figure 3-1 shows the dry gas composition for SRE products at 1, 5, and 10 atm; and SC ratios of 2, 3, and 4 mol mol⁻¹; in the temperature range from 300 to 900°C. According to the reformer equilibrium, the maximum H₂ composition in the range studied should be around 0.70; corresponding to temperatures higher than 600°C for all cases. In general, results on figure 4-1 indicate two significant trends that may be illustrated looking at fixed conditions of 5 atm, and SC=3 mol mol⁻¹:

- From 300 to 600°C H₂ and CH₄ experiments the most significant changes observed on selected set of operational conditions. In this range, a temperature increment cause a growth of the H₂ composition from 0.10 to around 0.60; while the CH₄ composition will decrease from 0.70 to 0.10, approximately. At the same time, CO and CO₂ composition vary slightly. CO composition experiment an augment from less than 0.01 at 300°C until 0.05 at 600°C, whereas the CO₂ composition is slightly reduced from 0.25 to 0.20 under the same range of temperature. As a result, operate at intermediate temperature -300 to 600 °C- do not favor CO production.
- From 700 to 900 °C there is an exchange of roles; H₂ and CH₄ compositions get minor changes, and tend to be stabilized. H₂ composition is close to it higher value -0.70- while CH₄ composition is less than 0.05. On the other hand, CO and CO₂ experiment significant changes, CO₂ decrease from 0.20 to 0.10 approximately; at the same time CO vary from 0.10 to 0.20. In consequence, this range ensures highest values for both H₂ and CO.

Changes in pressure and SC do not seem to produce extraordinary variations on tendencies described previously. It is important to note that an increase on SC produce a small shift of composition trends with respect to temperature. For the range under study, the best conditions for H₂ production are P=1 atm and SC=4 mol mol⁻¹ respectively, because allow to work at lower temperatures than the other cases.

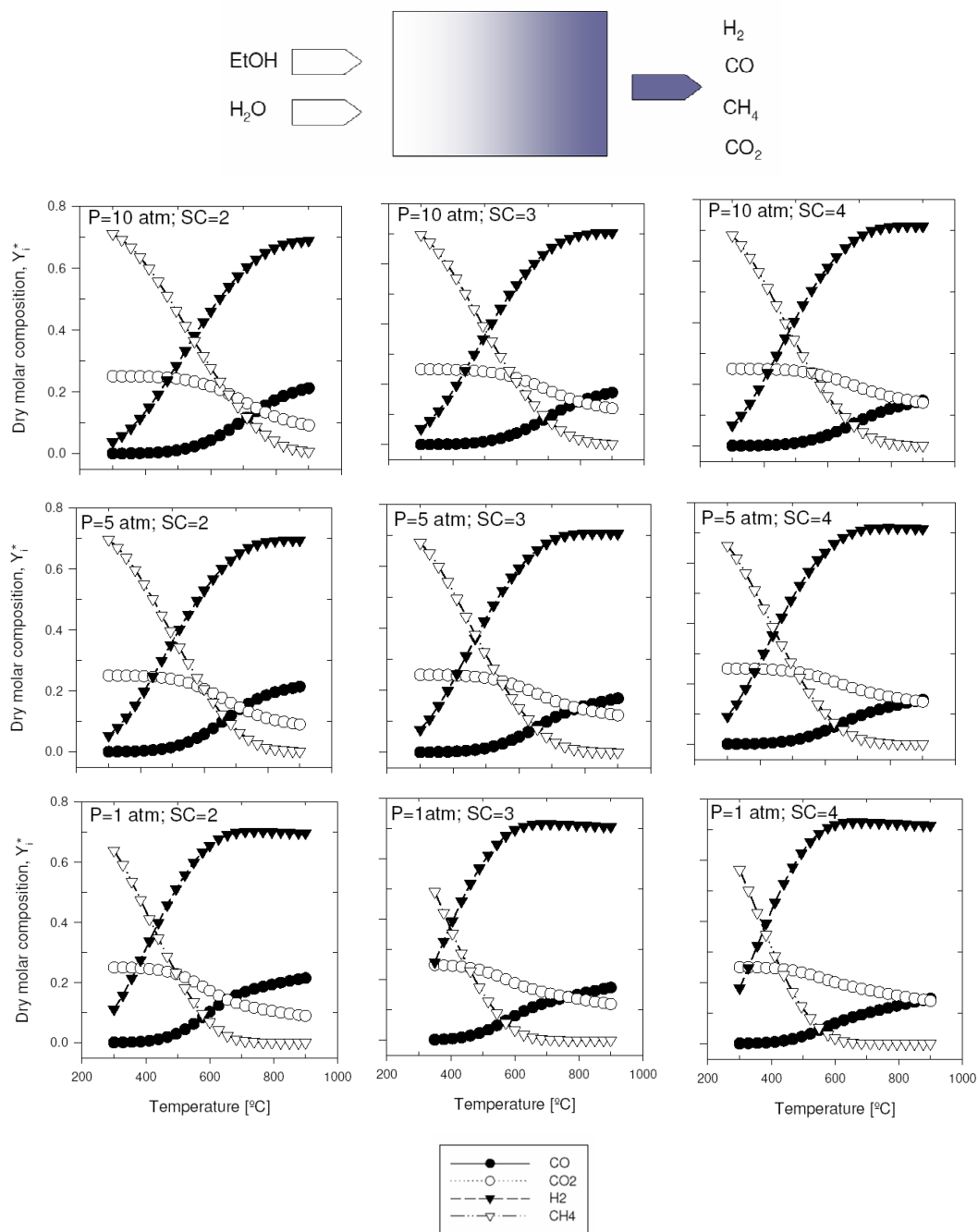


Figure 4-1. Results for reactor equilibrium composition for final products and yield of hydrogen for SRE at 1, 5, and 10 atm; and SC ratios of 2, 3, and 4 mol/mol; in the temperature interval from 300 to 900°C.

Figure 4-2 shows the dry gas composition for products of the SRM at 1, 5, and 10 atm; and SC ratios of 1, 2, and 4 mol mol⁻¹, in the temperature range from 300 to 900°C. H₂ and CH₄ compositions follow a similar trend of that observed for SRE reaction, first a temperature range where there is a strong variation; then after reach a critical temperature, values are stabilized. For instance, at 5atm and SC=2 H₂ composition grow from 0.10 at 300°C until 0.60 at 600°C; while in the range from 700 to 900°C H₂ composition becomes stable around 0.80. In relation to CH₄ composition change from 0.90 to around 0.25 as reaction temperature progress from 300 to 600 °C; and approach to complete methane conversion at 900°C. CO also follows a similar trend of that observed for SRE reaction; in the first range presents a slight increment –from 0 to around 0.10- while at higher temperatures CO composition reach a maximum value of 0.20. On the other hand, CO₂ shows a tendency typical of an intermediate compound, at low temperature the composition value is near to 0, then progress until around 0.10 at 600°C, and finally decrease at 900°C to 0.05 approximately. Again, as occurs with the SRE, changes in pressure does not modify significantly the results for SRM, but an increase on SC produce a shift of composition trends with respect to temperature. For the range under study, the best conditions for H₂ production are P=1 atm and SC=4 mol mol⁻¹ respectively, because allows to work at lower temperatures than the other cases.

Figure 4-3 shows the dry gas composition for products of the WGS at 1, 5, and 10 atm; and SC ratios of 1, 2, and 4 mol mol⁻¹, in the temperature interval from 300 to 900°C. In general, at lower temperatures WGS favors the CO conversion through CH₄ and CO₂ production; while at higher temperatures both CH₄ reforming and H₂ production reaches it maximum level. Again, changes in SC are more important than variations in pressure.

In conclusion, figures 4-1, 4-2 and 4-3 suggest that H₂, CO, CO₂ and CH₄ participate in reactions SRE, SRM and WGS. Equilibrium predicts that this dynamics could be modified in some extend, depending on SC and temperature values. It is important to note that CH₄ is a competitor for H₂ and might be of interest a shift of the equilibrium conditions to operate at the maximum H₂ yield region.

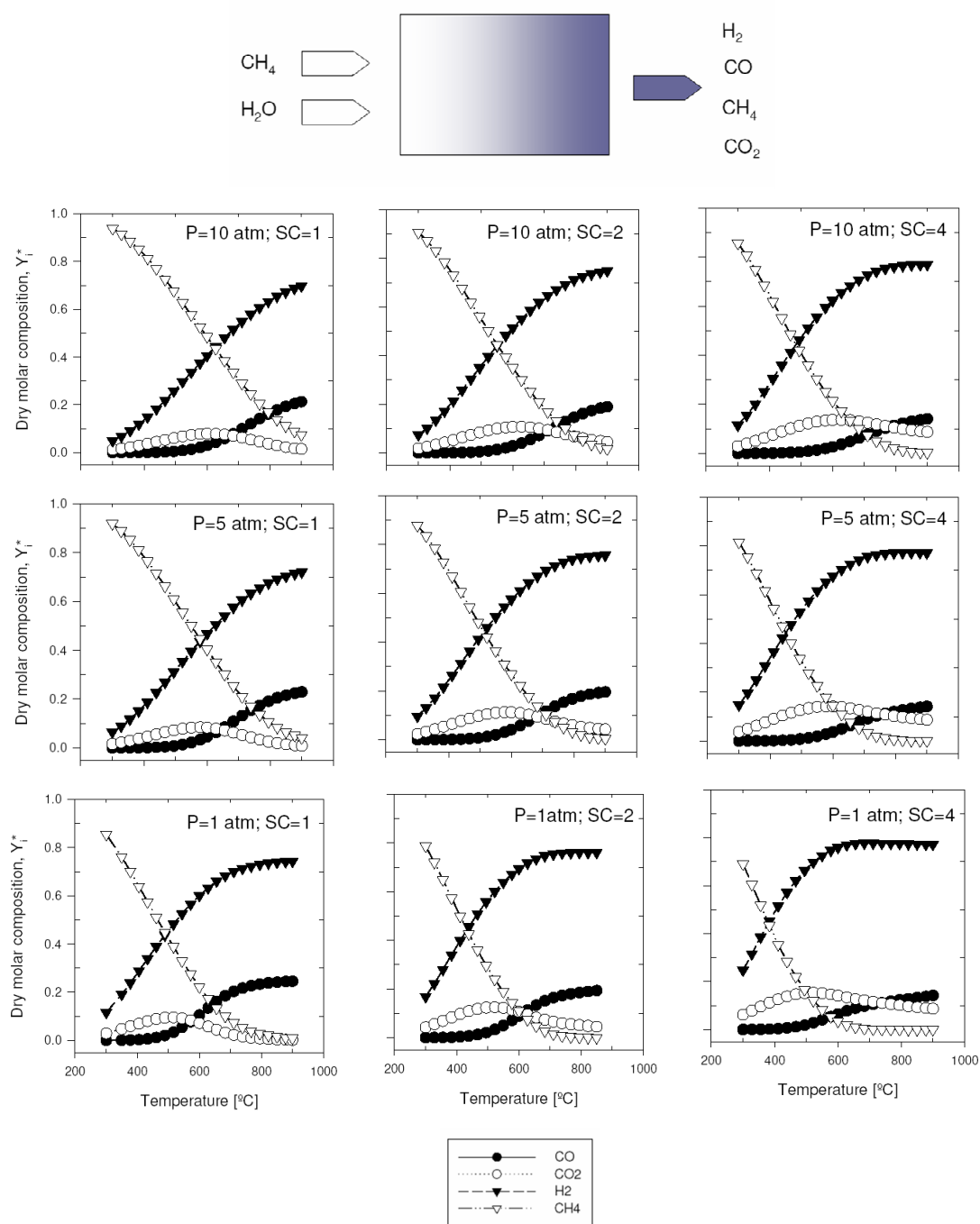


Figure 4-2. Results for reactor equilibrium composition for final products and yield of hydrogen for SRM at 1, 5, and 10 atm; and SC ratios of 2, 3, and 4 mol/mol; in the temperature interval from 300 to 900°C.

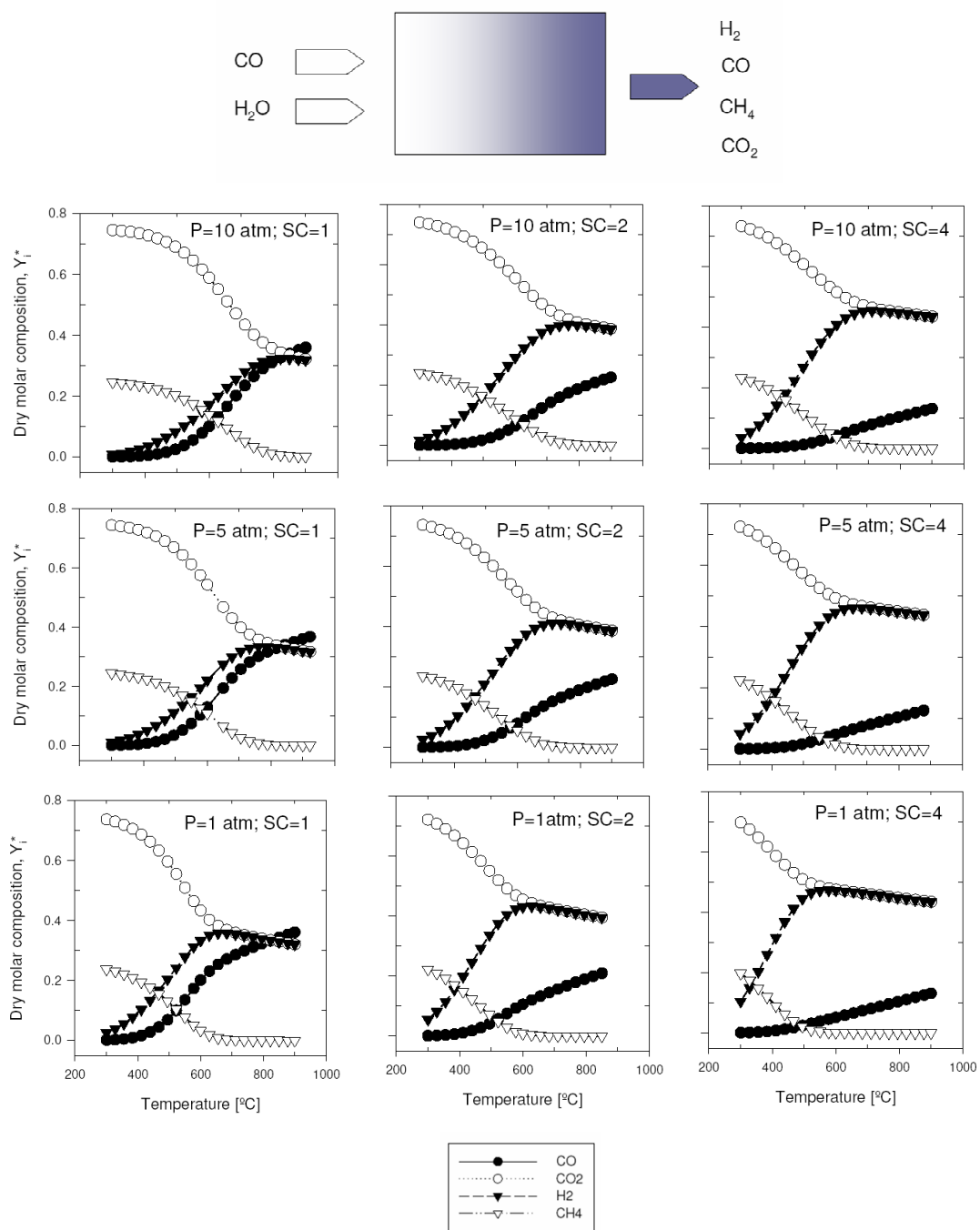


Figure 4-3. Results for reactor equilibrium composition for final products and yield of hydrogen for WGS at 1, 5, and 10 atm; and SC ratios of 2, 3, and 4 mol/mol; in the temperature interval from 300 to 900°C.

4-2 Process Thermodynamic Analysis

The performance of an auto-thermal fuel processor will be illustrated through thermodynamic analysis of two kind of process diagram showed on figures 3-4 and 3-6 respectively. On the first case, based on figure 3-4, the efficiency is evaluated using the simplest model: a black box diagram which employs the overall reaction stoichiometry (2-15) to describe the chemistry and simplify as much as possible the thermodynamic and other complexities due to mass and heat transport.

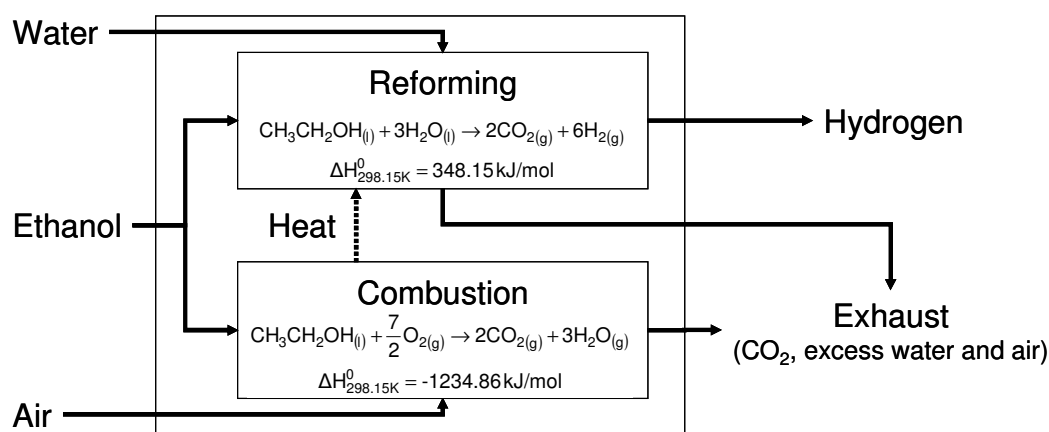


Figure 4-4. Black box diagram considering Steam Reforming of Ethanol reaction stoichiometry to evaluate the final product composition at the fuel processor.

Next, the second case consists on a fuel processor coupled with a separation device for H_2 purification, evaluated under a typical set of operational conditions. This case incorporated some limitations, for instance: reaction product composition restricted by thermodynamic equilibrium, heat recovery limited by temperature gradient, and hydrogen recuperation constrained by membrane separation efficiency.

4-2-1 Black Box Model

Usually, the fuel processor efficiency is evaluated by equation (4-1) (Lutz, 2003); which represents the ratio of chemical energy as hydrogen produced by the fuel processor divided by that contained in the ethanol feed to the system. On the other hand, chemical energies are calculated using the lower heating values (LHV) for ethanol and hydrogen. Then, the fuel processor efficiency expression is,

$$\eta_{LHV} = \frac{F_{H_2} \cdot LHV_{H_2}}{F_{EtOH_0} \cdot LHV_{EtOH}} \quad (4-1)$$

It was performed a screening of the operational conditions with the black box model (using the reaction stoichiometry) to evaluate possible effects on efficiency: SC from 1.5 to 6, excess air from 0 to 100%, and water in the exhaust streams at 100°C as vapor (top), and liquid (bottom). For energy balances it was considered the fuel processor as an adiabatic system; while the mass balance assume that all the inlet and outlet streams were at atmospheric pressure, both water and ethanol entered as liquids at 25°C, air entered dry at 25°C, and the hydrogen stream was at 60°C. The exhaust stream comprised all CO₂ from reforming and combustion, water and excess air, and was assumed to exit the system at 100°C, either with water as vapor or liquid. Figure 4-5 presents the efficiency and H₂ yield obtained in both cases.

Figure 4-5 shows that the maximum theoretical efficiency is around 0.92 obtained when the water at exhaust stream is condensed and stoichiometric quantities of SC and excess air are employed. If additional water is feed; the system efficiency will experience a significant reduction at higher values of SC when the excess of water is not condensed (vapor as exhaust stream). On the other hand, if it were employed a SC of 3 and 50% for excess air (common in real life operations) the efficiency will drop around 0.91 and 0.83 depending on which is the phase of the outlet streams (liquid or vapor respectively).

In conclusion, SC ratio has proven to be an important factor for the process efficiency; and depending on the proportion of water present, the complexity due to include a step for recover the latent heat in the vapor stream could be justified to increase the efficiency.

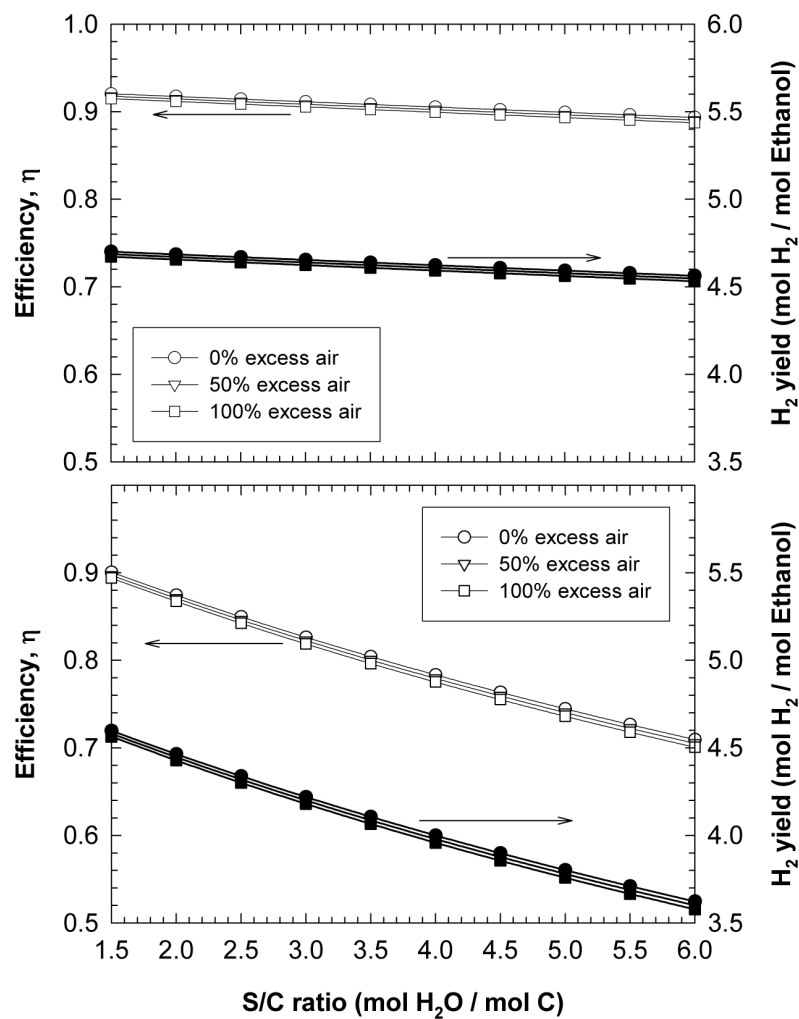


Figure 4-5. Stoichiometric analysis for the SRE: thermal efficiency (3-1), η_{LHV} , and hydrogen yield as a function of the SC ratio for the adiabatic system depicted on figure 3-4 with excess water in the exhaust streams at 100°C as liquid (top), and vapor (bottom); all inlet and outlet streams at atmospheric pressure.

4-2-2 Fuel processor integrated with H₂ membrane separation

Figure 4-6 presents a diagram of the second model, a fuel processor integrated with H₂ separation process. Operational conditions required for auto-thermal working regime are shown on figure 3-7 in terms of temperature, pressure and SC. Three cases are considerate: (i) reformer without WGS converter and with condensed excess water -top-, (ii) reformer with WGS and with condensed excess water -middle-, and (iii) reformer with WGS and without condensing excess water -bottom-. Additionally, operational variables are in the following range: SC from 1.5 to 6; reformer temperature from 400°C to 1000°C and pressure between 1.5 and 15 bar and H₂ separation factor fixed at 90%. The addition of a WGS unit helps to reduce the CO content in the outlet stream and at the same time increase the H₂ production rate beyond the thermodynamic limits.

Figure 4-7 indicates that the simplest process configuration (reformer without WGS converter) presents important restrictions for allowing auto-thermal operation. In fact, the reformer (i), at SC ratios below 3 the fuel processor hardly could be operated under the specified conditions; while for SC ratios between 3.0 and 4.5 there may exist two possible temperatures for each pressure; for instance, at 10 bar and a SC of 5, where the fuel processor could be operated auto-thermally at 744 and 980°C.

This complex behavior is a consequence of the thermodynamic equilibrium: at temperatures below 744°C and upper 980°C there is enough combustible to produce heat and maintain energy requirements; meanwhile in the middle range (from 744 to 980°C) the reactor does not produce enough fuel to cover the energy requirements with a H₂ separation factor of 90%. These two regions of abundant fuel production are related with the availability of compounds with energetic value, such as CO and CH₄. In fact, CO composition is high at temperatures around 1000°C and the same occurs with CH₄ composition, at temperatures below 750°C.

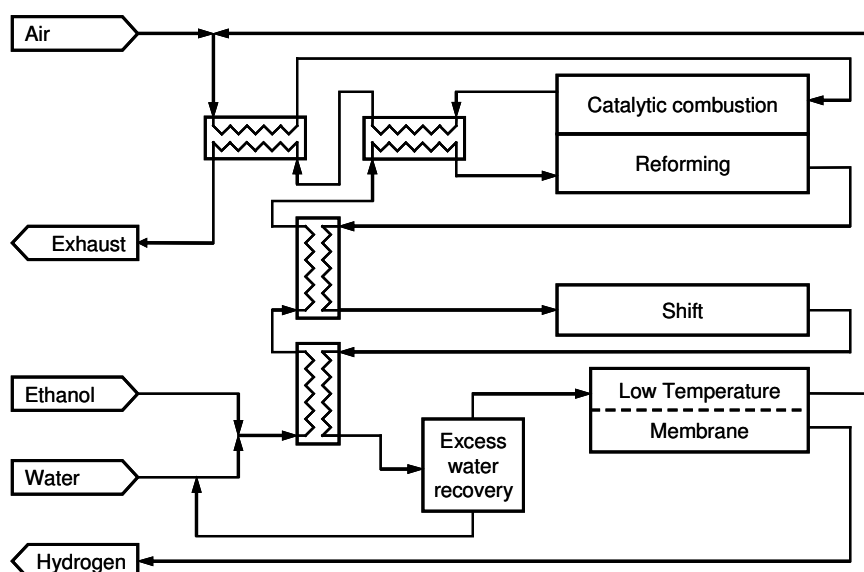


Figure 4-6. Diagram for the fuel processor integrated with a membrane separation unit for H₂ purification. Convenience for including WGS unit is analyzed by process modeling

On the other hand, results on figure 4-7 show that adding a WGS unit facilitates the fuel processor operation. So, for process configurations (ii) and (iii) -fuel processors with a WGS unit- can be operated under auto-thermal regime using any SC ratio from 1.5 to 6.0, under selected conditions of temperature and pressure. Also, the lower the SC ratio and the higher the pressure, the higher the temperature at which the reformer has to operate. This is because high pressure and low SC promote the formation of methane and there is an excess of fuel gas, a situation that has to be corrected by rising temperature to favor carbon monoxide instead, which is then consumed in the WGS reactor to produce more hydrogen. In summary, restrictions caused by final product composition can produce severe restrictions for operating under auto-thermal regime.

Also hydrogen recovery in the membrane separator has a major influence on the previous calculations. Figure 4-8 shows results for simulations of an adiabatic fuel processor with WGS and heat recovery from excess steam –condensed water–. Hydrogen recovery in the membrane separator is fixed at three levels: 80, 85 and 90%; while other operational conditions are set at SC ratio from 1.5 to 6, and pressure from 1 to 15 bar.

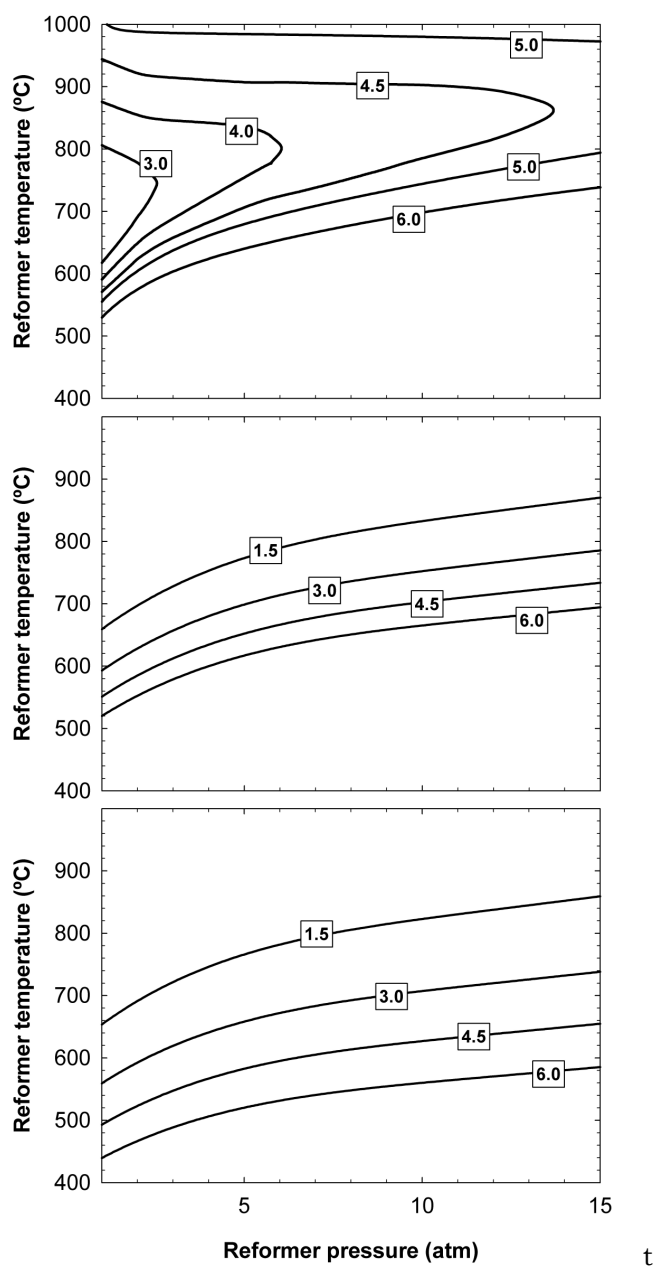


Figure 4-7. Reformer temperature required to achieve auto-thermal operation for three process configurations: (i) reformer without WGS and with condensed excess water -top-, (ii) reformer with WGS and with condensed excess water -middle-, and (iii) reformer with WGS and without condensing excess water -bottom-. Operational conditions are: SC from 1.5 to 6; temperature from 400°C to 1000°C and pressure from 1.5, to 15 bar; and H₂ separation factor fixed at 90%.

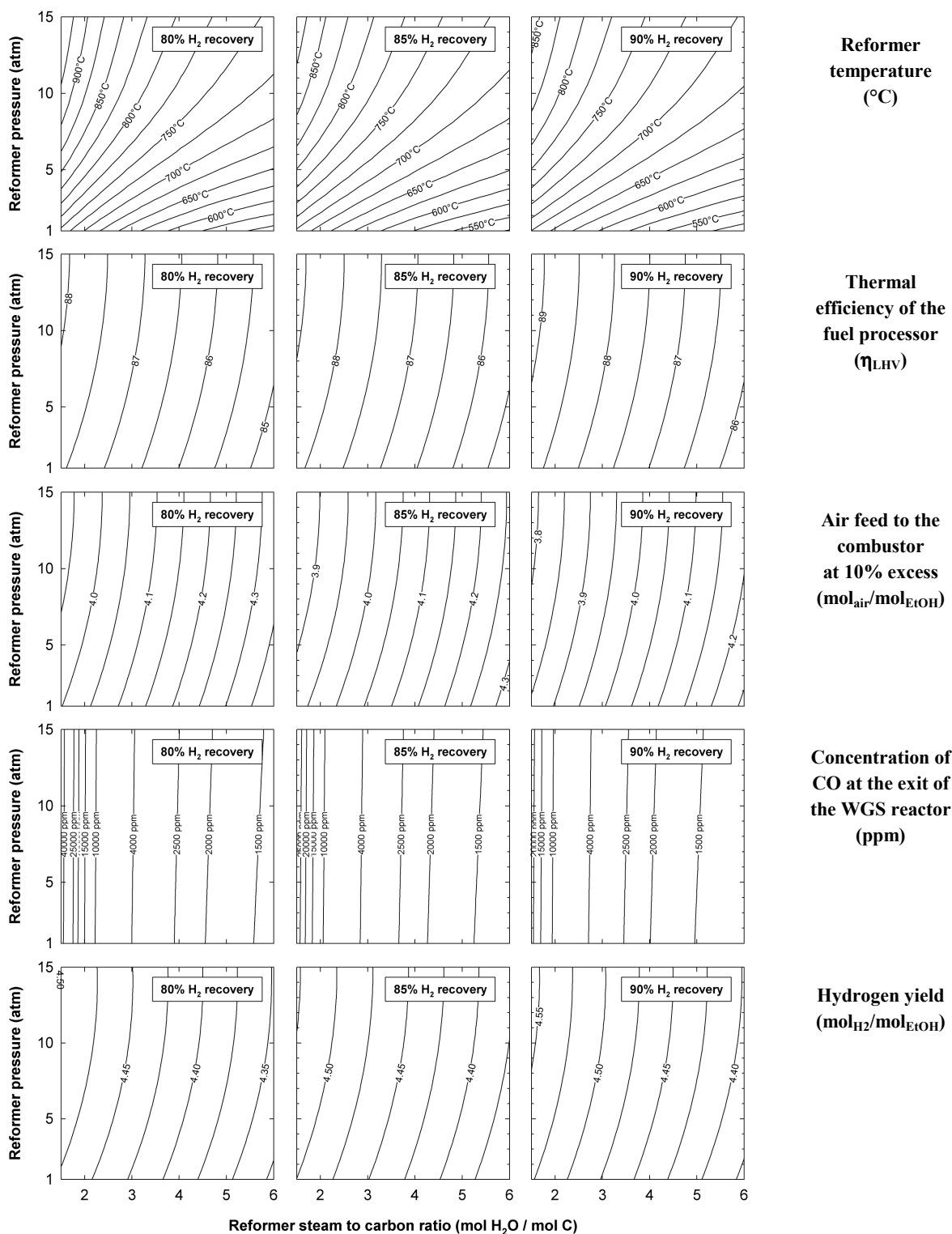


Figure 4-8. Result for a fuel processor with condensed excess water and WGS: reformer temperature required to achieve auto-thermal operation of the fuel processor, thermal efficiency of the system (η_{LHV}), air consumption at 10% air excess, CO concentration in the gas after the WGS reactor and H₂ yield, for an, at three levels of H₂ recovery in the membrane separator.

The dependent variables on figure 4-8 are: reformer temperature, thermal efficiency, yield of hydrogen, air required for the combustor at 10% excess, and concentration of CO in the product gas at the outlet of the WGS reactor. As predictable, the lower the hydrogen recovery in the membrane system the higher the reformer temperature has to be to produce less methane. For instance at a SC of 3 and a pressure of 10 bar, reformer temperature grows from 752°C at 90% recovery to 805°C at 80%.

Minor changes in thermal efficiency and hydrogen yield are observed, because it was assumed that latent heat from excess steam condensation was used to pre-heat the ethanol and water feeds. High SC ratios mean larger mass flows and a bulkier fuel processor, and also larger area requirements for the heat exchangers when latent heat has to be recovered, but SC ratios close to the stoichiometric (1.5) do not seem recommendable when the concentration of carbon monoxide in the gas, the critical parameter as far as PEMFC are concerned, is analyzed.

Figure 4-8 shows that at the stoichiometric SC ratio of 1.5 the concentration of CO after the WGS reactor decreased from 46000 ppm at a hydrogen recovery of 80% to around 22000 ppm at 90% recovery, and that it changes little with the reformer pressure. However, if the SC ratio is raised to a value of 3, then the CO concentration falls dramatically, to around 4100 ppm at 80% and 3200 ppm at 90% H₂ recovery.

The main conclusion from the previous thermodynamic analysis is that the occurrence of chemical equilibrium forces the reformer to operate at fairly high temperatures to achieve auto-thermal conditions in the fuel processor, unless large SC ratios are used and the latent heat of the excess steam is not recovered, which penalizes system efficiency and hydrogen yield. However, if SR catalysts could be designed to hinder methane formation reactions at low temperature, thus improving selectivity towards hydrogen instead of methane, the reformer could be operated at lower temperatures than those calculated from the equilibrium assumption. Additionally, efficient WGS catalysts and membranes with sufficient hydrogen fluxes and H₂/CO and H₂/CO₂ selectivity are required to develop an integrated ethanol fuel-processor.

4-3 Catalytic Tests and Thermodynamic Equilibrium

Figure 4-9 shows a comparison of the experimental and the equilibrium composition for three kinds of catalysts prepared using Ni, Co, and Rh as active phase and different metal oxides as support. Those catalysts were selected because researchers reported in the literature that it had an outstanding performance. Also is important to remark that original results include the presence of another by-products; but figure 4-9 shows only four of them: H₂, CH₄, CO and CO₂ –which are commonly the most important products, contributing to around 85% of the total-. In general, acetaldehyde is present in lower proportion than the rest of products. Composition is calculated assuming complete chemical equilibrium at this conditions of SC, temperature and pressure.

To analyze results on figure 4-9 is necessary to estimate if a point is locate near the diagonal or not. If this is the case, then it will represent an experimental point similar to the thermodynamic equilibrium. In general, Ni and Rh catalysts have their product compositions near the diagonal, and in consequence could be considered to be catalyzing the SRE to the thermodynamic equilibrium. On the other hand, Co catalyst represents a significant exception because gave a selectivity to H₂ and CH₄ markedly different to the equilibrium. The tendency shows consistently that Co produces more H₂ and less CH₄ than thermodynamic prediction. According to this, the Co catalyst may have a better ability to catalyze reactions to produce H₂ compared with the ability to produce CH₄.

The difference observed on final product composition at figure 4-9 could be explained by analyzing the reaction pathways for each catalyst. Usually, Ni and Rh based catalysts favor both decomposition and reforming reactions that appear in Table 2-4. Although, the tendency can be affected by factors such as temperature and catalyst support, there is a competition between two possible different pathways, such as ethanol dehydrogenation (2-16) and ethanol decomposition into CO, CH₄ and H₂ (2-18). Once the ethanol is converted, the rest of products react until the WGS equilibrium; however the methane reforming is not favored at this temperature range. On the other hand, a combination such as Co/ZnO catalysts favors the acetaldehyde production (2-16), but does not promote neither the ethanol decomposition (2-18) nor CH₄ formation (2-33); in consequence is possible to obtain a higher yield of H₂.

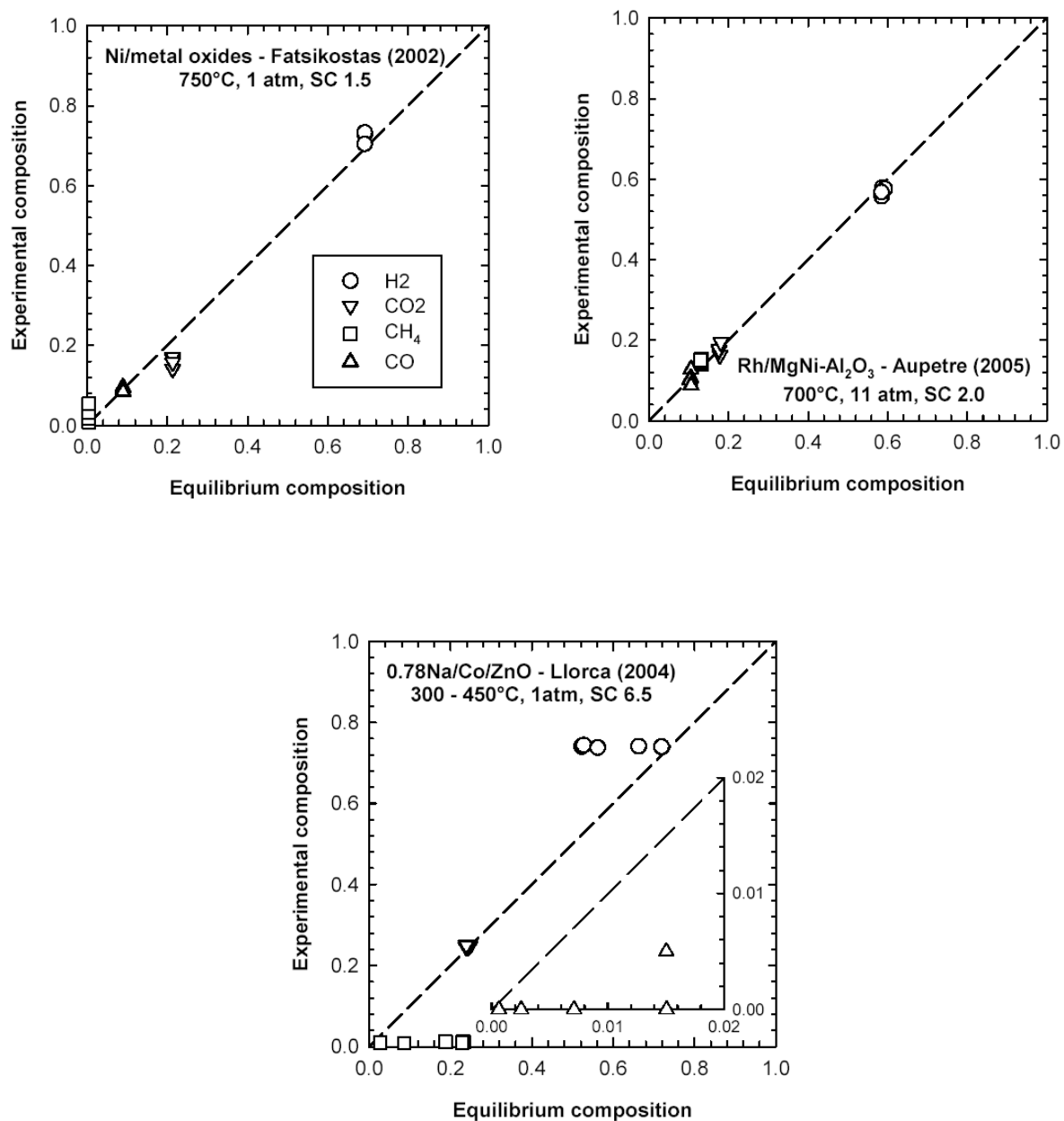


Figure 4-9 Experimental composition vs. thermodynamic equilibrium composition for three kind of catalyst reported in the literature. Ni catalyst over different metal oxides from reference (Fatsikostas, Kondarides et al. 2002), Rh catalyst over MgNi-Al₂O₃ support from reference (Aupetre, Descorme et al. 2005), and Co catalyst over ZnO support from reference (Llorca, Homs et al. 2004)

Major part of classical literature on kinetics and reactor design exposes topics on heterogeneous catalysis and thermodynamic equilibrium. Normally, the interaction between catalysis and thermodynamic is not discussed in depth; in particular, the question about how catalyst affects equilibrium in chemical reactors (Falconer, 1993). Falconer summarizes four typical statements on reactor design books:

- Thermodynamic equilibrium is unaltered by the presence of a catalyst.
- Catalysts change the rate of reaction, but not affect the equilibrium.
- Equilibrium in a reversible reaction is not changed by catalysts.
- Equilibrium conversion is not altered by catalysts.

in all these sentences there is any reference to the residence time on reactors. Actually, results on figure 4-9 indicate that (under this set of operational conditions and with this kind of reaction configuration) catalysts could be a significant element to decide if some reaction reaches thermodynamic equilibrium or not.

In other words, there are two kind of equilibrium as function of the residence time: infinite and finite. In this case, Ni based catalysts belong to the first category because catalyze all reactions. On the other hand, Co can be fit as finite equilibrium catalysts since constrains CH₄ production reactions. In consequence, Co catalyst does not change equilibrium constant; instead it does not allow the system to reach it corresponding state of minimum Gibbs free energy. As a result, the equilibrium composition might be different to the predicted by usual calculation, as shown figure 4-9.

Recently, studies on non-equilibrium thermodynamics have shown that increasing the model complexity is possible to reduce uncertainty in the evaluation of catalysts activity and selectivity (Bedeaux, et al. 2006). This requires questioning traditional assumptions, such as continuity assumption on chemical potentials without considering the surface presence. Actually, fast endothermic reactions may lead to significant gradients between a catalyst surface and the fluid media; which means that a complete description will require accounting for heat and mass fluxes over the surface.

In spite of previous considerations, the simple thermodynamic model used in the present work allowed to compare neutrally performance of different catalyst formulations on literature. Contrast between theoretical calculations and literature experiments have shown important differences between Co based catalyst and the other two formulations (Rh and Ni based catalysts). As a result, catalyst composition will influence in great extent the possible pathway on the multiple reactions dynamic. In consequence, catalyst screening constitutes a

fundamental step in the selection of proper candidates for developing catalytic plates to perform Steam Reforming of Ethanol on structured reactors.

References

1. Aspen Plus User Guide, vol. 1, Cambridge, USA: Aspen Technology, 2004.
2. Aupretre, F., C. Descorme, et al. (2005). "Ethanol steam reforming over $MgxNi_{1-x}Al_2O_3$ spinel oxide-supported Rh catalysts." *Journal of Catalysis* 233: 464-477.
3. Bedeaux, B., S. Kjelstrup, et al. (2006) "Non-equilibrium thermodynamics – A tool to describe heterogeneous catalysis." *Physical Chemistry Chemical Physics*, 8, 5421-5427.
4. Fatsikostas, A. N., D. I. Kondarides, et al. (2002). "Production of hydrogen for fuel cells by reformation of biomass-derived ethanol." *Catalysis Today* 75(1-4): 145-155.
5. Falconer, J.L. (1992) "The influence of catalyst on thermodynamic equilibrium." *Chemical Engineering Education*. 180-182.
6. Ioannides, T (2001). "Thermodynamic analysis of ethanol processor for fuel cells applications." *Journal of Power Sources* 92: 17-25
7. Llorca, J., N. Homs, et al. (2004). "In situ DRIFT-mass spectrometry study of the ethanol steam-reforming reaction over carbonyl-derived Co/ZnO catalysts." *Journal of Catalysis* 227(2): 556-560.
8. Vasudeva, K., N. Mitra, et al. (1996). "Steam Reforming of Ethanol for Hydrogen Production: Thermodynamic Analysis." *International Journal of Hydrogen Energy* 21(1): 13-18.

Chapter 5

Screening Catalysts Tests

This chapter describes the results for characterizing and testing powder catalysts. Two series of experiments with Packed Bed Reactor (PBR) were developed to compare possible effects on activity and selectivity caused by different operational factors. First, it was analyzed the performance of three catalysts containing Ni as active phase. Second, it was prepared, characterized and tested two different families of catalysts (using Ni or Co as active phase respectively) to study possible effects related with four different factors: temperature, catalyst formulation, SC, and contact time (W/Fao).

5-1 Screening Ni based catalysts

There exist several reviews which report and compare performance of diverse types of catalyst used for SRE (Haryanto, Fernando et al. 2005; Vaidya and Rodrigues 2006). However, this kind of comparison has to afford the difficulty of analyzing experimental results obtained using different reactors and operational conditions. Two possible options to guarantee an objective analysis are: to employ the same reactor under similar conditions and to define unique parameters for comparing results.

As a first attempt, it was developed a series of PBR experiments maintaining similar operational conditions and using three kinds of catalyst which contain Ni as active phase. Table 5-1 shows the operational conditions and the composition of the catalysts, labeled as: Hidrotalcite, Ni/La₂O₃-Al₂O₃ and Ni-Cu/La₂O₃-Al₂O₃. The objective of this experimental set was to evaluate possible influences of catalyst formulation on the reaction performance, basically on macroscopic activity, selectivity, and yield. Operational conditions were fixed closer to an industrial situation than a laboratory research.

Table 5-1 Composition of the catalysts and the operational conditions selected for the first series of PBR experiments.

Catalyst	Composition	Temperature [°C]	SC	W/Fao [min*g _{cat} *mol ⁻¹]
Hidrotalcite	Ni/Mg/Al 1:1:1	500	3	3.46
Ni/La ₂ O ₃ -Al ₂ O ₃	10%Ni, 5%La support: γAl ₂ O ₃	500	3	13.34
Ni-Cu/La ₂ O ₃ -Al ₂ O ₃	10%Ni, 2% Cu, 5%La support: γAl ₂ O ₃	500	3	13.20

Figure 5-1 shows results obtained maintaining equal conditions for temperature and SC (500°C and 3). For Hidrotalcite catalyst, the contact time was adjusted looking for a similar degree of ethanol conversion respect to the other catalysts. Ethanol conversion (X_a) was significantly greater for the Ni-Cu catalyst –approximately 35% after 120 min- and was similar for the other two catalysts -around 20% after 120 min-. Ni/La₂O₃-Al₂O₃ and Hidrotalcite catalysts present similar results concerned to the H₂ production and selectivity to main products. H₂ flow rate produced was around 0.6 mol h⁻¹ for the three catalysts after 120 min of reaction; while selectivity to the main products (H₂, CO₂, CH₄ and CO) was similar for Hidrotalcite and Ni/La₂O₃-Al₂O₃ - 2 mol H₂ mol EtOH reacted⁻¹ approximately- but is significantly reduced for Ni-Cu/La₂O₃-Al₂O₃ catalyst - around 1.1 mol H₂ mol EtOH reacted⁻¹ -. Under the conditions studied, Ni/La₂O₃-Al₂O₃ catalyst gives a lower carbon deposition rate on the catalytic bed; while the other two (Hidrotalcite and Ni-Cu/La₂O₃-Al₂O₃) present similar values. Note that the deposition of carbon contributes to the reduction both ethanol conversion and H₂ flow at higher times; in consequence is important to avoid it as much as possible.

The acidity of Al₂O₃ support promotes ethanol cracking and dehydration, which leads to carbon deposition (Fatsikostas, 2002). However, the impregnation of Al₂O₃ with La₂O₃ contributes to reduce the carbon deposition rate, at the same time that maintains the H₂ production. In consequence, first series of catalytic tests has proven that Ni/La₂O₃-Al₂O₃ catalyst may offer significant advantages for performing H₂ production by SRE.

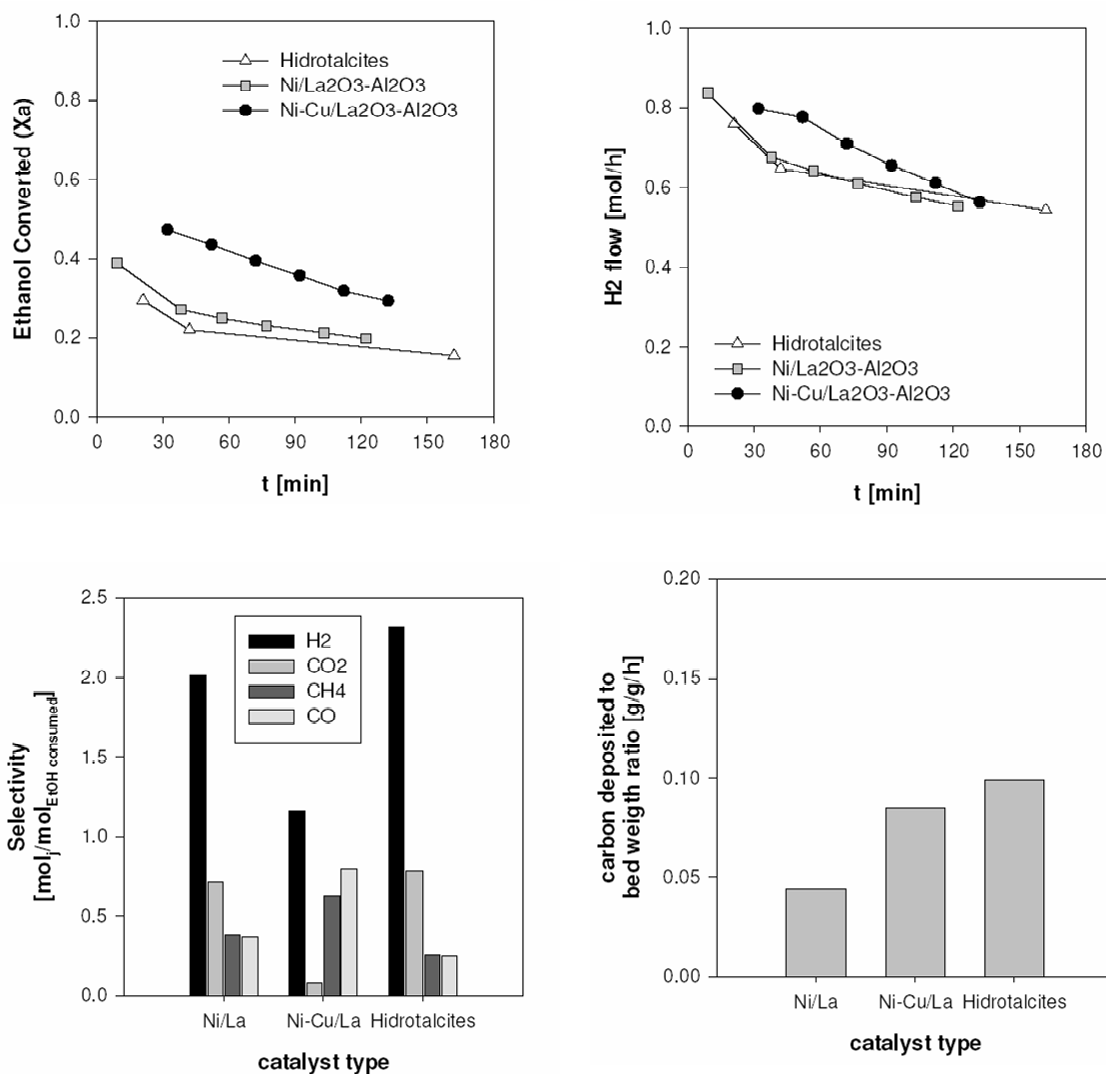


Figure 5-1 First series of Packed Bed Reactor experiments results using three catalyst formulations with Ni as an active phase, fixing temperature at 500°C, liquid flow rate 4 g min⁻¹ and SC at 3. In case of Hidrotalcite catalyst, the contact time was adjusted looking for a similar degree of ethanol conversion (X_a). Carbon deposited on the bed represents an minor fraction compared with an equivalent carbon flow rate of 30.9 g_C h⁻¹.

5-2 Characterizing Ni and CO Powder Catalyst

Analysis from sections 4-3 and 5-1 had shown that Co and Ni based catalysts appear suitable for the SRE reaction. Two catalyst families has been employed extensively in this work: Ni based ($\text{Ni/La}_2\text{O}_3\text{-}\gamma\text{Al}_2\text{O}_3$) prepared by impregnation and Co based prepared by precipitation (Co/ZnO , Co-Fe/ZnO , and Co-Mn/ZnO). Figure 5-2 presents an overall scheme summarizing details of powder catalysts. Among the set of catalysts showed on the overall scheme (figure 5-2), characterization is focused on samples Ni based ($\text{Ni/La}_2\text{O}_3\text{-}\gamma\text{Al}_2\text{O}_3$) prepared by impregnation and Co based prepared by precipitation (Co/ZnO , Co-Fe/ZnO , and Co-Mn/ZnO). Recently, similar Ni and Co catalyst were characterized by Sánchez- Sánchez et al (2007); and Torres et al. (2007) respectively. Hidrotalcite and commercial ICI 46/1 were extensively characterized by Markevich (2001).

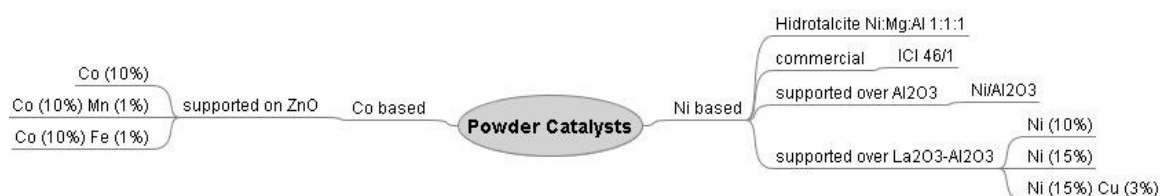
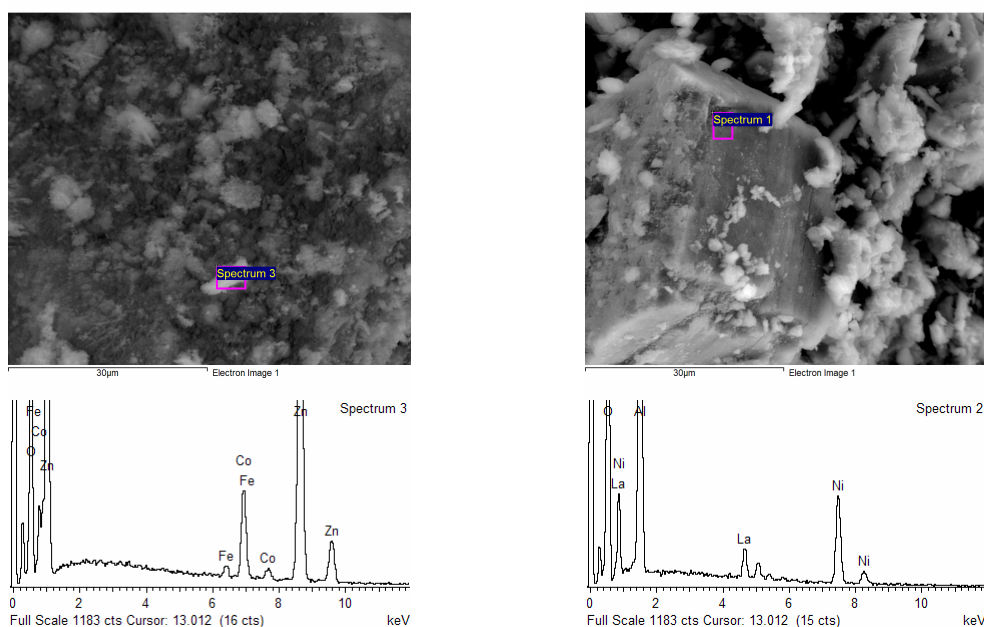


Figure 5-2 Schematic representation for powder catalysts used in this work.

Figure 5-3 presents ESEM images for Co and Ni catalysts and their elemental spectrum obtained by EDS analysis. Elements present in significant amounts, such as Co and Zn (for Co based catalysts), or Ni and La (for Ni based catalysts) are easily detected; while other elements which are less abundant, like Fe, presents a smaller signal response. Table 5-2 shows chemical composition measured by EDS; which verifies that catalysts were obtained close to desired proportions in the major part of cases. Chemical composition on Table 5-2 is based on average among multiple local measurements by EDS. Note that EDS presents higher uncertainty than AAS (and probably it should be used as a semi-quantitative information source) because EDS is a technique that gives optimal results with polish surfaces. However, in this case the particles present irregularities that may affect the way in which electrons are reflected from sample surface to instrument detector. For instance, Ni composition by EDS gave an important deviation for Ni15La08 catalyst (from theoretical 15% to measured 12.8%); in that case AAS test was carried out to confirm the EDS measurement. Actually, AAS estimated a Ni composition for Ni15La08 around 14%, which confirms a deviation higher than 1% for this particular EDS measure.

Table 5-2 Chemical composition of calcinated catalysts obtained from EDS and AAS techniques. Composition target was: 15% Ni and 8% La for Ni based catalyst; 10% Co for Co based catalyst; and 1% Fe or 1% Mn for promoter metals at Co-X/ZnO catalysts. EDS composition is reported in terms of average and standard deviation, in order to delimit the experimental uncertainty

Catalyst	%Ni	%La	%Co	%Mn	%Fe	AAS
Ni/La ₂ O ₃ -γAl ₂ O ₃ (Ni10La08)						10% Ni
Ni/La ₂ O ₃ -γAl ₂ O ₃ (Ni15La08)	12.8+/-1.3	5.1+/-0.9				14% Ni
Co/ZnO (Co10)			8.6+/-1.0			
Co-Mn/ZnO (Co10Mn01)			12.7+/-0.9	1.1+/-0.2		
Co-Fe/ZnO (Co10Fe01)			8.7+/-0.6		0.9+/-0.1	



(a) CoFe catalyst

(b) NiLa catalyst

Figure 5-3 Environmental Scanning Electron Microscopy (ESEM) images and EDS spectra for Co-Fe/ZnO and Ni/La₂O₃-γAl₂O₃ catalysts.

Figure 5-4 shows XRD spectra for Ni and Co catalysts. Note that the Ni catalysts support still remains as $\gamma\text{Al}_2\text{O}_3$ after the heat treatment employed in the two calcinations steps (at 900 and 550 °C respectively). Nickel remains in oxide form and requires the reduction treatment to be transformed into metallic nickel. Also, La peak reveals the formation of aggregates with aluminum oxides. Besides, the X-ray pattern for Co/ZnO catalysts indicates the presence in major proportion of ZnO and Co in oxide form. Fe and Mn are not detected with this technique. Table 5-3 presents Ni crystallite size calculated from the Scherrer equation,

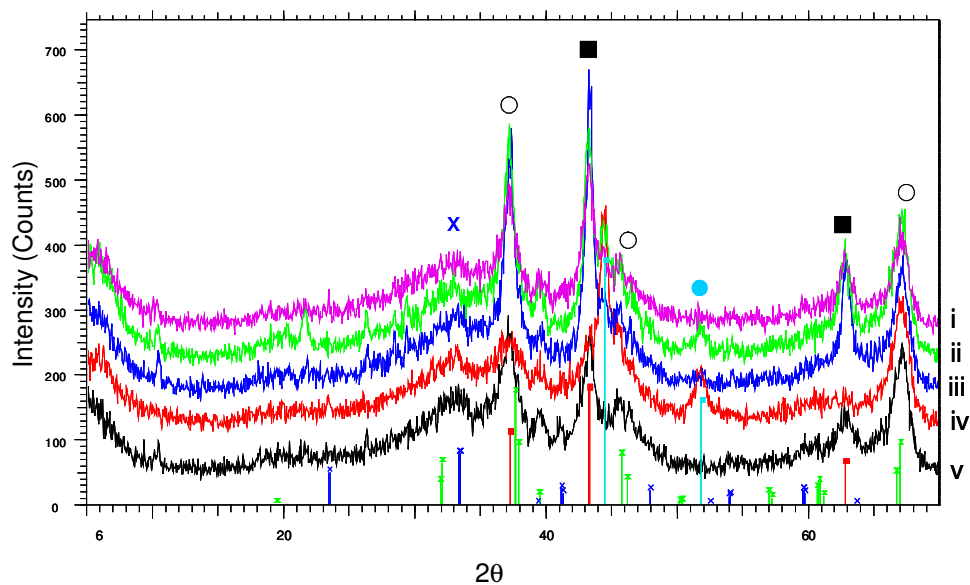
$$d_v = K \cdot \lambda / (\beta \cdot \cos(\vartheta)) \quad (5-1)$$

where d_v refers to the crystallite size weighted by volume, K is the Scherrer constant (somewhat arbitrary), λ is the wavelength of radiation, and β is the integral breadth of peak (in radians 2θ) located at angle θ . This approach does, however, neglect the effect that strain can have on crystallite size. Results on Table 5-3 show that reduction produces shrinking on La(AlO_3) particles and changing Ni particles from NiO to Ni; but Al_2O_3 support is difficulty altered.

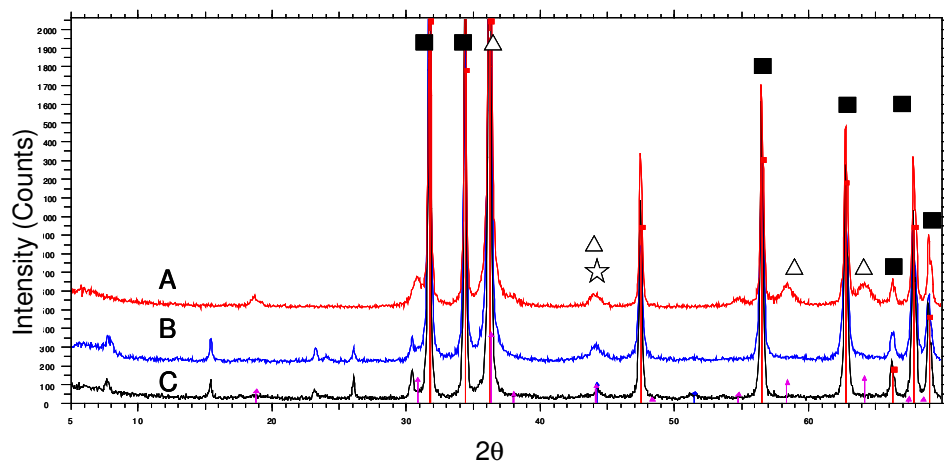
Table 5-3 Crystallite Size for Ni particles using the Sherrer equation

Catalyst	NiO		Ni		Al_2O_3	La(AlO_3)
	d (1 1 1) [nm]	d (2 0 0), [nm]	d (2 2 0), [nm]	d (2 0 0), [nm]	d (4 4 0), [nm]	d (1 0 4) d (1 1 0), [nm]
Spectra i Before Reduction	7.3	8.1	8.9	-	6.4	5.2
Spectra ii After Reduction	5.2	<5	<5	9.3	6.6	3.9

Figure 5-5 presents TEM image for Ni based catalyst; which evidences the formation of Ni-La-Al aggregate. Size measurements for Ni-La-Al aggregate with TEM images resulted around 20-40 nm, greater in size than Ni particles calculated from XRD experiments (figure 5-4 and table 5-2) which are 10 nm approximately. These results coincide with literature data for similar catalysts (Sánchez- Sánchez et al., 2007).



(a) Ni/La₂O₃-γAl₂O₃ catalyst



(b) Co/ZnO catalyst

Figure 5-4 X Ray Diffraction (XRD) profiles of several calcined samples of: **(a)** Ni/La₂O₃-Al₂O₃ catalysts before reduction –i, iii, v- and after reduction at 823K –ii, iv-; (■) Nickel Oxide, NiO; (○) aluminum oxide γAl₂O₃; (X) Lanthanum Aluminum Oxide, LaAlO₃; and (●)Nickel. **(b)** Co based catalysts before reduction – A=Co-Mn/ZnO, B=Co-Fe/ZnO, C=Co/ZnO - (■) Zinc Oxide, ZnO; (△) Cobalt Oxide, Co₂O₄, and (☆) Cobalt, Co. Fe and Mn are not detected with this technique.

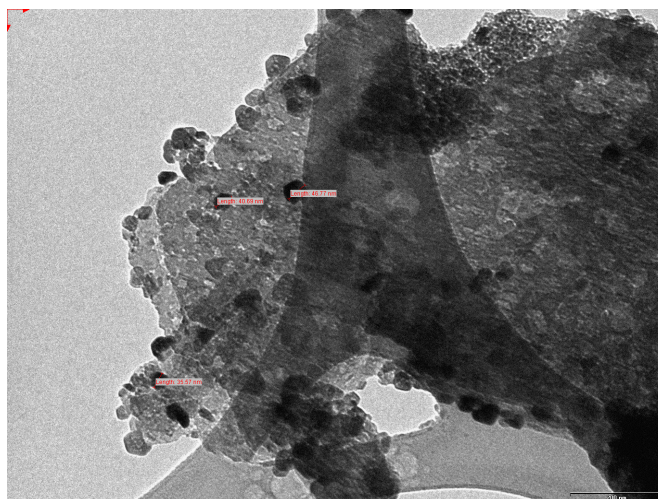


Figure 5-5 Transmission Electron Microscopy (TEM) images for fresh Ni/La₂O₃- γ -Al₂O₃ catalyst (Ni15La08).

Figures 5-6 and 5-7 show the catalyst properties related to porous structure, such as size distribution and pore volume, measured using BET isotherms. Table 5-4 presents BET surface area and pore volume measured by N₂ adsorption-desorption isotherms. Also is reported the metal dispersion for Ni catalysts.

Table 5-4 Catalyst properties from N₂ adsorption-desorption isotherms and H₂ chemisorption

Catalyst	BET Area, m ² /g	Pore Volume, cm ³ g ⁻¹	Metal Dispersion, %
γ -Al ₂ O ₃	164.6	0.25	
Ni10La08	52.8	0.19	3.0
Ni15La08	46.2	0.16	4.1
Co/ZnO	6.6	0.02	
CoFe/ZnO	14.9	0.05	
CoMn/ZnO	13.7	0.06	

Result on Table 5-4 reveal that Ni catalyst support experiences a significant reduction on the surface area, from 165 m² g⁻¹ to 50 m² g⁻¹ approximately due to calcination treatments; which produces a reduction in the available pore volume. Metallic dispersion is affected by La addition because part of porous space is filled with La and is not available for Ni; even when adding another calcination step at 900°C, it favors the intercalation of La between Ni and γ -Al₂O₃ phase (Sanchez- Sanchez, 2007). On the other hand, Co based catalysts present lower surface areas and pore volumes; pointing out the existence of a different surface structure. In general, catalytic studies based on powder catalysts showed surface area values for similar reforming catalysts as a consequence of the temperature conditions (Liberatori et al., 2007);

and recent works intended to optimize these parameters (Sanchez- Sanchez et al., 2007). This work is focused on the catalytic plate preparation rather than increase the support surface area.

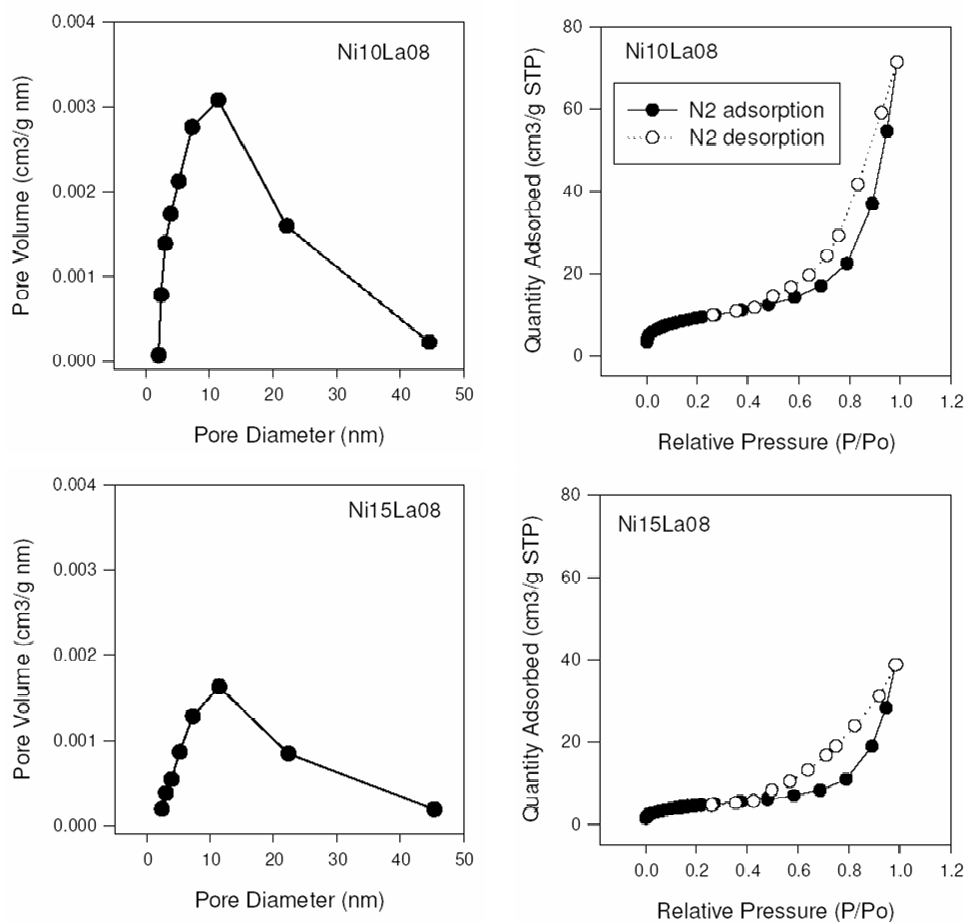


Figure 5-6 Quantity adsorbed as function of the relative pressure, and pore volume distribution from N₂ adsorption-desorption isotherms for the Ni/La₂O₃- γ -Al₂O₃ catalyst

Figure 5-6 reveals that pore volume is reduced as the Ni content increases; augment % Ni from 10 to 15 produces a reduction on the maximum pore volume from 0.30 cm³ g⁻¹ to less than 0.20 cm³ g⁻¹. It is expected to get a lower void pore volume when augment the amount of Ni impregnated on the pore. However, the pore diameter distribution does not change significantly with Ni content.

Figure 5-7 confirm that Co based catalysts present another kind of surface structure. The pore volume is changed through adding Mn and Fe promoters. Mn appears to affect the pore size distribution; while Fe seems to optimize the maximum pore volume to 0.20 cm³ g⁻¹; which is higher than original value of 0.15 cm³ g⁻¹ for Co/ZnO catalyst.

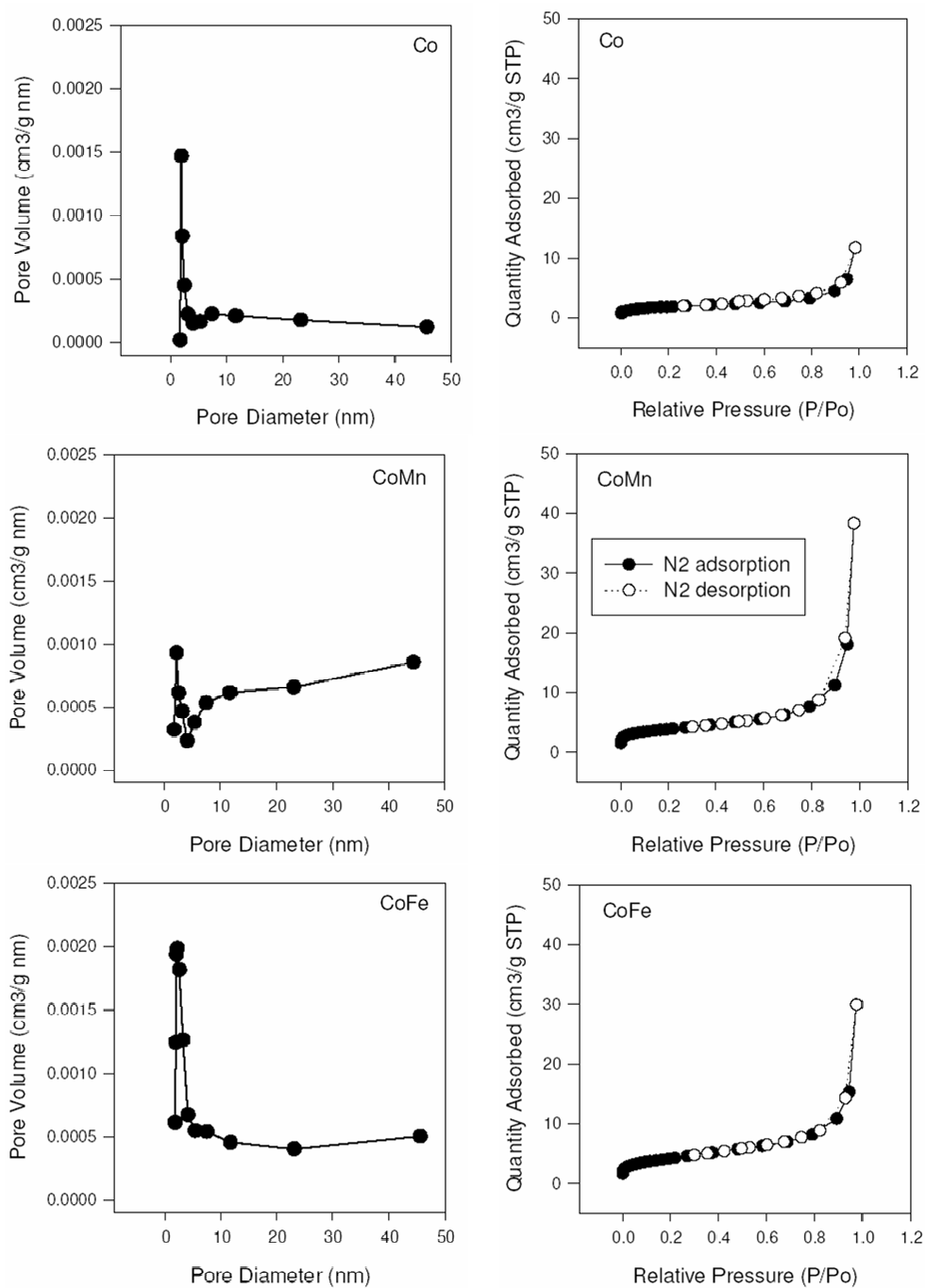
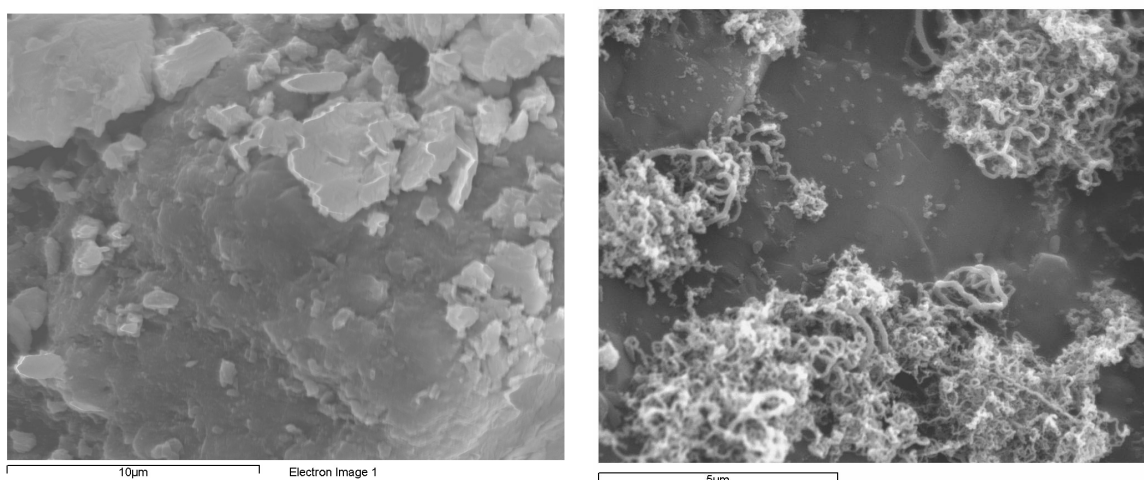


Figure 5-7 Quantity adsorbed as function of the relative pressure, and pore volume distribution from N₂ adsorption-desorption isotherms for Co based catalysts

Figure 5-8 shows SEM images for fresh and used samples from Ni15La08 catalyst after SRE reaction with PBR configuration. Comparing fresh catalyst (top image) and used catalyst (bottom image) reveals appearance of carbon accumulated on the surface as a consequence of the SRE reaction. Carbon deposition is an undesired event because progressively modifies the catalytic surface with reaction time; accelerating the catalyst deactivation, and reducing the catalyst capacity.



(a) Fresh catalyst

(b) Catalyst after 3 hours of reaction

Figure 5-8 Scanning Electron Microscopy images of Ni/La₂O₃- γ Al₂O₃ catalyst sample illustrating presence of carbon deposited after reaction inside Packed Bed Reactor: (a) before reaction (b) after three hours of Steam Reforming of Ethanol reaction under sever conditions (450°C; SC=2)

In summary, powder catalyst was characterized in terms of chemical composition and structural properties. It was determined that Ni and Co based catalysts contains elements close to the desired proportions. Structural parameters, such as surface area and pore volume, change with adding additional metals, such as oxide metals (basic support La₂O₃ in the case of Ni catalyst) and promoters (Mn and Fe in the case of Ni catalyst). It is expected to obtain differences in the catalytic tests as a result of modifying the catalyst formulation.

5-3 Performing Multifactorial Experiments

Two additional series of PBR experiments were developed to estimate significant influences of multiple factors (operational variables) on catalyst activity and selectivity. The response variables were ethanol conversion (X_a), and selectivity to main products (H_2 , CO , CO_2 , CH_4) and to intermediate products (C_2H_4 , C_2H_6 , C_2H_4O and $C_2H_4O_2$). The main factors evaluated were: temperature, catalyst formulation, SC and contact time (W/Fao). Table 5-5 shows the levels employed for each factor. In the case of contact time, there were employed two different scenes: low and high degree of ethanol conversion (Data Set I and Data Set II respectively).

Table 5-5 Operational factors selected for estimating significant influences on the experimental results according to the multifactorial experimental design.

Factor	Operational Variable	Level
A	Temperature [°C]	400 and 500
B	Catalyst	<ul style="list-style-type: none"> ▪ ICI-46-1 (20% Ni) ▪ Ni10La08 (10% Ni, 8% La) ▪ Ni15La08 (15% Ni, 8% La) ▪ CoMn (10% Co, 1% Mn) ▪ Co (10% Co) ▪ CoFe (10% Co, 1% Fe)
C	S/C	2 and 4
D	Contact Time	<ul style="list-style-type: none"> ▪ set I: ($X_a < 50\%$) 4.3; 5.7; 8.7; 33.1 ▪ set II: ($X_a > 50\%$) 148.54/238.98/458.41/1108.74
	W/Fao [min $g_{cat} mol^{-1}$]	

Table 5-6 reports the results of the analysis of variance for the experiments at low ethanol conversion (Set I). In this case, the most important factor is catalyst formulation (factor B) which had a significant effect at a 95% of probability for ethanol conversion and selectivity to all products. Also, it is important to note that both temperature (factor A) and contact time (factor D) has significant effects on ethanol conversion and H_2 selectivity. In contrast, SC (factor C) is the factor that has the lower level of influence. Related with the interactions between different factors, AB and AD seem to be significant and AC does not.

On the other hand, Table 5-7 shows the results obtained for the series of experiments at higher ethanol conversions (Set II). In this case, temperature and SC were fixed at 500°C and 4 respectively. Again, results indicates that the catalyst formulation have influence over the selectivity to CH₄, C₂H₆ and selectivity relation H₂/CH₄. However, contact time does not have a significant influence in the interval studied.

Table 5-6 Factor and interaction effects corresponding to Set I (X_a<50%) from the analysis of variance. Symbol x indicates a significant influence at 95% of probability.

Factor	Selectivity									
	X _a	H ₂	CO	CH ₄	CO ₂	C ₂ H ₄	C ₂ H ₆	C ₂ H ₄ O	C ₂ H ₄ O ₂	H ₂ / CH ₄
A (temperature)	X	X			X		X			
B (catalyst type)	X	X	X	X	X	X	X	X	X	X
C (S/C)	X									
D (W/Fao)	X	X		X						X
AB		X			X			X		
AC										
AD		X	X							

Table 5-7 Factor and interaction effects corresponding to Set II (X_a>50%) from the analysis of variance. Symbol x indicates a significant influence at 95% of probability.

Factor	Selectivity									
	X _a	H ₂	CO	CH ₄	CO ₂	C ₂ H ₄	C ₂ H ₆	C ₂ H ₄ O	C ₂ H ₄ O ₂	H ₂ / CH ₄
B (catalyst type)				X			X			X
D (W/Fao)										
BD										

Figure 5-9 shows the influence of SC on the ethanol conversion and H₂ flow produced. The SC ratio was fixed between 2-4 maintaining the same catalyst formulation, temperature and contact time (Ni15La08; 500°C and 10 g min mol⁻¹ respectively). Both ethanol conversion and H₂ production follow similar tendencies in the three cases. The SC=2 gives a lower value than the rest for the ethanol conversion, but the H₂ production presents similar results. Also, according to ethanol conversion and H₂ production diminishing rate, the catalyst deactivation appears to be strongest for SC 2 than the other cases.

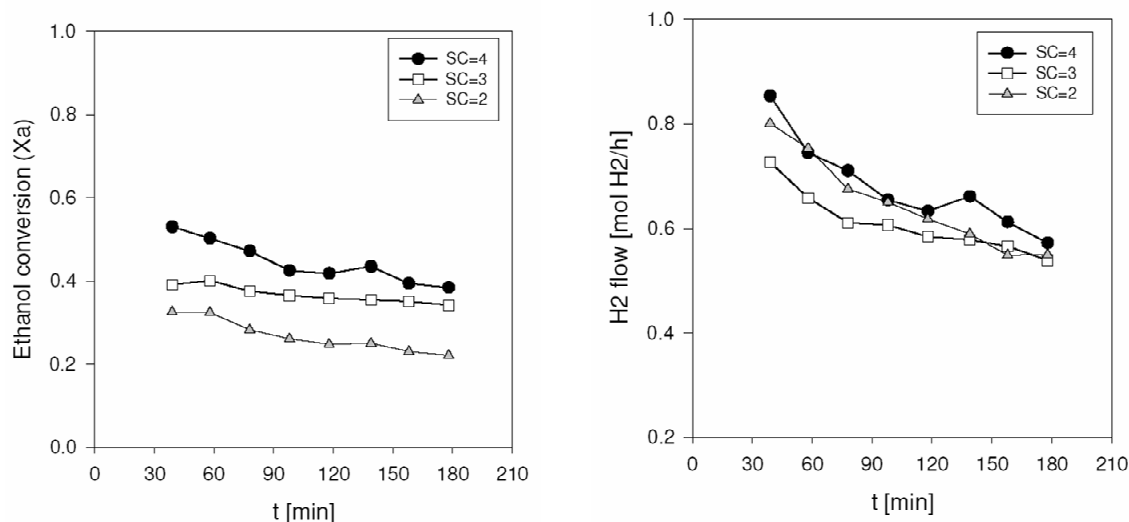


Figure 5-9 Effect of SC on H₂ flow and X_a; Temperature 500°C; W/Fao of 10 g min mol⁻¹; catalyst formulation Ni15La08

Figure 5-10 shows the molar yield of the different products for three Ni catalysts at two temperatures (400°C and 500°C). Operational conditions were fixed at SC of 4 and W/Fao of 9 g min mol⁻¹. Comparing selectivity to different products at the different temperatures, it is possible to detect which type of reaction predominates. For instance, at 400°C there is a significant proportion of C₂H₄O –around 0.6 mol mol⁻¹-, which points out that the dehydrogenation reaction eq (2-19) may be favored. On the other hand, at the temperature of 500°C, it is observed an important increase of H₂ and CO₂ yields – H₂ increase from 1.3 mol mol⁻¹ at 400°C to 3.0 mol mol⁻¹ at 500°C, while CO₂ augment from 0.2 to 0.7 mol mol⁻¹ respectively- with a significant reduction of the C₂H₄O. Then, as temperature increases, Ni catalysts favor SR reactions, such as eq (2-29) and eq (2-30). In addition, it is interesting to note that CH₄ and CO yields also increases with temperature; especially the Ni15La08 catalysts presents the most significant increase – CH₄ increase from 0.1 at 400°C to 0.3 mol mol⁻¹ at 500°C while CO yield augment from 0.3 to 0.45 mol mol⁻¹ respectively- which suggests a marked tendency to favor decomposition reactions by eq (2-20). In contrast, ethylene maintains a similar yield while both C₂H₆ and C₂H₄O₂ are not detected at significant levels.

Figure 5-11 shows molar yield for different catalyst formulations using Co as active phase (Co/ZnO, CoFe/ZnO and CoMn/ZnO) and experimental conditions similar to figure 5-10: two temperatures (400 and 500°C) maintaining constants SC at 4 and W/Fao at 9 g min mol⁻¹.

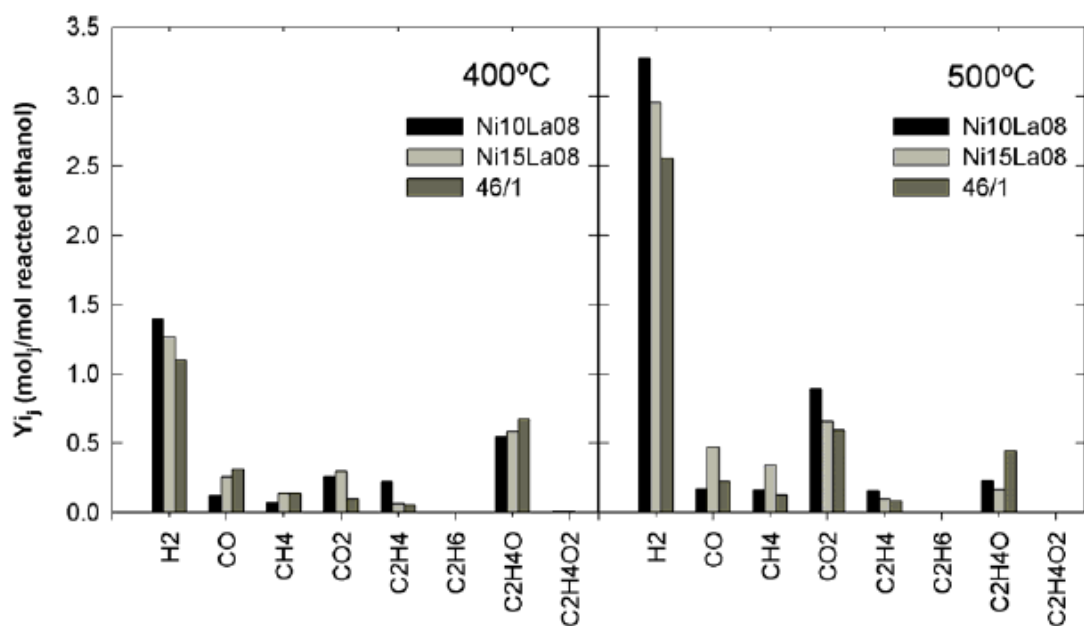


Figure 5-10 Intermediate and final products yield for three kind of Ni based catalysts. Experiments performed under similar operational conditions (400°C and 500°C respectively, SC=4, W/Fao=9 g min mol⁻¹)

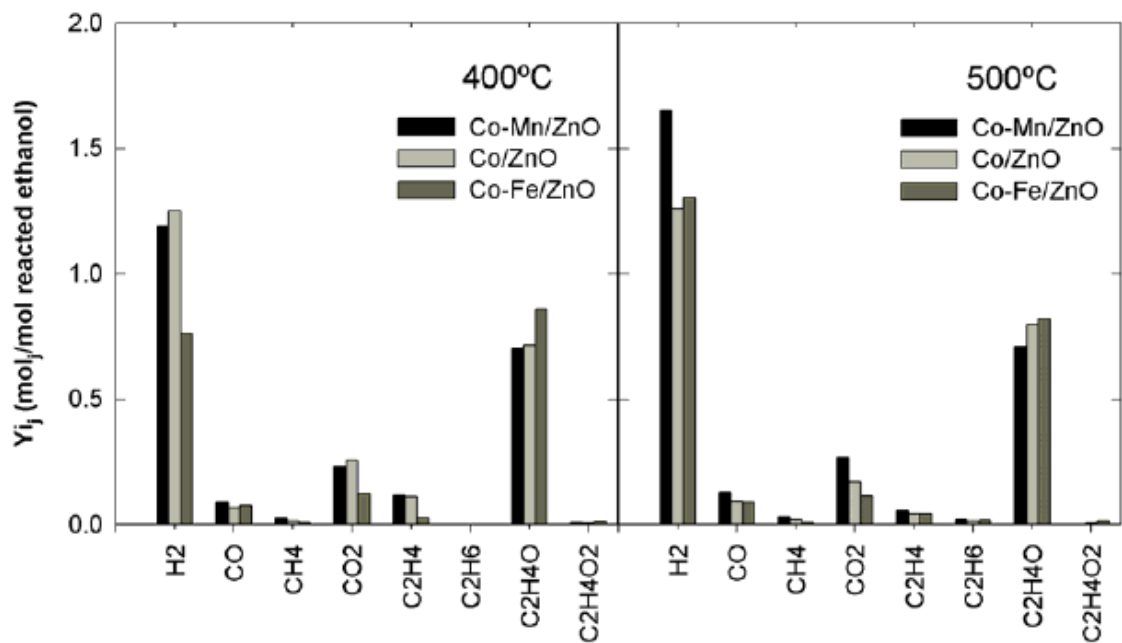


Figure 5-11 Intermediate and final products yield for three kind of Ni based catalysts. Experiments performed under similar operational conditions (400°C and 500°C respectively, SC=4, W/Fao=9g min mol⁻¹).

Figure 5-11 indicates that H_2 and C_2H_4O increase with temperature; meaning that Co catalysts tends to favor H_2 production through ethanol dehydrogenation (2-19) and possibly through acetaldehyde reforming (2-31) and (2-32). Also important is to note that reactions to produce CO and CH_4 do not seem to be promoted with temperature under those conditions in contrast to the Ni catalyst. Co-Mn/ZnO catalyst may be the most active at $500^\circ C$ to reforming reactions according to the H_2 yield compared with the other Co catalysts while Co and Co-Mn presents a similar behavior.

Figure 5-12 presents the ethanol conversion and H_2 yield for two Ni based catalysts (Ni15La08 and ICI 46/1) and two Co based catalysts (Co-Fe/ZnO and Co-Mn/ZnO) at $500^\circ C$, SC 4 and different contact time values. Ethanol conversion has been reached after $600 \text{ g min mol}^{-1}$ for all catalysts. Ni catalysts present a higher H_2 yield at low contact times (around $2.8 \text{ mol}_{H_2} \text{ mol}_{EtOH \text{ reacted}}^{-1}$ at 9 g min mol^{-1} while Co catalysts is in the order of $1.5 \text{ mol}_{H_2} \text{ mol}_{EtOH \text{ reacted}}^{-1}$). However, at high ethanol conversion the Co catalysts increase their H_2 yield around $4.3 \text{ mol}_{H_2} \text{ mol}_{EtOH \text{ reacted}}^{-1}$ while Ni catalysts yield does not increase more than $3.6 \text{ mol}_{H_2} \text{ mol}_{EtOH \text{ reacted}}^{-1}$.

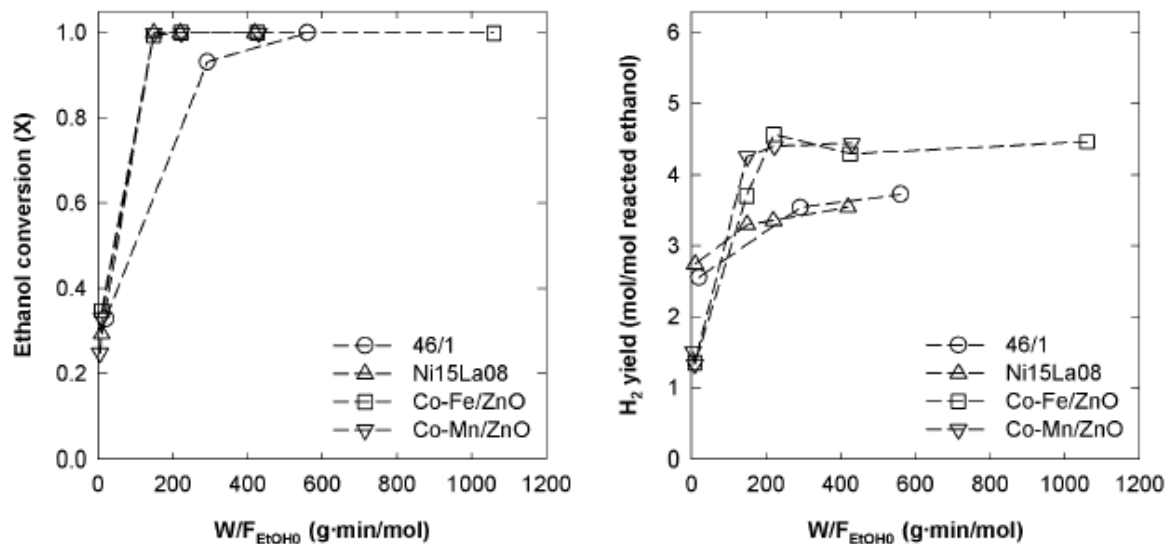


Figure 5-12. Ethanol conversion and H_2 yield as a function of the contact time for Ni and Co based catalysts under similar operational conditions (SC=4, T=500°C)

Figure 5-13 presents the equilibrium products selectivity predicted by the thermodynamic, and it compares with the experimental selectivity for Ni based catalysts. Experimental results are obtained changing the contact time and maintaining the same conditions than experiments in figure 5-12 (at 500°C and SC 4). The intermediate products presented at mayor proportions were CH₄ and C₂H₄O, but only at contact times lower than 300 g min mol⁻¹. Ni15La08 catalyst produced the lower proportion of acetaldehyde; which indicates that it may not favor the ethanol decomposition reaction (2-19) or if acetaldehyde is produced, it may catalyze the reforming reaction that consumes this intermediate product (2-31) and (2-32). Again, ethylene presents a similar selectivity for both Ni catalysts.

On the other hand, figure 5-13 also indicates that in the case of Ni based catalysts the final products (H₂, CO, CO₂, CH₄) tends to be catalyzed until values approximately equal than that predicted by thermodynamic equilibrium. This observation agrees with result presented on others work in the literature and reviewed in figure 4-9. Also, selectivity for CO, CH₄ and CO₂ for Ni catalysts (ICI and Ni15La08) presents similar trends; they were stabilized after 300 g min mol⁻¹.

Figure 5-14 shows the selectivity to both final and intermediate products at different contact times for three catalyst formulations containing Co (Co-Fe/ZnO, Co-Mn/ZnO). It were maintained constants the SC and Temperature (4 and 500°C in that order) as in figures 5-12 and 5-13. Contrary with Ni catalyst results (figure 5-13), in the case of Co based catalysts the selectivity to final products H₂, CO, and CH₄ tends to be different to that predicted by thermodynamic equilibrium. Especially important are the cases of H₂ and CH₄ selectivity which are stabilized at 0.69 and 0.029 while the equilibrium predicts values of 0.63 and 0.11 respectively. Again, this observation is in concordance with other catalytic tests reported in literature (figure 4-9).

Another difference observed between Ni and Co catalysts is related with the selectivity to intermediate products. Especially important is to remark that Co catalysts, as shown figure 5-14, produce ethane and acetaldehyde in major proportions than the Ni catalysts (figure 5-13); pointing out the difference in reaction pathways that follows each of them.

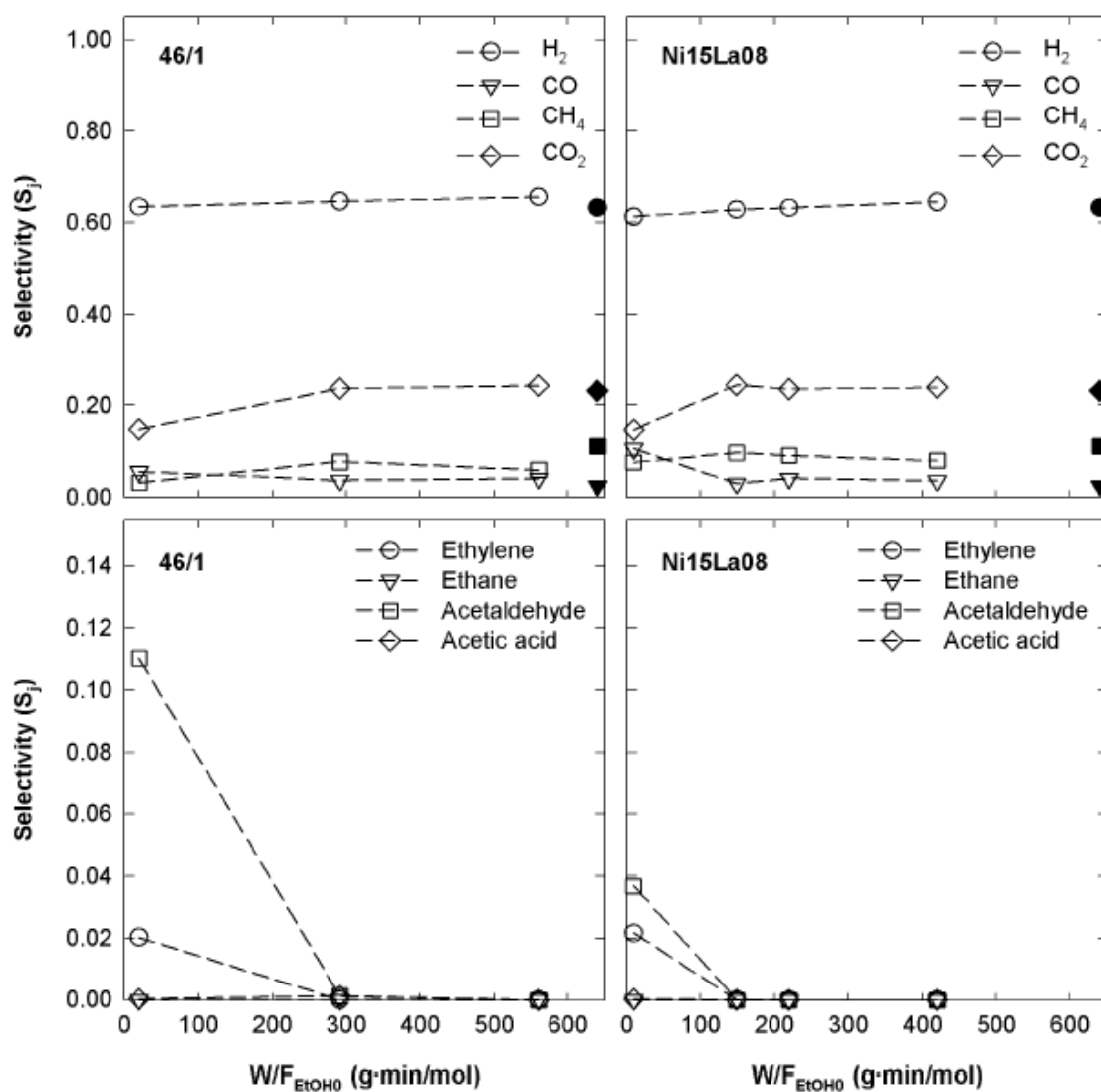


Figure 5-13 Ni catalyst selectivity to final (H₂, CO, CO₂, CH₄) and intermediate products (C₂H₄, C₂H₆, C₂H₄O, C₂H₄O₂) as a function of the contact time (W/F_{ao}). Operational conditions were: Temperature at 500°C and SC at 4. Black symbols represents the equilibrium selectivity

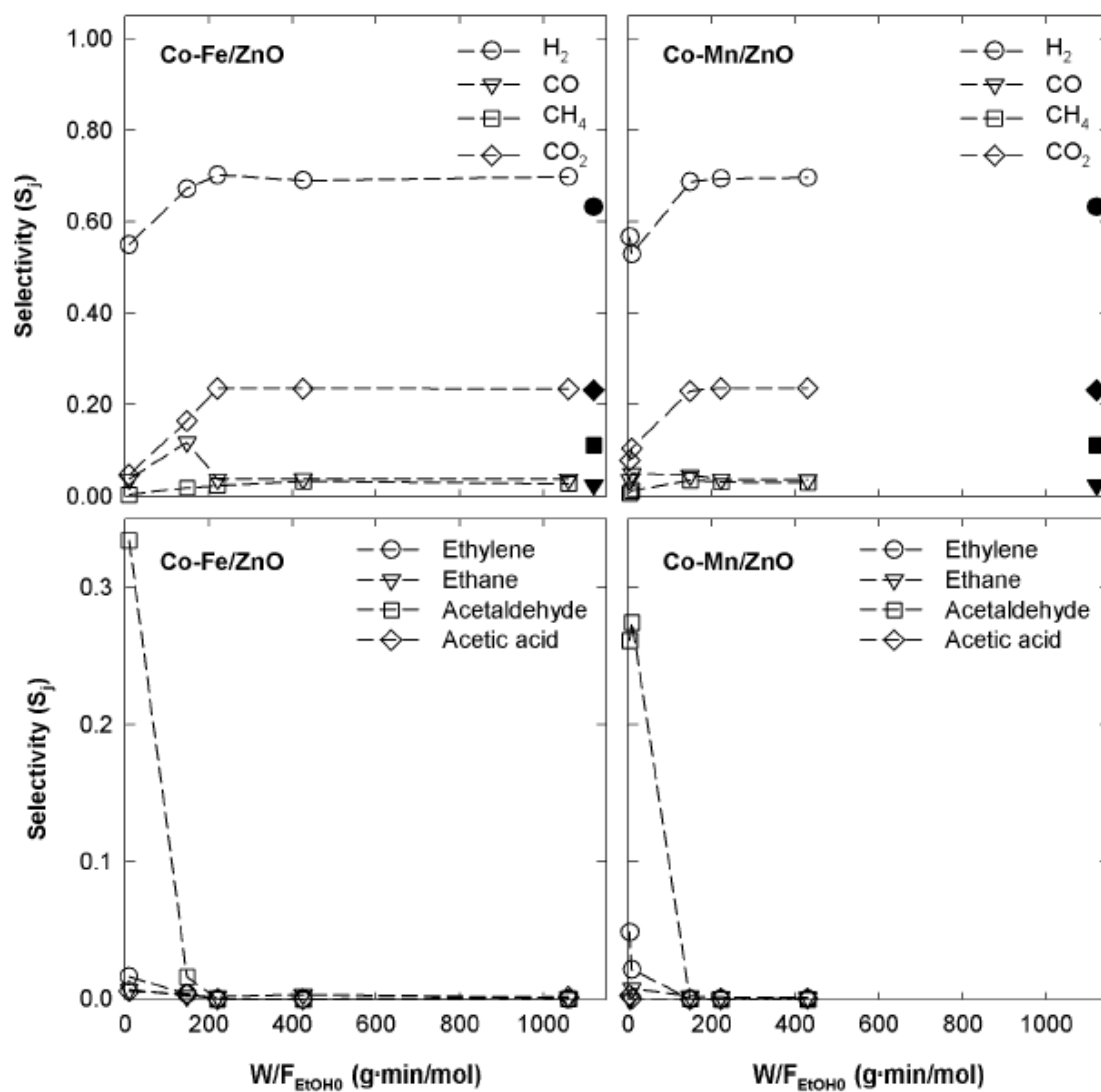


Figure 5-14 Co catalyst selectivity to final (H_2 , CO , CO_2 , CH_4) and intermediate products (C_2H_4 , C_2H_6 , C_2H_4O , $C_2H_4O_2$) as a function of the contact time (W/F_{ao}). Operational conditions were: Temperature at $500^\circ C$ and SC at 4. Black symbols represents the equilibrium selectivity

Figure 5-15 shows H_2 to CH_4 selectivity ratio for different contact times for Ni and Co based catalysts. It were maintained constants the SC and Temperature (4 and $500^\circ C$ correspondingly). In concordance with observations in figure 5-14; Co catalysts present a H_2 to CH_4 selectivity ratio higher than equilibrium, stabilized around 23 and $5.7 \text{ mol}_{H_2} \text{ mol}_{CH_4}^{-1}$ respectively. On the other hand, Ni catalysts tend to the produce a final composition similar to thermodynamic equilibrium.

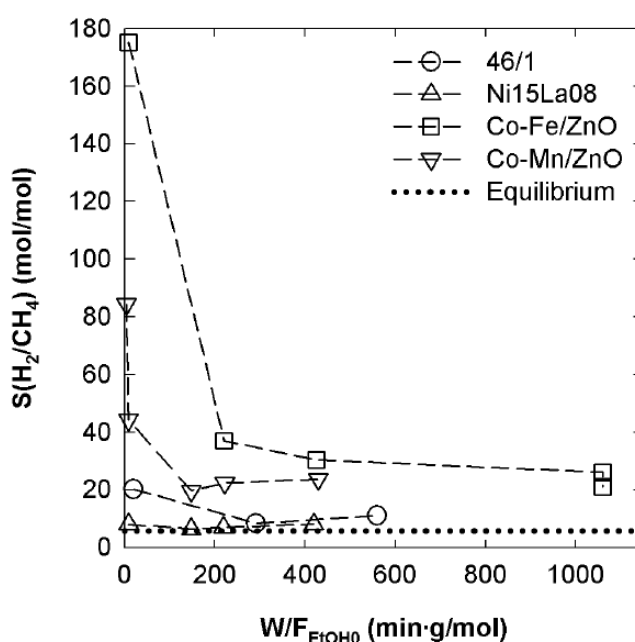


Figure 5-15 H_2 to CH_4 selectivity ratio for Ni and Co based catalysts as a function of the contact time (W/Fao). Operational conditions were: Temperature at $500^\circ C$ and SC at 4. Dot line represents equilibrium

In conclusion, both Ni and Co based catalysts are active for the SRE under the conditions studied (temperature from 400 to $500^\circ C$; SC from 2 to 4 and contact time from 9 to $1000 \text{ g min mol}^{-1}$). The Co catalysts favor the formation of acetaldehyde and reduce the possibilities of ethanol and acetaldehyde cracking; in consequence it produces a H_2 to CH_4 ratio above the equilibrium. On contrary, Ni catalysts promote the cracking and reforming reactions and results in selectivity to final products closer to the equilibrium.

Under the conditions studied, catalyst screening showed that CH_4 is the main competitor with H_2 production, and contact time is a crucial factor to reach equilibrium proportions. At last, Ni and Co catalysts are suitable candidates for developing catalytic plates to incorporate into structured CWR.

References

1. Aupretre, F., C. Descorme, et al. (2005). "Ethanol steam reforming over $Mg_xNi_{1-x}Al_2O_3$ spinel oxide-supported Rh catalysts." *Journal of Catalysis* 233: 464-477.
2. Fatsikostas, A. N., D. I. Kondarides, et al. (2002). "Production of hydrogen for fuel cells by reformation of biomass-derived ethanol." *Catalysis Today* 75(1-4): 145-155.
3. Haryanto, A., S. Fernando, et al. (2005). "Current status of hydrogen production techniques by steam reforming of ethanol: A review." *Energy & Fuels* 19(5): 2098-2106.
4. Liberatori, J.W.C., R.U. Ribeiro, et al. (2007) "Steam reforming of ethanol on supported nickel catalysts" *Applied Catalysis A* 327: 197-204
5. Llorca, J., N. Homs, et al. (2004). "In situ DRIFT-mass spectrometry study of the ethanol steam-reforming reaction over carbonyl-derived Co/ZnO catalysts." *Journal of Catalysis* 227(2): 556-560.
6. Markevich, M., X. Farriol, et al (2001) "Hydrogen production by steam reforming of vegetable oils using nickel-based catalysts" *Industrial and Engineering Chemistry Research*, 40 (22): 4757-4766.
7. Sánchez-Sánchez, M.C., R.M. Navarro, et al (2007) "Ethanol steam reforming over Ni/La- Al_2O_3 catalysts: Influence of lanthanum loading" *Catalysis Today*, 129 (3-4): 336-345.
8. Torres, J.A., J. Llorca, et al (2007) "Steam reforming of ethanol at moderate temperature: Multifactorial design analysis of Ni/La $_2O_3$ - Al_2O_3 , and Fe- and Mn-promoted Co/ZnO catalysts" *Journal of Power Sources*, 169 (1): 158-166.
9. Vaidya, P. D. and A. E. Rodrigues (2006). "Insight into steam reforming of ethanol to produce hydrogen for fuel cells." *Chemical Engineering Journal* 117(1): 39-49.

Chapter 6

Catalytic Plate Tests

This chapter presents numerical and experimental analyses focused on catalytic plates in a Catalytic Wall Reactor. Results are grouped into four main sections, according to the analysis methodology: (i) simulate conceptually the reforming channel using a 2D model to evaluate temperature and concentration profiles; (ii) characterize the prepared plates coated with Ni and Co catalysts; (iii) test the catalytic plates for SRE, SRM, and WGS reactions; and (iv) simulate a co-current CWR configuration to evaluate thermal limitations between endothermic and exothermic coupling using a 1D model.

6-1 Conceptual 2D Simulation for Catalytic Plates

This section presents a conceptual analysis through multiphysic simulation on 2D for the employed catalytic plate configuration. Multiphysic approach is useful to accomplish diverse physical phenomena, which in the case of heterogeneous catalysis covers mass and heat transport mechanisms couple with catalytic reaction. The objective of this exploratory study is to anticipate possible operational regime on the CWR unit, constructed to perform catalytic plate tests. First is described the mathematical model and then are showed most important results, in terms of concentration, temperature, and dimensionless groups.

6-1-1 Mathematical Model

A 2D model is employed for determining concentration and temperature profiles inside the CWR configuration used in the experiments. Mathematical model is described on Table 6-1; which is similar to that exposed by Zafir (Zafir and Gavriilidis, 2001). Catalytic plate is assumed adiabatic and symmetric at the centerline of the gas flow channel, as shown on figure 6-1. The model includes: (i) mass and heat balances at the gas phase, through axial convection, conduction, and diffusion at both directions; and (ii) heat balance at the solid block, principally by conduction. Main assumptions are: steady state, ideal gas behavior, chemical reaction only at the catalytic wall; catalyst layers are thin enough to neglect intra-

phase transport; and negligible radiation and pressure drop. Finally, diffusion and conduction at reactor outlet are specified to be zero.

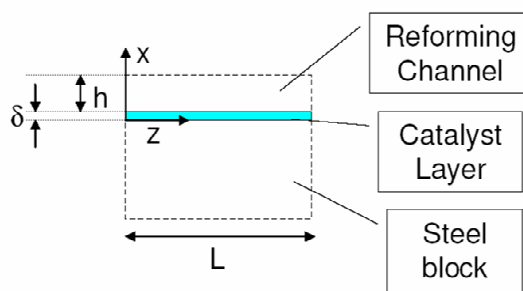


Figure 6-1 Diagram of studied catalytic plate, an adiabatic reactor with symmetry at the centerline of the channel. Main assumptions are: steady state, ideal gas behavior, chemical reaction only at the catalyst layers; which are thin enough to neglect intra-phase transport. The geometry factors are: the catalytic plate thickness δ , the channel thickness h , the block thickness H , and the plate length, L

It is consider that the diffusion coefficient is a temperature function as follows,

$$D = D_0 \left(\frac{T}{T_0} \right)^{1.75} \quad (6-1)$$

where T_0 and D_0 refer to initial value of temperature and diffusion coefficient respectively. Average temperature and concentration are calculated by eq (3-12).

It is a common practice to compute dimensionless groups such as Nu , Sh , and Da to evaluate reaction performance with mass/heat transport mechanism. In this case, it is employed this definitions,

$$Nu = \frac{q}{(T - T_{ave}) k_f} \frac{x}{\delta} \quad (6-2)$$

$$Sh = \frac{J}{(C - C_{ave}) D} \frac{x}{\delta} \quad (6-3)$$

$$Da = \frac{k_0 \cdot \exp(E/RT) \cdot d_{eq}}{C \cdot D} \quad (6-4)$$

where T_{ave} and C_{ave} are the average temperature and concentration for the gas phase, computed by eqs (3-12), q is the local heat rate, J is the local mass flow, x is the axial length, and deq is the equivalent diameter for a square channel.

Table 6-1 Mathematical model applied to CWR shown on figure 6-1

Solid			
$0 = \frac{\partial}{\partial x} \left(k \frac{\partial T}{\partial x} \right) + \frac{\partial}{\partial z} \left(k \frac{\partial T}{\partial z} \right)$	Energy Balance		(6-5a)
Gas phase			
$\rho u_z \frac{\partial w_i}{\partial z} = \frac{\partial}{\partial x} \left(\rho D \frac{\partial w_i}{\partial x} \right) + \frac{\partial}{\partial z} \left(\rho D \frac{\partial w_i}{\partial z} \right)$	Mass Balance		(6-5b)
$\rho u_z c_p \frac{\partial T}{\partial z} = \frac{\partial}{\partial x} \left(k \frac{\partial T}{\partial x} \right) + \frac{\partial}{\partial z} \left(k \frac{\partial T}{\partial z} \right)$	Energy Balance		(6-5c)
$\frac{\partial}{\partial z} (\rho u_z) = 0$	Momentum Balance		(6-5d)
$\rho = \frac{P}{RT} \frac{1}{\sum \left(\frac{w_i}{MW_i} \right)}$	Ideal Gas		(6-5e)
Boundary conditions			
$\left. \frac{\partial y}{\partial x} \right _{x=h} = \left. \frac{\partial T}{\partial x} \right _{x=h} = \left. \frac{\partial u_z}{\partial x} \right _{x=h} = 0$	Symmetry	Channel center	(6-5f)
$\left. \frac{\partial}{\partial x} \left(\rho D_i \frac{\partial w_i}{\partial x} \right) \right _{x=0} = -r_i \cdot MW_i$	Reaction		(6-5g)
$\left. \frac{\partial}{\partial x} \left(k_s \frac{\partial T}{\partial x} \right) \right _{x=0} = r \cdot (-\Delta H_{rxn}) + \left. \frac{\partial}{\partial x} \left(k_g \frac{\partial T}{\partial x} \right) \right _{x=0}$	Heat consumption	Catalyst layer	(6-5h)
$u_z = 0$	No slip		(6-5i)
$\left. \frac{\partial T}{\partial z} \right _{z=L} = \left. \frac{\partial u_z}{\partial z} \right _{z=L} = \left. \frac{\partial w_i}{\partial z} \right _{z=L} = 0$	Zero flux	Channel outlet	(6-5j)
$T = T_0, \quad u_z = u_0, \quad w_j = w_{j,0}$	Feed conditions	Channel inlet	(6-5k)

Table 6-2 shows main factors employed, such as reactor geometry, inlet conditions and kinetic parameters. Geometry and operational conditions are similar to those used on experiments, while uncertain kinetic parameters such as reaction rate constant and activation energy are screened at different levels. Mass flow rate from 0.01 to 1.00 corresponds to Re numbers from 20 to 2000 respectively. Exploration of the Re number effects on heat and mass transport is limited to flow rates in the experimental range.

Table 6-2 Factors used for calculation: reactor geometry, inlet conditions and kinetic parameters

Geometry	Channel	0.2 cm by 2cm by 5cm
	Plate	100 μ m by 2cm by 5cm
Feed conditions	SC	4 mol _{H₂O} /mol _C
	T ₀	773
	Mass flow rate	from 0.01 to 1.00 g min ⁻¹
Linear Kinetic	Reaction rate constant	from 10 to 10 ⁴ s ⁻¹
	Activation energy	from 64 to 130 kJ mol ⁻¹

Mathematical model consists of a set of partial differential equations (PDEs) solved using Femlab 3.0 (Comsol, 2004); which is a commercial package based on finite element method. Kinetic expression is simplified as much as possible because is the principal source of uncertainty in the model. There are solved several cases to evaluate sensitivity over kinetic parameters, such as activation energy and reaction rate constant. Otherwise, gas phase and solid blocks are studied separately to facilitate the analysis. Mathematical model is selected based on previous works (Donsi F., Di Benedetto A. et al 2006); which have shown that in the presence of a catalytic reaction, the channel can be divided into two principal zones, characterized by the development of momentum, heat and mass boundary layers.

6-1-2 Gas Phase Results

First, for the gas phase, resistance caused by conduction through the steel block is assumed to be negligible in comparison with the heat transport resistance between the catalytic layer and the gas flow.

Figure 6-2 shows velocity contour at mass flow rate $m=0.1 \text{ g min}^{-1}$. It can be observed two marked regions in function of the axial position: in the first zone, near the inlet, radial gradients are perturbed by entrance effects; while the rest maintains a stable profile on radial direction. This contour can be related by the development of momentum boundary layer. Velocity contours are not affected significantly by kinetic parameters, such as frequency factor or activation energy because is considered a system under diluted conditions (i.e. water and argon are in excess compared with ethanol and all the products).

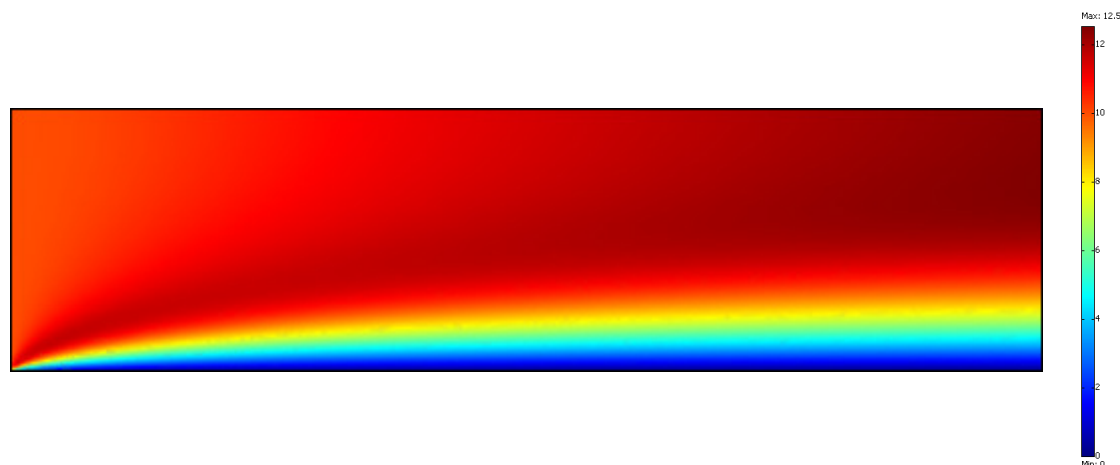


Figure 6-2 Contour plot for gas phase velocity at mass flow rate of $m=0.1 \text{ g min}^{-1}$. Other models parameters are: $E_a=97 \text{ kJ mol}^{-1}$ and $k_o=100 \text{ s}^{-1}$.

Figure 6-3 presents contour plots for temperature and ethanol concentration at the flow channel at one level of the reaction rate constant ($k_o=100 \text{ s}^{-1}$). Mass flow rate and activation energy are fixed at 1 g min^{-1} and 97 kJ mol^{-1} respectively. Contour plot is adjusted for comparison purposes by fixing ranges of concentration (from 1.70 to 1.75 mol m^{-3}). Temperature is approximately constant (around 773 K).

The concentration gradient between bulk and catalyst surface increases with the axial coordinate because the ethanol consumption augments with reactants residence time. The same dynamics follows for the temperature gradient and the heat consumption. In addition, as higher k_o , higher the reduction in temperature because the heat demand of the endothermic reaction is proportional to the reaction rate. In general, temperature contour appears to be isothermal; while concentration is progressively affected by axial diffusion and the development boundary layer with high values on the axial coordinate.

Figure 6-4 presents results for catalytic wall and bulk fluid at four levels of the reaction rate constant; again with activation energy at 97 kJ mol^{-1} and mass flow rate at 0.1 g min^{-1} . Temperature and concentration profiles at the catalytic wall shown on figures 6-4a and 6-4b indicate that both variables follow a similar tendency: decrease progressively with augments on the reaction rate constant. Both, temperature and concentration profiles present two main regions in function of the axial length, which are a zone with a significant declining (near the inlet) followed by another region where the variable is almost constant (next to the outlet) or present a lower decline rate. This performance coincide with observations on previous works (Donsi F., Di Benedetto A. et al 2006); there are two zones, first a region where the variable is affected by entrance effects, and then a second region where dominates the reaction dynamics.

In addition, temperature and concentration profiles for the bulk fluid at the outlet can be observed on figures 6-4c and 6-4d. Near the catalytic wall ($x=0$), the variables are significantly lower than at the channel center ($x=10^{-3}$). Also, as high is the reaction rate constant; higher is the gradient experienced by the fluid between the wall and the channel center. In summary, under these conditions the reaction rate constant has a major influence on the heat and mass transport behavior; in particular there is a strong influence of k_o on the radial profiles of temperature and concentration.

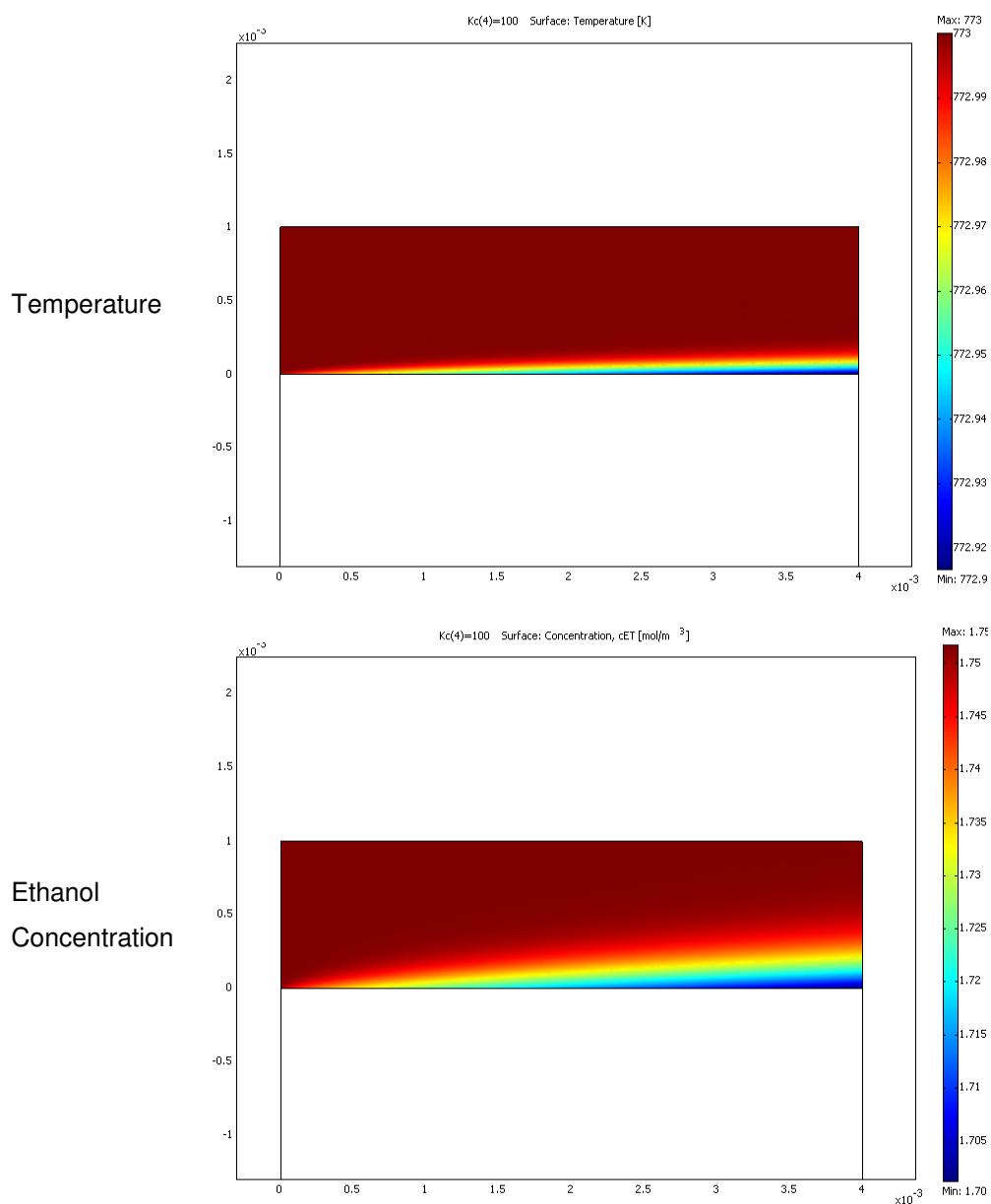


Figure 6-3 Contour plot for gas phase temperature and concentration under central level of reaction rate constant. Other models parameters are: $Ea=97 \text{ kJ mol}^{-1}$ and $m=1 \text{ g min}^{-1}$. Gas phase temperature is around 773 K and concentration varies from 1.70 to 1.75 mol m⁻³.

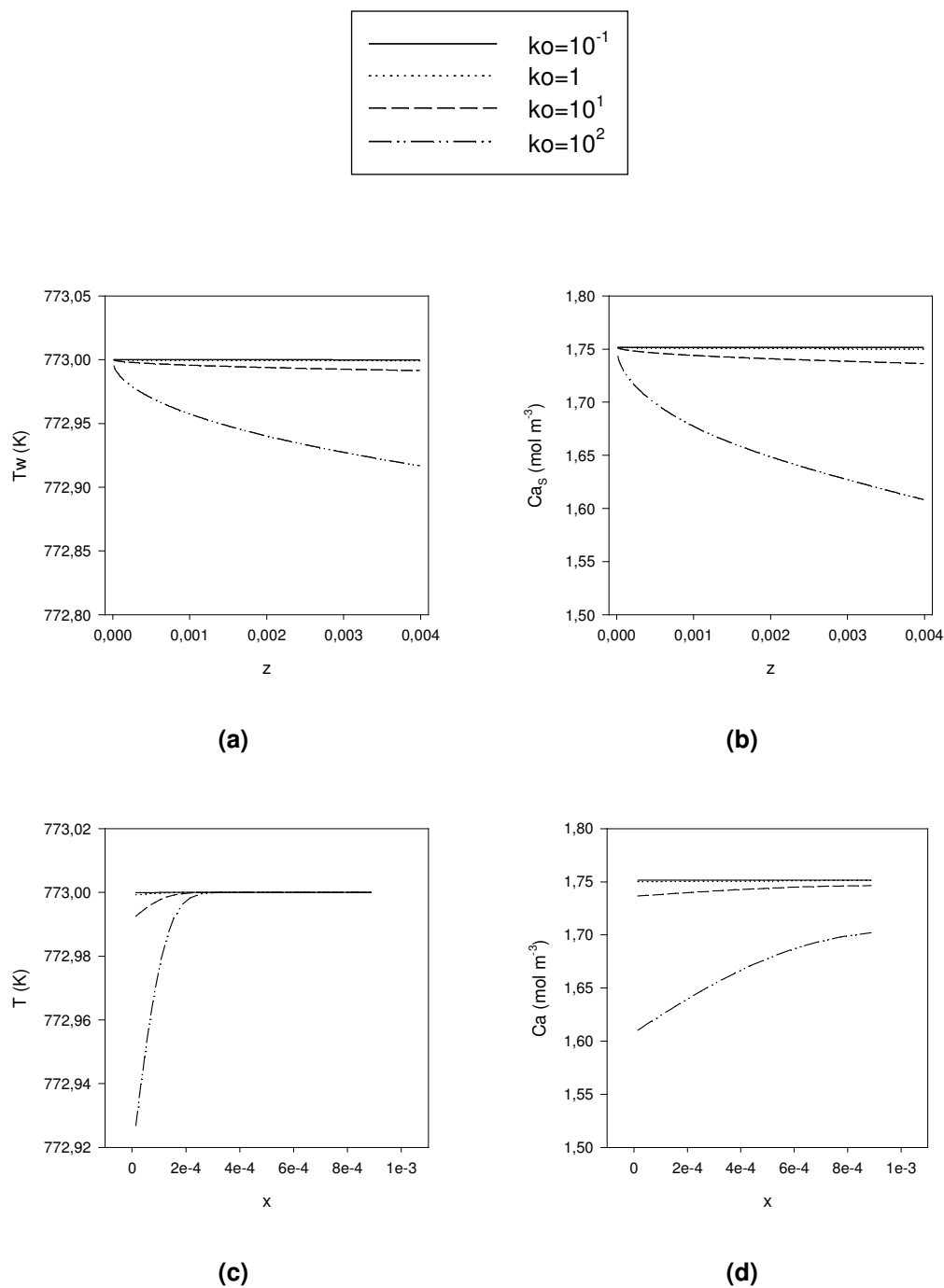


Figure 6-4 Temperature and concentration profiles for base case $-Ea=97 \text{ kJ mol}^{-1}$ and $m=0.1 \text{ g min}^{-1}$; with four reaction rate constants $-k_o$ from 10^{-1} to 10^2 ; (a) Wall Temperature; (b) Wall concentration (c) Bulk temperature at the outlet (d) Bulk concentration at the outlet

Figure 6-5 presents concentration and temperature contour plots at the gas phase for two levels of activation energy. Mass flow rate and reaction rate constant are fixed at 0.1 g min^{-1} and 10^2 s^{-1} respectively. Contour plot is adjusted for comparison purposes by fixing range temperature, from 770 to 773 K. Temperature contours reflect that diminishing the activation energy accelerates variations in temperature. Actually, this is an expected result because a lower value of activation energy implies that the reaction presents a lower energy barrier; which causes an increment on the reaction rate at equal temperature conditions. This is contributes to augment the concentration gradients, since reactant consumption is proportional to the reaction rate.

Figure 6-6 presents dimensionless groups Nu , Sh , and Da as function of axial coordinate, at three levels of mass flow rate from 0.01 to 1.00 g min^{-1} . Reaction rate constant is fixed at 10 s^{-1} and activation energy is 97 kJ mol^{-1} . Both Nu and Sh numbers present two main regions as function of axial length, similar to the wall temperature and concentration profiles observed on figures 6-4a and 6-4b. First region, near the inlet, where exists a marked declining of dimensionless numbers. Second, next to the outlet, where temperature and concentration is almost constant and the dimensionless groups also tend to the asymptotic values. In this zone, Nu and Sh are stabilized around 6.7 and 19.3 respectively; which compare with results for similar problems found in literature (Tronconi et al. 2005; Donsi et al. 2006).

On the other hand, Da is approximately $5.0 \cdot 10^{-3}$. Small values of Da indicate that, under these conditions, CWR system is controlled by the reaction rate (kinetic time is higher than convective time). This circumstance takes place independently of the mass flow rate.

Figure 6-6 indicates that as high is the mass flow rate (equivalent to the Re number), the dimensionless groups tends to be shift; i.e. they will be significantly higher in the overall axial direction. Actually, Sh and Nu at 1.0 g min^{-1} are far from the asymptotic value at the reactor outlet by factors around 1.8 and 2.6 respectively. At higher gas velocities the resistance to axial diffusion increase and it is demanded major heat and mass fluxes to sustain the reaction rate.

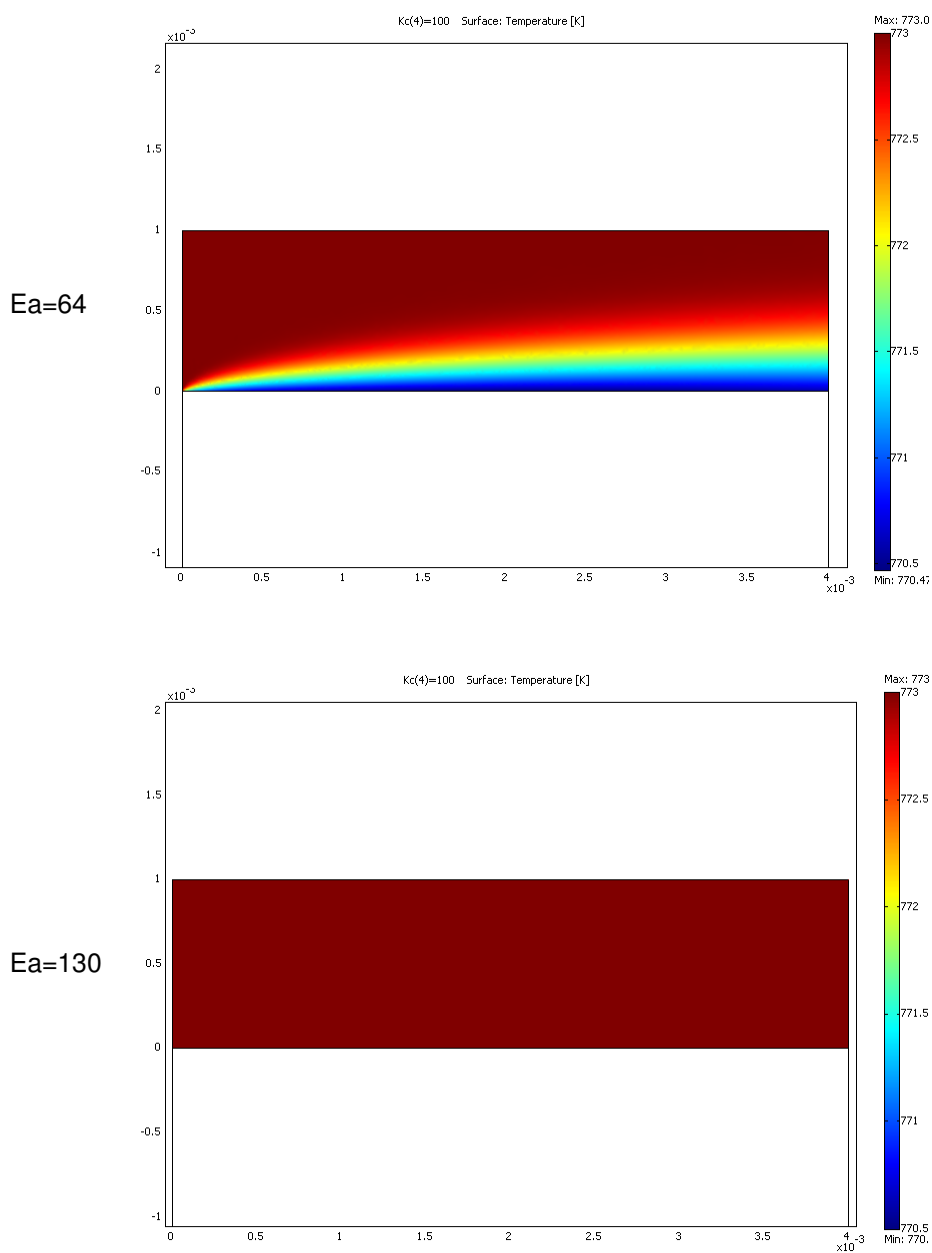


Figure 6-5 Contour plot for the gas phase temperature and concentration under two different levels of activation energy. Other models parameters are: $ko=10^2$ and $m=0.01$ g/min. Temperature range covers from 770 to 773 K

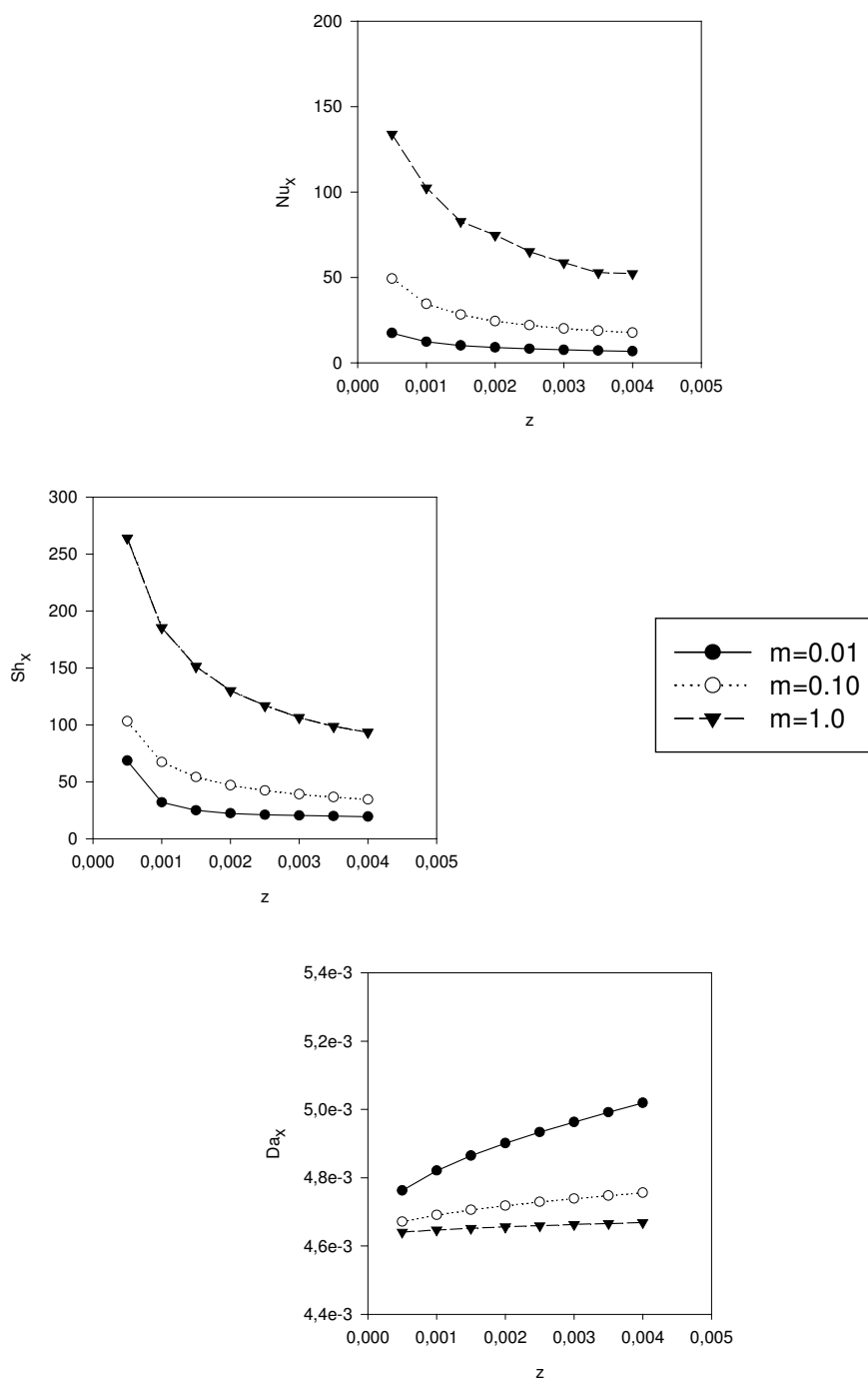


Figure 6-6 Dimensionless groups Nu , Sh , and Da as function of axial length for three levels of the mass flow rate, from 0.01 to 1.00 g min⁻¹. Reaction rate constant is fixed at 10 s⁻¹ while activation energy is 97 kJ mol⁻¹.

In summary, gas phase results shows that the CWR performance is affected by mass flow rate and kinetic parameters. The catalytic channel could be divided into two zones, which are characterized by the development of momentum, heat and mass boundary layers. In the first zone, radial gradients are influenced by the entrance effects; while in the second the reaction rate is the principal element that affects radial gradients.

6-1-3 Solid Block Results

This section analyzes the heat transfer by conduction inside the solid block. It is considered that the reaction rate on the catalytic plate is hold on the upper boundary ($y=0$); maintaining the concentration and temperature conditions described previously. On the other hand, the temperature on the lower boundary ($y=H$) is set to 793 K as result of the action of an external control system that tries to satisfy the energy requirements for maintaining the reaction. At last, the lateral walls are considered adiabatic.

Figure 6-7 presents the temperature contour inside the steel block at the reactor outlet; considering two levels of mass flow rate, from 0.1 g min^{-1} to 1.0 g min^{-1} . The main mechanism for describing heat transfer is conduction through a solid. In the two cases, contour plot indicates that heat demand is uniform through the reactor length. Actually, this reflects that there is an adequate covering of the energy demand; which means that CWR channel and block can be considered proper to work under isothermal regime.

Figure 6-8 presents the temperature profile at $z=L$ inside the steel block at the reactor outlet using four levels of reaction rate constant describing reaction in the catalytic surface. Comparing results in figure 6-4 and 6-8 illustrate the thermal gradients caused by extend of the reaction rate. For instance, at the catalytic wall ($y=0$) the maximum temperature gradient on the block (figure 6-8) is around $5 \text{ }^\circ\text{C}$ that corresponds to reaction rate constant 10^2 s^{-1} . Others cases resulted in lower temperature gradients. Temperature profile is linear inside the block, indicating that heat transport by conduction is as fast as heat demand by the reaction rate.

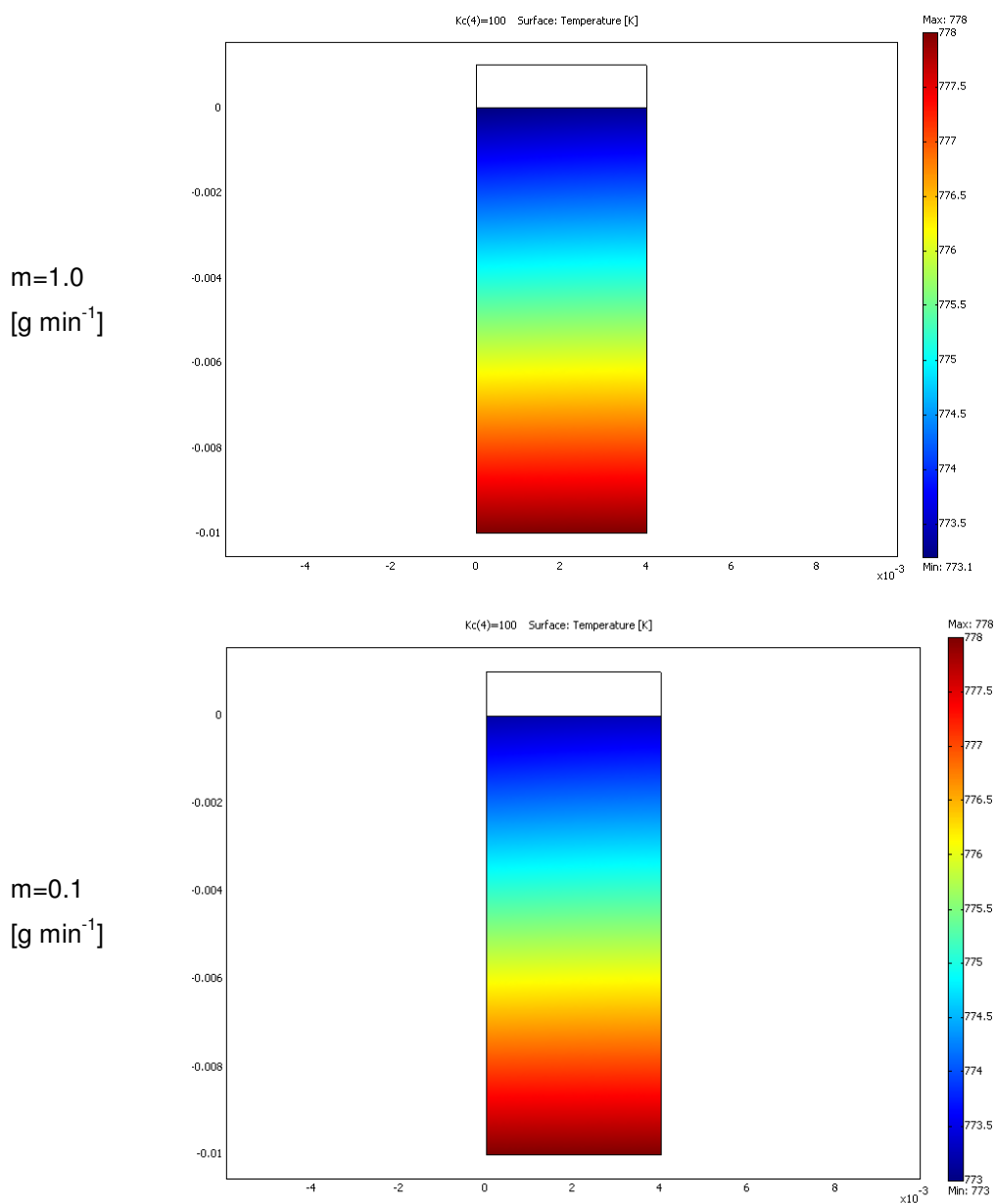


Figure 6-7 Contour plot for block temperature under two different levels mass flow rate. Other models parameters are: $Ea=97 \text{ kJ mol}^{-1}$ and $k_0=10^2 \text{ s}^{-1}$. Temperature range covers from 773 to 778 K. Boundary conditions are set as: 778 K at lower wall (5 °C higher than T_0) and heat required to maintain reaction rate at catalytic wall.

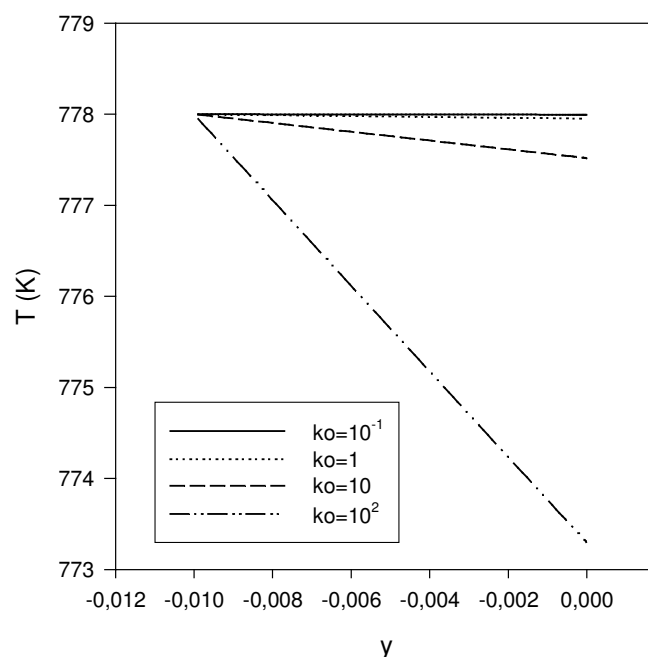


Figure 6-8 Temperature profile at $z=L$ inside the steel block, considering three levels of the reaction rate constant from 10^{-1} to 10^2 s^{-1} , mass flow rate at 0.10 g min^{-1} while the activation energy is 97 kJ mol^{-1} . Boundary conditions are set as: 778 K at lower wall ($5 \text{ }^\circ\text{C}$ higher than T_0) and heat required to maintain reaction rate at catalytic wall.

In conclusion, resistance by heat conduction through steel block can be considered simple than the resistance between the gas phase and the catalytic wall. Only if the CWR system is operated under extreme mass flow rate the temperature gradient across solid block should be considered carefully. Conceptual model of the CWR unit has shown that operational regime can be considered isothermal in the gas channel, while the steel block allows an adequate transmission of the required heat.

6-2 Supported Catalyst Preparation

Characterization of catalytic coatings over metallic plates is centered basically in the washcoating for Ni/La₂O₃- γ -Al₂O₃ because it offers multiple options for process optimization compared with deposit by precipitation of Co/ZnO. Figure 6-9 presents a triangular diagram describing slurry composition in terms of binder, acid, and bohemite content. The objective is to screen possible effects on the coating deposition method as function of slurry properties. Binders that gave better results were Poli-Vinyl Alcohol (PVA) and Triton. Poli-Ethylene Imine (PEI) was discarded because is not easy to handle it for obtaining repetitive solutions due to it high viscosity. Water is the solvent employed in all experiments; maintaining the water to alumina ratio around 3.3 g_{H₂O} g_{Al₂O₃}⁻¹.

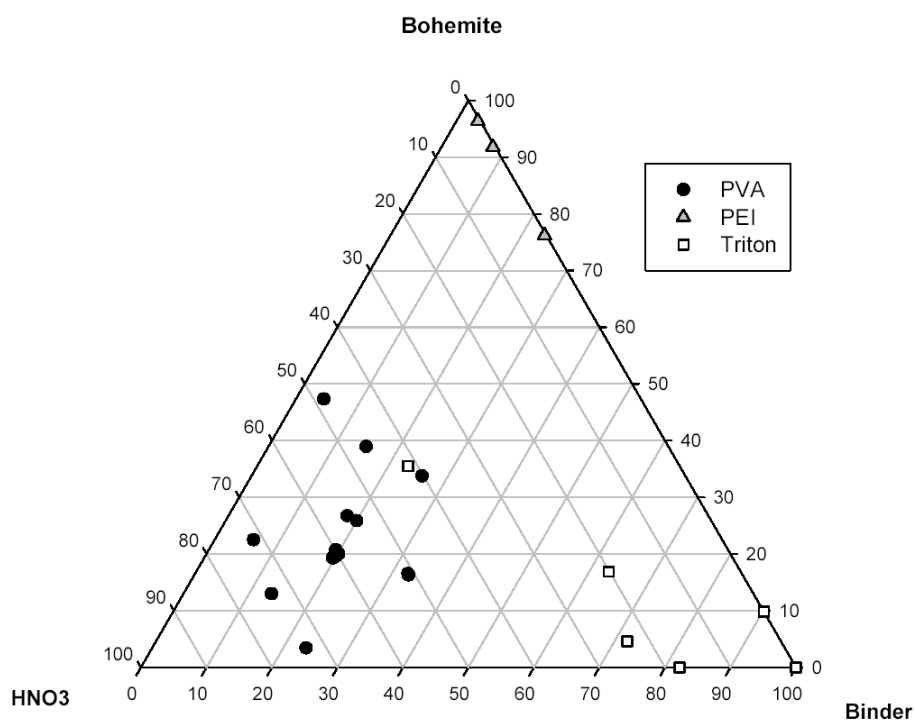


Figure 6-9 Recipes screen for preparing the slurry to impregnate the Ni based catalyst over FeCrAl plates. Ternary (triangular) diagram represents the slurry composition; based on the three main components: acid, binder, and bohemite.

After several preliminary tests, it was found that adding bohemite (dispersed in 10% aqueous sol) helps to maintain the slurry viscosity in the appropriate range to perform the washcoat. Major attempts were focused on the PVA binder, but Triton gave similar results. Figure 6-10 shows ESEM images for first series of coated plates, prepared from two kinds of slurry with extreme variations for three main slurry components: acid from 2.38 to 4.05 mol $\text{mol}_{\text{Al}_2\text{O}_3}^{-1}$; bohemite from 0.03 to 0.13 g $\text{g}_{\text{Al}_2\text{O}_3}^{-1}$; and PVA binder from 0.6 to 2.0 g $\text{g}_{\text{Al}_2\text{O}_3}^{-1}$.

ESEM images on figure 6-10 maintain focus at the center of the coating, while the metallic plate is horizontal positioned just below the coat. From figure 6-10 is observed that coat layer obtained with slurry 421 has a more uniform thickness compare with coat from slurry 428. In consequence, this slurry composition was selected as reference point to carry on the optimization process.

Second series of coated plates consists in evaluate sensibility to bohemite sol and binder content, maintaining fixed the acid content. It was try to reduce PVA mass fraction used on slurry 421 by increasing bohemite content to maintain slurry viscosity. Then, PVA binder was in the range from 0.05 to 0.20 g $\text{g}_{\text{Al}_2\text{O}_3}^{-1}$; and bohemite from 0.1 to 6.0 g $\text{g}_{\text{Al}_2\text{O}_3}^{-1}$. ESEM images for second series of coating are shown on figure 6-11. It is important to remark that in this kind of images the focus is maintained at the center of the coating, the metallic plate is horizontal and just below the coat, and the image region which is unfocused belongs to coating at other planes, behind of the focused sector.

At first sight, images on figure 6-11 seem to be similar in terms of coating density and morphology. Related to coat thickness, PVA content appears to be a determinant variable because images with higher PVA levels (solutions 434, 421, and 432) gives greater thickness than the other. The other variable screened, bohemite content, does not perform significant variations on coating thickness under these conditions.

On the other hand, figure 6-12 presents additional ESEM images, but from a horizontal perspective in relation to the catalytic coating; using two magnification factors and two electron detector types.

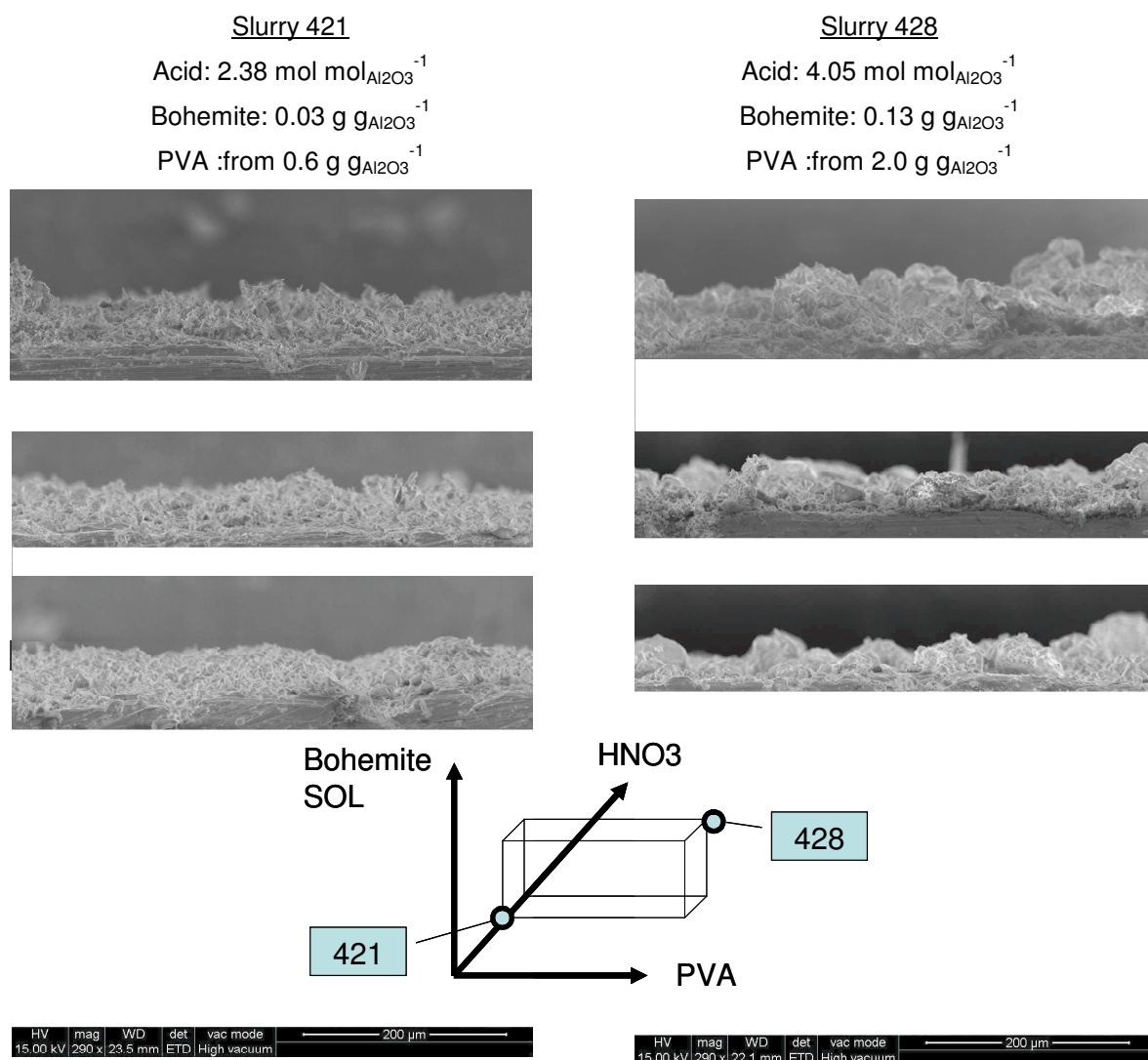


Figure 6-10 Environmental Scanning Electron Microscopy images from lateral perspective of first series of catalytic plates prepared with extreme variation in the slurry compound: acid from 2.38 to 4.05 mol mol_{Al₂O₃}⁻¹; bohemite from 0.03 to 0.13 g g_{Al₂O₃}⁻¹; and PVA from 0.6 to 2.0 g g_{Al₂O₃}⁻¹. Magnification and length scale are the same for every image. Images maintain: focus at the center of the coating, horizontal position, metal at bottom, and coating on top. Image region which is unfocused belongs to coating at other planes, behind of the focused sector.

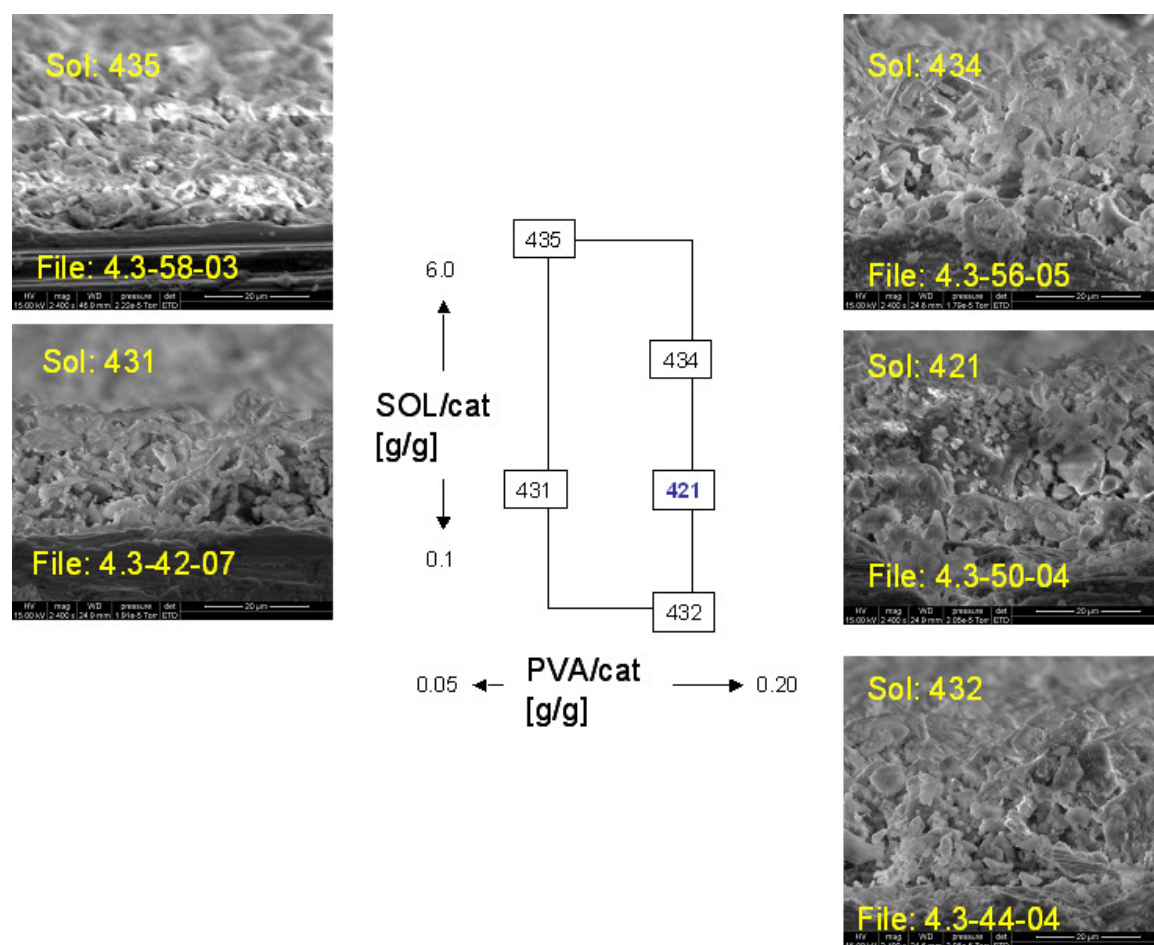
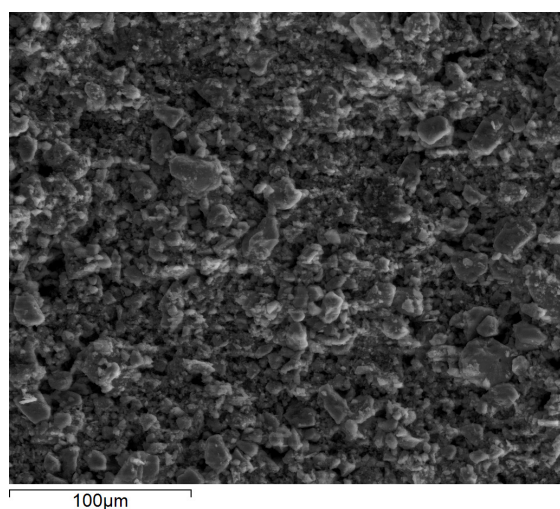
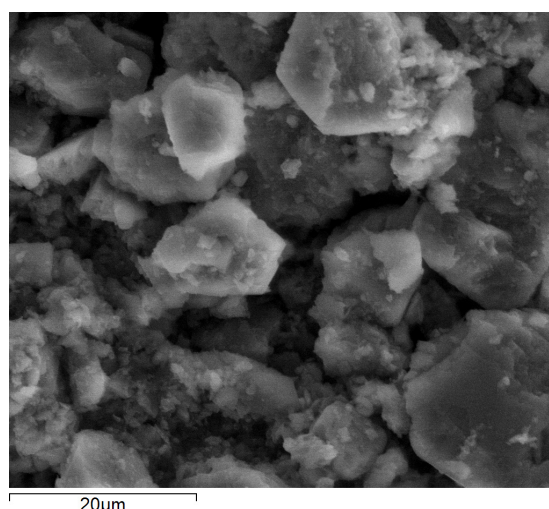


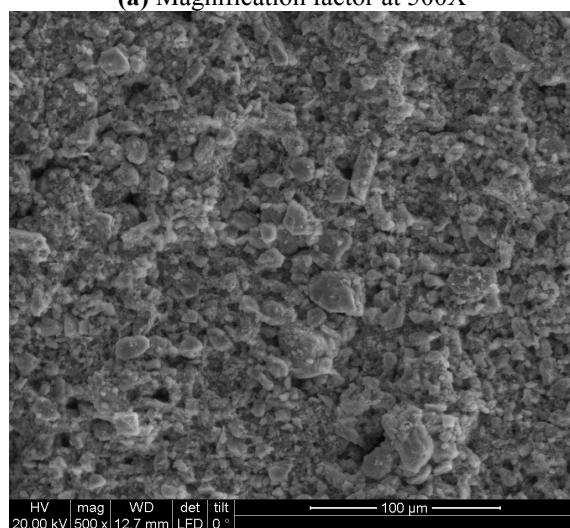
Figure 6-11 Environmental Scanning Electron Microscopy images from lateral perspective of Ni/La₂O₃- γ Al₂O₃ for second series of catalytic plates prepared with slurries with following composition: acid 2.38 mol mol_{Al₂O₃}⁻¹; bohemite from 0.1 to 6.0 g g_{Al₂O₃}⁻¹; and PVA from 0.05 to 0.20 g g_{Al₂O₃}⁻¹. Magnification and length scale are the same for every image. Images maintain: focus at the center of the coating, horizontal position, metal at bottom, and coating on top. Image region which is unfocused belongs to coating at other planes, behind of the focused sector.



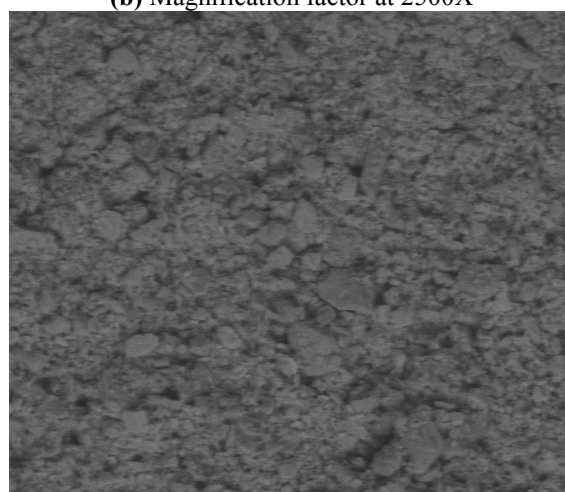
(a) Magnification factor at 500X



(b) Magnification factor at 2500X



(c) Electron scattering detector



(d) Back Scattering detector

Figure 6-12 Environmental Scanning Electron Microscopy images from Ni/La₂O₃- γ Al₂O₃ catalytic coating on metallic plates. It is employed a horizontal perspective at different magnification factors and using two kinds of electron detectors.

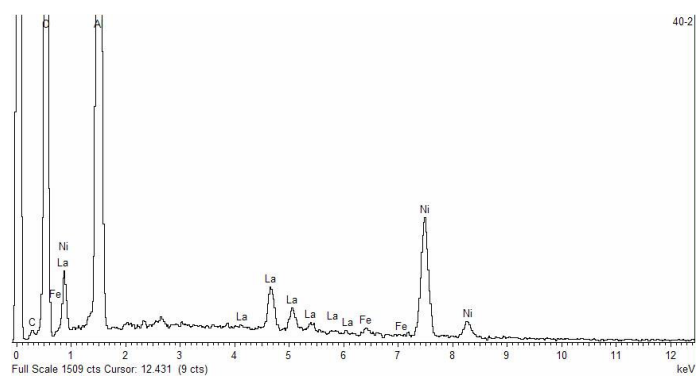
All images on figure 6-12 were made after calcinations of catalytic coat, and show a homogeneous distribution of the catalytic particles, which seems similar to powder catalyst images on figure 5-3.

Figure 6-13 shows EDS spectra and XRD pattern for Ni/La₂O₃-γAl₂O₃ catalytic plates. Plate coating composition by EDS gave similar result compared to powder catalyst chemical composition analyses; presented previously on table 5-2 and and figure 5-3. Also XRD analysis for plates catalysts resulted similar to related XRD pattern for powder catalyst on figure 5-4.

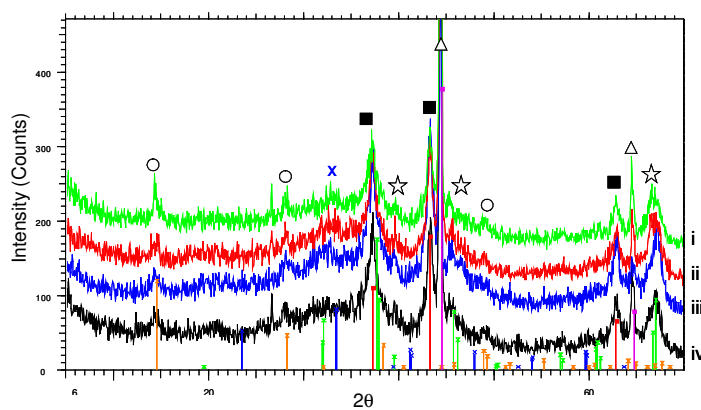
Table 6-3 presents thickness, morphological and compositional results obtained for Ni/La₂O₃-γAl₂O₃ catalytic coatings. Thickness and morphological measurements were made using IFME^(c) software, while compositional results corresponds to EDS analysis, such as spectra show on figure 6-13. Principal parameters are: average thickness around 30μm; and mean void size, near 1 μm.

Table 6-3 Thickness, Coating Parameters (from IFME) and EDS results

	Mass to Area ratio [g mm ⁻²]	Thickness [μm]	Assimetry, %	Regularity	Mean Void size, [μm]]	%Ni	%La
Mean							
Value	0.0241	32.1	10.2	0.002	1.017	13.5	5.8
Standard							
Deviation	0.0051	6.5	2.1	0.001	0.103	0.5	0.2



(a) EDS spectra



(b) XRD pattern

Figure 6-13 EDS and X-ray diffraction spectra for Ni/La₂O₃- γ -Al₂O₃ catalyst coating before reduction: (■) Nickel Oxide, NiO; (☆) aluminum oxide γ -Al₂O₃; (X) Lanthanum Aluminum Oxide, LaAlO₃; (○) bohemite, and (△) Iron chromium Fe-Cr

Figure 6-14 shown vibration tests to evaluate coating adhesion to metallic support. In all cases the total weight loss were around 0.1 % for a total catalyst coating around 100 mg. These results coincide with catalyst losses under chemical reaction performed during an average time of 10 hours; which presented insignificant catalyst losses for both Co and Ni plates, lower than 1% for catalysts coating around 100 mg.

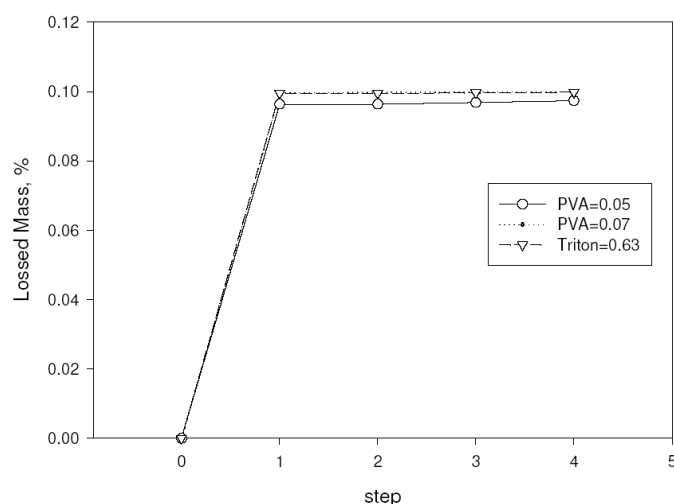


Figure 6-14 Vibration test using 30 min steps, frequency from 20 to 50 Hz; acceleration from 2G to 10 G and velocity from 67 to 350 mms^{-1} . The coating was made from slurries with PVA and Triton, in the same way than plates used for the catalytic tests.

In summary, characterization of supported coating on metallic plates has shown that Ni/La₂O₃- γ Al₂O₃ coat by impregnation method resulted in catalyst with chemical composition similar to the original powder catalyst. In addition, coat presents a homogeneous distribution in horizontal and lateral directions; with an average thickness between 30-40 μm . Results obtained with adherence tests by vibration mechanism predicted that coats were well adhered to the metallic surface; which later was demonstrated to be in concordance with experimental observation under real chemical reaction performance. Deposition by washcoating has proven to be an adequate method to produce catalytic plates to be tested on structured CWR.

6-3 Catalytic Wall Reactor Experiments

This section presents experimental results for SRE, SRM and WGS reactions using metallic plates coated with Ni and Co catalysts, into a structured CWR. Operational conditions were similar to those employed for SRE experiments with PBR configuration, being the case base temperature around 500°C and SC at 4. For the reactions SRM and WGS, the SC is increased from 10 to 45. Table 6-4 shows the overall set of operational condition for evaluating catalytic plates performance under the three reactions studied.

Changes in chemical reaction are analyzed from a qualitative perspective; in concrete, by measuring the variation in composition using MS intensity signal at four compounds: C₂H₆O, H₂, CO, and CH₄. The signals for CO₂, C₂H₄O, and H₂O (presented on Apendix B) are not take into account for this analysis because are sensitive to signal fluctuations caused by the evaporation system. The signals for the rest of products (C₂H₄, C₂H₆, CO₂, and C₂H₄O) present even higher uncertainty; so it composition should be measured with other instruments to get quantitative information, such as selectivity and yield.

Table 6-4 Operational conditions for evaluating Ni and Co catalytic plates for Steam Reforming of Ethanol, Steam Reforming of Methane, and Water Gas Shift

Catalyst	Temperature [°C]	Reaction	SC	Catalyst [mg]
Ni/La ₂ O ₃ -γ Al ₂ O ₃	450	SRE	4	100
	480	SRE	4	100
	480	SRM	from 10 to 45	100
	480	WGS	from 10 to 45	100
CoFe/ZnO	480	SRE	4	80 and 110
	480	SRM	10	100
	480	WGS	10	100

For the purpose of the present work, it is considered that the MS intensity signal of C_2H_6O , H_2 , CO , and CH_4 allows the study of the reaction activity; while selectivity and yield should be similar to that obtained with the PBR experiments.

6-3-1 Steam Reforming of Ethanol

First, on the figure 6-15 is explored temperature effects on SRE performance using catalytic plates with $Ni/La_2O_3-\gamma Al_2O_3$ catalyst. Activity is evaluated through C_2H_6O , CO and H_2 intensity signals as function of the time on stream, while operational conditions are fixed at 100 mg catalyst, mass flow rate 1 ml h^{-1} , SC at 4, and set point temperature at $450^\circ C$ and $480^\circ C$ respectively. It is presented a reference line at times lower than zero, to illustrate the signal variation between feed and products streams.

Figure 6-15 indicates that changes in temperature affect the Ni catalyst performance; because when temperature is augmented from 450 to $480^\circ C$ is obtained an increase on average conversion from 0.50 to 0.99. Also, the C_2H_6O and H_2 signals show a marked decline tendency, indicating the catalyst deactivation which may be caused by carbon deposition, as occurred in the PBR experiments. This declination is higher at $450^\circ C$ (figure 6-15b) where the reaction thermodynamic and kinetic mechanism favor decomposition reactions, such equations from (2-19) to (2-28) rather than reforming reactions, like equations from (2-29) to eq(2-39). Note that the signal fluctuations are consequence of small pressure variations due to the system for evaporating the liquid phase.

Figure 6-16 presents the performance for plates coated with $CoFe/ZnO$ catalyst, under similar conditions where is obtained a complete conversion using Ni plate (SC at 4, temperature at $480^\circ C$, and mass flow rate at 1 ml h^{-1}), but exploring effects on catalyst mass weight, from 80 mg to 110 mg. Again, the activity is evaluated through C_2H_6O , CO and H_2 intensity signals as function of the time on stream. The average conversion for Co plates is 0.32 using 80 mg and reaches 0.38 with 110 mg. It is expected that Co catalyst should produce a minor ethanol conversion because catalyze selectively the dehydrogenation reaction pathway eq(2-19), contrary to Ni catalyst that catalyze also the dehydration path, eq(2-20).

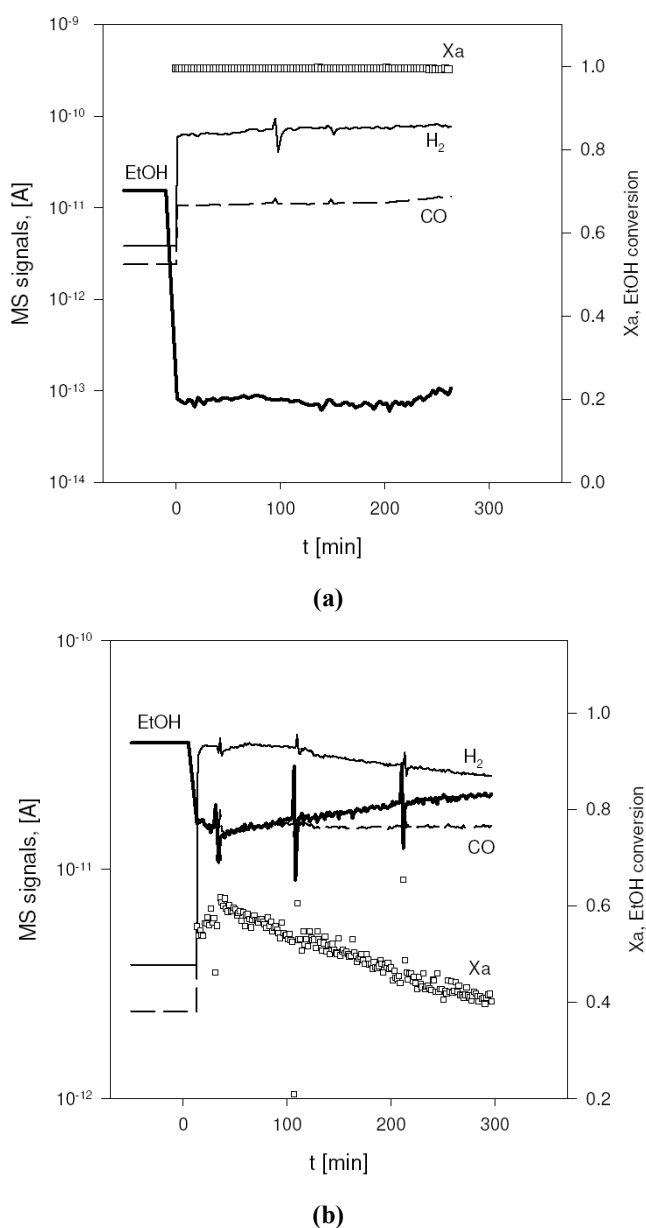
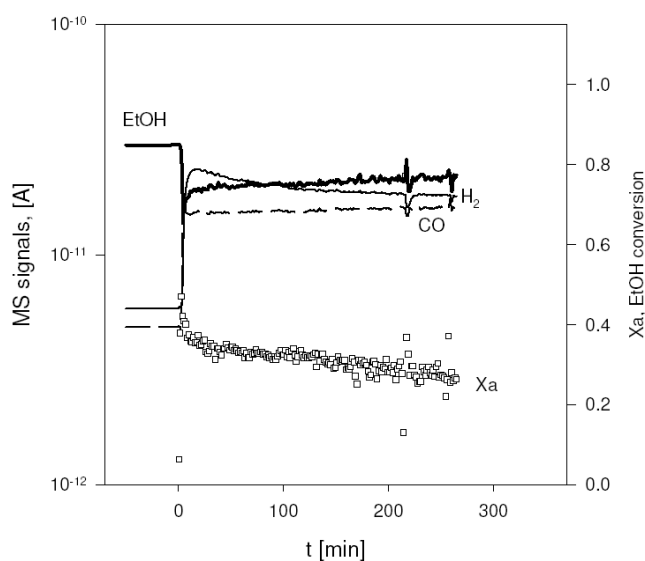
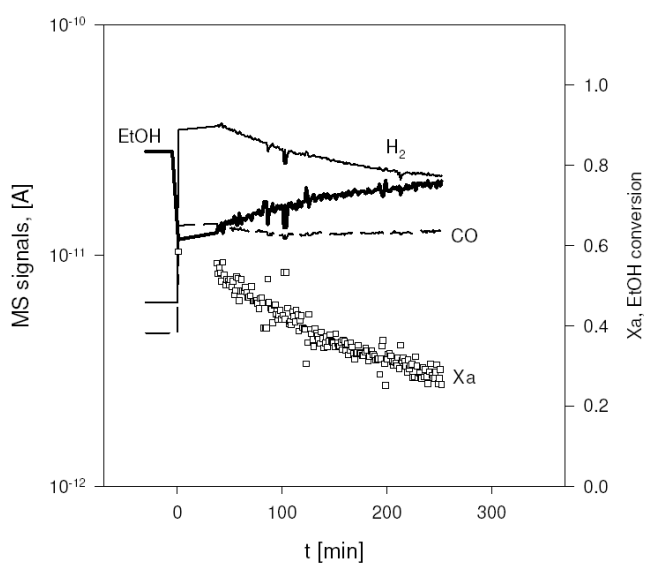


Figure 6-15 Steam Reforming of Ethanol through Ni catalyst supported on metallic plates, using operational conditions 100 mg catalyst, SC=4, $m=1\text{ml h}^{-1}$. (a) average conversion 0.99, temperature 480°C; (b) average conversion 0.50, temperature 450°C. It is presented a reference line at times lower than zero, to illustrate the signal variation for each component between feed and products streams.



(a)



(b)

Figure 6-16 Steam Reforming of Ethanol through Co catalyst supported on metallic plates, using operational conditions temperature 480°C, SC=4, $m=1\text{ml h}^{-1}$. (a) 80 mg catalyst, average conversion 0.32; (b) 110 mg catalyst, average conversion 0.38. It is presented a reference line at times lower than zero, to illustrate the signal variation for each component between feed and products streams.

Comparing the ethanol signals on figures 6-15 and 6-16, Co plate presents a lower level of ethanol conversion in relation to Ni plate; however the ethanol signal for Co seems to be more stable at higher reaction times than Ni case. Also the H₂ signal present different tendencies, while Co plate (figure 6-16) approaches to a stable level after 200 min, the Ni catalyst (figure 6-15) maintains variations under the studied range.

The differences on activity between Ni and Co catalysts could be linked with the preferential reaction paths, observed previously in the PBR experiments. The Co presents a higher selectivity to ethanol dehydrogenation; then is reduced the presence of intermediates that leads to carbon deposition, such as C₂H₄.

Figure 6-17 presents temperature at different axial positions as function of the time on stream in the case of SRE using Ni catalyst. Block temperature was fixed at 478°C, and catalyst weight at 100 mg. It was obtained complete ethanol conversion; which means that heat demand was the highest possible under these conditions. The temperature gradient in the axial direction is around 1.7°C for a reactor length of 5cm; which means 0.34 °C cm⁻¹ approximately.

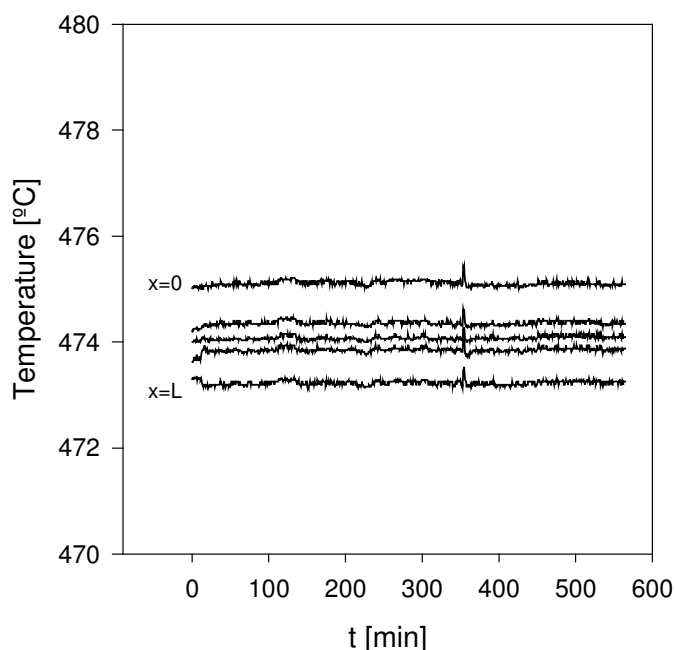


Figure 6-17 Temperature at different axial positions for the Steam Reforming of Ethanol Ni at ethanol conversion $X_a=0.99$, using operational conditions: temperature 478°C, SC from 4, and 100 mg catalyst

It is important to note that the catalytic plate is located near the lateral walls on the steel block, as shown figure 3-6. Although these walls are covered with an insulator material, possibly exists heat losses near the borders. In consequence, the temperature gradient observed in the axial direction might be originated by those heat losses on the lateral block walls. An alternative way to reduce the heat losses is positioning the catalytic plate at the center of the block, but this imply to construct another reactor device. On the other hand, figure 6-17 shows that the CWR presents a stable temperature during almost 10 h operation; which demonstrates the possibilities of CWR configuration for performing catalytic reactions under appropriated thermal control. This experimental result and the 2D simulation prediction; showed that the metallic plate is an ideal structured system that permit the necessary thermal transport for sustaining SRE energy requirements.

6-3-2 Steam Reforming of Methane and Water Gas Shift

Figure 6-18 presents SRM and WGS reactions performed with Co and Ni plates; under following operational conditions: temperature at 480°C, SC at 10, and catalyst weight from 100 mg (Ni) to 110 mg (Co). Other SC ratios were performed, such as 30 and 45, but it was not possible to detect significant variations on the reaction performance.

Figure 6-18 points out that the Co plate presents a relative high CO conversion for the WGS reaction, with an average value stabilized around 0.35; while for the Ni plate the average CO conversion is approximately 0.10. Comparing the H₂ and CO signals for the WGS reactions on the two catalysts, Co seems to produce a more stable tendency than Ni after 40 min of reaction. On the other hand, for the SRM reaction both Ni and Co catalyst present similar average CH₄ conversion, around 0.10; although CH₄ and H₂ signals seems to be more stable for the Ni catalyst. The low conversion degree observed experimentally on the SRM coincides with the thermodynamic simulation; that predicts unfavorable CH₄ reforming at this condition of temperature. At last, comparing experimental results for WGS and SRM could be concluded that under these conditions, WGS is catalyzed better than SRM.

In conclusion, CWR experiments shown that both Ni and Co plates are active for the SRE reaction and selective to H₂ production. CWR has proved to be an efficient reactor configuration to maintain a stable thermal performance. Finally, catalytic plates prepared by impregnation and precipitation has proven to be sufficiently well adhered to perform the three catalytic reactions: SRE, SRM, and WGS.

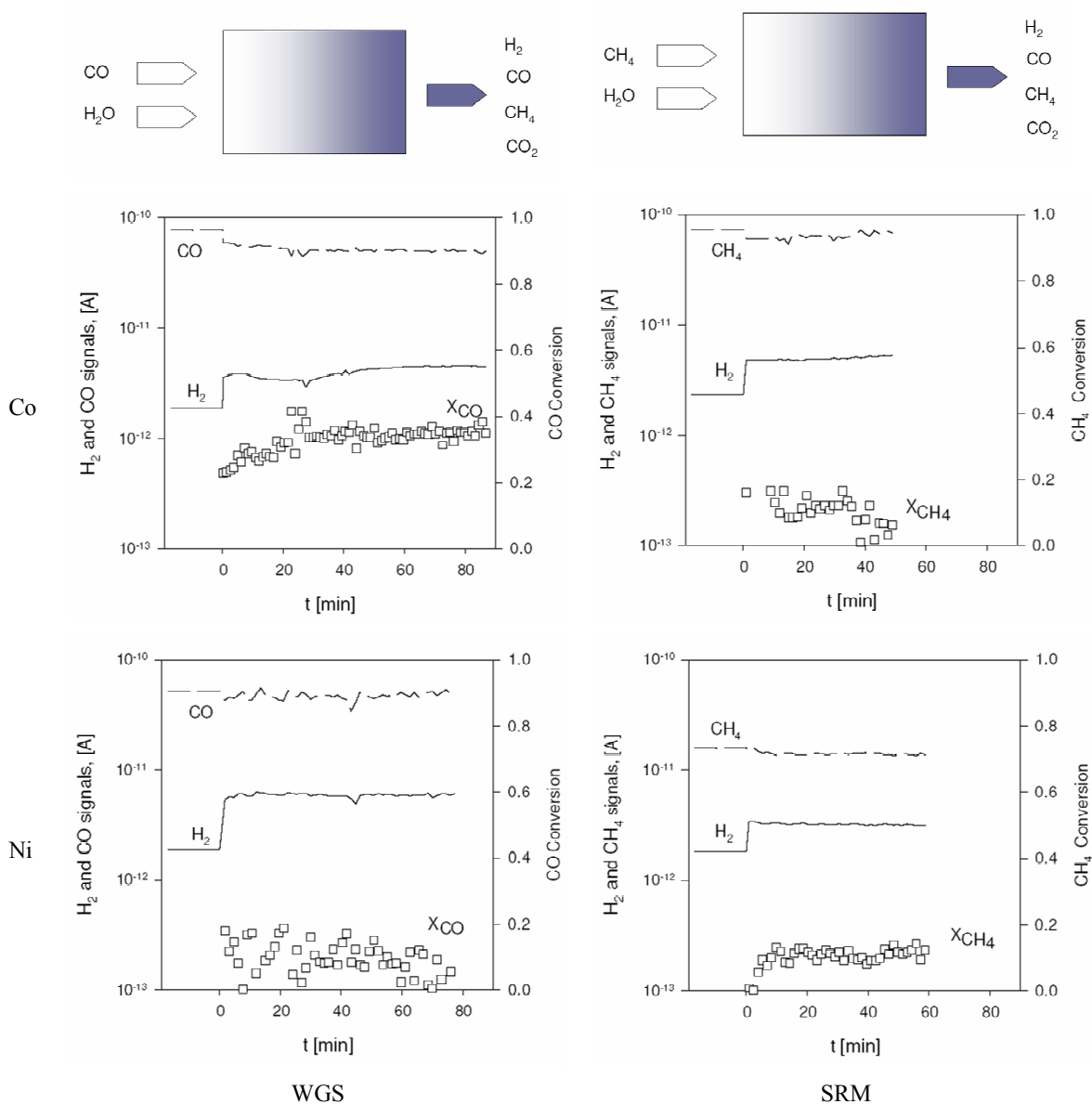


Figure 6-18 Steam Reforming of Methane and Water Gas Shift with Ni and Co catalyst supported on metallic plates, using se operational conditions: temperature 480°C, SC at 10, and catalyst weight from 100 mg (Ni) to 110 mg (Co)

6-4 Simulation of Catalytic Wall Reactor in 1D

CWR can be modeled through a conceptual 1D model for exploring thermal behavior, in particular, the dynamic between heat generation and heat consumption. Figure 6-19 illustrates the configuration selected for studying the system sensitivity to operational conditions and kinetic parameters.

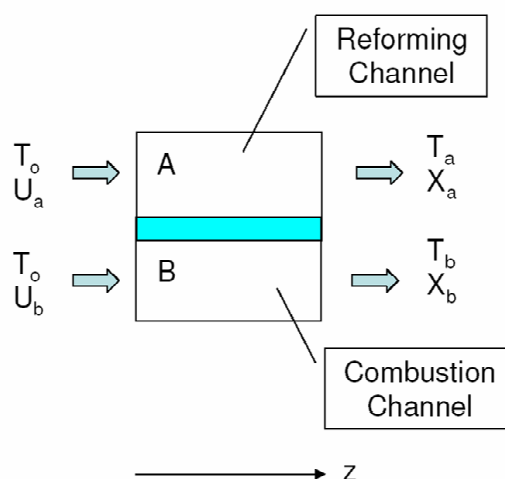


Figure 6-19 CWR conceptual model for coupling exothermic and endothermic reactions, such as SR (channel A) with combustion (channel B). Co-current flow is considered to simplify as much as possible the sensitivity analysis.

1D model is employed for describing an adiabatic CWR system, similar to used by Zanfır, (Zanfır and Gariilidis, 2002); which is shown on figure 6-19. The 1D model is based on following assumptions: no radial gradients exist in fluid and solid phases, kinetics are first-order, properties of fluid and solid phases are constant, and channels of same height. The differential 1D mass and energy equations, with respective boundary conditions, can be described as follows,

$$u_{z,j} \cdot \frac{dx_j}{dz} = k_j \exp\left(\frac{E_j}{RT}\right) (1 - x_j) \quad (6-6a)$$

$$\left(u_z \cdot \rho \cdot c_p\right)_j \frac{dT}{dz} = \left(-\Delta H_j\right) \cdot k_j \cdot \exp\left(\frac{E_j}{RT}\right) \cdot C_{j0} \cdot (1 - x_j) \quad (6-6b)$$

$$T = T_o, \quad x_a = 0, \quad x_b = 0, \quad \text{at } z = 0 \quad (6-6c)$$

where the variables are: exothermic reaction conversion (x_B), endothermic reaction conversion (x_A), and absolute temperature (T). Thermal gradients between endothermic and exothermic channel is neglected. Constant parameters are: activation energy (E), pre-exponential factor of linear kinetic (k), heat of reaction (ΔH), gas constant (R), specific heat (c_p), initial concentration (C_0), channel height (h), and axial velocity (u_z). The index j refers to endothermic or exothermic reaction. Defining some dimensionless groups and simplifying terms, the set of eq (6-6) can be arranged as,

$$\frac{dx_a}{dx_b} = \frac{K}{V} \exp\left(\frac{\gamma}{\theta}\right) \left(\frac{1-x_a}{1-x_b}\right) \quad (6-6d)$$

$$\frac{d\theta}{dx_b} = B_b + B_b \cdot V \cdot \frac{dx_a}{dx_b} \quad (6-6e)$$

$$\theta = 1, \quad x_a = 0, \quad \text{at} \quad x_b = 0 \quad (6-6f)$$

where the dependent variable is x_B , and independent variables are x_A , and θ (dimensionless temperature). Dimensionless factors and variables are expressed as,

$$\text{Dimensionless temperature} \quad \theta = \frac{T}{T_0} \quad (6-7a)$$

$$\text{Ratio of pre-exponential factors} \quad K = \frac{k_a}{k_b} \quad (6-7a)$$

$$\text{Ratio of inlet velocities} \quad V = \frac{u_a}{u_b} \quad (6-7b)$$

$$\text{Dimensionless difference of activation energies} \quad \gamma = \frac{E_a - E_b}{RT_0} \quad (6-7c)$$

$$\text{Heat effect numbers} \quad B_j = \frac{(-\Delta H)_j C_{j0}}{(\rho_a \cdot cp_a \cdot V + \rho_b \cdot cp_b) T_0} \quad (6-7d)$$

Actually, set of equations (6-6) is an Ordinary Differential Equation (ODE) that can be solved using Runge-Kutta numerical methods. Also, as the temperature can be forward integrate from eq (6-6e), the final set of equations is,

$$\frac{dx_a}{dx_b} = \frac{K}{V} \exp\left(\frac{\gamma}{1 + B_a \cdot V \cdot x_a + B_b \cdot x_b}\right) \left(\frac{1-x_a}{1-x_b}\right) \quad (6-8a)$$

$$\theta = 1 + B_b \cdot x_b + B_a \cdot V \cdot x_a \quad (6-8b)$$

in this way is maintained the boundary condition as eq (6-6c). It is considered a CWR as large as necessary to achieve complete conversion of combustion reaction, x_B .

Two cases are studied for simulating catalysts with different kinetic behavior; Table 6-5 shows model parameters selected on each case; where the main difference is that kinetics for case II presents a higher exothermic reaction rate than case I. The idea is to explore CWR thermal sensitivity to differences in catalytic behavior.

Table 6-5 Kinetic and model parameters for cases I and II. CB0 to CA0 ratio was fixed at 0.773

Kinetic Parameters						
	ko [s-1]		E[kJ mol ⁻¹]		ΔH [J mol ⁻¹]	
	B	A	B	A	B	A
Case I	4.0e3	2.0e3	100	90	-8.0e5	1.7e5
Case II	2.0e5	2.0e3	130	90	-8.0e5	1.7e5

Model Parameters		
	Case I	Case II
K	0.500	0.010
γ	1.556	6.224
V	1.429	1.429
Ba	-0.214	-0.214
Bb	0.778	0.538

The parameter K corresponds to pre-exponential factors ratio, as defined by eq. (6-7a) and provides a measure for the ratio of catalyst activities (Zanfir and Gavriilidis, 2002). In general, K is proportional to the heat consumption by SR reaction; while is inversely proportional to the heat production by combustion reaction. Changes in K can be achieved by modifying the catalyst loading for either endothermic reaction or exothermic reaction; but also may be resulted from other events, such as catalyst deactivation.

Figure 6-20 shows numerical simulation results in terms of x_A and θ , as function of x_B . At incomplete conversion, independent variables (x_A and θ) present larger variations on case II; in concrete a change of x_B from 0 to 0.2 represents an increment from 0 to 0.59 for x_A . This advance of the endothermic reaction is associated with a reduction in θ from 1.0 to 0.97 because the connection between chemical rate and heat consumption. In comparison with case II, case I presents a moderate heat consumption, reflected in slight variations of x_A and θ over the same x_B range (at x_B range from 0 to 0.20, x_A varies from 0 to 0.30, while θ increases from 1 to 1.07). In summary, figure 3-11 point out that an increase on K (from case I to II) modifies the heat balance at zones with incomplete conversion levels and affects significantly the temperature profile.

Figure 6-20 also indicates that, under selected conditions, it is necessary a temperature increase around 1.47 times the initial temperature to maintain an adiabatic operation at complete x_B conversion. In fact, once conversion reaches a critical value is necessary to augment progressively θ to get an increase on x_A . For instance, case II requires a temperature augment from 0.97 to 1.47 to increase x_A from 0.59 to 1.0. Also for case I the temperature is gradually increased until final value of 1.47. This temperature increase means operating in the range from 500 to 863°C; which represents an assumable risk considering the kind of materials use to construct reactor devices, such as metallic plates. Finally, is important to remark that at complete conversions cases I and II converge to the same result because the way in which the reactor size was defined; which is the length required for consuming all the combustion feed.

There are two forward alternatives to optimize CWR performance from results observed on figure 6-20:

- Maintain x_B and x_A under the incomplete conversion regime, by separating desired products (such as hydrogen) and recycling by-product with some energetic value (such as non-converted ethanol, carbon monoxide and methane produced)
- Employ different conditions (changing parameters such as velocities ratio $-V-$, initial temperature $-T_0-$, and initial concentrations relation $-C_{A0}$ to C_{B0} ratio) or even CWR configuration.

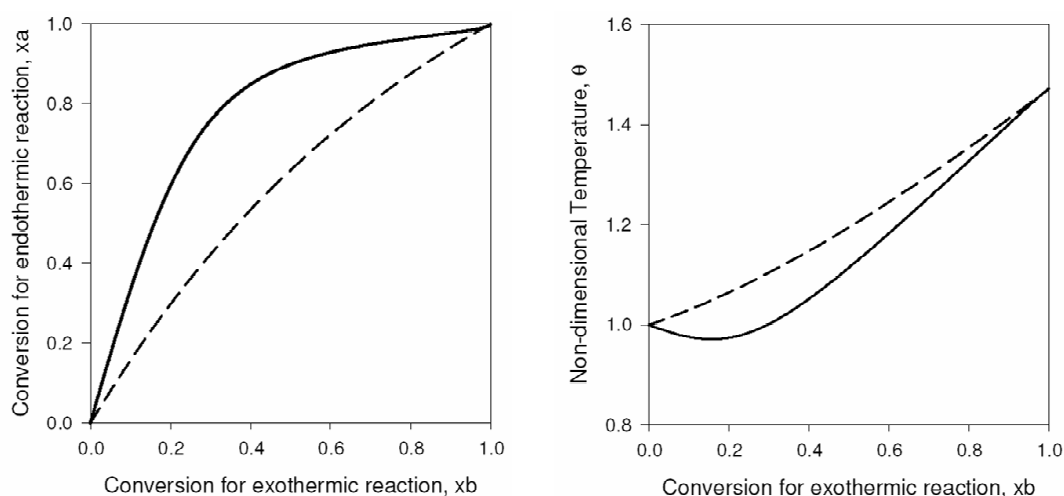


Figure 6-20 Results expressed in terms of dimensionless independent variables –conversion of the endothermic reaction (x_A) and temperature (θ)- as function of the dependent variable - conversion of the exothermic reaction (x_B)-; considering a CWR with complete combustion conversion (x_B from 0 to 1). Case base I (dashed line) and II (solid line) employ different kinetic parameters to simulate different catalytic behavior. Model parameters are shown on Table 6-5

Figure 6-21 shows a sensibility analysis -using a “one factor at a time” approach- in terms of main operational parameters: V from 5/3.5 to 10/3.5, T_0 from 773 to 723 K, and C_{A0} to C_{B0} ratio, from 1.75/1.35 to 1.75/0.94, exploration is performed around case I model. Normalized sensibility, $S(y, \phi_j)$, is calculated as (Zanfiri and Gavriilidis, 2002),

$$S(y, \phi_j) = \frac{\phi_j}{y} \frac{\Delta y}{\Delta \phi_j} \quad (6-9)$$

where ϕ_j represents the input parameter (V , T_0 , and C_{B0} to C_{A0} ratio respectively) and y is the variable under study (x_A and θ).

Figure 6-21 shows that major sensibility occurs under incomplete conversion; in particular a variation in initial temperature produces the most significant changes on x_A and θ : a reduction in T_0 leads to diminish the kinetic rate, making smaller x_A and θ . On the other side, the parameter V seems to produce a slight influence on x_A and even a lower variation on θ . The negative sign indicates that increasing V will reduce x_A and θ ; because increasing the endothermic flow rate or diminishing the exothermic velocity

leads to more heat consumed and the system temperature is reduced. Finally, the initial concentration C_{ao} presents the weakest sensitivity respect to x_A ; since only is present on the energy balance equation through B_j dimensionless group.

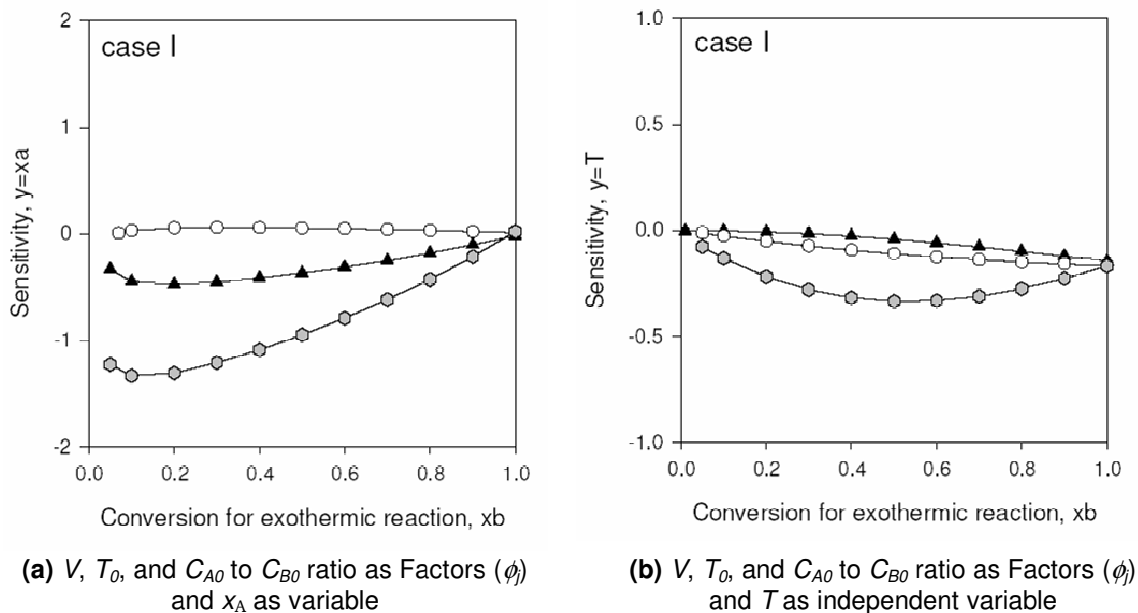


Figure 6-21 Normalized sensitivity for case I using conversion of endothermic reaction (x_A) and dimensionless temperature (θ) as variables under study; varying velocities ratio V from 5/3.5 to 10/3.5 (black triangle), T_0 from 773 to 723 K (gray circle), and C_{A0} to C_{B0} ratio from 1.75/1.35 to 1.75/0.94 (white circle)

In summary, 1D model has proven that CWR configuration with co-current endothermic and exothermic channels constitute a suitable option for SRE. The sensitivity of CWR temperature with respect to main operational variables was investigated. For this simple model, it was found that thermal performance of the system is highly sensible to initial temperature; while velocity and concentration ratios appear to affect in lower proportion. Temperature augment along the CWR suggests that is required an appropriate distribution of exothermic catalyst in the plate. Modeling improvement will require a better description of the endothermic reaction kinetic. Regardless this limitation, 1D model gives an overall perspective on the heat management possibilities using a structured reactor.

References

1. Donsi, F., A. Di Benedetto, et al. (2006) "Effect of the Re number on heat and mass transport in a catalytic monolith." *Catalysis Today* 498-505.
2. FEMLAB 3.0 User's Guide, Stockholm, Sweden: Comsol, 2004.
3. Tronconi, E., G. Groppi "A study on the thermal behavior of structured plate-type catalysts with metallic supports for gas/solid exothermic reactions." *Chemical Engineering Science* 55 6021-6036.
4. Zanfiri, M., A. Gariilidis (2001). "Modeling of a catalytic plate reactor for dehydrogenation-combustion coupling." *Chemical Engineering Science* 56 2671-2683.
5. Zanfiri, M., A. Gariilidis (2002). "Parametric sensitivity in catalytic plate reactors with first order endothermic-exothermic reactions." *Chemical Engineering Journal* 86 277-286.

Chapter 7

Conclusions and Future Work

7-1 Conclusions

Steam Reforming of Ethanol can be performed at high thermal efficiency if the design of the fuel processor is based on structured catalytic wall reactors with integrated heat recovery coupled to a separation unit for hydrogen purification. Catalytic plates have proven to be a key component on CWR because improves significantly the heat transfer which is required to sustain endothermic reactions.

7-1-1 Thermodynamic Analysis

- Thermodynamic analysis shows that at SC ratios from 3 to 5 and pressures of up to 10 bar, the temperature in the reformer should be around 550 to 750 °C to ensure auto-thermal operation of the system.
- Extensive research during the last decade provided active catalysts from Co, Ni, and Rh that show promising potential for Steam Reforming Ethanol. These candidates appear suitable for the temperature and SC ratios ranges of interest for developing auto-thermal fuel processors based on structured reactors with integrated heat recovery and hydrogen purification.
- For CWR system are required reforming catalysts with high activity and selectivity towards hydrogen instead of methane at moderate temperature. Under the conditions studied, Co-based catalysts has proven to offer a significant advantage because their lower selectivity towards methane, although a deeper study should be developed to confirm this trend.

7-1-2 Screening Catalysts Preparation and Evaluation

- Co- and Ni-based catalysts that were tested are active for the Steam Reforming of Ethanol at a moderate temperature, from 400 to 500°C, and Steam to Carbon ratios from 2 to 4.
- For Ni-based catalysts, ethanol dehydrogenation dominates at low temperature, but Steam Reforming reactions become dominant at 500°C. Upon complete conversion of ethanol and acetaldehyde, the distribution of final products approaches chemical equilibrium, which denotes that these catalysts are active for the water shift and methane steam reforming equilibrium reactions as well.
- Co-based catalysts favor ethanol dehydrogenation into acetaldehyde, which is then converted through steam reforming. The reversible shift reaction is also promoted by these catalysts and the relationship among the yields of carbon oxides approaches that of equilibrium. On the contrary, these catalysts do not promote methane-forming reactions like ethanol cracking and acetaldehyde decarbonilation, nor they facilitate the reverse methane steam reforming reaction. This results on a final product in which the ratio between hydrogen and methane selectivity is well above equilibrium. The catalytic behavior of cobalt is enhanced by promotion with iron or manganese through the formation of bimetallic particles, which facilitates cobalt reducibility. This suggests that Co-Mn/ZnO and Co-Fe/ZnO catalysts have a good potential for their use in fuel processors for ethanol reforming that operate at moderate temperature.

7-1-3 Catalytic Plates Preparation, Evaluation, and Catalytic Wall Reactor Simulation

- Well adhered Ni and Co catalytic coatings on FeCrAl plates were obtained by impregnation and precipitation methods. Concentrations of the slurry key components (PVA binder and bohemite solution) were optimized to produce a homogeneous and stable coating.

- A CWR configuration has been designed, developed and tested to evaluate plate performance under high endothermic reactions. Catalytic tests have proven that Co and Ni based catalytic plates are active and stable for SRE.
- Numerical simulation has shown that the constructed CWR maintains a thermal performance adequate for evaluating catalytic plates under uniform temperature profile. Significant reduction in temperature gradients is achieved to compare CWR with PBR configurations. On the other hand, 1D model showed significant aspects on CWR thermal balance using two co-current channels with endothermic and exothermic reactions.

7-2 Future Work

This work has shown that technically is possible to produce hydrogen using catalytic plates into a CWR configuration. However, a complete development of reliable and economic viable fuel processor for Fuel Cell applications still requires the study of several important points. Among multiple recommendations, future line research should be focus on three main priorities: (i) obtain a reliable kinetic for the endothermic SRE reaction to improve numerical predictions and process control that will allow to find the optimal catalyst distribution on plates, (ii) develop a separation module to implement chemical reaction coupled with H₂ separation unit, and (iii) perform stability tests for estimating system stability under real working conditions.

It is important to remark the importance of basic research to gain significant advances in practical situations such as the present challenge of fuel cell applications. For example, this central aspect was recently remarked by the Royal Swedish Academy of Sciences, awarding to Gerhard Ertl with the Nobel Prize in chemistry for 2007 for his studies of fundamental molecular processes on gas-solid interfaces. In relation to this work, research in theoretical modeling will provide a deeper understanding on the relations among concerned complex phenomena. A better CWR configuration must be obtained if is incorporated information from basic research in areas such as thermodynamic equilibrium and its relation with heterogeneous catalysis, or molecular interaction at catalytic surface.

Chapter 7: Conclusions

A-1 Heat and Mass Transport Constrains

Principal constrains caused by heat and mass transport, presents in catalytic systems under study, are described in this section. Two relevant cases are presented: single pellet and catalytic plate.

A1-1 Heat and Mass Diffusion Limitations inside Catalyst Pellets

Transporting disguises within a catalyst particle may be caused by four different possible combinations among mass/heat transports and internal/external paths. It is used an approach recommended on classical references of chemical reaction engineering (Fogler, 2001; Froment, 1990; Carberry, 1975). Figure A1-1 illustrates two possible resistances under a catalyst particle in a gas stream. First, effect caused by concentration gradient inside an isothermal pellet is considerate on figure A1-2. Then, non-isothermal reaction is discussed on figure A1-3.

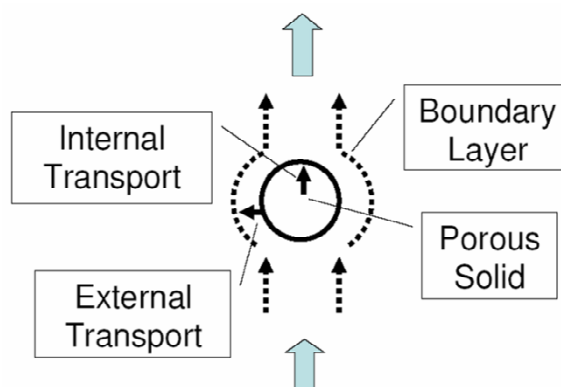


Figure A1-1 Possible trajectories for mass/heat transport using as framework a catalyst particle into a convective gas stream. Internal transport (intra-particle) basically implies diffusion through a porous media; while external transport involves a balance between diffusion and convection processes.

Isothermal reaction

This case represents the interaction between two kinds of phenomena: reaction on catalyst pellet coupled with fluid diffusion from catalyst surface to active sites on catalyst pores (internal transport). The simplest case is a first order reaction onto a slab geometry catalyst. The mass balance can be represented by the set of equations (A1-1) as follows,

$$\frac{d}{dz} \left(D_{e,j} \frac{dC_j}{dz} \right) = (kC_j) \cdot \rho_s \quad \text{Mass Balance} \quad (\text{A1-1a})$$

$$(C_j)_{y=R} = C_S \quad \text{Boundary condition at the catalyst wall} \quad (\text{A1-1b})$$

$$\left(\frac{dC_j}{dy} \right)_{y=0} = 0 \quad \text{Boundary condition at the catalyst center} \quad (\text{A1-1c})$$

It is a common practice to relate geometry and material parameters (k , De , ρ , and L) through Thiele modulus, ϕ , which is a dimensionless factor defined as,

$$\phi = L \sqrt{\frac{k\rho_s}{D_e}} \quad (\text{A1-2})$$

The equation (A1-1) indicates that there is a concentration profile in the pellet. Diffusion resistance does not allow the reactant to be transported through porous solid as quickly as the reaction in the active sites takes place. In consequence, if the concentration gradients between surface and bulk catalyst increase, higher the resistance to diffusion. Figure A1-2a shows the analytical solution of eq (A1-1) under isothermal conditions. The concentration profile is expressed as the ratio between radial and surface concentrations in function of the radial position. Thiele modulus, ϕ , is a measure of the diffusion limitations; higher ϕ values correspond to lower diffusion resistance compared with the reaction rate. At higher values of ϕ the concentration profile is accentuated; while at lower values of ϕ , the profile is flat.

In addition, it is useful to employ a factor to account for diffusion effects; then the effectiveness factor is defined as the ratio between reaction rate with diffusion resistance - $r_j(obs)$ - and reaction rate at surface concentration - $r_j(C_{j,s})$ -, written as,

$$\eta = \frac{r_j(obs)}{r_j(C_{j,s})} \quad (\text{A1-3})$$

as shown figure A1-2b, η approach to 1 at lower ϕ , that means as smaller is the catalyst particle, easier is the diffusion and the reaction rate must be the limiting factor. While at higher values of Thiele modulus, effectiveness is closer to 0, which means that concentration at surface is strongly limited by diffusion. Results are similar for other kind of geometries, such as spherical or cylindrical (Froment, 1990).

Otherwise, external mass transfer can be consider using the same approach, but including an additional diffusion term into the boundary condition, to reflect the mass

diffusion between bulk fluid and solid particle. Then, the boundary condition at the surface by combining external and diffusion resistances is expressed as,

$$\frac{d}{dz} \left(D_{e,j} \frac{dC_j}{dz} \right)_s = k_g (C_{j,0} - C_{j,s}) \quad (\text{A1-4})$$

where $C_{j,s}$ is unknown surface concentration, and $C_{j,0}$ is the bulk concentration. The overall efficiency, η_g , is computed in terms of Thiele modulus, ϕ , efficiency, η , and using other dimensionless group for mass transfer, the modified Sherwood number, Sh_m . The expressions on equations (A1-5) and (A1-6) present Sh_m definition and global effectiveness factor η_g ,

$$Sh_m = \frac{k_g \cdot L}{D_{e,j}} \quad (\text{A1-5})$$

$$\frac{1}{\eta_g} = \frac{1}{\eta} + \frac{\phi^2}{Sh_m} \quad (\text{A1-6})$$

as shown on figure A1-2c, an increase on mass transfer rate (higher Sh_m) increases global efficiency at fixed value of Thiele modulus.

An important application of theoretical models on figure A1-2 is that serves as guide for predicting if experimental reaction rate is expected to be limited by diffusion limitation or not. The Weisz-Prater criteria is a classical test for evaluating internal diffusion, expressed as follows,

$$C_{WP} = \eta \phi^2 = \frac{-r_j(ops) \rho_s R^2}{D_e C_{j,s}} \quad (\text{A1-7})$$

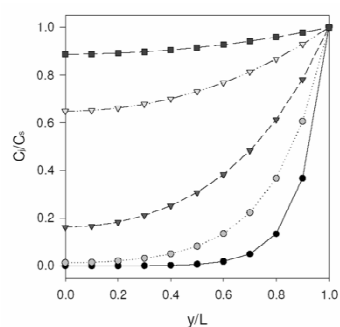
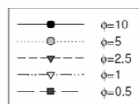
where D_e is effective diffusivity, $C_{j,s}$ is concentration at the catalyst surface, and R is catalyst ratio. If C_{WP} is lower than 1, then diffusion limitations are expected to be important (Fogler, 2001). On the other hand, if C_{WP} is higher than 1, usually there will not be significant limitations, but on some cases a more detailed analysis is required (Froment, 1990).

Mears criteria is other classical test for evaluating external diffusion as follows,

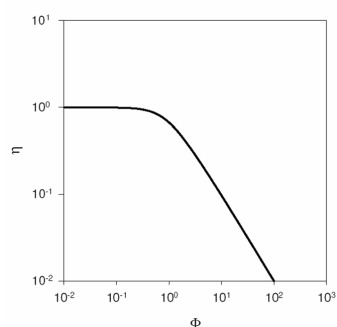
$$\frac{-r_A(ops) \rho_b R n}{k_c C a_b} < 0.15 \quad (\text{A1-8})$$

Where n is reaction order, R refers to particle radius, ρ_b is the bed density, ρ_c is catalyst density and $-r_A(ops)$ is the measured reaction rate. If this expression is accomplished, it is expected to found that concentration gradients between bulk flow and external catalyst surface are not influencing significantly the reaction rate.

(a) Concentration profile for linear kinetic and internal diffusion at isothermal conditions



(b) Effectiveness with internal diffusion at isothermal conditions



(c) Global effectiveness by coupling internal and external diffusion, at isothermal conditions

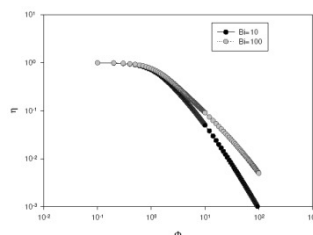


Figure A1-2 Disguises caused by internal diffusion on an isothermal catalyst pellet: (a) surface to radial concentration ratio as function of axial position; (b) efficiency factor for slab geometry as function of Thiele modulus (c) Global effectiveness by coupling internal and external diffusion, under isothermal conditions

Non-isothermal reaction

Similar theoretical treatment can be performed to account for thermal gradients inside catalyst particle. Figure A1-3 presents internal and global efficiencies for non-isothermal reactions. The starting point is, again, the mass and heat balances at the catalyst pellet. Using slab geometry, these equations are as follow,

$$\frac{d}{dz} \left(D_{e,j} \frac{dC_j}{dz} \right) = r_j(C_j, T) \cdot \rho_s \quad (\text{A1-9})$$

$$-\frac{d}{dz} \left(\lambda_e \frac{dT}{dz} \right) = (-\Delta H_{RX}) \cdot r_j(C_j, T) \cdot \rho_s \quad (\text{A1-10})$$

where λ is the pellet thermal conductivity, normally around $4 \cdot 10^{-3} \text{ J s}^{-1} \text{ cm}^{-1} \text{ K}^{-1}$. These equations must be solved simultaneously because are couple through the reaction rate term. For complete conversion, $C_j=0$, the maximum temperature difference is

$$\frac{\Delta T_{\max}}{T} = \frac{(-\Delta H_{RX})D_{e,j}C_{j,S}}{\lambda_e T_s} \equiv \beta \quad (\text{A1-11})$$

where concentration and temperature are evaluated at surface conditions, and β is the dimensionless Prater number that represents the maximum relative expansion or reduction, in pellet temperature. Another useful dimensionless group is the Arrhenius number, defined as

$$\gamma = \frac{E}{RT} \quad (\text{A1-12})$$

where R is the ideal gas constant.

It is important to point out that exothermic reactions ($\beta > 0$) can present an effectiveness factor higher than 1, as a consequence of favorable temperature difference between pellet center and it surface. On the other hand, on endothermic reactions ($\beta < 0$) the efficiency is always lower than 1, because temperature will be lower inside pellet than on the surface. Figure A1-4a shows results for the effectiveness factor in terms of internal and non-isothermal catalyst particle. For large β and a narrow range of γ , there are three possible values of ϕ , because the term of heat generation on eq (A1-10) produces a non-linear equation which has multiple solutions under steady state. Figure A1-3b presents the global effectiveness by coupling simultaneous mass/heat diffusion with external/internal gradients; which differs significantly from previous cases with only internal mass diffusion, or only thermal diffusion, figures A1-2b and A1-3a respectively.

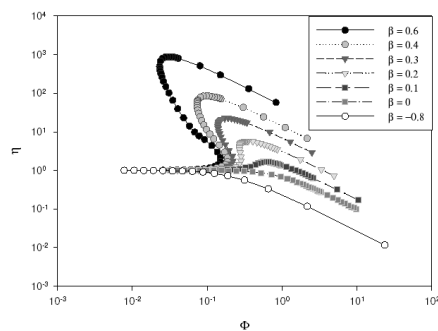
Another criteria proposed by Mears considers that temperature in the bulk flow is similar to the external catalyst surface if next expression is satisfied,

$$\left| \frac{[-\Delta H_{RX}][r_A(obs)\rho_b R][E]}{hT^2 R_g} \right| < 0.15 \quad (\text{A1-13})$$

where h is the heat transfer coefficient, R_g is the gas constant, ΔH_{RX} is the reaction enthalpy, and E is the activation energy.

In conclusion, mass and thermal diffusion could influence significantly on the reaction rate for endothermic and exothermic reactions. Then, it is important to reduce as much as possible the options of transport disguises by configuring the reactor in an appropriated way.

(a) Internal Effectiveness under Non-Isothermal conditions



(b) Global Effectiveness by coupling two kinds of mass diffusion: External Non-Isothermal and Internal Isothermal

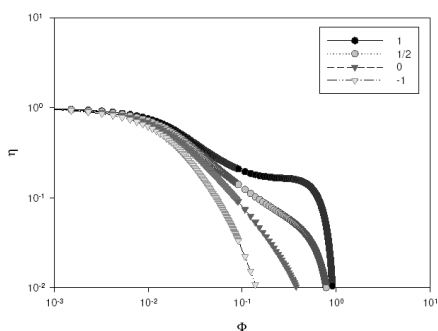


Figure A1-3 Effects of external and internal thermal and mass diffusion on catalyst effectiveness for linear kinetics: (a) Internal Non-Isothermal catalyst, with $\gamma=30$ and diverse values for β , (b) Simultaneous thermal and mass diffusion: External Non-Isothermal and Internal Isothermal; $\gamma=10$ and four levels for β

A1-2 Effectiveness factors for a Catalyst Plate

Effectiveness factors for the catalyst plate configuration have been studying by Montané et al (2008) assuming a simplified one-dimensional model for the reaction system. Next section presents their main results; in particular, those directly related to the Catalytic Wall Reactor employed in the experiments presented in this thesis (chapter 6).

1D model is schematized in Figure A1-4. The simultaneous reaction and diffusion inside the catalyst plate was described by the energy balance and individual mass balances - equations (A1-14) and (A1-15)-, where the effective thermal conductivity (λ_e) and diffusivities inside the catalysts (D_{ej}) were assumed to be independent of temperature and gas composition. nR is the number of reactions occurring simultaneously in the catalyst, r_i is the rate of the i^{th} reaction, ΔH_{Ri} is the enthalpy of the i^{th} reaction, and R_j is the global rate of reaction of species j . Boundary conditions for the integration of the set of differential equations that describe the system -equations (A1-16) to (A1-19)- included mass and heat transfer from the bulk gas to the catalyst plate surface, and assumed that the catalyst layer was

deposited on top of a metal surface that had a constant temperature (T_W), equal to the temperature of the bulk gas (T_G).

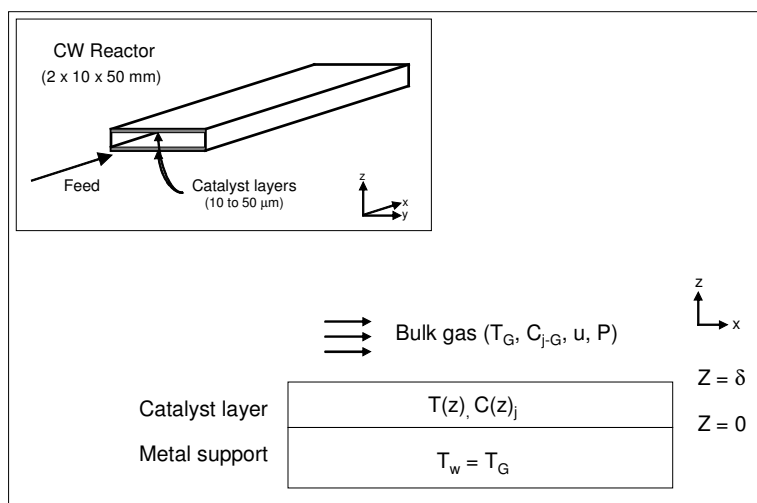


Figure A1-4 Schematic diagram of the catalytic-wall reactor and the simplification to a one-dimensional model.

$$\frac{d^2T}{dz^2} = \frac{\sum_{i=1}^{nR} (-r_i)(\Delta H_{Ri})}{\lambda_e} \quad (\text{A1-14})$$

$$\frac{d^2C_j}{dz^2} = \frac{-R_j}{D_{ej}} \quad (\text{A1-15})$$

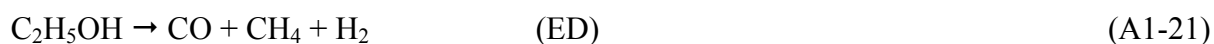
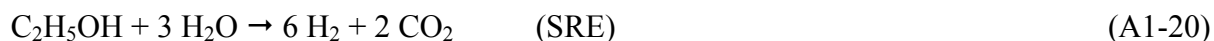
$$\frac{dC_j}{dz} = \frac{k_{mj}}{D_j} (C_{jG} - C_j); \text{ at } z = \delta \quad (\text{A1-16})$$

$$\frac{dT}{dz} = \frac{h_L}{\lambda_G} (T_G - T); \text{ at } z = \delta \quad (\text{A1-17})$$

$$T = T_W = T_G; \text{ at } z = 0 \quad (\text{A1-18})$$

$$\frac{dC_j}{dz} = 0; \text{ at } z = 0 \quad (\text{A1-19})$$

The reaction rates were calculated using the kinetic equations from Sahoo et al. (2007), who proposed a model based on three main simultaneous reactions, ethanol steam-reforming (SRE), ethanol decomposition (ED) and water-gas shift (WGS):



Average mass (k_{mj}) and heat transfer (h_L) coefficients were calculated using the correlations proposed by Hawthorn (1974). Gas properties, such as thermal conductivity, viscosity, and molecular and effective diffusion coefficients, were estimated according to the methods recommended by Reid et al. (1987). Integration of the differential equations was performed numerically with MatLab.

After calculation of the concentration and temperature profiles inside the catalyst layer, the internal (η_j) and the global (Ω_j) effectiveness factors for species j were calculated according to equations (A1-23) and (A1-24), respectively. The internal effectiveness factor for species j was calculated as the ratio between the actual amount of j that reacted in the catalyst (M_j), and the amount of j that should react if all the catalyst were at the concentration and temperature of the surface ($M_{j,\delta}$). Similarly, the global effectiveness factor was calculated as the ratio between M_j and the amount of j that should react if all the catalyst were at the temperature and concentration of the bulk gas ($M_{j,G}$).

$$\eta_j = \frac{M_j}{M_{j,\delta}} = \frac{\int_{z=0}^{\delta} R_j dz}{\delta \cdot R_{j,\delta}} \quad (\text{A1-23})$$

$$\Omega_j = \frac{M_j}{M_{j,G}} = \frac{\int_{z=0}^{\delta} R_j dz}{\delta \cdot R_{j,G}} \quad (\text{A1-24})$$

Reaction rates, and consequently effectiveness factors, are influenced by multiple variables of the system: thickness of the catalyst layer, gas composition, temperature, pressure, and gas velocity. Therefore, the effect of each variable was examined in detail. Reaction rates are higher at low conversion because the concentration of ethanol and water are high and the concentration of products low. This is the situation where it is most likely that mass and heat transfer may limit the observed reaction rate of the system. Hence, the effectiveness factors were first calculated for a gas mixture that corresponds to an ethanol conversion of 5%, at a steam to carbon (SC) ratio of 2, atmospheric pressure and a gas velocity of 10 m/s. The thickness of the catalyst layer was varied between 5 and 1000 μm , and the gas temperature was from 673 to 973K.

Figure A1-5 shows that the internal effectiveness factor was close to one for catalyst layers thinner than 50 μm at all temperatures, but there was a significant drop at larger thickness due to transport limitations inside the catalyst layer. The global effectiveness factor,

which also accounts for the external interfacial transport limitations, was always significantly lower than the internal factor even for the thinnest catalyst layers at high gas temperature, showing that the interfacial mass and heat transfer limitations were playing a dominant role. Figure A1-6 shows the dimensionless temperature profiles inside the catalyst plate. When the thickness was below $100\mu\text{m}$ the catalyst layer may be considered almost isothermal, since the temperature difference between the catalyst surface and the bulk gas was of only 1K for a gas temperature of 973K . For thicker catalyst layers, the temperature difference augmented considerably due to heat transfer limitations between the gas and the surface of the catalyst layer. Figure A1-7 shows the dimensionless concentration profiles for ethanol. Below 773K ethanol concentration was almost constant and equal to that of the gas phase for catalyst thickness below $100\mu\text{m}$. At higher temperatures the occurrence of mass-transfer limitations became dominant. For catalyst thickness below $50\mu\text{m}$ the ethanol concentration inside the catalyst was almost uniform but clearly below that of the bulk gas, which point to the occurrence of external mass-transfer predominantly. At a catalyst thickness above $100\mu\text{m}$ the internal mass-transfer limitations became dominant and steeper concentration profiles inside were observed inside the catalyst layer. An equivalent behavior was obtained for the concentration profiles of water and reaction products.

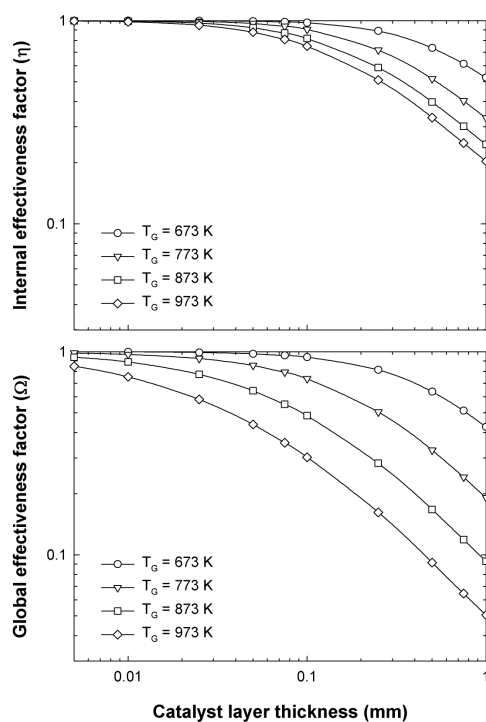


Figure A1-5 Steam reforming of ethanol at an SC ratio of 2 and atmospheric pressure. Internal (η) and global (Ω) effectiveness factors for ethanol at gas temperatures of 673, 773, 873 and 973K, and a thickness of the catalyst layer between 5 and $1000\mu\text{m}$.

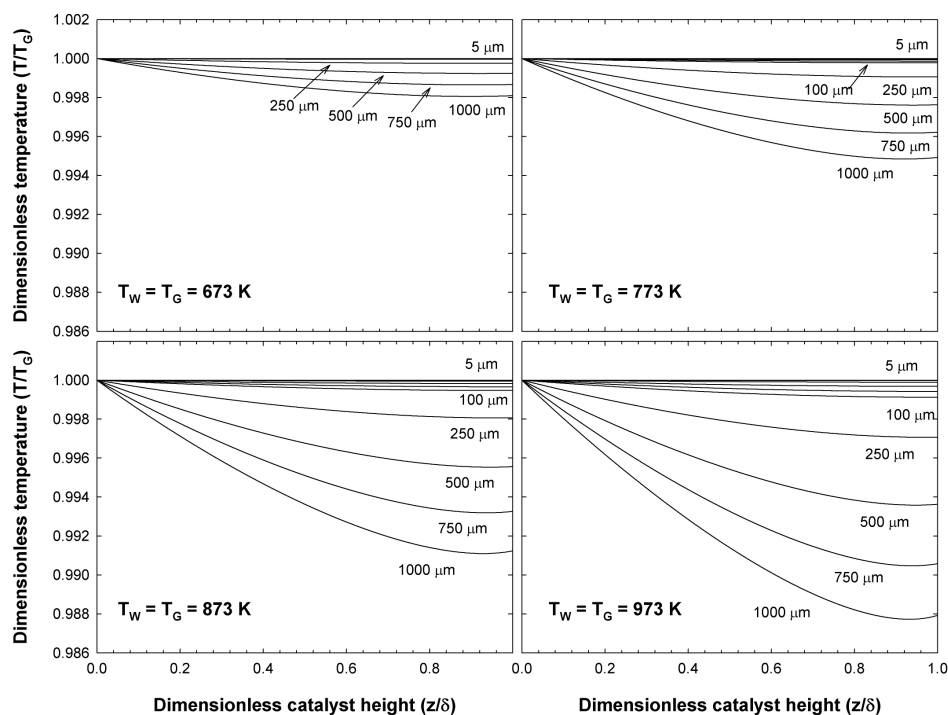


Figure A1-6 Steam reforming of ethanol at an SC ratio of 2 and atmospheric pressure. Dimensionless temperature profiles in the catalyst film at gas temperatures of 673, 773, 873 and 973K, and a thickness of the catalyst layer of 5, 10, 25, 50, 75, 100, 250, 500, 750 and 1000 μm .

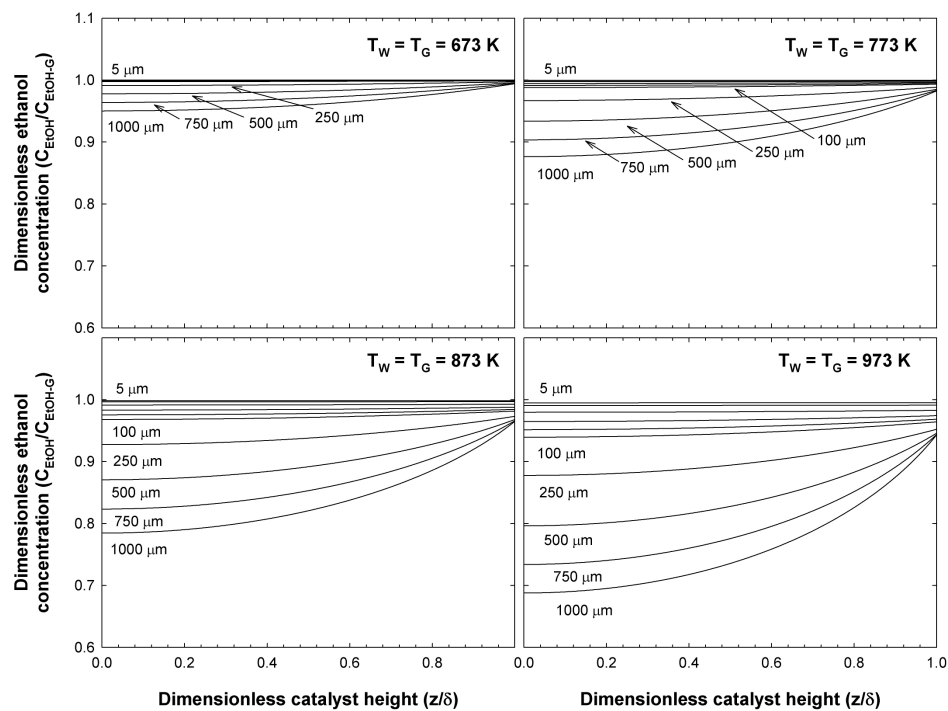


Figure A1-7 Steam reforming of ethanol at an SC ratio of 2 and atmospheric pressure. Dimensionless ethanol concentration profiles in the catalyst film at gas temperatures of 673, 773, 873 and 973K, and a thickness of the catalyst layer of 5, 10, 25, 50, 75, 100, 250, 500, 750 and 1000 μm .

In conclusion, results show that it is possible to perform reforming experiments that are almost free of heat and mass transport limitations in a Catalytic Wall Reactor using a thickness of the catalyst layer below 50 μm .

References

1. Carberry, James J. Chemical and catalytic reaction engineering. New York: McGraw-Hill. 642 p. 1976.
2. Fogler, H. Scott. Elements of chemical reaction engineering. 4th ed. Upper Saddle River, NJ: Prentice-Hall. 1080 p. 2006.
3. Froment (1989). Chemical reactor: analysis and design. Wiley. New York. 664 p. 1990.
4. Hawthorn, AIChE Symp. Ser. 70 (1974) 428.
5. D. Montané and J.A. Torres. "Ni based Catalytic Plates Prepared by Washcoating Method". Universitat Rovira I Virgili. Department d'Enginyeria Química. Work in progress, to be submitted for publishing on February 2008.
6. D.R. Sahoo, S. Vajpai, S. Patel and K.K. Pant. Kinetic modeling of steam reforming of ethanol for the production of hydrogen over Co/Al₂O₃ catalyst. Chemical Engineering Journal 125 (2007) 139-147.
7. R.C. Reid, J.M. Prausnitz and B.E. Poling. The properties of gases and liquids. 4th edition. McGraw-Hill, 1987.

A-2 Catalyst Preparation Procedures

A2-1 Preparation of Powder Catalysts for Screening SRE

Objective

Preparation of the catalyst Ni/La₂O₃/Al₂O₃ by the impregnation technique.

Material

Agimatic E.
Erlenmeyer 250 ml.
Oven.

Reactives

Niquel and lanthanum nitrate salts.
Alumina (γ -Al₂O₃).
Ultrapure water.
Gases (Hydrogen and Nitrogen).

Procedure

- 1. First Impregnation of the support (γ -Al₂O₃) with La.*
 - 1.1. Prepare the aqueous slurry using the appropriate quantities of γ -Al₂O₃ and La.
 - 1.2. Mixing during 30 minutes.
 - 1.3. Evaporate the water at 70°C and mixing at 300 rpm (6 h approximately)
 - 1.4. Dry during the night at 105°C (aprox. 14 h).
- 2. First Oxidation*
 - 2.1. If the oven presents carbon impurities, heat at 900°C during 2 h and wait until it reach atmospheric temperature again.
 - 2.2. Oxidate the La-Al₂O₃ at 900 °C during 30 h employing a 2°C/min ramp.
- 3. Second Impregnation of the support (La₂O₃/ γ -Al₂O₃) with Ni.*
 - 3.1. Prepare the slurry using the appropriate quantities of La/ γ -Al₂O₃ and Ni.
 - 3.2. Mixing during 30 minutes.
 - 3.3. Evaporate the water at 70°C and mixing at 300 rpm (6 h approximately).
 - 3.4. Dry during the night at 105°C (aprox. 14 h).
- 4. Second Oxidation*
 - 4.1. If the oven presents carbon impurities, heat at 500°C during 2 h and wait until it reach atmospheric temperature again.
 - 4.2. Oxidate the Ni/La₂O₃-Al₂O₃ at 500°C during 2 h employing a 1°C/min ramp.
5. Reduce under H₂ atmosphere at 500°C during 5 h; using a ramp of 1°C/min.

A2-2 Preparation of Catalytic Plates for Testing the CWR

Objective

To impregnate the metallic plate with a Ni/Al₂O₃ catalyst.

Material

Erlenmeyer 250 ml

Oven

Reactives

Bohemite, Ni catalyst supported on alumina (Ni/ γ -Al₂O₃)

Nitric acid solution (0.4% wt)

Ultrapure water, acetone.

FeCrAlloy^(R).

Gases (Hydrogen and Nitrogen).

Procedure

- Bohemite solution preparation.*
 - 1.1. Prepare an aqueous solution with 0,4% HNO₃ weight.
 - 1.2. Prepare a solution of 10% weight Bohemite using the 0.4% HNO₃ solution.
 - 1.3. Mixing during 10 min.
 - 1.4. Wait for two days. Take measures of pH and viscosity.
- Impregnation with bohemite.*
 - 2.1. Clean the FeCrAlloy^(R) plates with acetone and also using the ultrasound bath with ethanol as solvent.
 - 2.2. Oxide the plates at 900°C for 10 h employing a ramp of 3 °C/min from T_{amb} to 600°C and 0.5 °C/min from 600°C until 900°C.
 - 2.3. Clean again.
 - 2.4. Apply the dip coating procedure: immersion during 15 s and retire with a velocity around 3cm/min.
 - 2.5. Dry at ambient temperature during 30 min.
- Impregnation with γ -alumina.*
 - 3.1. Prepare a slurry using the appropriate proportion of: {aqueous solution, 10% HNO₃}/ $\{\gamma$ -Al₂O₃} and {H₂O}/{(Ni/ γ -Al₂O₃)}. Optionally, include additional binders, such as PVA.
 - 3.2. Mixing during 16 h in a close reactor at ambient temperature.
 - 3.3. Employ the paint applicator equipment: let the plate immersed under the slurry during 1 min and move the applicator using a velocity around 3cm/min.
 - 3.4. Dry the plates at 105 °C during 5 min.
- Reduce under H₂ atmosphere at 500°C during 5 h; using a ramp of 1°C/min.

Date:

Series:

Time

Sample	Mixing [min]		Evaporating [h]		Drying [h]		Calcinations [h]		Reduction [h]	Observations
	M1	M2	E1	E2	S1	S2	C1	C2	R1	

Date:

Series:

Weight [g]

Sample	m_{la} (La Salt weight)	m_{ni} (Ni Salt weight)	m_{al} Al_2O_3	m_{la-al} La_2O_3/Al_2O_3	m_{final}	Observations

Date:

Series:

Temperature [°C]

Sample	M1	M2	E1	E2	C1	C2	R1	Observations